Electromechanical cooling and parametric amplification of an ultrahigh-Q mechanical oscillator

Thibault Capelle

THÈSE DE DOCTORAT
DE SORBONNE UNIVERSITE

Spécialité : Physique

École doctorale : « Physique en Île-de-France »

réalisée

Laboratoire Kastler Brossel

présentée par

Thibault Capelle

pour obtenir le grade de :

DOCTEUR DE SORBONNE UNIVERSITE

Sujet de la thèse :

Electromechanical cooling and parametric amplification of an ultrahigh-Q mechanical oscillator

devant le jury composé de :

M.	Eddy COLLIN	Rapporteur
Mme.	Eva Weig	Rapporteuse
M.	Antoine HEIDMANN	Directeur de thèse
M.	Samuel DELEGLISE	Co-Directeur de thèse
M.	Thibaut JACQMIN	Co-Directeur de thèse
M.	Albert SCHLIESSER	Examinateur
M.	Bernard Perrin	Examinateur

Contents

Remerciements

Je tenais avant tout à remercier l'ensemble des personnes qui ont rendu ce manuscrit possible et qui m'ont soutenu durant ces quatre années de travail assez intenses. Tout d'abord, mes encadrants : Samuel, Thibaut, Tristan, Pierre-Françis et Antoine pour vos conseils et votre accompagnement tout autant que pour les discussions animées du midi ou du soir. Mes collègues, Rémi, Édouard, Ferhat et Michael pour le soutien mutuel et l'accompagnement jusque dans certains cortège :)

Les mécaniciens, Carou, Sébastien et Gaël sans qui de nombreuses pièces des expériences ici présentées n'auraient jamais existé. L'atelier d'électronique aussi : Loïc et Brigitte, qui ont subi une monopolisation presque constante du heat gun sans rechigner.

Les services de cryogénie de la fac, sans qui bien peu de choses auraient été possible, Christian, Florin, et bien sur une mention spéciale pour l'inénarrable Richard et ses expressions fleuries. Les services administratifs, bien sur : Laetitia, Romain, Stéphanie et bien sur Valérie qui nous a tou.te.s communiqué sa bonne humeur. Bonne chance aussi à Viki pour ses études de socio !

Les échantillons dont nous allons parler ont été réalisés dans différentes salles blanches parisienne avec l'aide de nombreux.ses technicien.ne.s et ingénieur.e.s, qui ont passé des heures et des heures à me former, m'aider et me conseiller dans l'élaboration des recettes que je vais décrire. Je tiens tout particulièrement à les remercier : Michael, José et Aurélie pour le département de physique de l'ENS, Loic et Erwann pour la salle blanche de l'INSP, et Christine et Faouzi pour la salle blanche de l'Observatoire de Paris.

Je tiens également à remercier celles et ceux avec qui j'ai partagé des expériences politiques assez intenses (et parfois sportives :)), à l'extérieur du laboratoire dans le comité de mobilisation de l'Université, mais aussi dans le laboratoire lui-même au sein du CGL dont je suis ma foi très fier d'avoir contribué à la création. Tamara, bien sur, qui m'a suivi dans toutes ces aventures, mais aussi Valentin, Léo, Ferhat, Simon, Thibault, Pauline, Lucile, Dominique et tant d'autres !

Finalement, je n'aurais probablement pas tenu aussi longtemps en thèse sans le soutien indéfectible de mon entourage le plus proche, d'abord ma famille, qui a été très présente pendant ces quatre dernière années, et qui m'a encouragé durant tout mon parcours scientifique. Enfin, je pense évidemment à toi Suzanne, que je ne remercierai jamais assez de m'avoir supporté pendant tout ce temps :)

Introduction

In 1607, young german physicist Johannes Kepler made detailed observations of a comet that is known nowadays as the Halley comet. In particular, he noticed in his book "De Cometis", published in 1619 [Kep19], that the tail of the comet was systematically pointing in a direction opposite to the sun. He conjectured that "the tail of a comet is composed by a matter the Sun rays are chasing away by their impulse out of the body of the comet". This hypothesis is the first known evocation of the force light can induce upon matter. It is only in the 19th century, with the discovery of Maxwell's equations [Max73], that the scientific community reached a consensus on the existence of this force, denominated radiation pressure.

Figure .1: A picture of the Halley comet taken during its last apparition, in 1986.

The first laboratory experiments demonstrating radiation pressure were performed in 1901[NH01]. The concept gained in interest in the late 1970s with the proposal from Ashkin[Ash78] to use strongly focused laser beams to control dielectric particles. Crucially, the proposal noticed that this force can be used to cool down the particles. Laser cooling then rapidly became a standard technique in the atomic physics community [Ste86].

In parallel, the action of light on mechanical resonators was first theoretically[BM67] and experimentally[BMT70] investigated by Braginski, who predicted that the damping of the resonator could be modified by radiation pressure. The apparition of extra damping or amplification was induced by the complex feedback mechanism at play in a Fabry-Perot resonator involving a movable mirror.

In the following decades, the interest in coupling light to mechanical resonators grew significantly. This optomechanical coupling was first actively studied in the context of interferometric measurements, where the position of a mirror can be inferred with high precision by measuring the phase acquired by light upon reflection. In this case,

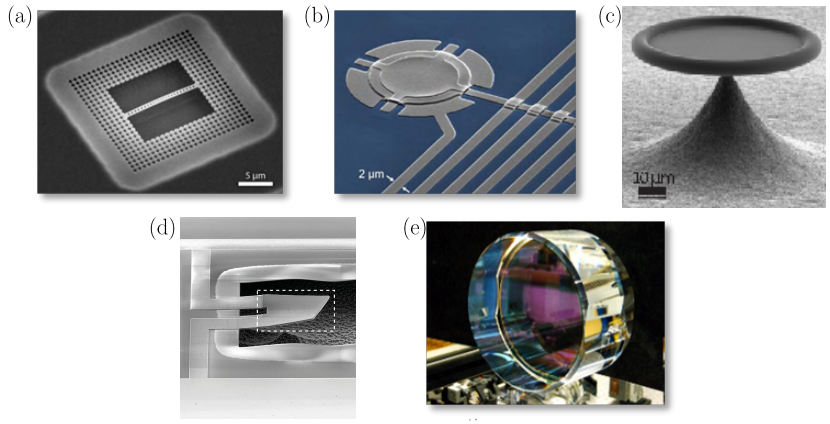

Figure .2: Pictures of different optomechanical systems: (a) A Silicon nanobeam patterned with a 1D-periodic array of holes. A defect at the center is colocalizing a phononic and a photonic mode in a small mode volume [CASN+11]. (b) One electrode of the capacitance of a microwave LC circuit is free to move in a drum mode [TdL+11] (c) A silica microtoroid couples an optical whispering gallery mode to a mechanical breathing mode of the disk [SRA+08] (d) The flexural mode of an aluminium nitride plate is modifying the capacitance of an LC circuit [OHA+10] (e) The meter-scale mirrors of the gravitational wave interferometers are coupled via radiation pressure to their arm cavities

the competition between the quantum fluctuations of light and the effect of radiation pressure gives rise to a lower limit to the sensitivity achievable by such system[Cav81]. This sensitivity limit, directly related to Heisenberg's uncertainty principle, has been recently reached experimentally in gravitational wave interferometers [MWG+20]. The corresponding extreme sensitivity to relative length variations of $h \sim 10^{-22}$ has enabled in 2015 the first detection of a gravitational wave[CC16]: a very small deformation of space time induced by the merging of a binary black hole system.

Alternatively, the possibility to use radiation pressure to control the motion of the mechanical resonator itself has triggered a new line of research, that has evolved over the last 20 years into a very active field, coined quantum optomechanics. In strong analogy with cold atom experiments, the main objective is to control the quantum state of the mechanical system thanks to its interaction with light. A number of mechanical systems, of various shapes and masses have been coupled to various electromagnetic resonators, both in the optical and the microwave domain. Important results include the first demonstration of ground state cooling in 2011 [TdL+11], the optomechanical generation of squeezed light [SNGH+13, NTM+17], entanglement between an electromagnetic field and a mechanical resonator[PTSL13], or entanglement between two mechanical oscillators [OKDP+18].

The motivations for these researches are numerous: from a fundamental point-of-view, bringing a macroscopic mechanical resonator in a well-controlled quantum state could enable to investigate potential gravity-induced decoherence mechanisms [KPJ+08]. Some have even speculated that such a quantum-gravitational effect might be the key to elucidate the quantum-to-classical transition [Pen14]. On the other hand,

quantum control of mechanical resonators opens interesting perspectives for sensing and quantum information applications. For instance, Magnetic Resonant Force Microscopy exploits the extreme sensitivity of nano-mechanical resonators to an external force to image spins in a solid-state matrix. A sensitivity down to the single electronic spin has even been demonstrated by a pioneering experiment performed at IBM [RBMC04]. Improving the sensitivity by another three orders of magnitude, down to the single nuclear-spin level, would enable imaging of individual bio-molecules in-situ, revolutionizing pathogenesis and the drug discovery process in general [SGB$^+$95]. The universal coupling capabilities, long-lifetime, and compactness of mechanical resonators is also interesting for quantum information applications. For instance, mechanical resonators are able to store fragile quantum states in long-lived mechanical oscillations, and could thus be used as quantum memories [CKY$^+$18]. They have also been proposed as a bridge linking together incompatible quantum systems, such as optical and microwave photons [APP$^+$14].

During this thesis, we have developed a new optomechanical platform, based on a suspended silicon nitride membrane initially developed in the group of J. Harris [ZSJ$^+$08]. This mechanical resonator is a very popular mechanical system as it combines a very high mechanical quality factor, low mass, and it can be easily functionalized with a nano-magnet for spin-sensing applications [FMR$^+$19]. Furthermore, it features low optical losses and can thus easily be interfaced with an optical cavity, as initially demonstrated in Yale [ZSJ$^+$08]. In this work, we have been able to measure the properties of such a mechanical system in the 10 - 300 mK range by coupling it to a superconducting resonant cavity, and found exceptional mechanical quality (the measured lifetime of ~ 30 s exceeds by 2 orders of magnitude that of electromechanical systems previously interfaced with microwave photons). Furthermore, we have used microwave photons as a cold bath to reduce the thermal occupation of the membrane approximately thousand-folds. These experiments are a first step towards more complex manipulations of the mechanical quantum state. In particular, the choice of a superconducting resonator, rather than an optical cavity, is guided by the ambition to use the rich toolbox of superconducting circuit technologies as a non-Gaussian resource to generate non-classical states. As an example, we have developed, in collaboration with the cQED group of ENS, a single microwave photon detector that could be used to herald non-classical states of the mechanical resonator.

This manuscript is divided in 7 chapters: In chapter I, we derive the theoretical framework of optomechanics and introduce some useful concepts to describe our experimental results. In chapter II, we describe and characterize the mechanical properties of the suspended membranes used throughout this work. These resonators, vibrating in the MHz range, are coupled to GHz photons by forming a mechanically compliant microwave cavity. These microwave electromechanical systems, their micro-fabrication, and the measurement setup used for their characterization is described in chapter III. Chapter IV is dedicated to the microwave and electromechanical characterization of these systems. We present our cooling experiment in chapter V, along with some proposed optimizations. Having demonstrated most of the aspects of these optimizations, we are confident that they will enable us to reach the quantum ground state shortly. The main loss mechanism of the planar superconducting resonators employed in this work is traceable to a bath of two-level systems [WHW$^+$09]. In chapter VI,

we describe an original pump-probe technique [CFI$^+$20] to characterize the associated non-linear damping. Finally, we describe future directions of the experiments in chapter VII. This includes a mechanical optimization by "soft-clamping" of the membrane—-a technique that was originally introduced by the Copenhaguen group—-the single microwave photon detector developed in collaboration with ENS, and the possible heralding experiments enabled by this device.

Chapter I: Theory of cavity optomechanics

In this section we derive some theoretical background from the field of optomechanics that will be useful for understanding the results of this PhD. Although the major part of those phenomena could have been understood using a classical formalism, we will consistently use a quantum mechanical picture in this derivation.

I.1: A quantum harmonic oscillator

A mechanical resonator can be fully described by a set of normal modes, each of them represented by a position operator $\hat{\mathrm{x}}$ (taken as a small excursion from an equilibrium position, and for the sake of simplicity assumed here to be unidimensional), a mass m, a mechanical frequency $\Omega_m/2\pi$, a loss rate Γ_m and a momentum operator $\hat{p}$. In the quantum framework, those operators do not commute, and we have $[\hat{\mathrm{x}}, \hat{p}] = i\hbar$. We assume that this resonator undergoes such an elastic force that we are able to write down its Hamiltonian in the following form:

$$\widehat{H} = \frac{\hat{p}^2}{2m} + \frac{m\Omega_\mathrm{m}^2}{2}\hat{x}^2 \tag{I.1.1}$$

If now we introduce the operators [CtBF18]:

$$\hat{b} \overset{\text{def}}{=} \frac{1}{\sqrt{2}}\left(\sqrt{\frac{m\Omega_\mathrm{m}}{\hbar}}\hat{x} + i\frac{1}{\sqrt{m\hbar\Omega_\mathrm{m}}}\hat{p}\right) \tag{I.1.2}$$

$$\hat{b}^\dagger \overset{\text{def}}{=} \frac{1}{\sqrt{2}}\left(\sqrt{\frac{m\Omega_\mathrm{m}}{\hbar}}\hat{x} - i\frac{1}{\sqrt{m\hbar\Omega_\mathrm{m}}}\hat{p}\right), \tag{I.1.3}$$

respectively called *annihilation* and *creation* operators, we are able to rewrite the previous Hamiltonian in the form $\widehat{H} = \hbar\Omega_\mathrm{m}\left(\hat{b}^\dagger\hat{b} + \frac{1}{2}\right)$, the constant part stemming from the non commutativity of the two variables $\hat{x}$ and $\hat{p}$. If we consider the eigenvectors $|n\rangle$ of the phonon number operator $\hat{N} \overset{\text{def}}{=} \hat{b}^\dagger\hat{b}$, associated to the eigenvalues $n \in \mathbb{N}$, we

see that the Hamiltonian is diagonal in this basis, called the *Fock basis*, and that the eigenenergies are discrete, with values : $E_n = \hbar\Omega_{\mathrm{m}}\left(n+\frac{1}{2}\right)$.

The energy of the system in a Fock state $|n\rangle$ is that of a set of identical particles of energy $\hbar\Omega_{\mathrm{m}}$. These bosonic particles are called *phonons*. The actions of the previous operators on the Fock states are:

$$\begin{aligned}\hat{b}|0\rangle &= 0\\ \forall n \in \mathbb{N}^*, \hat{b}|n\rangle &= \sqrt{n}|n-1\rangle\\ \forall n \in \mathbb{N}, \hat{b}^\dagger|n\rangle &= \sqrt{n+1}|n+1\rangle,\end{aligned}$$

which explains their denomination : the *creation* operator creates a phonon, whereas the *annihilation* operator destroys one. The non conservative characteristic of this process translates into the fact that those are not Hermitian operators.

We can then compute the mean values of observables $\langle ... \rangle$ using the formula, valid for a system at equilibrium with a thermostat at the temperature T : $\langle A\rangle = \frac{\mathrm{Tr}(Ae^{-\beta H})}{\mathrm{Tr}(e^{-\beta H})} = \frac{1}{Z}\sum\limits_{n\in\mathbb{N}}\langle n|A|n\rangle e^{-\beta E_n}$, where $\beta = \frac{1}{k_{\mathrm{B}}T}$ and Z is called the *partition function* of the system, $Z = \sum\limits_{n\in\mathbb{N}} e^{-\beta E_n}$. For example,

$$\Delta\hat{x}^2 = \langle\hat{x}^2\rangle = \frac{\hbar}{2m\Omega_{\mathrm{m}}}\left\langle \hat{b}^2 + \hat{b}^{\dagger 2} + \hat{b}\hat{b}^\dagger + \hat{b}^\dagger\hat{b}\right\rangle \tag{I.1.4}$$

$$= \frac{\hbar}{2m\Omega_{\mathrm{m}}}\left\langle \hat{b}\hat{b}^\dagger + \hat{b}^\dagger\hat{b}\right\rangle \tag{I.1.5}$$

$$= \frac{\hbar}{m\Omega_{\mathrm{m}}}\left(\left\langle \hat{b}^\dagger\hat{b}\right\rangle + \frac{1}{2}\right) \tag{I.1.6}$$

$$= \frac{\hbar}{m\Omega_{\mathrm{m}}}\left(\frac{1}{e^{\frac{\hbar\Omega_{\mathrm{m}}}{k_{\mathrm{B}}T}}-1} + \frac{1}{2}\right), \tag{I.1.7}$$

where $\frac{1}{e^{\frac{\hbar\omega}{k_{\mathrm{B}}T}}-1} \overset{\mathrm{def}}{=} n_{\mathrm{B}}$ is the *Bose-Einstein statistics*, which yields the number of *bosonic* particles at a given frequency $\omega/2\pi$ for a given temperature T. The constant term $\frac{\hbar}{2m\Omega_{\mathrm{m}}}$, which appears in the right hand side of equation (I.1.7), is a quantum signature. It is a consequence of the *Heisenberg inequalities*, stating that one cannot access a full knowledge of two conjugated variables at the same time ($\Delta\hat{x}\Delta\hat{p} \geq \hbar/2$). In the classical case, the mechanical resonator variance of position can be computed using the equipartition theorem, stating that $\frac{1}{2}m\Omega_{\mathrm{m}}^2\Delta\hat{x}^2 = \frac{1}{2}k_{\mathrm{B}}T$, which gives $\Delta\hat{x}^2 = \frac{k_{\mathrm{B}}T}{m\Omega_{\mathrm{m}}^2}$. The two formulas are compared in figure I.1, where we introduced $x_{\mathrm{ZPF}} \overset{\mathrm{def}}{=} \sqrt{\frac{\hbar}{2m\Omega_{\mathrm{m}}}}$, the typical motion amplitude of the mechanical resonator when emptied of all thermal phonons. ZPF stands for *Zero Point Fluctuations*, and $T_{\mathrm{lim}} \overset{\mathrm{def}}{=} \hbar\Omega_{\mathrm{m}}/k_{\mathrm{B}}$ is the typical temperature below which the quantum nature of this oscillator becomes conspicuous. Indeed, when $T \ll T_{\mathrm{lim}}$, the variance is essentially equal to x_{ZPF}^2, regardless of the temperature, which means that the quantum noise dominates, whereas thermodynamics predicts that the noise of the harmonic oscillator can be arbitrarily low when the temperature is decreased. On the other hand, at high temperature, *i.e.* when $T \gg T_{\mathrm{lim}}$

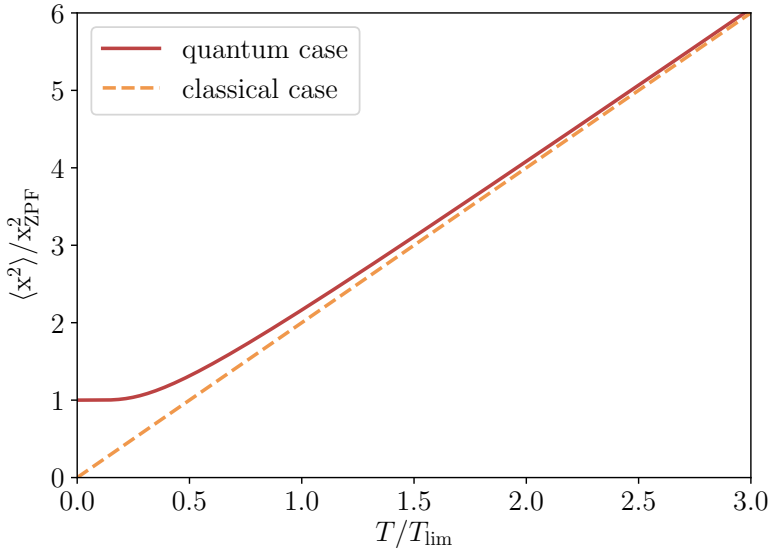

Figure I.1: Mechanical noise $\langle \hat{x}^2 \rangle / x^2_{\mathrm{ZPF}}$ at thermal equilibrium, in the quantum case or in the classical case, versus the temperature measured in unit of T_{lim}

.

the two formulas give the same results, which is expected since the quantum theory must be consistent with the classical one in the high temperature limit.

We will work with resonators whose mechanical frequencies are typically in the MHz range, which gives $T_{\mathrm{lim}} \approx 50\ \mu K$. As we can see, this range of temperature is well below what could be achieved with regular cryogenic techniques. Nonetheless, we will see below how we intend to achieve a low enough temperature by coupling the mechanical degree of freedom to a microwave field acting as a "cold reservoir".

I.2: Coupling to the environment

The model introduced in section I.1 does not include any dissipation mechanism, yet experimentally realistic systems are open systems, able to exchange energy with their environment. In this section we are going to derive the effect of this coupling to the mechanical oscillator's behavior.

I.2.a: Heisenberg-Langevin equation of a mechanical oscillator coupled to a thermal bath

We can show [CDG+10] that the temporal evolution of the annihilation operator for such systems is described by a quantum Langevin equation, where this energy exchange mechanism is characterized by the loss rate Γ_{m}:

$$\frac{d}{dt}\hat{b}(t) = \frac{i}{\hbar}[\hat{\mathrm{H}},\hat{b}(t)] - \frac{\Gamma_{\mathrm{m}}}{2}\hat{b}(t) + \sqrt{\Gamma_{\mathrm{m}}}\hat{b}_{\mathrm{in}}(t), \tag{I.2.1}$$

where $\hat{b}_{\rm in}(t)$ is an input mode coming from the environment. We can see that this input term allows the commutator $[\hat{b}, \hat{b}^\dagger]$ to stay constant and equal to one, despite the dissipation process. The input field is a bosonic thermal field fulfilling the commutation relation:

$$\langle \hat{b}_{\rm in}^\dagger(t)\hat{b}_{\rm in}(t')\rangle = n_{\rm B}\delta(t-t') \tag{I.2.2}$$

and

$$\langle \hat{b}_{\rm in}(t)\hat{b}_{\rm in}^\dagger(t')\rangle = (n_{\rm B}+1)\delta(t-t'), \tag{I.2.3}$$

such that the incoming power is $P_{\rm in} \overset{\rm def}{=} \hbar\Omega_{\rm m} n_{\rm B}$. We then have:

$$\frac{d}{dt}\hat{b}(t) = (-i\Omega_{\rm m} - \Gamma_{\rm m}/2)\,\hat{b}(t) + \sqrt{\Gamma_{\rm m}}\hat{b}_{\rm in}(t). \tag{I.2.4}$$

I.2.b: Position spectrum of a mechanical oscillator coupled to a thermal bath

The counterparts of the formulas (I.2.2) and (I.2.3) in the frequency domain are[1]:

$$\langle \hat{\tilde{\mathbf{b}}}_{\rm in}^\dagger(\Omega)\hat{\tilde{\mathbf{b}}}_{\rm in}(\Omega')\rangle = 2\pi n_{\rm B}\delta(\Omega+\Omega') \tag{I.2.5}$$

and

$$\langle \hat{\tilde{\mathbf{b}}}_{\rm in}(\Omega)\hat{\tilde{\mathbf{b}}}_{\rm in}^\dagger(\Omega')\rangle = 2\pi(n_{\rm B}+1)\delta(\Omega+\Omega'). \tag{I.2.6}$$

The spectrum $\mathcal{S}_{\hat{O}\hat{O}}$ of any observable $\hat{O}$ can be determined by expressing its Fourier transform as a function of input noises and by using the definition $\langle \hat{O}(\Omega)\hat{O}(\Omega')\rangle \overset{\rm def}{=} 2\pi\mathcal{S}_{\hat{O}\hat{O}}(\Omega)\delta(\Omega+\Omega')$. For instance, taking the Fourier transform of the equation (I.2.4):

$$\hat{\tilde{\mathbf{b}}}(\Omega) = \frac{\sqrt{\Gamma_{\rm m}}\hat{\tilde{\mathbf{b}}}_{\rm in}(\Omega)}{i(\Omega_{\rm m}-\Omega)+\Gamma_{\rm m}/2}, \tag{I.2.7}$$

the position operator in the Fourier space as a function of the input noises reads:

$$\tilde{\hat{x}}(\Omega) = x_{\rm ZPF}(\hat{\tilde{\mathbf{b}}}(\Omega) + \hat{\tilde{\mathbf{b}}}^\dagger(\Omega)) \tag{I.2.8}$$

$$= \sqrt{\Gamma_{\rm m}}x_{\rm ZPF}\left[\frac{\hat{\tilde{\mathbf{b}}}_{\rm in}(\Omega)}{i(\Omega_{\rm m}-\Omega)+\Gamma_{\rm m}/2} + \frac{\hat{\tilde{\mathbf{b}}}_{\rm in}^\dagger(\Omega)}{-i(\Omega_{\rm m}+\Omega)+\Gamma_{\rm m}/2}\right], \tag{I.2.9}$$

from which we can compute the spectral density:

$$S_{\hat{x}\hat{x}}^c(\Omega) = \Gamma_{\rm m}x_{\rm ZPF}^2\left[\frac{n_{\rm B}+1}{(\Gamma_{\rm m}/2)^2+(\Omega_{\rm m}-\Omega)^2} + \frac{n_{\rm B}}{(\Gamma_{\rm m}/2)^2+(\Omega_{\rm m}+\Omega)^2}\right], \tag{I.2.10}$$

[1] the Fourier transform convention used here is $\hat{\tilde{\mathbf{b}}}(\Omega) \overset{\rm def}{=} \int_{-\infty}^{\infty} d\tau \hat{b}(\tau)e^{i\Omega\tau}$ and $\hat{b}(t) \overset{\rm def}{=} \frac{1}{2\pi}\int_{-\infty}^{\infty} d\Omega \hat{\tilde{\mathbf{b}}}(\Omega)e^{-i\Omega t}$

Note that the spectrum is asymmetric: $S^c_{\hat{x}\hat{x}}(\Omega) \neq S^c_{\hat{x}\hat{x}}(-\Omega)$. We can get more insight about this feature by introducing the *Wiener Khintchine Theorem*, which unravels the link between the spectrum and the autocorrelation function $G_{\hat{x}\hat{x}}(t) \overset{\text{def}}{=} \langle \hat{x}(t)\hat{x}(0)\rangle$:

$$S^c_{\hat{x}\hat{x}}(\Omega) = \int_{-\infty}^{\infty} dt e^{i\Omega t} G_{\hat{x}\hat{x}}(t), \tag{I.2.11}$$

As we can see, this spectrum is perfectly symmetric in the classical case. Indeed, $S^c_{\hat{x}\hat{x}}(-\Omega) = \int_{-\infty}^{\infty} dt e^{i\Omega t}\langle \hat{x}(0)\hat{x}(t)\rangle$, and in the classical case $\hat{x}(0)$ and $\hat{x}(t)$ are scalars, thus commuting. However, in the quantum regime, this is not the case and this asymmetry is a quantum signature that we will try to exhibit in this PhD. More quantitatively, this phenomenon is due to the asymmetry of the energy exchange processes between the system and its reservoir, and the spectrum actually fulfills a *detailed balance condition*[CDG$^+$10] which can be written:

$$S^c_{\hat{x}\hat{x}}(-\Omega) = e^{-\hbar\Omega/k_\mathrm{B}T} S^c_{\hat{x}\hat{x}}(\Omega). \tag{I.2.12}$$

As expected, in the limit of high temperature $T \gg \hbar\Omega_\mathrm{m}/k_\mathrm{B}$, the spectrum asymmetry is negligible and we retrieve the classical feature. In the following, we will refer to the symmetrized spectral density $S^s_{\hat{x}\hat{x}}(\Omega) \overset{\text{def}}{=} \frac{1}{2}(S^c_{\hat{x}\hat{x}}(-\Omega) + S^c_{\hat{x}\hat{x}}(\Omega)) = \frac{1}{2}S^c_{\hat{x}\hat{x}}(\Omega)(1 + e^{-\hbar\Omega/k_\mathrm{B}T})$. Integrating this function gives:

$$\int_{-\infty}^{\infty} S^s_{\hat{x}\hat{x}}(\Omega)\frac{d\Omega}{2\pi} = x^2_{\mathrm{ZPF}}\left(\frac{1}{2} + n_\mathrm{B}(T,\Omega_\mathrm{m})\right), \tag{I.2.13}$$

thus measuring this quantity provides the occupation number of this resonator.

I.3: Electromechanical coupling

In the previous section we described the evolution of a mechanical oscillator coupled to its sole natural environment. It is however possible to couple this system also to an external optical degree of freedom. The latter has numerous applications, which includes for example cooling[TdL$^+$11] or amplification[DRAL19], and some of them will be covered in the last section. In this section, we will focus on the quantum mechanical description of a mechanical oscillator coupled to both its natural environment and an external electromagnetic degree of freedom.

I.3.a: Steady-state of an electromagnetic cavity

An electromagnetic cavity is essentially a set of boundary conditions for the electromagnetic field that exhibits one or several resonances (*i.e.* frequencies at which the signal in the cavity will be considerably higher than the others after a Dirac-like field perturbation). For the sake of simplicity, we will consider only one electromagnetic mode, with a given frequency $\omega_c/2\pi$. As in the previous section, we introduce creation ($\hat{a}^\dagger$) and annihilation ($\hat{a}$) operators for elementary excitations inside this cavity that are now called *photons* [CtDRG97]. The dynamics of photons is the same than that of phonons described in section I.1. It is given by the Hamiltonian of a harmonic oscillator: $\hat{H} = \hbar\omega_c(\hat{a}^\dagger\hat{a} + \frac{1}{2})$.

Let us introduce the damping rate $\kappa/2\pi$ for the mode $\hat{a}$. Contrary to the phonon case, here we need to consider more than one loss channel. Indeed, we will inject a source signal inside the cavity, using a *coupling* port with a coupling rate $\kappa_c/2\pi$, and there will be some internal loss mechanisms represented by an internal loss rate $\kappa_0/2\pi$. Those two loss rates fulfill the relation $\kappa = \kappa_0 + \kappa_c$. The Langevin equation reads:

$$\frac{d}{dt}\hat{a} = (-i\omega_c - \kappa/2)\hat{a} + \sqrt{\kappa_c}\hat{a}_{\text{in}} + \sqrt{\kappa_0}\hat{a}_{\text{in},0}, \tag{I.3.1}$$

where $\hat{a}_{\text{in}}$ represents the input source signal, while $\hat{a}_{\text{in},0}$ represents the noise coming from the thermal environment. Since we will usually use strong sources and work at a temperature low enough to ensure an electromagnetic thermal occupancy of 0 (throughout this work, the electromagnetic frequency considered are in the GHz range and we operate at sub-Kelvin cryogenic temperatures), we will usually neglect this last term.

If we assume a monochromatic source at a frequency $\omega_l/2\pi$, we can go to the rotating frame, by introducing $\hat{a}_r \overset{\text{def}}{=} e^{i\omega_l t}\hat{a}$, $\hat{a}_{\text{in,r}} \overset{\text{def}}{=} e^{i\omega_l t}\hat{a}_{\text{in}}$ and $\hat{a}_{\text{in,0,r}} \overset{\text{def}}{=} e^{i\omega_l t}\hat{a}_{\text{in},0}$, which leaves, if we neglect the quantum noise source:

$$\frac{d}{dt}\hat{a}_r = (i\Delta - \kappa/2)\hat{a}_r + \sqrt{\kappa_c}\hat{a}_{\text{in,r}}, \tag{I.3.2}$$

where $\Delta = \omega_l - \omega_c$. From eq. (I.3.2) we can derive the steady state value $\overline{\hat{a}_r}$ by cancelling the temporal derivative term:

$$\overline{\hat{a}_r} = \frac{\sqrt{\kappa_c}\hat{a}_{\text{in,r}}}{\kappa/2 - i\Delta} \tag{I.3.3}$$

The signal received at the output of the experiment, $\hat{a}_{\text{out}}$, is then found using an *input-output relation*, that depends on the coupling scheme. Different coupling configurations are presented in figure I.2.

I.3.a.i "Hanger" configuration

For example, in the so-called "hanger" geometry, this relation is the following:

$$\hat{a}_{\text{out}} = \hat{a}_{\text{in}} - \sqrt{\frac{\kappa_c}{2}}\hat{a}_r = \left(1 - \frac{\eta}{1 - \frac{2i\Delta}{\kappa}}\right)\hat{a}_{\text{in}}, \tag{I.3.4}$$

where $\eta \overset{\text{def}}{=} \frac{\kappa_c}{\kappa}$, and where the second equality used the steady state value (I.3.3), where the coupling rate κ_c has been divided by two to take into account that the resonator is as coupled to the input mode as it is to the output mode. This is a lorentzian response which represents a circle in the complex plane, whose center is $(1 - \frac{\eta}{2},0)$ and whose radius is $\frac{\eta}{2}$. In this configuration, a photon in the cavity that is scattered in the coupling line has two equiprobable outcomes: the left and the right-propagating modes of the coupling line. Since only the latter is being measured by the output line of the experiment, half of the information is lost. However, this configuration allows quite usefully to couple to several microwave cavities at once, if their frequencies are separated by more than one cavity linewidth.

I.3.a.ii Reflection configuration

In the reflection configuration, only one port is used for probing the system: the transmission line is interrupted to allow some of the incoming cavity photons to be scattered in the reflected transmission mode. The corresponding input output relation reads:

$$\hat{a}_{\text{out}} = -\hat{a}_{\text{in}} + \sqrt{\kappa_c}\hat{a}_r = \left(-1 + \frac{2\eta}{1 - \frac{2i\Delta}{\kappa}}\right)\hat{a}_{\text{in}}, \tag{I.3.5}$$

which is also a lorentzian resonance, drawing a circle in the complex plane, but this time the center would be in $(-1+\eta,0)$ and the radius is η. Contrary to the previous case, all the scattered photons from the cavity to the transmission line are measured. This is why the radius of the circle is twice the radius of the circle in the previous configuration.

I.3.a.iii Transmission configuration

Finally, in the transmission configuration, the cavity is coupled to an input and an output line, with respective couplings $\kappa_{\text{c,in}}$ and $\kappa_{\text{c,out}}$, which usually verify $\kappa_{\text{c,out}} \gg \kappa_{\text{c,in}}$ in order to promote the scattering of a photon from the resonator to the output line compared to the scattering of a photon from the resonator to the input line, where it would not be measured. The corresponding input-output relation reads:

$$\hat{a}_{\text{out}} = \sqrt{\kappa_{\text{c,out}}}\hat{a}_r = \frac{\sqrt{\eta_{\text{in}}\eta_{\text{out}}}}{1 - \frac{2i\Delta}{\kappa}}\hat{a}_{\text{in}}, \tag{I.3.6}$$

where $\kappa = \kappa_0 + \kappa_{\text{c,in}} + \kappa_{\text{c,out}}$, $\eta_{\text{in}} \overset{\text{def}}{=} \frac{\kappa_{\text{c,in}}}{\kappa}$, and $\eta_{\text{out}} \overset{\text{def}}{=} \frac{\kappa_{\text{c,out}}}{\kappa}$. There is also a lorentzian response, which thus draws a circle in the complex plane, whose center is $(\sqrt{\eta_{\text{in}}\eta_{\text{out}}}/2,0)$ and whose radius is $\sqrt{\eta_{\text{in}}\eta_{\text{out}}}/2$.

Contrary to the two previous configurations, the transmission is close to zero far away from the resonance. This allows this configuration to be used as a bandpass filter, with central frequency $\omega_c/2\pi$ and bandwidth $\kappa/2\pi$.

I.3.b: Hamiltonian of an optomechanical cavity

An optomechanical cavity is a cavity whose frequency $\omega_c/2\pi$ depends on the position $\hat{x}$ of a mechanical oscillator (see figure I.3). We denote by $\hat{a}$ ($\hat{a}^\dagger$) the annihilation (creation) operator of a photon in this electromagnetic mode, and $\hat{b}$ ($\hat{b}^\dagger$) the annihilation (creation) operator of a phonon in the mechanical mode. We have, restraining ourselves to small displacements of the mechanical oscillator, the following hamiltonian:

$$\hat{H} = \hbar\Omega_{\text{m}}\hat{b}^\dagger\hat{b} + \hbar\omega_0(\hat{x})\hat{a}^\dagger\hat{a} \tag{I.3.7}$$

$$\approx \hbar\Omega_{\text{m}}\hat{b}^\dagger\hat{b} + \hbar\left(\omega_0(0) + \frac{\partial\omega_0}{\partial\hat{x}}(0)\hat{x}\right)\hat{a}^\dagger\hat{a} \tag{I.3.8}$$

$$= \hbar\omega_0\hat{a}^\dagger\hat{a} + \hbar\Omega_{\text{m}}\hat{b}^\dagger\hat{b} + \hbar G x_{ZPF}(\hat{b} + \hat{b}^\dagger)\hat{a}^\dagger\hat{a}, \tag{I.3.9}$$

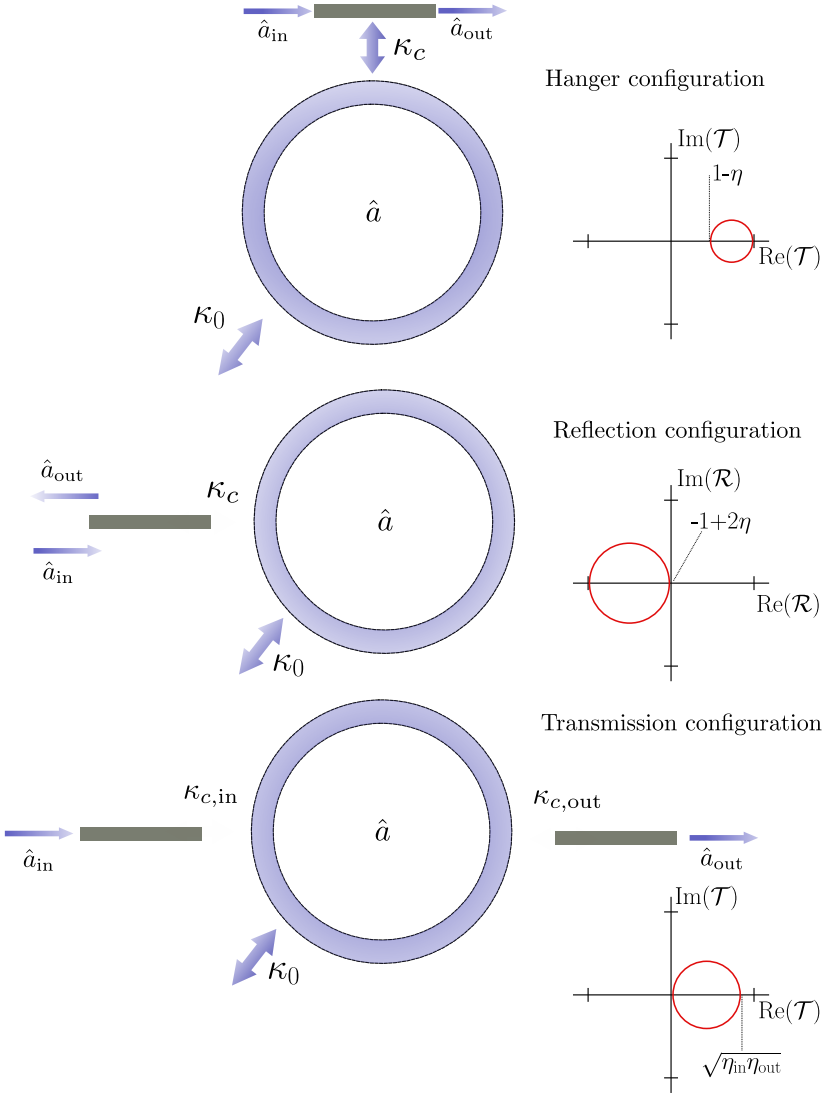

Figure I.2: Three possible configurations for interacting with a cavity. The input (output) signal is represented by $\hat{a}_{\text{in}}$ ($\hat{a}_{\text{out}}$), the light blue circle represents the cavity, and the grey rectangles represent the waveguides. For each configuration, the shape of the resonance (*i.e* the reflection or transmission close to the resonance frequency) in the complex plane is represented. For the first two configurations, the value of η is set to $\frac{1}{2}$. For the last one, the two couplings are chosen arbitrarily.

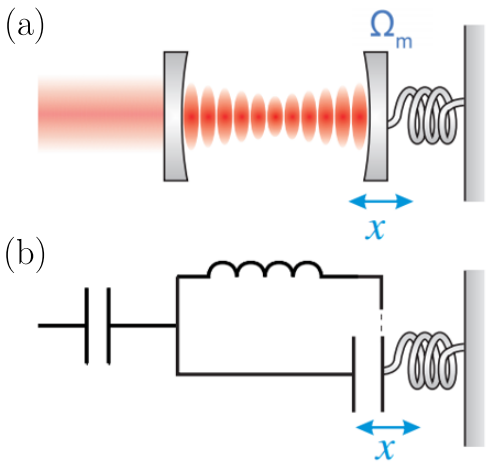

Figure I.3: Two possible schematical representations of an optomechanical cavity. (a) In the optical domain: a Fabry-Perot cavity with an end mirror able to move with a mechanical mode of a mechanical oscillator. (b) In the microwave domain: a LC circuit with one electrode of the capacitor able to move with a mechanical mode of a mechanical oscillator.

where we introduced $G \overset{\text{def}}{=} \frac{\partial\omega_0}{\partial\hat{x}}(0)$, $x_{ZPF} = \sqrt{\frac{\hbar}{2m\Omega_\mathrm{m}}}$ the zero-point fluctuations of the mechanical resonator, $\Omega_\mathrm{m}/2\pi$ and m respectively the mechanical frequency and the effective mass of the mechanical mode, and where we used the simplified notation $\omega_0(0) = \omega_0$. Let us also introduce the one photon optomechanical coupling $g_0 \overset{\text{def}}{=} Gx_{ZPF}$, which corresponds to the frequency shift the cavity will undergo when the resonator moves by its zero-point fluctuations:

$$\hat{H} = \hbar\Omega_\mathrm{m}\hat{b}^\dagger\hat{b} + \hbar\omega_0\hat{a}^\dagger\hat{a} + \hbar g_0(\hat{b}+\hat{b}^\dagger)\hat{a}^\dagger\hat{a}. \tag{I.3.10}$$

The effect of such coupling is however in most cases too small to be seen when one photon only is in the cavity. To generate a measurable interaction, we will pump the system with a strong classical field at a frequency $\omega_l/2\pi$. This will displace the electromagnetic mode close to a coherent state of amplitude α. The electromagnetic and mechanical field operators, as well as the input field operator, can then be written:

$$\begin{aligned}\hat{a}_r &\approx \alpha + \hat{a}_1\\ \hat{b} &\approx \beta + \hat{b}_1\\ \hat{a}_{\mathrm{in,r}} &\approx \alpha_{\mathrm{in,c,r}} + \hat{a}_{\mathrm{in,c,r}},\end{aligned}$$

where $\hat{b}_1$, $\hat{a}_1$ and $\hat{a}_{\mathrm{in},1}$ have zero mean value and correspond to small fluctuations around those fields. The Langevin equations then read:

$$\frac{d}{dt}\hat{a}_r = \left(i(\Delta_c - g_0(\hat{b}+\hat{b}^\dagger)) - \kappa/2\right)\hat{a}_r + \sqrt{\kappa_c}\hat{a}_{\mathrm{in,c,r}} + \sqrt{\kappa_0}\hat{a}_{\mathrm{in,0,r}} \tag{I.3.11}$$

$$\frac{d}{dt}\hat{b} = \left(-i\Omega_\mathrm{m} - \Gamma_\mathrm{m}/2\right)\hat{b} - ig_0\hat{a}_r^\dagger\hat{a}_r + \sqrt{\Gamma_\mathrm{m}}\hat{b}_\mathrm{in}, \tag{I.3.12}$$

where $\Delta_c \stackrel{\text{def}}{=} \omega_l - \omega_c$. At zeroth order, this equation gives:

$$\alpha = \frac{1}{-i\left(\Delta_c - g_0(\beta+\beta^*)\right) + \kappa/2}\sqrt{\kappa_c}\alpha_{\text{in,c,r}} \tag{I.3.13}$$

$$\beta = \frac{-ig_0|\alpha|^2}{i\Omega_\text{m} + \Gamma_\text{m}/2} \tag{I.3.14}$$

$x_{\text{ZPF}}(\beta+\beta^*)$ corresponds here to a static shift due to the radiation pressure. We see that the second equation can be injected back into the first one, resulting in a third degree equation that can under certain conditions have up to three solutions. This situation is called the electromagnetic bistability and has been observed experimentally [DMM+83]. It arises because the intracavity intensity depends on the detuning due to the filtering of the cavity, while the detuning depends on the intracavity intensity due to the radiation pressure force. From now on, we will exclusively consider situations where this equation only has a single solution, and we will deal with this static shift by introducing a modified detuning $\tilde{\Delta}_c \stackrel{\text{def}}{=} \Delta_c - g_0(\beta+\beta^*)$. At first order we now have:

$$\frac{d}{dt}\hat{a}_1 = \left(i\tilde{\Delta}_c - \kappa/2\right)\hat{a}_1 - ig_0\alpha(\hat{b}_1 + \hat{b}_1^\dagger) + \sqrt{\kappa_c}\hat{a}_{\text{in,c,r}} + \sqrt{\kappa_0}\hat{a}_{\text{in,0,r}} \tag{I.3.15}$$

$$\frac{d}{dt}\hat{b}_1 = \left(-i\Omega_\text{m} - \Gamma_\text{m}/2\right)\hat{b}_1 - ig_0(\alpha\hat{a}_1^\dagger + \alpha^*\hat{a}_1) + \sqrt{\Gamma_\text{m}}\hat{b}_\text{in} \tag{I.3.16}$$

We see that this dynamics corresponds to the effective linear Hamiltonian, in a frame rotating at the drive frequency:

$$\hat{H} = -\hbar\Delta\hat{a}^\dagger\hat{a} + \hbar\Omega_\text{m}\hat{b}^\dagger\hat{b} + \hbar g_0(\alpha\hat{a}^\dagger + \alpha^*\hat{a})(\hat{b}+\hat{b}^\dagger), \tag{I.3.17}$$

where we removed, as we will henceforth do for clarity, the suffixes and the accents. The situation is thus reduced to two harmonic oscillators, linearly coupled with an effective coupling rate $g_0\alpha$.

I.3.c: Equations of motion

I.3.c.i Adiabatic elimination of the optical mode

Note that in the experiments described in this manuscript, the two coupled oscillators are evolving at different timescales. While $\hat{a}$ reaches its steady-state rapidly at a rate $\kappa/2\pi \approx 100$ kHz, $\hat{b}$ decays at a rate orders of magnitude smaller $\Gamma_\text{m}/2\pi \approx 1$ mHz. Such a huge difference can be used to perform a so called *adiabatic elimination* of the electromagnetic mode. In the following we are going to derive the mechanical occupation by using such elimination, which is equivalent to tracing the dynamics of the shared electromagnetic and mechanical system over the electromagnetic degree of freedom [WRNZK07].

First, let us take the Fourier transform of equations (I.3.16) and (I.3.15) and their

hermitian conjugates:

$$\left[-i(\Omega+\tilde{\Delta}_c)+\kappa/2\right]\hat{\tilde{\mathbf{a}}}_1(\Omega) = -ig_0\alpha(\hat{\tilde{\mathbf{b}}}_1^\dagger(\Omega)+\hat{\tilde{\mathbf{b}}}_1(\Omega)) + \sqrt{\kappa_c}\hat{\tilde{\mathbf{a}}}_{\mathrm{in},c}(\Omega) + \sqrt{\kappa_0}\hat{\tilde{\mathbf{a}}}_{\mathrm{in},0} \tag{I.3.18a}$$

$$\left[-i(\Omega-\tilde{\Delta}_c)+\kappa/2\right]\hat{\tilde{\mathbf{a}}}_1^\dagger(\Omega) = +ig_0\alpha^*(\hat{\tilde{\mathbf{b}}}_1^\dagger(\Omega)+\hat{\tilde{\mathbf{b}}}_1(\Omega)) + \sqrt{\kappa_c}\hat{\tilde{\mathbf{a}}}_{\mathrm{in},c}^\dagger(\Omega) + \sqrt{\kappa_0}\hat{\tilde{\mathbf{a}}}_{\mathrm{in},0}^\dagger \tag{I.3.18b}$$

$$[-i(\Omega-\Omega_\mathrm{m})+\Gamma_\mathrm{m}/2]\,\hat{\tilde{\mathbf{b}}}_1(\Omega) = -ig_0(\alpha\hat{\tilde{\mathbf{a}}}_1^\dagger(\Omega)+\alpha^*\hat{\tilde{\mathbf{a}}}_1(\Omega)) + \sqrt{\Gamma_\mathrm{m}}\hat{\tilde{\mathbf{b}}}_\mathrm{in}(\Omega) \tag{I.3.18c}$$

$$[-i(\Omega+\Omega_\mathrm{m})+\Gamma_\mathrm{m}/2]\,\hat{\tilde{\mathbf{b}}}_1^\dagger(\Omega) = +ig_0(\alpha\hat{\tilde{\mathbf{a}}}_1^\dagger(\Omega)+\alpha^*\hat{\tilde{\mathbf{a}}}_1(\Omega)) + \sqrt{\Gamma_\mathrm{m}}\hat{\tilde{\mathbf{b}}}_\mathrm{in}^\dagger(\Omega). \tag{I.3.18d}$$

Considering the last two equations, we realize that the operator $\hat{\tilde{\mathbf{b}}}_1^\dagger(\Omega)$ is approximately equal to $\hat{\tilde{\mathbf{b}}}_1(\Omega)$ multiplied by a factor $\frac{-i(\Omega-\Omega_\mathrm{m})+\Gamma_\mathrm{m}/2}{-i(\Omega+\Omega_\mathrm{m})+\Gamma_\mathrm{m}/2}$, which means that we can assume $\hat{\tilde{\mathbf{b}}}_1^\dagger(\Omega)+\hat{\tilde{\mathbf{b}}}_1(\Omega) \underset{\Omega\approx\Omega_\mathrm{m}}{\approx} \hat{\tilde{\mathbf{b}}}_1(\Omega)$ and $\hat{\tilde{\mathbf{b}}}_1^\dagger(\Omega)+\hat{\tilde{\mathbf{b}}}_1(\Omega) \underset{\Omega\approx-\Omega_\mathrm{m}}{\approx} \hat{\tilde{\mathbf{b}}}_1^\dagger(\Omega)$ in equations (I.3.18a) and (I.3.18b), in the limit of a well isolated system, with $\Gamma_\mathrm{m} \ll \Omega_\mathrm{m}$, which is the relevant framework for this PhD. The adiabatic elimination is then performed by keeping in mind that only the Fourier frequencies close to the natural resonator frequency $\pm\Omega_\mathrm{m}$ are relevant to the problem. In practice, we will check a posteriori that $\hat{\tilde{\mathbf{a}}}_1(\Omega)$ only takes non-negligible values when $|\Omega\pm\Omega_\mathrm{m}| \ll \Omega_\mathrm{m}, \kappa$. This is the so called weak-coupling regime, where the (electromagneticly-dressed) mechanical mode is still a high-Q resonant mode with a bandwidth well within the electromagnetic resonator bandwidth. The corresponding condition $g_0\alpha \ll \kappa, \Gamma_\mathrm{m}$ has been fulfilled in all the experiments described in this manuscript. Under this approximation, we can replace, in equations (I.3.18a) and (I.3.18b), Ω by Ω_m $(-\Omega_\mathrm{m})$ for $\Omega > 0$ $(\Omega < 0)$ when injecting them into equations (I.3.18c) and (I.3.18d). We are left with:

$$[-i(\Omega-(\Omega_\mathrm{m}+\delta_\mathrm{opt}))+(\Gamma_\mathrm{m}+\Gamma_\mathrm{opt})/2]\,\hat{\tilde{\mathbf{b}}}_1(\Omega) \underset{\Omega>0}{=} \mathrm{sgn}(\Gamma_\mathrm{opt})\sqrt{|\Gamma_\mathrm{opt}|}\hat{\mathcal{A}}_\mathrm{opt}(\Omega) + \sqrt{\Gamma_\mathrm{m}}\hat{\tilde{\mathbf{b}}}_\mathrm{in}(\Omega) \tag{I.3.19}$$

$$[-i(\Omega+(\Omega_\mathrm{m}+\delta_\mathrm{opt}))+(\Gamma_\mathrm{m}+\Gamma_\mathrm{opt})/2]\,\hat{\tilde{\mathbf{b}}}_1^\dagger(\Omega) \underset{\Omega<0}{=} \mathrm{sgn}(\Gamma_\mathrm{opt})\sqrt{|\Gamma_\mathrm{opt}|}\hat{\mathcal{A}}_\mathrm{opt}^\dagger(\Omega) + \sqrt{\Gamma_\mathrm{m}}\hat{\tilde{\mathbf{b}}}_\mathrm{in}^\dagger(\Omega) \tag{I.3.20}$$

with $\mathrm{sgn}(x) \overset{\mathrm{def}}{=} 1$ if $x > 0$ or -1 if $x < 0$ and:

$$\Gamma_\mathrm{opt} \overset{\mathrm{def}}{=} C\Gamma_\mathrm{m}\mathrm{Re}\left[A_+ - A_-\right] \tag{I.3.21}$$

$$A_\pm \overset{\mathrm{def}}{=} \frac{1}{1-i\frac{\Omega_\mathrm{m}\pm\tilde{\Delta}_c}{\kappa/2}} \tag{I.3.22}$$

$$\delta_\mathrm{opt} \overset{\mathrm{def}}{=} \frac{C\Gamma_\mathrm{m}}{2}\mathrm{Im}\left[A_+ - A_-\right] \tag{I.3.23}$$

$$\hat{\mathcal{A}}_\mathrm{opt}(\Omega) \overset{\mathrm{def}}{=} \frac{A_+}{\sqrt{||A_+|^2-|A_-|^2|}}\mathcal{N}_\mathrm{in}(\Omega) - \frac{A_-}{\sqrt{||A_+|^2-|A_-|^2|}}\mathcal{N}_\mathrm{in}^\dagger(\Omega), \tag{I.3.24}$$

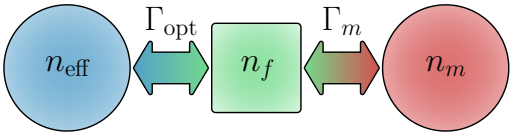

Figure I.4: The mechanical oscillator (green) has a final occupation n_f which results from its coupling at a rate $\Gamma_{\rm m}$ to its natural thermal bath (red), whose occupation is $n_{\rm m}$, and at a rate $\Gamma_{\rm opt}$ to an effective bath (blue), whose occupation is $n_{\rm eff}$.

where $\eta \overset{\text{def}}{=} \kappa_c/\kappa$, $\mathcal{N}_{\rm in} \overset{\text{def}}{=} -ie^{-i\Psi_\alpha}\left(\sqrt{\eta}\hat{\tilde{\mathbf{a}}}_{\rm in,c} + \sqrt{1-\eta}\hat{\tilde{\mathbf{a}}}_{\rm in,0}\right)$, Ψ_α is such that $\alpha = |\alpha|e^{i\Psi_\alpha}$ and finally $C \overset{\text{def}}{=} \frac{4g_0^2|\alpha|^2}{\kappa\Gamma_{\rm m}}$ is the *cooperativity*, a dimensionless number quantifying the ratio between the coherent optomechanical coupling rate, $g_0|\alpha|$, and the two loss rates, $\kappa/2$ and $\Gamma_{\rm m}/2$. Equations (I.3.19) and (I.3.20) describe an harmonic oscillator coupled to two thermal baths, as described in figure I.4: the environment, with occupation $n_{\rm m}$ and at a rate $\Gamma_{\rm m}$, and an effective bath with an occupation:

$$n_{\rm eff} \overset{\text{def}}{=} \frac{|A_-|^2(n_{\rm opt}+1) + |A_+|^2 n_{\rm opt}}{|A_+|^2 - |A_-|^2} \approx \frac{|A_-|^2}{|A_+|^2 - |A_-|^2}, \tag{I.3.25}$$

where $n_{\rm opt}$ is the occupation of the electromagnetic bath, assumed to be close to 0 in the last equality. This assumption will be consistently made in the following. The coupling to this second bath occurs at a rate $\Gamma_{\rm opt}$. Indeed, $\hat{\mathcal{A}}_{\rm opt}$ fulfills $[\hat{\mathcal{A}}_{\rm opt}(\Omega), \hat{\mathcal{A}}^\dagger_{\rm opt}(\Omega')] = 2\pi\delta(\Omega+\Omega')$ and $\langle \hat{\mathcal{A}}^\dagger_{\rm opt}(\Omega)\hat{\mathcal{A}}_{\rm opt}(\Omega')\rangle = 2\pi\delta(\Omega+\Omega')n_{\rm eff}$. Those two parameters characterizing this electromagnetic effective bath are represented in figure I.5 for different values of $\tilde{\Delta}_c/\Omega_{\rm m}$ and $\kappa/\Omega_{\rm m}$. Three situations are possible: $n_{\rm eff} > 0$ and $\Gamma_{\rm opt} > 0$ (for $\tilde{\Delta}_c < 0$), $|n_{\rm eff}| \to +\infty$ and $\Gamma_{\rm opt} \to 0$ (for $\tilde{\Delta}_c \to 0$), or $n_{\rm eff} < 0$ and $\Gamma_{\rm opt} < 0$ (for $\tilde{\Delta}_c > 0$). This last situation corresponds to an electromagnetic bath giving energy to the mechanical resonator through phonon creation, and will be more thoroughly investigated in section I.4.c. In every situation where $\Gamma_{\rm m} + \Gamma_{\rm opt} > 0$, the occupation n_f of the mechanical oscillator reaches the equilibrium value:

$$n_f \overset{\text{def}}{=} \frac{\Gamma_{\rm opt} n_{\rm eff} + \Gamma_{\rm m} n_{\rm B}}{\Gamma_{\rm opt} + \Gamma_{\rm m}}. \tag{I.3.26}$$

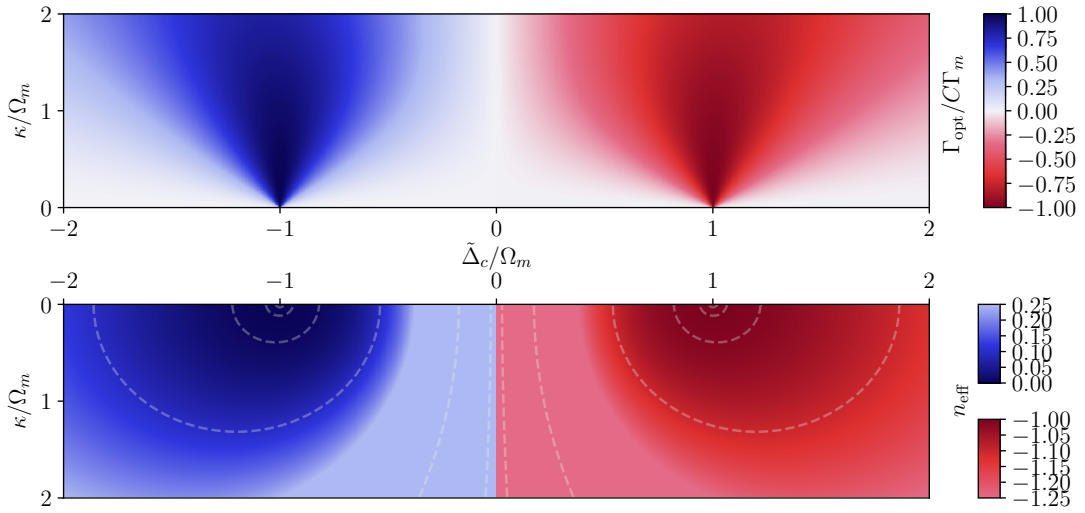

Figure I.5: Top: reduced damping (in blue) or heating (in red) due to the optomechanical interaction for various reduced detunings and linewidths. Bottom: effective bath occupation $n_{\rm eff}$. Dashed lines correspond to levels logarithmically spaced around 0 (left) and -1 (right). The behavior of $n_{\rm eff}$ when $\tilde{\Delta}_c \to 0$ is truncated in the colormap for readability, but we have $n_{\rm eff} \to +\infty$ for $\tilde{\Delta}_c \to 0^-$ and $n_{\rm eff} \to -\infty$ for $\tilde{\Delta}_c \to 0^+$

I.3.c.ii Position spectrum of the mechanical oscillator

To have the most accurate physical intuition of the resulting spectrum, we can decompose it in three parts:

$$\mathcal{S}_{\hat{\rm x}\hat{\rm x}}(\Omega) = \left(\mathcal{S}_{\hat{\rm x}\hat{\rm x}}(\Omega)\right)_{\rm vac} + \left(\mathcal{S}_{\hat{\rm x}\hat{\rm x}}(\Omega)\right)_{\rm therm} + \left(\mathcal{S}_{\hat{\rm x}\hat{\rm x}}(\Omega)\right)_{\rm back}, \tag{I.3.27}$$

where:

$$\left(\mathcal{S}_{\hat{\rm x}\hat{\rm x}}(\Omega)\right)_{\rm vac} \overset{\rm def}{=} x_{\rm ZPF}^2 \frac{\Gamma_{\rm m} + \Gamma_{\rm opt}}{\left(\frac{\Gamma_{\rm eff}}{2}\right)^2 + (\Omega - \Omega_{\rm eff})^2} \tag{I.3.28}$$

$$\left(\mathcal{S}_{\hat{\rm x}\hat{\rm x}}(\Omega)\right)_{\rm therm} \overset{\rm def}{=} x_{\rm ZPF}^2 \Gamma_{\rm m} \left[\frac{n_{\rm B}}{\left(\frac{\Gamma_{\rm eff}}{2}\right)^2 + (\Omega - \Omega_{\rm eff})^2} + \frac{n_{\rm B}}{\left(\frac{\Gamma_{\rm eff}}{2}\right)^2 + (\Omega + \Omega_{\rm eff})^2}\right] \tag{I.3.29}$$

$$\left(\mathcal{S}_{\hat{\rm x}\hat{\rm x}}(\Omega)\right)_{\rm back} \overset{\rm def}{=} x_{\rm ZPF}^2 \Gamma_{\rm opt} \left[\frac{n_{\rm eff}}{\left(\frac{\Gamma_{\rm eff}}{2}\right)^2 + (\Omega - \Omega_{\rm eff})^2} + \frac{n_{\rm eff}}{\left(\frac{\Gamma_{\rm eff}}{2}\right)^2 + (\Omega + \Omega_{\rm eff})^2}\right], \tag{I.3.30}$$

where $\Gamma_{\rm opt}$, that represents an extra damping of the oscillator, and $\delta_{\rm opt}$, that represents a coupling induced frequency shift, often referred to as the *optical spring effect*, are taken into account with a modified mechanical frequency $\Omega_{\rm eff} \overset{\rm def}{=} \Omega_{\rm m} + \delta_{\rm opt}$ and a modified loss rate $\Gamma_{\rm eff} \overset{\rm def}{=} \Gamma_{\rm m} + \Gamma_{\rm opt}$.

The effect of the coupling to the two environments interacting with the resonator, the thermal one resulting from the term proportional to $\hat{\tilde{\mathbf{b}}}_{\rm in}$ in equation (I.3.19), and the effective electromagnetic one resulting from the term proportional to $\hat{\mathcal{A}}_{\rm opt}$ in the same equation, are splitted in two. On the first hand, an asymmetric part, due to the commutation relations of $\hat{\tilde{\mathbf{b}}}_{\rm in}^\dagger$, $\hat{\tilde{\mathbf{b}}}_{\rm in}$, $\hat{\tilde{\mathbf{a}}}_{\rm in,c}$, $\hat{\tilde{\mathbf{a}}}_{\rm in,c}^\dagger$, $\hat{\tilde{\mathbf{a}}}_{\rm in,0}$ and $\hat{\tilde{\mathbf{a}}}_{\rm in,0}^\dagger$, is shown in $\left(\mathcal{S}_{\hat{\mathrm{x}}\hat{\mathrm{x}}}(\Omega)\right)_{\rm vac}$. This part exists even without any population in the two environments, it represents the minimum noise imposed by the Heisenberg uncertainty. As expected, the integral of this vacuum noise gives rise to a contribution $x_{\rm zpf}^2$ in the position variance, irrespective of the relative contribution of the natural and electromagnetic environments to the total resonator damping $\Gamma_{\rm eff}$. This stems from the fact that both environments contribute to the vacuum noise in proportion to their respective damping $\Gamma_{\rm m}$ and $\Gamma_{\rm opt}$. On the other hand, a symmetric part gives rise to $\left(\mathcal{S}_{\hat{\mathrm{x}}\hat{\mathrm{x}}}(\Omega)\right)_{\rm therm}$ for the coupling to the thermal environment and $\left(\mathcal{S}_{\hat{\mathrm{x}}\hat{\mathrm{x}}}(\Omega)\right)_{\rm back}$ for the electromagnetic environment. The latter, which corresponds to the quantum noise of the electromagnetic mode after being transducted by the optomechanical interaction, could also be interpreted as the *backaction* of the position measurement induced by the light. This will be described in further details in section I.3.d.

I.3.d: electromagnetic measurement of mechanical motion

While equations (I.3.19) and (I.3.20) are describing the evolution of the mechanical oscillator, in most experiments we only have access to the electromagnetic part of the system. Let us therefore derive the electromagnetic spectrum. Assuming a reflection cavity configuration, we have the input-output relation: $\hat{\tilde{\mathbf{a}}}_{\rm out}(\Omega) = -\hat{\tilde{\mathbf{a}}}_{\rm in,c}(\Omega) + \sqrt{\kappa_c}\hat{\tilde{\mathbf{a}}}(\Omega)$, from which we will compute the spectrum of one quadrature of the output spectrum, for instance $\hat{X}_{{\rm opt},\theta} \overset{\rm def}{=} \frac{e^{-i\theta}\hat{\tilde{\mathbf{a}}}_{\rm out} + e^{i\theta}\hat{\tilde{\mathbf{a}}}_{\rm out}^\dagger}{\sqrt{2}}$, with $\theta \in \mathbb{R}$. We have:

$$\hat{X}_{{\rm opt},\theta}(\Omega) = \hat{\xi}_\theta(\Omega) + \mathcal{G}_\theta(\Omega)\hat{x}(\Omega), \tag{I.3.31}$$

where:

$$\begin{aligned}\hat{\xi}_\theta(\Omega) \overset{\rm def}{=} \frac{1}{\sqrt{2}}\Bigg\{ & e^{-i\theta}\left[(-1+2\eta B_+)\,\hat{\tilde{\mathbf{a}}}_{\rm in,c} + 2\sqrt{\eta(1-\eta)}B_+\hat{\tilde{\mathbf{a}}}_{\rm in,0}\right] \\ & + e^{i\theta}\left[(-1+2\eta B_-)\,\hat{\tilde{\mathbf{a}}}_{\rm in,c}^\dagger + 2\sqrt{\eta(1-\eta)}B_-\hat{\tilde{\mathbf{a}}}_{\rm in,0}^\dagger\right]\Bigg\}\end{aligned} \tag{I.3.32}$$

$$x_{\rm ZPF}\mathcal{G}_\theta(\Omega) \overset{\rm def}{=} \sqrt{\frac{C\eta\Gamma_{\rm m}}{2}}\left(-ie^{-i\theta'}B_+ + ie^{i\theta'}B_-\right), \tag{I.3.33}$$

where the latter can be understood as the gain of the position measurement, and where $\theta' \overset{\rm def}{=} \theta - \Psi_\alpha$ and $B_\pm \overset{\rm def}{=} \frac{1}{1-i\frac{\Omega\pm\tilde{\Delta}_c}{\kappa/2}}$. The resulting electromagnetic spectrum, defined by $\langle\hat{X}_{{\rm opt},\theta}(\Omega)\hat{X}_{{\rm opt},\theta}(\Omega')\rangle = 2\pi\delta(\Omega+\Omega')\mathcal{S}_{\hat{X}\hat{X}}(\Omega)$, can be decomposed in three parts:

$$\mathcal{S}_{\hat{X}\hat{X}}(\Omega) = \mathcal{S}_{\rm shot}(\Omega) + |\mathcal{G}_\theta(\Omega)|^2\mathcal{S}_{\hat{x}\hat{x}}(\Omega) + \mathcal{S}_{\hat{x}{\rm shot}}(\Omega) \tag{I.3.34}$$

The first term corresponds to the photon *shot noise* which is the quantum noise of the incoming light and reads $\mathcal{S}_{\rm shot}(\Omega) = \frac{1}{2}$. The second term is the mechanical noise amplified by the gain $|\mathcal{G}_\theta(\Omega)|^2$. In addition, the extra cross-spectrum $\mathcal{S}_{\hat{x}\rm shot}(\Omega)$ results from the correlation between the shot noise and the backaction noise. The antisymmetric part of this spectrum exactly compensates the antisymmetric part of the mechanical spectrum, therefore ensuring that the total spectrum $\mathcal{S}_{\hat{X}\hat{X}}(\Omega)$ is symmetric in frequency. Indeed, it is expected from a free space observable like $\hat{X}_{{\rm opt},\theta}$ to commute with itself at any time [KMY+12]: $\forall(t,t') \in \mathbb{R}^2, [\hat{X}_{{\rm opt},\theta}(t),\hat{X}_{{\rm opt},\theta}(t')] = 0$, and therefore to have a symmetric spectrum. It is interesting to factorize those noises by the gain $|\mathcal{G}_\theta(\Omega)|^2$ to highlight that the optomechanical system behaves as an effective amplifier for the mechanical motion measurement with gain $|\mathcal{G}_\theta(\Omega)|^2$, and to be able to compare every noise contribution with the mechanical spectrum:

$$\begin{aligned}\mathcal{S}_{\hat{X}\hat{X}}(\Omega) &\overset{\rm def}{=} |\mathcal{G}_\theta(\Omega)|^2 \mathcal{S}^{\rm meas}_{\hat{x}\hat{x}}(\Omega) \\ &= |\mathcal{G}_\theta(\Omega)|^2 \left[(\mathcal{S}_{\hat{x}\hat{x}})_{{\rm shot},\theta}(\Omega) + \mathcal{S}^s_{\hat{x}\hat{x}}(\Omega) + (\mathcal{S}^s_{\hat{x}\hat{x}})_{{\rm cross},\theta}(\Omega)\right]\end{aligned} \tag{I.3.35}$$

where $\mathcal{S}^s_{\hat{x}\hat{x}}(\Omega)$ is the symmetrized mechanical spectrum, of which we recall the definition $\mathcal{S}^s_{\hat{x}\hat{x}}(\Omega) \overset{\rm def}{=} \frac{1}{2}\left(\mathcal{S}_{\hat{x}\hat{x}}(\Omega) + \mathcal{S}_{\hat{x}\hat{x}}(-\Omega)\right)$,

$$(\mathcal{S}_{\hat{x}\hat{x}})_{{\rm shot},\theta}(\Omega) \overset{\rm def}{=} \frac{1}{2|\mathcal{G}_\theta(\Omega)|^2} \tag{I.3.36}$$

is the shot noise referred to the input of this effective amplifier and:

$$\begin{aligned}(\mathcal{S}^s_{\hat{x}\hat{x}})_{{\rm cross},\theta}(\Omega) \overset{\rm def}{=} \frac{1}{2}\frac{1}{\left(\frac{\Gamma_{\rm eff}}{2}\right)^2 + (\Omega - \Omega_{\rm eff})^2} \times \\ \left\{\left(\frac{\Gamma_{\rm eff}}{2} + i(\Omega - \Omega_{\rm eff})\right)\frac{B^*_+ e^{i\theta'} + B^*_- e^{-i\theta'}}{B^*_- e^{-i\theta'} - B^*_+ e^{i\theta'}} + {\rm c.c}\right\}\end{aligned} \tag{I.3.37}$$

is the symmetrized cross spectrum referred to the input of this effective amplificator, expressed here for $\Omega > 0$.

I.4: Fundamental effects in cavity optomechanics

These equations are leading to quite complex behaviors in the general case. However, only a few special cases will be relevant both for this work and for getting more insight about what consequences the optomechanical interaction has on the mechanical oscillator behavior.

I.4.a: Standard Quantum Limit

Let us first consider the case $\tilde{\Delta}_c = 0$. In this situation where the laser is resonant with the cavity, small position fluctuations from the resonator has no effect to the intensity of the field, but the modification of the resonance condition is transduced in the phase

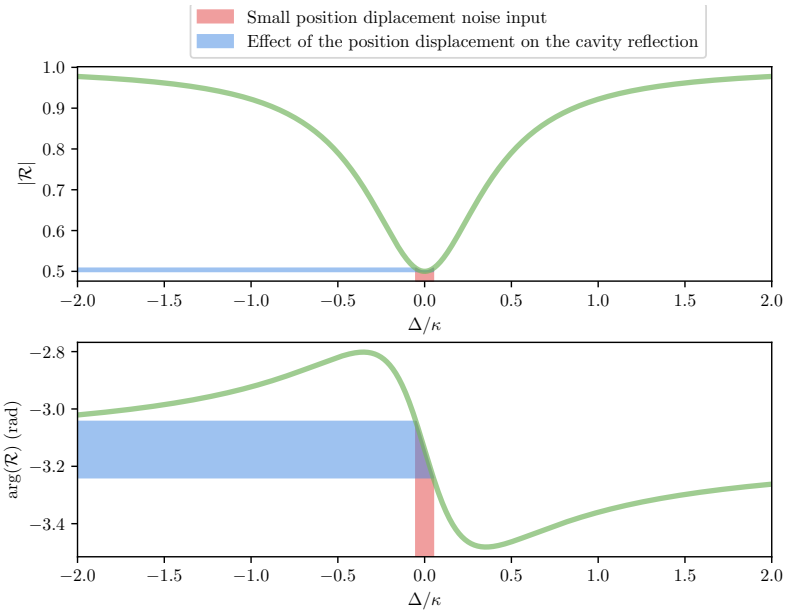

Figure I.6: amplitude (top) and phase (bottom) of the reflection of an optomechanical cavity close to resonance. The effect of a small position displacement of the mechanical resonator on the cavity frequency is shown in red, while its transduction in term of reflection is shown in blue. As expected, at first order, all the information is transduced into the phase quadrature.

of the electromagnetic field, as illustrated in figure I.6. It is typically the situation used in ultrasensitive interferometric measurements, where we compare the phase of the reflected field to a known phase reference, or to another arm of an interferometer, in order to assess the effective length of the cavity. This is for instance the case in gravitational wave interferometers.

We can see from (I.3.21) and (I.3.23) that at resonance, $\delta_{\text{opt}} = 0$. In this case,

$$\Gamma_{\text{opt}} = C\Gamma_{\text{m}} \left(|A_+|^2 - |A_-|^2 \right) \to 0. \tag{I.4.1}$$

The electromagnetic bath contribution of the right hand side of eq (I.3.19) then reads:

$$\text{sgn}(\Gamma_{\text{opt}}) \sqrt{|\Gamma_{\text{opt}}|} \hat{\mathcal{A}}_{\text{opt}}(\Omega) = \frac{\sqrt{C\Gamma_{\text{m}}}}{1 + i\frac{\Omega_{\text{m}}}{\kappa/2}} \left(\mathcal{N}_{\text{in}}(\Omega) - \mathcal{N}_{\text{in}}^{\dagger}(\Omega) \right), \tag{I.4.2}$$

which is commuting: $\left[\sqrt{|\Gamma_{\text{opt}}|} \hat{\mathcal{A}}_{\text{opt}}(\Omega), \sqrt{|\Gamma_{\text{opt}}|} \hat{\mathcal{A}}_{\text{opt}}^{\dagger}(\Omega) \right] = 0$. Therefore in this case the part of the resulting mechanical spectrum due to this electromagnetic noise is purely symmetric in frequency: this cannot be represented by a bath of bosonic modes with an effective temperature, but by a purely classical drive. This is consistent with the fact that $\Gamma_{\text{opt}} \to 0$: there are as many phonons converted to photons than the reciprocal phenomenon, thus the dynamics of the resonator is not changed. However, those exchanges still gives rise to a heating mechanism. It can indeed be noted that if we keep the notations of the previous section, the product $\Gamma_{\text{opt}} n_{\text{eff}}$ maintains a

finite value, and thus the formula (I.3.26) still holds. The heated resonator reaches an equilibrium occupation of $n_f = n_\mathrm{B} + \frac{C}{1+\left(\frac{\Omega_\mathrm{m}}{\kappa/2}\right)^2}$. The position spectrum here reads:

$$\mathcal{S}_{\hat{x}\hat{x}}^{\mathrm{meas}}(\Omega) = 4\frac{x_\mathrm{ZPF}^2}{\Gamma_\mathrm{m}}\frac{1}{1+\left(\frac{\Omega-\Omega_\mathrm{m}}{\Gamma_\mathrm{m}/2}\right)^2}\left[n_\mathrm{B}+1/2+\frac{C}{1+\left(\frac{\Omega_\mathrm{m}}{\kappa/2}\right)^2}\right] + \left(\mathcal{S}_{\hat{x}\hat{x}}\right)_\mathrm{shot}(\Omega), \quad \text{(I.4.3)}$$

where this symmetric spectrum is expressed for $\Omega > 0$ and where we choose to extract the phase quadrature (setting $\theta = \pi/2$), since at zero detuning all the information lies in this quadrature. In this configuration, note that the symmetric part of the cross spectrum vanishes. Moreover, note that the backaction noise is proportional to the light intensity, whereas the shot noise is inversely proportionnal to the light intensity. This generates a trade-off with an optimal intensity, which is called the *Standard Quantum Limit* (SQL). This intensity is such that:

$$C_\mathrm{SQL} = \frac{1}{4}\left[1+\left(\frac{\Omega_\mathrm{m}}{\kappa/2}\right)^2\right] \quad \text{(I.4.4)}$$

The variation of the total added noise (corresponding to the shot noise and backaction noise contributions) are shown in figure I.7 for a wide range of cooperativities around the Standard Quantum Limit. Three insets are describing the different noise contributions close to the mechanical frequency for a cooperativity below the SQL (I.7(a)), above the SQL (I.7(c)) or exactly at the SQL (I.7(b)). In the latter, the added noise reaches a minimum equal to the vacuum noise contribution. Currently, the shot noise and backaction are the main noises limiting the sensitivity of gravitational wave detectors [CAL+19][2].

I.4.b: Resolved sideband cooling

Let us now focus on the case $\tilde{\Delta}_c \approx -\Omega_\mathrm{m}$, in the so called *resolved sideband regime*, which corresponds to $\Omega_\mathrm{m} \gg \kappa$. In this regime the filtering of the cavity allows to completely suppress one of the sidebands, in this case the *red* sideband at $\omega = \omega_l - \Omega_\mathrm{m}$. We can write the expression of the Hamiltonian (I.3.17) in an interaction picture with respect to $\hat{H}_0 \overset{\mathrm{def}}{=} \hbar\Omega_\mathrm{m}\hat{b}^\dagger\hat{b} - \hbar\Delta\hat{a}^\dagger\hat{a}$:

$$\hat{H} = \hbar g_0(\alpha^*\hat{a}e^{i\Delta t} + \alpha\hat{a}^\dagger e^{-i\Delta t})(\hat{b}e^{-i\Omega_\mathrm{m}t} + \hat{b}^\dagger e^{i\Omega_\mathrm{m}t}). \quad \text{(I.4.5)}$$

In equation (I.4.5), there are two rapidly oscillating terms that can be neglected. This approximation is called the Rotating Wave Approximation (RWA), and corresponds to neglecting the processes where the energy conservation does not hold. The Hamiltonian therefore boils down to:

$$\hat{H}_\mathrm{int} = \hbar g_0(\alpha^*\hat{a}\hat{b}^\dagger + \alpha\hat{a}^\dagger\hat{b}) \quad \text{(I.4.6)}$$

[2] In this particular case, the interesting measurement bandwidth lies far away from the mechanical resonances of the mirrors, such that the SQL can be approached even in the presence of a large thermal occupation

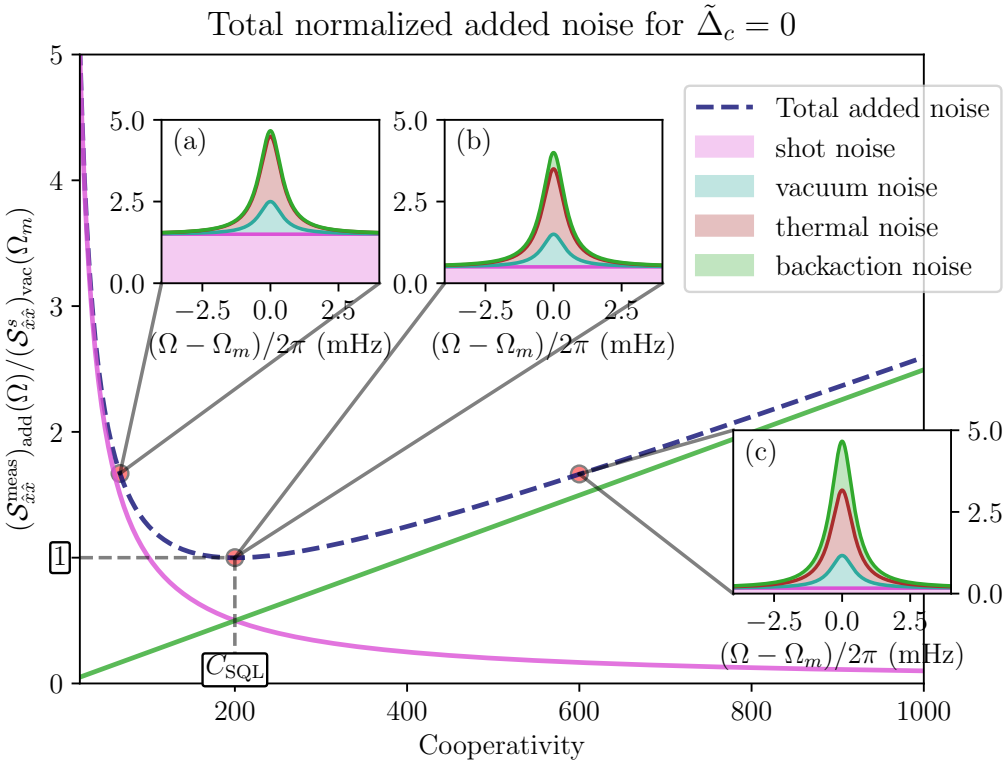

Figure I.7: Total normalized mechanical added noise $(\mathcal{S}^{\rm meas}_{\hat{x}\hat{x}})_{\rm add}(\Omega)/(\mathcal{S}_{\hat{x}\hat{x}})_{\rm vac}(\Omega_{\rm m})$ for $\tilde{\Delta}_c = 0$ versus the cooperativity. On the main axis, only the backaction (green) and shot noise (pink) are represented. The three insets represent all the noise contributions (including vacuum (blue) and thermal noise (red) assuming one phonon occupation) versus the frequency for a cooperativity: (a) below the SQL cooperativity, (b) exactly at the SQL or (c) above the SQL. Below the SQL, the shot noise is dominant, whereas above the SQL the backaction noise is dominant. Exactly at the SQL, the total added noise reaches a minimum equals to the vacuum noise contribution. $\eta = 1$ and a reflection cavity configuration are here assumed.

This is a *beam splitter* Hamiltonian : the processes allowed correspond to a swap between photons and phonons, while the corresponding coherent evolution is a periodic exchange between the mechanical state and the electromagnetic state, at a frequency $|\alpha|g_0/2\pi$. The first process, called an anti-Stokes process, corresponds to the scattering of a photon from the pump to the electromagnetic cavity, and the annihilation of a phonon. The reciprocal process is also possible. This interaction will be useful either for reading the mechanical state by copying its state to the electromagnetic resonator and reading it, or, by using the differences between the two reservoirs the system is interacting with, to dissipate the phonons in the electromagnetic environment, leading to an optomechanical cooling phenomenon.

Indeed, in this configuration, equation (I.3.21) reads:

$$\Gamma_{\rm cool} \approx 4C\Gamma_{\rm m}\left(\frac{\Omega_{\rm m}}{\kappa}\right)^2 \frac{1}{\frac{1}{4}+4\left(\frac{\Omega_{\rm m}}{\kappa}\right)^2} \approx C\Gamma_{\rm m}, \tag{I.4.7}$$

while equation (I.3.25) reads $n_{\rm eff} \approx 0$, which means the mechanical oscillator is coupled to a cold bath at a rate $\Gamma_{\rm opt}$ and a hot bath at a rate $\Gamma_{\rm m}$, leading to the equilibrium occupation:

$$n_f \stackrel{\rm def}{=} \frac{\Gamma_{\rm m} n_{\rm B} + \Gamma_{\rm opt} n_{\rm eff}}{\Gamma_{\rm m}+\Gamma_{\rm opt}} \approx \frac{n_{\rm B}}{1+C}. \tag{I.4.8}$$

The cooling mechanism can be alternatively understood with the figure I.9: the pump, with a lower energy than the electromagnetic cavity, drives the transition between the state $|0,m\rangle$, to $|1,m-1\rangle$, where the first number in the ket designates the number of photons in the cavity, and the second number is the number of phonons in the mechanical resonator. Since the decay rate κ of excitations in the electromagnetic cavity is the dominating rate in the problem, this process efficiently evacuates thermal phonons into the electromagnetic environment. The rate of this process is $\Gamma_{\rm m}C$, and needs to be compared to the rate of entrance of new phonons from the mechanical environment (jumps from $|0,n\rangle$ to $|0,n+1\rangle$), which is $\Gamma_{\rm m} n_{\rm B}$.

We see from (I.4.8) that a prerequisite for achieving ground state cooling is to reach $1+C \gg n_{\rm B}$. This means that for a typical dilution fridge able to reach 10 mK, and for mechanical resonators with a frequency of the order of the MHz, a cooperativity of $C \gg 200$ is required. In this configuration, the backaction noise, which is proportional to $\Gamma_{\rm opt} n_{\rm eff}$, vanishes.

Since in the sideband resolved limit the upper sideband is totally suppressed ($|A_-|^2 = 0$), the effective electromagnetic environnement is purely asymmetric in frequency. Indeed, the electromagnetic part of the right hand side of equation (I.3.19) reads:

$$\mathrm{sgn}(\Gamma_{\rm opt})\sqrt{|\Gamma_{\rm opt}|}\hat{\mathcal{A}}_{\rm opt}(\Omega) = \sqrt{C\Gamma_{\rm m}}\mathcal{N}_{\rm in}(\Omega), \tag{I.4.9}$$

which is proportional to the annihilation operator of electromagnetic input modes. The antisymmetry of this process results from the zero electromagnetic occupation that was assumed. Consequently, the backaction from the environment vanishes ($n_{\rm eff} \to 0$). Furthermore, the cross spectrum between the output shot noise and displacement noise (see eq.(I.3.37)) reads:

$$(\mathcal{S}^s_{\hat{x}\hat{x}})_{\text{cross},\theta}(\Omega) = -\Gamma_{\text{eff}}/2 \frac{1}{\left(\frac{\Gamma_{\text{eff}}}{2}\right)^2 + (\Omega - \Omega_{\text{eff}})^2} \tag{I.4.10}$$

As a result, the contributions of the symmetrized cross-spectrum and vacuum noise in the total spectrum given by Eq (I.3.35) perfectly cancel each other:

$$\begin{aligned} \mathcal{S}_{\hat{X}\hat{X}}(\Omega) &= |\mathcal{G}_\theta(\Omega)|^2 \left[(\mathcal{S}_{\hat{x}\hat{x}})_{\text{shot},\theta}(\Omega) + (\mathcal{S}^s_{\hat{x}\hat{x}}(\Omega))_{\text{vac}} + (\mathcal{S}^s_{\hat{x}\hat{x}}(\Omega))_{\text{therm}} + (\mathcal{S}^s_{\hat{x}\hat{x}})_{\text{cross},\theta}(\Omega)\right] \\ &= |\mathcal{G}_\theta(\Omega)|^2 \left[(\mathcal{S}_{\hat{x}\hat{x}})_{\text{shot},\theta}(\Omega) + (\mathcal{S}^s_{\hat{x}\hat{x}}(\Omega))_{\text{therm}}\right]. \end{aligned} \tag{I.4.11}$$

This spectrum is thus the sum of a constant term, the shot noise, and a lorentzian term, the thermal noise. The shot noise level decreases as $1/C$, however, at the same time, the thermal peak has a width $\Gamma_{\text{eff}} = \Gamma_{\text{m}}(1+C)$, and a total area proportional to $n_f = n_{\text{th}}/(1+C)$. For a given mechanical noise spectrum $\mathcal{S}_{\hat{x}\hat{x}}$, it is useful to express this area in term of a number n of mechanical phonons, according to the relation [TDCB$^+$09]:

$$n \stackrel{\text{def}}{=} \mathcal{S}_{\hat{x}\hat{x}}(\Omega_{\text{m}}) \frac{\Gamma_{\text{eff}}}{2x^2_{\text{ZPF}}}. \tag{I.4.12}$$

We can then apply this definition to the shot noise to define the imprecision noise in terms of phonon number:

$$n_{\text{imp}} \stackrel{\text{def}}{=} \left(\frac{x^2_{\text{ZPF}}}{C\eta\Gamma_{\text{m}}}\right)\left(\frac{\Gamma_{\text{m}}(1+C)}{2x^2_{\text{ZPF}}}\right) = \frac{1+C}{2\eta C}, \tag{I.4.13}$$

which converges towards a finite value $\frac{1}{2\eta}$. For a given environmental occupation n_{B}, however, the visibility of the Lorentzian peak due to thermal noise has a non-monotonic behavior as a function of C::

$$\mathcal{V} \stackrel{\text{def}}{=} \mathcal{S}^{\text{therm}}_{\hat{x}\hat{x}}(\Omega_{\text{eff}})/(\mathcal{S}_{\hat{x}\hat{x}})_{\text{shot}}(\Omega_{\text{eff}}) = \frac{4n_{\text{B}}\eta C}{(1+C)^2}. \tag{I.4.14}$$

This non-trivial dependence results from a trade-off between the gain of our measurement, that grows linearly with C, and the extra damping caused by the cooling process, which grows as $1+C$. As a result, the visibility is maximum for a cooperativity of one, and converges towards zero for very high or very low cooperativities. These two quantities are plotted in figure I.8.

I.4.c: Parametric amplification

The last interesting case we will encounter is the case $\Delta_c \approx \Omega_{\text{m}}$, in the resolved sideband regime, where we supress the *blue* sideband at $\omega = \omega_l + \Omega_{\text{m}}$. In this configuration the interacting part of the Hamiltonian boils down to:

$$\hat{H}_{\text{int}} = \hbar g_0(\alpha^* \hat{a}\hat{b} + \alpha \hat{a}^\dagger \hat{b}^\dagger) \tag{I.4.15}$$

This is a *Parametric Down Conversion* Hamiltonian, allowing the creation and annihilation of photon-phonon pairs. The second process, called a Stokes process, corresponds

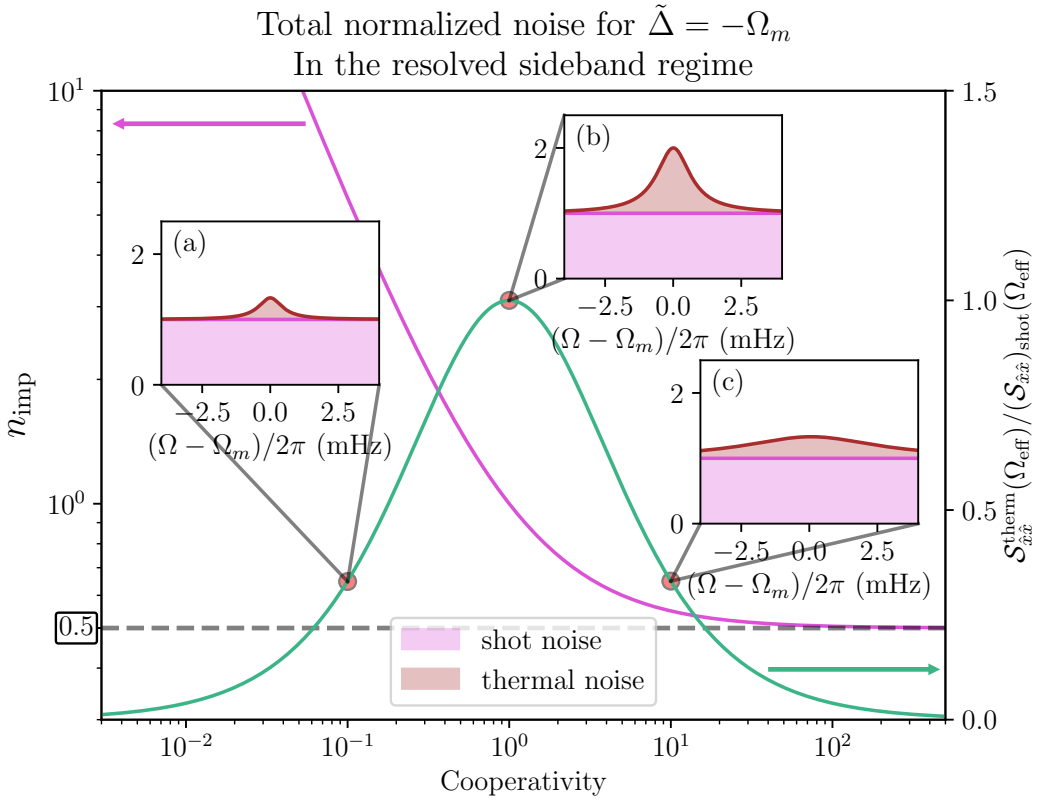

Figure I.8: (main axis, left, pink) Total added noise (*i.e.* shot noise) expressed in phonon number versus the cooperativity. (main axis, right, blue) Visibility of the peak versus the cooperativity. Insets: Total noise (*i.e.* shot noise (pink) and thermal noise (red)) normalized to the shot noise level versus the frequency close to the mechanical frequency, for different cooperativities. All those plots are assuming a resolved sideband cooling scheme, with $\tilde{\Delta}_c = -\Omega_{\mathrm{m}}$, $\eta = 1$ and $n_{\mathrm{B}} = 1$.

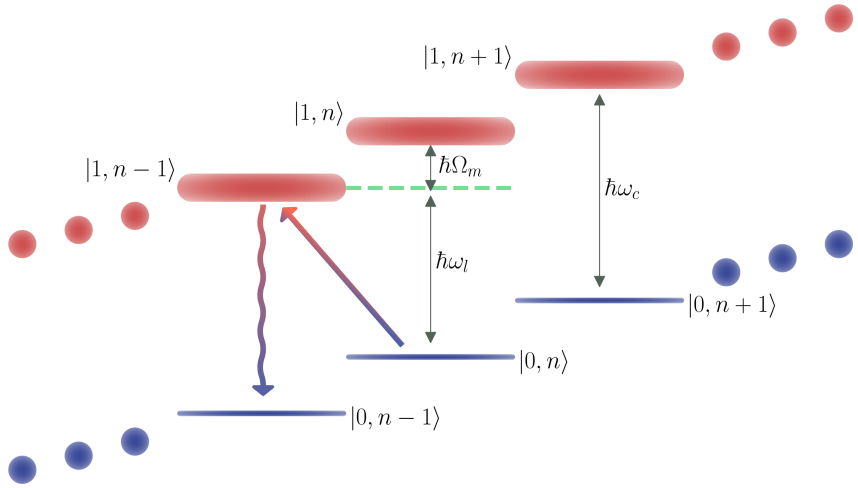

Figure I.9: Representation of the levels of energy for the joint mechanical+electromagnetic system. Red (blue) lines correspond to states for which the electromagnetic cavity contains one (zero) photon apart from the occupation imposed by the drive, while the thick straight arrow corresponds to the transition created by the coherent evolution of the sideband cooling hamiltonian, and the thick undulating arrow correponds to the rapid electromagnetic decay of the cavity

to the scattering of a photon from the pump to the electromagnetic cavity, and the creation of a phonon in the mechanical resonator. The coherent evolution associated with this Hamiltonian is the exponential growth of a two-mode squeezed state. In this configuration, equation (I.3.21) reads:

$$\Gamma_{\rm cool} \approx -4C\Gamma_{\rm m}\left(\frac{\Omega_{\rm m}}{\kappa}\right)^2 \frac{1}{\frac{1}{4}+4\left(\frac{\Omega_{\rm m}}{\kappa}\right)^2} \approx -C\Gamma_{\rm m}. \tag{I.4.16}$$

Notice a negative sign, which corresponds to a heating of the mechanical resonator at a rate $C\Gamma_{\rm m}$, while phonons are thermalizing to the environment at a rate $\Gamma_{\rm m}$. We see that if $C > 1$, the dynamics is unstable. Indeed, when $\Delta_c = +\Omega_{\rm m}$, equation (I.3.17) shows that the coherent evolution of the system still corresponds to the evolution of two linearly coupled harmonic oscillators, but that the mechanical harmonic oscillator now has a negative mass. This translates into a source of incoming phonons from the electromagnetic bath at a rate $C\Gamma_{\rm m}$, which has to be compared to the rate of thermalization with the environment, which is $\Gamma_{\rm m}$. When the incoming rate of phonons exceeds the outgoing rate, the unstable dynamics appears. We will use this instability for amplification purposes by entering this regime for short periodes of time in the framework of this PhD.

I.4.c.i High-cooperativity limit and parametric amplification

Let us focus on the high cooperativity case, where $C > 1$ and the dynamics is unstable. In such a configuration, the relevant quantum Langevin equations are in the temporal domain, since there is no equilibrium reached. In an interaction picture with respect to $\hat{H}_0 \stackrel{\rm def}{=} -\hbar\tilde{\Delta}_c\hat{a}^\dagger\hat{a} + \hbar\Omega_{\rm m}\hat{b}^\dagger\hat{b}$, we have:

$$\frac{d}{dt}\hat{a} = -\kappa/2\hat{a} - ig_0\alpha\hat{b}^\dagger + \sqrt{\kappa}\hat{\mathcal{A}}_{\rm in} \tag{I.4.17}$$

$$\frac{d}{dt}\hat{a}^\dagger = -\kappa/2\hat{a}^\dagger + ig_0\alpha^*\hat{b} + \sqrt{\kappa}\hat{\mathcal{A}}^\dagger_{\rm in} \tag{I.4.18}$$

$$\frac{d}{dt}\hat{b}^\dagger = -\Gamma_{\rm m}/2\hat{b}^\dagger + ig_0\alpha^*\hat{a} + \sqrt{\Gamma_{\rm m}}\hat{b}^\dagger_{\rm in} \tag{I.4.19}$$

$$\frac{d}{dt}\hat{b} = -\Gamma_{\rm m}/2\hat{b} - ig_0\alpha\hat{a}^\dagger + \sqrt{\Gamma_{\rm m}}\hat{b}_{\rm in}, \tag{I.4.20}$$

where $\hat{\mathcal{A}}_{\rm in} \stackrel{\rm def}{=} \sqrt{\eta}\hat{a}_{\rm in,c} + \sqrt{1-\eta}\hat{a}_{\rm in,0}$ and $\eta = \kappa_c/\kappa$. The adiabatic elimination is here performed by considering that when we are interested in the evolution of the mechanical oscillator, the electromagnetic resonator is in its steady state, because $\kappa \gg \Gamma_{\rm m}$, and thus we have $\frac{d}{dt}\hat{a} \approx 0$ and $\frac{d}{dt}\hat{a}^\dagger \approx 0$. This system can then be solved, leading to:

$$\hat{b}^\dagger(t) = \hat{b}^\dagger(0)h_b(t) + (h_b \circledast \hat{\mathcal{N}})(t) \tag{I.4.21}$$

$$\hat{b}(t) = \hat{b}(0)h_b(t) + (h_b \circledast \hat{\mathcal{N}}^\dagger)(t) \tag{I.4.22}$$

where $\Gamma_b \stackrel{\rm def}{=} C\Gamma_{\rm m}$, $h_b(t) \stackrel{\rm def}{=} e^{(C-1)\Gamma_{\rm m}t/2}$, and $\hat{\mathcal{N}}(t) \stackrel{\rm def}{=} \sqrt{C\Gamma_{\rm m}}(ie^{-i\Psi})\hat{\mathcal{A}}_{\rm in}(t) + \sqrt{\Gamma_{\rm m}}\hat{b}^\dagger_{\rm in}(t)$, Ψ is such that $\alpha = |\alpha|e^{i\Psi}$ and $\circledast$ is the convolution product. As expected, when the

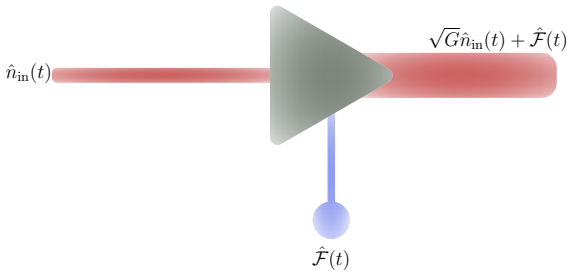

Figure I.10: Schematics of a linear phase preserving bosonic amplifier: the input signal is amplified by a gain $\sqrt{G}$ while some noise $\hat{\mathcal{F}}(t)$ is added to the output.

condition $C > 1$ holds, the mechanical position operator will undergo an exponential growth, that will be limited only by non linear behavior at very high amplitude.

In equations (I.4.21) and (I.4.22), the gain of the amplification, equals to $h_b(t)$, comes with an added noise, $(h_b \circledast \hat{\mathcal{N}})(t)$, due to both the mechanical thermal noise due to dissipation and to the electromagnetic noise transduced by the optomechanical interaction. This is in fact a general feature of every amplifier.

Indeed, every linear phase preserving (*i.e.* for which the same gain applies to both quadratures) amplifier can be modelled as presented in figure I.10 [CDG+10]: the input signal is amplified with a gain $\sqrt{G}$ while some noise $\hat{\mathcal{F}}(t)$ is added, leading to an output $\hat{n}_{\rm out}(t) \stackrel{\rm def}{=} \sqrt{G}\hat{n}_{\rm in}(t) + \hat{\mathcal{F}}(t)$. This extra noise ensures that the bosonic commutation relations are not modified by the amplifier, as in the quantum Langevin equation derivation for a lossy cavity: $[\hat{n}_{\rm in}(t),\hat{n}^\dagger_{\rm in}(t')] = [\hat{n}_{\rm out}(t),\hat{n}^\dagger_{\rm out}(t')] = \delta(t-t')$. From this condition follows: $[\hat{\mathcal{F}}(t),\hat{\mathcal{F}}^\dagger(t')] = (1-G)\delta(t-t')$. Note that an amplifier is an active device bringing energy to the system. As a consequence of the great variety of mechanisms able to provide this extra energy, there is no particular requirements for the value of $\langle\hat{\mathcal{F}}^\dagger(t)\hat{\mathcal{F}}(t')\rangle$, except a lower bound. Indeed, if we focus on the observables $\hat{X}_{\rm in} \stackrel{\rm def}{=} \frac{\hat{n}_{\rm in}+\hat{n}^\dagger_{\rm in}}{\sqrt{2}}$ and $\hat{X}_{\rm out} \stackrel{\rm def}{=} \frac{\hat{n}_{\rm out}+\hat{n}^\dagger_{\rm out}}{\sqrt{2}}$ we have:

$$\langle\hat{X}^\dagger_{\rm out}(t)\hat{X}_{\rm out}(t')\rangle = G\langle\hat{X}^\dagger_{\rm in}(t)\hat{X}_{\rm in}(t')\rangle + \frac{1}{2}\langle\hat{\mathcal{F}}(t)\hat{\mathcal{F}}^\dagger(t') + \hat{\mathcal{F}}^\dagger(t)\hat{\mathcal{F}}(t')\rangle \tag{I.4.23}$$

$$\geq G\langle\hat{X}^\dagger_{\rm in}(t)\hat{X}_{\rm in}(t')\rangle + \frac{|G-1|}{2}\delta(t-t'), \tag{I.4.24}$$

where the triangular identity has been used. To compare the added noise to the input of the amplifier, it is interesting to factorize this result by the gain G. The added noise $\mathcal{N}_{\rm add}$, defined by $\langle\hat{X}^\dagger_{\rm out}(t)\hat{X}_{\rm out}(t')\rangle \stackrel{\rm def}{=} G\left[\langle\hat{X}^\dagger_{\rm in}(t)\hat{X}_{\rm in}(t')\rangle + \hat{\mathcal{N}}_{\rm add}\delta(t-t')\right]$ then fulfills:

$$\mathcal{N}_{\rm add} \geq \frac{|G-1|}{2G}. \tag{I.4.25}$$

Note that $\mathcal{N}_{\rm add}$ is more often expressed as a *noise temperature*, defined by $T_N \stackrel{\rm def}{=} \mathcal{N}_{\rm add}\hbar\omega/k_{\rm B}$. $\mathcal{N}_{\rm add}$ converges towards $\frac{1}{2}$ in the limit of very high gain $G \gg 1$. This corresponds to the addition of half a quantum of noise.

Let us first derive the electromagnetic output fields for the blue detuned strongly pumped optomechanical system. Injecting back equations (I.4.22) and (I.4.21) in equations (I.4.18) and (I.4.17), the electromagnetic occupation reads:

$$\hat{a}(t) = (-ie^{i\Psi_\alpha})\sqrt{\frac{C\Gamma_{\rm m}}{\kappa}}\left[\hat{b}^\dagger(0)h_b(t) + (h_b \circledast \hat{\mathcal{N}})(t)\right] + \frac{2}{\sqrt{\kappa}}\hat{\mathcal{A}}_{\rm in} \tag{I.4.26}$$

$$\hat{a}^\dagger(t) = (ie^{-i\Psi_\alpha})\sqrt{\frac{C\Gamma_{\rm m}}{\kappa}}\left[\hat{b}(0)h_b(t) + (h_b \circledast \hat{\mathcal{N}}^\dagger)(t)\right] + \frac{2}{\sqrt{\kappa}}\hat{\mathcal{A}}^\dagger_{\rm in}. \tag{I.4.27}$$

Assuming a reflection cavity configuration:

$$\hat{a}_{\rm out} = -\hat{a}_{\rm in,c} + \sqrt{\kappa_c}\hat{a}, \tag{I.4.28}$$

the output reads:

$$\hat{a}_{\rm out}(t) = s_{\rm noise}(t) + s_{\rm sig}(t) \tag{I.4.29}$$

$$\hat{a}^\dagger_{\rm out}(t) = s^\dagger_{\rm noise}(t) + s^\dagger_{\rm sig}(t), \tag{I.4.30}$$

where:

$$s_{\rm sig}(t) \stackrel{\rm def}{=} (-ie^{i\Psi_\alpha})\sqrt{\eta C\Gamma_{\rm m}}\hat{b}^\dagger(0)h_b(t) \tag{I.4.31}$$

$$s_{\rm noise}(t) \stackrel{\rm def}{=} (-\hat{a}_{\rm in,c} + 2\sqrt{\eta}\hat{\mathcal{A}}_{\rm in})(t) + (-ie^{i\Psi_\alpha})\sqrt{\eta C\Gamma_{\rm m}}(h_b \circledast \hat{\mathcal{N}})(t) \tag{I.4.32}$$

are respectively the signal and noise terms. To compute the added noise in this transient amplification scheme, an approach slightly different than the generic formalism used above for propagating modes should be used. Indeed, the input and output of this amplifier cannot be defined as propagating modes. As expressed by formula 1.4.31, upon the action of the blue sideband drive, the initial mechanical field $\hat{b}^\dagger(0)$ is transferred onto a particular propagating mode of the output line, defined by the diverging waveform $h_b(t)$. In practice, one can switch off the drive after a given time t, and try to retrieve the initial mechanical field $\hat{x}(0)$ by applying the right temporal filtering over the noisy outgoing signal. We hence introduce the observables:

$$\mathcal{S}_{\rm noise/sig} \stackrel{\rm def}{=} \frac{1}{\sqrt{\int_0^t h_b^2(t')dt'}}\int_0^t \frac{s_{\rm noise/sig} + s^\dagger_{\rm noise/sig}}{\sqrt{2}}(t')h_b(t')dt'. \tag{I.4.33}$$

In the limit of a hich cooperativity ($C \gg 1$), and long enough pulse duration such that $\Gamma_{\rm m}(C-1)t \gg 1$, we find that:

$$\mathcal{S}_{\rm sig} \approx \sqrt{\eta e^{\Gamma_{\rm m}Ct}}\frac{\hat{x}(0)}{\sqrt{2}x_{\rm ZPF}}. \tag{I.4.34}$$

We are therefore observing an amplifier with a gain $\eta e^{\Gamma_m C t}$ acting on the input signal $\frac{\hat{x}(0)}{\sqrt{2}x_{\mathrm{ZPF}}}$[3] Let us now study the noise of $\mathcal{S}_{\mathrm{noise}}$, by inspecting the second moment of $\mathcal{S}_{\mathrm{noise}}$:

$$\mathcal{N}_{\mathrm{noise/sig}} \overset{\mathrm{def}}{=} \langle \mathcal{S}^{\dagger}_{\mathrm{noise/sig}} \mathcal{S}_{\mathrm{noise/sig}} \rangle \tag{I.4.35}$$

We find, in the same limit taken in equation I.4.34:

$$\mathcal{N}_{\mathrm{sig}} \approx \eta e^{\Gamma_m C t} \left(n_{\mathrm{m,ini}} + \frac{1}{2} \right) \tag{I.4.36}$$

$$\mathcal{N}_{\mathrm{noise}} \approx \eta e^{\Gamma_m C t} \left(n_{\mathrm{opt}} + \frac{1}{2} \right), \tag{I.4.37}$$

where $n_{\mathrm{m,ini}} \overset{\mathrm{def}}{=} \langle \hat{b}^{\dagger}(0)\hat{b}(0) \rangle$ is the "useful" signal. We see that in close analogy with the general framework of a linear phase preserving amplifier presented above, when expressed in the relevant variables, the system could be described as an amplifier with a gain $\eta e^{\Gamma_m C t}$ and added noise equal to $n_{\mathrm{opt}} + \frac{1}{2}$, which reaches the lower bound established for the propagating mode model seen above in the limit of low electromagnetic occupancy $n_{\mathrm{opt}} \approx 0$.

This is generally the case for a parametric amplifier using another degree of freedom (here, an electromagnetic mode) to add energy to the system : the minimum noise that has to be added corresponds to the vacuum noise of such additional mode.

I.4.c.ii Low cooperativity limit and sideband thermometry

In the low cooperativity limit ($C < 1$), the system is stable and it makes sense to look at the resulting spectrum. Equation (I.3.25) here reads $n_{\mathrm{eff}} \approx -1$ and the cross spectrum reads:

$$(\mathcal{S}_{\hat{x}\hat{x}})_{\mathrm{cross},\theta}(\Omega) = \frac{\Gamma_{\mathrm{eff}}}{2} \frac{1}{\left(\frac{\Gamma_{\mathrm{eff}}}{2}\right)^2 + (\Omega - \Omega_{\mathrm{eff}})^2}. \tag{I.4.38}$$

In these conditions, we find that all the terms proportional to Γ_{opt} in eq (I.3.35) compensate exactly, leaving:

$$\begin{aligned} \mathcal{S}_{\hat{X}\hat{X}}(\Omega) &= |\mathcal{G}_{\theta}(\Omega)|^2 \left[(\mathcal{S}_{\hat{x}\hat{x}})_{\mathrm{shot},\theta}(\Omega) + (\mathcal{S}^{s}_{\hat{x}\hat{x}}(\Omega))_{\mathrm{vac}} + (\mathcal{S}^{s}_{\hat{x}\hat{x}}(\Omega))_{\mathrm{therm}} + (\mathcal{S}^{s}_{\hat{x}\hat{x}}(\Omega))_{\mathrm{back}} + (\mathcal{S}^{s}_{\hat{x}\hat{x}})_{\mathrm{cross},\theta}(\Omega) \right] \\ &= |\mathcal{G}_{\theta}(\Omega)|^2 \left[(\mathcal{S}_{\hat{x}\hat{x}})_{\mathrm{shot},\theta}(\Omega) + x^2_{\mathrm{ZPF}} \Gamma_m \frac{n_B + 1}{\left(\frac{\Gamma_{\mathrm{eff}}}{2}\right)^2 + (\Omega - \Omega_{\mathrm{eff}})^2} \right], \end{aligned} \tag{I.4.39}$$

where this expression of this symmetric spectrum holds for $\Omega > 0$. The spectrum, as in the case of the resolved sideband cooling, is the sum of a constant noise, the shot noise, and a lorentzian. However, when in the former case this lorentzian was proportional to n_B, in the latter it is is proportional to $n_B + 1$. This discrepancy allows to perform an

[3] note that we change the phase reference for the annihilation operator: $\hat{x}(0) = x_{\mathrm{ZPF}}(\hat{b}(0)(ie^{-i\Psi_\alpha}) + \hat{b}^{\dagger}(0)(-ie^{i\Psi_\alpha}))$

absolute thermometry of the mechanical resonator [KMY$^+$12, SNCH$^+$12, SNCH$^+$13]: the ratio of the areas under the thermal peak measured for the two detunings is equal to $1 + \frac{1}{n_\mathrm{B}}$, independently of the experimental setup.

In this chapter, we derived the theoretical framework describing the quantum behavior of a mechanical oscillator, first only coupled to its natural thermal environment (see section I.2), then to an electromagnetic degree of freedom as well (see section I.3). In the last section, we saw how to use this external degree of freedom to cool down or amplify the mechanical oscillator. In the next chapter, we will describe the design, fabrication and characterization of mechanical oscillators that were made to be coupled to microwave cavities.

Chapter II: High stressed silicon nitride membranes

The analysis made in chapter I can be used to assess the requirements a mechanical resonator needs to fulfill in order to be coupled efficiently to an optical cavity. In particular, if we restrain ourselves to the ability to reach the motional ground state, we can focus on the lowest occupation achievable for a mechanical resonator through resolved sideband cooling, for a high initial occupation and a high cooperativity:

$$n_{\min} \approx \frac{k_{\mathrm{B}} T \kappa}{2\hbar^2 G^2 |\alpha|^2} \Gamma_{\mathrm{m}} m_{\mathrm{eff}}. \tag{II.0.1}$$

Examining the expression II.0.1, we can already see that it scales as $m_{\mathrm{eff}}\Gamma_{\mathrm{m}}$. Thus, the resonator should have a low effective mass m_{eff}, and a low relaxation rate Γ_{m}. In addition to these requirements, working with mechanical frequencies comparable to ~ 1 MHz is required to escape the low frequency technical noise of electromagnetic sources.

Various materials and geometries have been used in the optomechanical community for realizing mechanical oscillators. In particular we can cite Silica microtoroid [SRA$^+$08], or Galium Arsenide microdisk [DBS$^+$10] breathing modes, Aluminium suspended wires [TDCB$^+$09] or membranes [TdL$^+$11], Silicon [CASN$^+$11] or Lithium Niobate [AAWW$^+$19] suspended nanobeams patterned with a phononic crystal, Silica levitating nanoparticles [DRD$^+$20], bulk acoustic phonons in Quartz [KHK$^+$19], Aluminium Nitride [OHA$^+$10] or Sapphire [CKY$^+$18], flexural modes of inverted conical Gallium Arsenide nanopillars [PSL$^+$13], vibration of acoustic modes of a superfluid ^{4}He bubble [SKB$^+$19], or surface acoustic waves in Quartz [MKP$^+$17].

On the other hand, stoechiometric silicon nitride (Si_3N_4) drew a significant attention in the community during the past decade: as shown in figure II.1, the amount of articles tackling the subject has been growing exponentially with time. Indeed, nanomembranes made with the material show unprecedented quality factors, thanks to a mechanism denoted by *dissipation dilution* [FEG$^+$19]. Moreover, they are both optically and microwave-compliant. Thus, they are good candidates to realize quantum memories, that are coupled either to optical or microwave circuits (or both).

Silicon nitride resonators have been implemented in various geometries, from thin square [YCS15] or round [SMB$^+$18] membranes, frame membranes [SPMdL$^+$16], nanos-

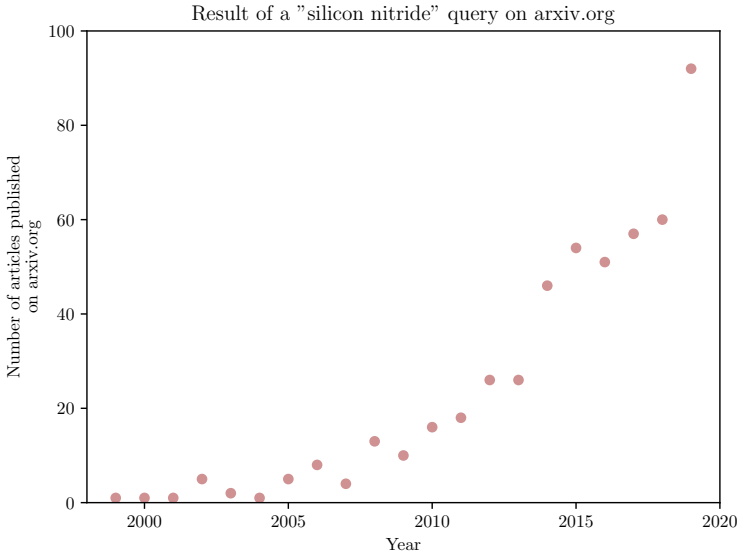

Figure II.1: Number of articles comprising "silicon nitride" or "Si_3N_4" in its abstract or title that were published per year on the website arxiv.org.

trings [FKM+12], trampolines [RMBS16], 1D [GDS15, GFE+18] or 2D [TBPS17, RFAmca+19] phononic crystal structures or even more complex geometries [WBL+17].

In this work, we made square membranes. We developed numerous nanofabrication recipes and characterization tools to fabricate and improve their characteristics. Subsequently, we were able to couple them to a microwave cavity and to perform optomechanical cooling, optomechanical amplification, and some other interesting experiments that will be further described in chapter III and IV.

This chapter is organized as follows. First, we will describe the mechanical modes of a square membrane and the *dissipation dilution* mechanism. Then, we will present the nanofabrication recipe of the membranes used in this work. Finally, we will present the membrane characterization techniques we developed.

II.1: Mechanical modes of a square membrane

In this section, we derive analytical formulas for mode frequencies and shapes. Then we compute the mode effective mass, and finally we list all the loss channels of membranes, and explain the mechanism called dissipation dilution, which allows to reach extremely high quality factors.

II.1.a: Mode shape and frequency

Let us consider a square membrane, of size a and thickness h, such that $h \ll a$. Let us assume that it is strongly and uniformly stressed in the x and y directions, and that it is clamped on all edges. The increase of potential energy due to its small out of plane displacement w is [TYW74]:

$$V = \frac{\sigma h}{2} \int_{-a/2}^{a/2} \int_{-a/2}^{a/2} dxdy \left[\left(\frac{\partial w}{\partial x} \right)^2 + \left(\frac{\partial w}{\partial y} \right)^2 \right], \tag{II.1.1}$$

where σ is the in plane stress. The kinetic energy reads:

$$K = \frac{\rho h}{2} \int_{-a/2}^{a/2} \int_{-a/2}^{a/2} \dot{w}^2 dxdy, \tag{II.1.2}$$

with ρ the mass density of the membrane. Let us decompose the solution on a sinusoidal basis :

$$w(x,y,t) = \sum_{n=1}^{\infty} \sum_{m=1}^{\infty} p_{mn}(t) \chi_{mn}(x,y), \tag{II.1.3}$$

where:

$$\chi_{mn}(x,y) \stackrel{\text{def}}{=} \sin\left(\frac{n\pi}{a}(x + \frac{a}{2}) \right) \sin\left(\frac{m\pi}{a}(y + \frac{a}{2}) \right). \tag{II.1.4}$$

Note that this solution automatically satisfies the position boundary condition:

$$w(x = \pm\frac{a}{2}) = w(y = \pm\frac{a}{2}) = 0. \tag{II.1.5}$$

The potential energy thus reads:

$$V = \frac{\sigma h \pi^2}{8} \sum_{n=1}^{\infty} \sum_{m=1}^{\infty} p_{mn}^2 \left(m^2 + n^2 \right), \tag{II.1.6}$$

while the kinetic energy is:

$$K = \frac{\rho h a^2}{8} \sum_{n=1}^{\infty} \sum_{m=1}^{\infty} \dot{p}_{mn}^2 \tag{II.1.7}$$

We can then derive the canonical Hamilton equations:

$$\frac{\rho h a^2}{4} \ddot{p}_{mn} + \frac{\sigma h \pi^2}{4} \left(m^2 + n^2 \right) p_{mn} = 0, \tag{II.1.8}$$

from which the derivation of the mechanical frequencies is straightforward:

$$f_{mn} = \frac{1}{2a} \sqrt{\frac{\sigma \left(m^2 + n^2 \right)}{\rho}} \tag{II.1.9}$$

The frequencies f_{nn} are non degenerates and the modes node lines draw a rectangular grid, with equations $y_i = -\frac{a}{2} + i\frac{a}{n}$ and $x_j = -\frac{a}{2} + j\frac{a}{n}$ for (i,j) in $[\![0,n]\!]^2$. The mode amplitude reads:

$$w \propto \sin\left(\frac{n\pi}{a}(x + \frac{a}{2}) \right) \sin\left(\frac{n\pi}{a}(y + \frac{a}{2}) \right) \tag{II.1.10}$$

On the other hand, due to the membrane symmetry, the frequencies f_{mn}, with $m \neq n$ are degenerate. The mode amplitude is:

$$w \propto A \sin\left(\frac{n\pi}{a}(x + \frac{a}{2}) \right) \sin\left(\frac{m\pi}{a}(y + \frac{a}{2}) \right) + B \sin\left(\frac{m\pi}{a}(x + \frac{a}{2}) \right) \sin\left(\frac{n\pi}{a}(y + \frac{a}{2}) \right) \tag{II.1.11}$$

The frequencies and mode shapes obtained with those formulas show a remarkable agreement with FEM simulations, as shown in figure II.2.

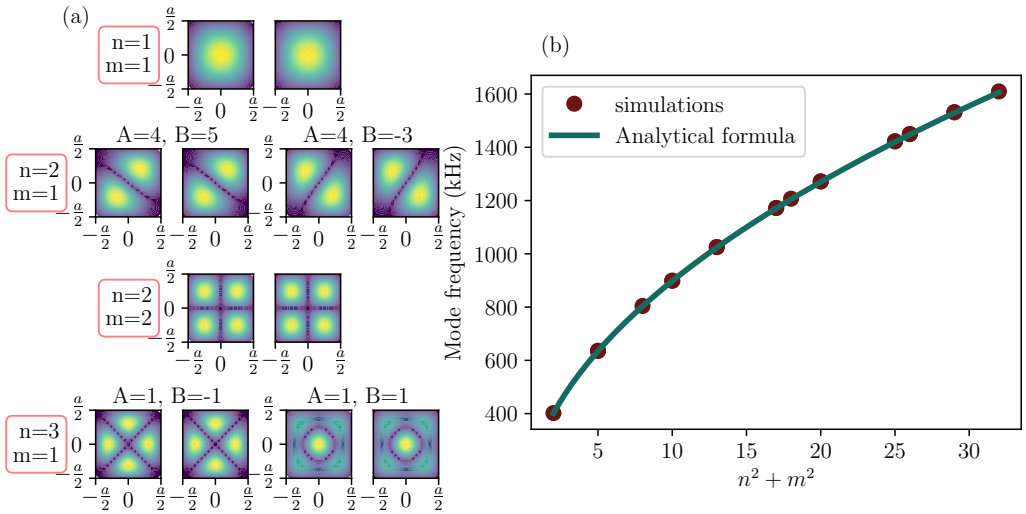

Figure II.2: (a) mode shapes for the first 6 modes of a square membrane. For each mode, the simulated mode shape is on the left, while the mode shape given by the formulas II.1.10 and II.1.11 are on the right. (b) Frequencies of the first 20 modes of a square membrane of width $a = 1$ mm, thickness $h = 100$ nm and internal stress $\sigma = 1$ GPa. The simulated frequencies are presented as dots, while the straight line correspond to the formula II.1.9

II.1.b: Mode effective mass

The definition of the effective mass is not unique, the only requirement being the definition of the potential energy:

$$\frac{1}{2}m_{\text{eff}}\omega_{nm}^2 x(t)^2 = \frac{1}{2}\omega_{nm}^2 \int_{-a/2}^{a/2}\int_{-a/2}^{a/2} \rho w(x,y,t)^2 h dx dy. \tag{II.1.12}$$

The definition we chose to use is:

$$x_{nm}(t) \overset{\text{def}}{=} \max\left(w(x,y,t)\right). \tag{II.1.13}$$

The corresponding effective mass is:

$$m_{\text{eff}} \overset{\text{def}}{=} \int_{-a/2}^{a/2}\int_{-a/2}^{a/2} \left(\frac{\rho w(x,y,t)}{x_{nm}(t)}\right)^2 h dx dy. \tag{II.1.14}$$

With this convention, the effective mass of any mode of a square membrane is:

$$m_{\text{eff}} \overset{\text{def}}{=} \frac{m}{4}, \tag{II.1.15}$$

where $m \overset{\text{def}}{=} \int_{-a/2}^{a/2}\int_{-a/2}^{a/2} \rho h dx dy$ is the mass of the membrane. Note that physical quantities such as the minimum occupation reached through resolved sideband cooling (see eq. II.0.1) are independent on the chosen definition of the effective mass. Indeed,

in this case it implies that a scaling of m_{eff} is compensated by a scaling of $x(t)^2$, and thus of G^2. For instance, a square membrane with a width of 1 mm and thickness of 100 nm has an effective mass of approximately 80 ng, while for a square membrane with a width of 300 μm it is approximately 7 ng.

II.2: Mode losses

II.2.a: Quality factor in the presence of multiple loss channels

It is possible for each mode to compute an energy loss per oscillation ΔW, which leads to the definition of a quality factor:

$$Q \overset{\text{def}}{=} \frac{2\pi W}{\Delta W}, \tag{II.2.1}$$

where W is the total energy stored in the mechanical mode. Consequently, the quality factor can be understood as the number of oscillations a mechanical oscillator can perform before the amplitude of its oscillations fades significantly. Under multiple loss mechanisms, the total loss per cycle can be summed up, leading to the total quality factor:

$$\frac{1}{Q} = \sum_i \frac{1}{Q_i}, \tag{II.2.2}$$

where the different (Q_i) are the quality factors associated with each loss mechanisms.

II.2.b: Loss channel 1: gas damping

First of all, a mechanical oscillator can exchange some energy with the air molecules it is in contact with. This is referred to as gas damping. In practice, this mechanism does not play a significant role since most optomechanical experiments are performed at very low pressure in a dedicated vacuum tank. This will be the case in this work.

II.2.c: Loss channel 2: radiation losses

The second loss mechanism is the exchange of energy between the modes of the mechanical resonator and its substrate. It is referred to as radiation losses, has been investigated thoroughly and the expression of the associated quality factor for a square membrane is [VS14]:

$$Q_{\text{rad}} \approx 1.5\xi \frac{\rho_S}{\rho} \eta^3 \frac{a}{h} \frac{n^2 m^2}{(n^2+m^2)^{3/2}}, \tag{II.2.3}$$

where ρ_S is the mass density of the substrate, ξ is a parameter ranging from 0 to 1 and depending on the clamping of the substrate, and η represents the impedance mismatch between the two mediums. It is given by:

$$\eta \overset{\text{def}}{=} \sqrt{\frac{E_S}{\sigma}\frac{\rho}{\rho_S}}, \tag{II.2.4}$$

where E_s is the Young modulus of the substrate. The last factor in eq.II.2.3 indicates that the loss increases for high order modes, which have been observed experimentally [VS14].

II.2.d: Loss channel 3: intrinsic material loss

The last loss mechanism is called internal damping, and corresponds to loss mechanisms happening inside the bulk material. Their effect is captured by introducing a complex part to the Young modulus of the material. Consequently, the strain $\epsilon(t) = \mathrm{Re}(\epsilon_0 e^{j\omega t})$ reacts with a delay when subject to a stress $\sigma(t) = \mathrm{Re}(\sigma_0 e^{j\omega t})$.

The associated loss, for a square membrane, reads[YPR12]:

$$\Delta W = \frac{\pi E \sin(\phi) h^3}{12(1-\nu^2)} \int_{-a/2}^{a/2} \int_{-a/2}^{a/2} \left(\frac{\partial^2 w}{\partial x^2} + \frac{\partial^2 w}{\partial y^2} \right)^2 dxdy \tag{II.2.5}$$

Evaluated on the mode shapes derived in section II.1, this gives the following result:

$$Q_{\mathrm{int}}^{-1} = \frac{\pi^2 \sin(\phi) \lambda^2 (n^2+m^2)}{4(1-\nu^2)}, \tag{II.2.6}$$

where $\lambda \overset{\mathrm{def}}{=} \sqrt{\frac{Eh^2}{3\sigma a^2}}$ is a small (of the order of 10^{-3} in our case) dimentionless parameter quantifying the ratio of elastic energy versus the strain energy.

II.2.e: Dissipation dilution mechanism

However, this is a naive picture, since in fact the Ansatz solution we proposed in eq. II.1.4 does not exactly fulfill the boundary conditions. Indeed, clamped membranes also impose the derivative of the position to be equal to zero at the edges. Although this does not affect the mode frequency or the general mode shape, it is not possible to neglect it for the computation of the intrinsic losses. This problem can be addressed by adding an exponential correction to the mode shape close to the edges[YPR12]:

$$\chi_{mn}(x,y) = \gamma(m,x)\gamma(n,y), \tag{II.2.7}$$

where:

$$\gamma(m,x) = \sin\left(\frac{m\pi}{a}(x + \frac{a}{2}) \right) + \epsilon_{x,m} \frac{m\lambda\pi}{2} \left[e^{-\frac{|x|-\frac{a}{2}}{\lambda a/2}} - \cos\left(\frac{m\pi}{a}(|x| - \frac{a}{2}) \right) \right]. \tag{II.2.8}$$

In the last equation,

$$\forall x < 0, \epsilon_{x,m} = 1 \tag{II.2.9}$$

$$\forall x > 0, \epsilon_{x,m} = (-1)^m \tag{II.2.10}$$

The resulting intrinsic Q factor, up to the second order in λ is:

$$Q_{\mathrm{int}}^{-1} = \frac{\sin(\phi)}{1-\nu^2} \left(\lambda + \frac{\pi^2}{4} \lambda^2 (n^2+m^2) \right). \tag{II.2.11}$$

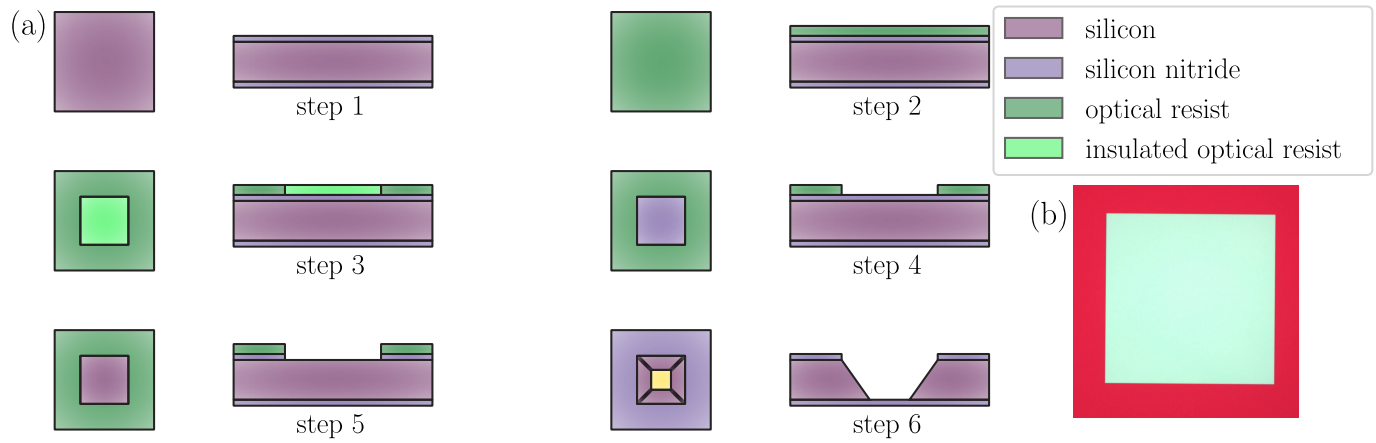

Figure II.3: (a) Nanofabrication process for making a square membrane. (b) picture of a fabricated membrane

Dissipation dilution consists in applying a large in-plane stress to the membrane, therefore reducing the parameter λ. As can be seen in equation II.2.11, this allows to reach high quality factors. A method used for Si_3N_4 deposition, called Low Pressure Chemical Vapor Deposition (LPCVD), allows, using the discrepancy between the thermal expansion coefficients of silicon nitride and silicon, to deposit a strongly ($\sim$ 1 GPa) pre-stressed thin (down to $\sim$ 10nm) silicon nitride film on top of a silicon wafer. An order of magnitude can be computed for the membranes used throughout this work, using evaluations of ϕ from the literature [VS14]. It follows:

$$Q_{\text{int}} \approx 7 \times 10^6. \tag{II.2.12}$$

As we will see, those values are typically on the same order of magnitude than the values measured experimentally, which indicates that this loss mechanism plays an important role.

Finally, note that equation II.2.11 show that for a high stressed membrane the losses are dominated by the curvature at the edges. This observation pushed the optomechanical community to develop the concept of soft clamping, whose purpose is to suppress the exponential bending of the edges of the membranes using clever geometries [TBPS17]. Among the future optimization steps of this experiment is the incorporation of those techniques (see section VII.1).

II.3: Nanofabrication process

In this section we will describe the different fabrication steps used to make the square membrane described in the previous section.

To make silicon nitride membranes, we start with a FZ grown high resistivity $\langle 100 \rangle$ 4" silicon wafer with a thickness of 525 ± 25 μm, LPCVD coated on both side with 100 nm of high stress ($\sim$ 1 GPa) stoechiometric silicon nitride (Step 1). We then cut it into squares of 3 cm per 3 cm using a diamond saw. 9 membranes are made from this chip, which is cut into 9 squares of 1 cm per 1 cm after step 6.

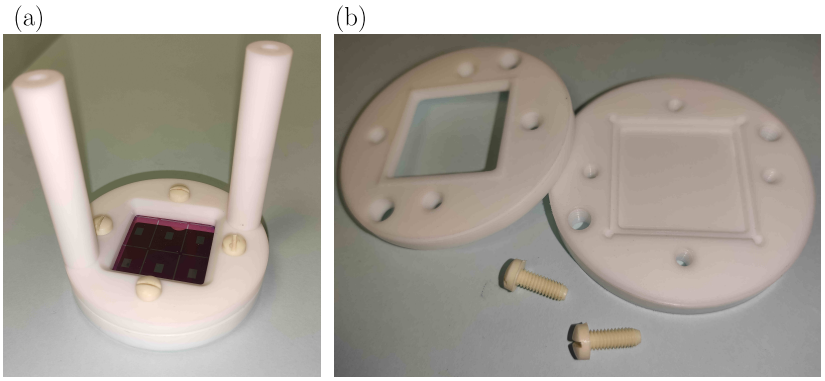

Figure II.4: (a) Picture of the closed PTFE homemade holder used for the etching of square membranes, with a dummy sample inside. (b) Picture of the opened holder, with PEEK screws.

We first define a square opening using laser or optical lithography on the back side of the sample (step 2 & 3). We proceed with a simple cleaning procedure : 10 min into hot (50 °C in bain-marie) Acetone with ultrasounds, then rinse it in Isopropanol for 20 s, then dry it with a nitrogen gun.

We then define, on the 9 samples of 1 cm per 1 cm, a square opening, alignement marks and pre-cutting rectangles (whose purposes are to facilitate the separation of the 9 individual samples after the KOH etching). This is done through either UV lithography in a MJB4 by a 20 s illumination, or laser lithography in a LW405C with a dose of 200 μC/cm^2. The development is made in AZ726MIF for around 50 s followed by DI water for 15 s, then the sample is dried using a nitrogen gun. The silicon nitride is then removed using a Corial Reactive Ion Etching (RIE, step 4). The program is CHF_3 50 sccm, O_2 6 sccm 20 mTorr 70 W plasma for 3 min 30 s.

After the leftover resist has been removed in a standard acetone cleaning (step 5), the samples are placed in a homemade PTFE holder (see Fig. II.4) and immersed in a 30 % KOH solution maintained at 85 °C for $\sim$ 5 h 40 m (step 6). The silicon nitride acts as a mask for the KOH etching, and the etching is anisotropically following the cristalline axis of the silicon sample, as shown in Step 6, creating a slope with an angle of 54,7 degrees with the horizontal plane.

After the end of the etching, the KOH is removed with a 85 °C DI water bath for 1 min, followed by a step by step replacement of the hot and contaminated with KOH DI water by a clean room temperature DI water, and then the sample is further rinced in a new clean DI water bath, followed by an isopropanol bath and a nitrogen gun drying.

Finally, a last cleaning step is performed in a 30 min 1:3 piranha bath. The result of a typical square membrane after those steps can be seen in figure II.3 (b).

II.4: Drum modes optical characterization

In this section we describe the optical characterization tools that we set up to measure mechanical modes frequencies, quality factors, and shapes.

II.4.a: Interferometric measurement

II.4.a.i Experimental setup

To measure the position of the mechanical oscillator, we perform a homodyne measurement using a Michelson interferometer (see figure II.5). The optical source used in this experiment is a fibered Mephisto Nd :Yag laser beam at 1064 nm. First, its polarization is set using the polarizing beamsplitter (PBS) C_1. Then, the PBS C_2 splits the beam into a local oscillator, used as a phase reference, and a probe beam reflecting on the sample inside a vacuum tank. A half waveplate λ_1 placed before the PBS C_2 is used to tune the power ratio between the local oscillator and the total input power. The local oscillator consists in a simple mirror M_1 mounted on a piezoelectric actuator. The latter has two purposes. The first one is aligning the interferometer: while injecting a strong sinusoidal signal in the piezo, the amplitude of the modulation at the output of the interferometer is a measure of the quality of the interferometer's alignment. The second purpose is the locking of the interferometer: to maintain the maximum sensitivity, a feedback loop slowly actuates the piezo, therefore changing the length of the local oscillator arm.

The probe beam is focused on the sample by means of the convergent lens L_1 (f=30 mm), which stands outside the vacumm chamber, very close to the tank window. A fraction of the probe beam reflects on the sample and goes back to the polarizing beam splitter C_2, where it is recombined with the local oscillator beam. The phase acquired by the probe beam is compared to the local oscillator with the PBS C_3 and the two photodiodes P_1 & P_2, in a balanced detection scheme, where the half waveplate λ_4 is used for balancing the signals on the two photodiodes. This allows to measure the position of the mechanical oscillator with a precision of the order of the wavelength. The two quarter waveplate λ_2 & λ_3 are used to rotate the polarization by 90 degrees over a roundtrip, such that the local oscillator beam and the probe beam are properly recombined on one output port of the interferometer. Finally, to image the mechanical oscillator and to aim the probe beam at a specific spot of the membrane, the mirror M_2 is transparent to visible light, and a Thorlabs CMOS camera is placed behind. In order to provide illumination to the sample, a bright fibered halogen lamp S is used.

II.4.a.ii Output signal

We will now derive the signal resulting from this measurement. The action of a half waveplate oriented by an angle θ with respect to one of the polarization axis of the beam splitter is represented easily, using Jones calculus, by the matrix:

$$\mathbb{S}_\theta \stackrel{\text{def}}{=} -i \begin{pmatrix} \cos(2\theta) & \sin(2\theta) \\ \sin(2\theta) & -\cos(2\theta) \end{pmatrix}. \tag{II.4.1}$$

As a consequence, if the input beam has the Jones representation $\begin{pmatrix} 1 \\ 0 \end{pmatrix}$, after the first waveplate the state is now:

$$-i \begin{pmatrix} \cos(2\alpha_1) \\ \sin(2\alpha_1), \end{pmatrix} \tag{II.4.2}$$

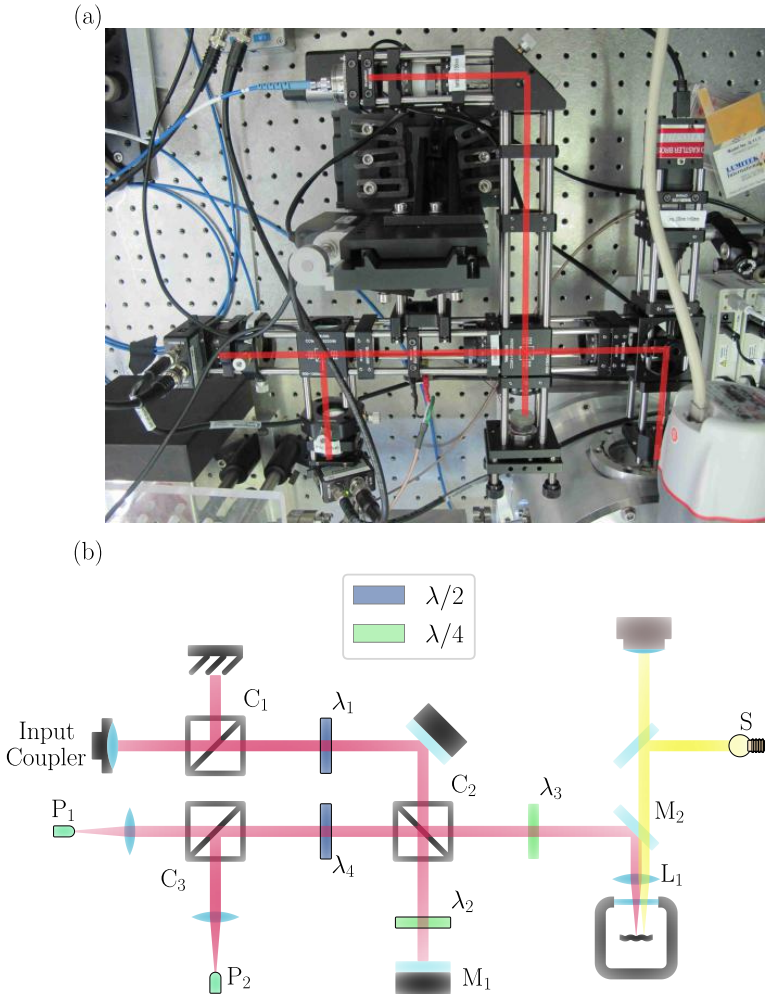

Figure II.5: (a) Interferometer picture. The light path is colored in red. (b) Schematics describing the optical elements

where α_1 is the angle formed by the axis of the waveplate with the reference axis. The state of the beam before the output half waveplate is:

$$-i\begin{pmatrix}\cos(2\alpha_1)e^{i\phi_0}\\ \sin(2\alpha_1)re^{i\phi(x)}\end{pmatrix}, \tag{II.4.3}$$

where r is the reflection of the membrane, ϕ_0 is the phase acquired in a round trip in the local oscillator arm, $\phi(x)$ is the phase acquired in a round trip in the sample arm, and x is the position of the mechanical oscillator. After the second half waveplate, whose angle is α_2, the state becomes:

$$-\begin{pmatrix}\cos(2\alpha_2)\cos(2\alpha_1)e^{i\phi_0}+\sin(2\alpha_2)\sin(2\alpha_1)re^{i\phi(x)}\\ \sin(2\alpha_2)\cos(2\alpha_1)e^{i\phi_0}-\cos(2\alpha_2)\sin(2\alpha_1)re^{i\phi(x)}\end{pmatrix}. \tag{II.4.4}$$

The last polarizing beam splitter and the two photodiodes allows to measure the modulus squared of the two components of this last vector independently. The two electric signals are then subtracted, leading to:

$$\mathcal{S}=\left[\cos(2\alpha_1)^2-r^2\sin(2\alpha_1)^2\right]\cos(4\alpha_2)+r\sin(4\alpha_1)\sin(4\alpha_2)\cos(\phi(x)-\phi_0) \tag{II.4.5}$$

To suppress the classical noise of the laser, the balanced detection should be tuned to 50 % of the power in each photodiode in average, *i.e* $\alpha_2=\pi/8$. The fine tuning is made by measuring the suppression of the relaxation peak of the laser. To this end, the noise eater of the laser is intentionally turned off and the height of the peak after subtraction is repeatedly measured while changing α_2 (see figure II.6 (b)).

Then, the maximum sensitivity is reached for the same angle in the first half waveplate, $\alpha_1=\pi/8$. Finally, the maximum sensitivity of the cosine curve is obtained for $\langle\phi(x)-\phi_0\rangle=\pi/4$. The optimization of the coupling is done by sending a large sinusoidal signal to the piezoelectric actuator of the local oscillator end mirror. The amplitude of the induced motion should be enough to cover several fringes. By looking at the optical signal induced by this motion, we can see what voltage at the output corresponds to $\langle\phi(x)-\phi_0\rangle=\pi/4$, as well as the precise transfer function of the interferometer. A feedback loop is then used to lock the interferometer on its peak sensitivity.

To measure the sensitivity of the interferometer, the noise eater is turned off. Therefore, the scaling of both the classical noise of the laser and the noise measured far away from this peak with the input optical power can be compared (see figure II.6 (a)). We observe a linear scaling of the noise with the input power in the region $1.5-1.6$ MHz, and a quadratic scaling of the noise with the input power in the region of the relaxation peak of the laser. This is a signature that the balanced detection is limited by the shot noise of the laser at this frequency.

II.4.b: Frequency measurement

The mode frequency is deduced from the spectrum of the balanced detection signal. At the mechanical frequency, a Lorentzian peak appears (see figure II.7). The spectrum is then compared with and without a beam block in front of the membrane to discriminate the peaks due to a mechanical mode to the ones due to electronical noise.

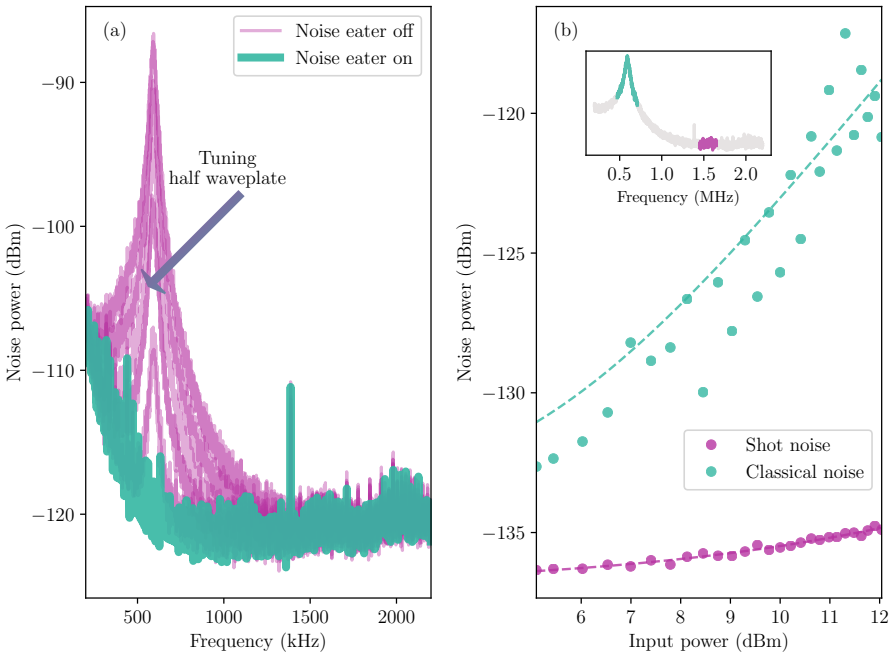

Figure II.6: (a) Measured spectrum of the output signal of the interferometer. The large peak corresponds to classical noise due to the relaxation oscillation of the laser. In blue: the detection is balanced and the noise eater is ON. In pink: the noise eater is OFF. The different curves are taken for different angles of the last half waveplate. Notice the reduction of the noise peak of the laser due to the balancing of the detection. (b) (Blue) Scaling of the noise of the relaxation peak of the laser with the input power together with a power law fit. The fitted exponent is ~ 2.18. (Pink) Same curves for the region between 1.5 and 1.6 MHz. The fitted exponent is ~ 0.97. Inset: representation of on typical spectrum measured with the interferometer at a given optical input frequency. The frequency range the dots are extracted from are colored accordingly.

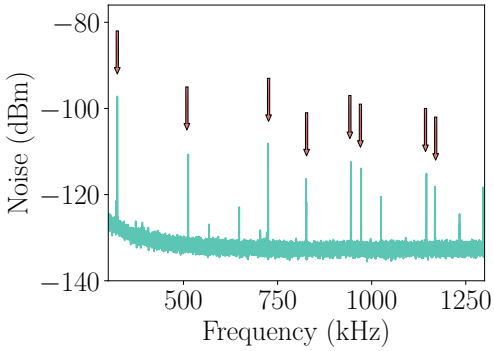

Figure II.7: Spectrum of the balanced detection signal when the interferometer is measuring a square membrane of width 1 mm, thickness 100 nm and internal stress ~ 1 GPa. The arrows indicate the measured modes.

II.4.c: Ringdown measurement of the quality factor

Although the quality factor can be inferred from the width of the Lorentzian peak, a better measurement is obtained by the so-called "ringdown" technique.

II.4.c.i Principle

A strong excitation drives the resonator towards an amplitude considerably larger than the Brownian motion amplitude. The excitation is then stopped and an amplitude demodulation of the signal measured by the interferometer is performed. The quadratures $X(t)$ and $Y(t)$ are obtained by using the following demodulation technique: the modulated signal $\mathcal{S}_{\rm in}(t)$ has a slowly varying envelope $\mathcal{A}(t)$ carrying the desired information. An internal source creates a signal $\mathcal{S}_0(t)$ at the carrier frequency, and mixes it with the modulated signal before filtering it with a lowpass filter whose cutoff frequency is small compared to the carrier frequency. This provides the quadrature $X(t)$. The other quadrature $Y(t)$ is obtained in parallel by applying a $\pi/2$ dephasing before the mixing (see figure II.8).

Then we compute the amplitude $\mathcal{A}(t) \stackrel{\rm def}{=} \sqrt{X(t)^2 + Y(t)^2}$, while the phase reads $\phi(t) \stackrel{\rm def}{=} \arctan(Y(t)/X(t))$.

Neglecting the thermal noise, the evolution of a mechanical oscillator of mechanical frequency $\Omega_{\rm m}/2\pi$ and of decay rate $\Gamma_{\rm m}/2\pi$ can be computed from the following Langevin equation (see section I.2.a):

$$\frac{d}{dt}\hat{b}(t) = (-i\Omega_{\rm m} - \Gamma_{\rm m}/2)\,\hat{b}(t) \tag{II.4.6}$$

$$\frac{d}{dt}\hat{b}^\dagger(t) = (i\Omega_{\rm m} - \Gamma_{\rm m}/2)\,\hat{b}^\dagger(t), \tag{II.4.7}$$

which reads:

$$x(t) = (x(0)\cos(\Omega_{\rm m}t) + y(0)\sin(\Omega_{\rm m}t))\,e^{-\Gamma_{\rm m}/2t}, \tag{II.4.8}$$

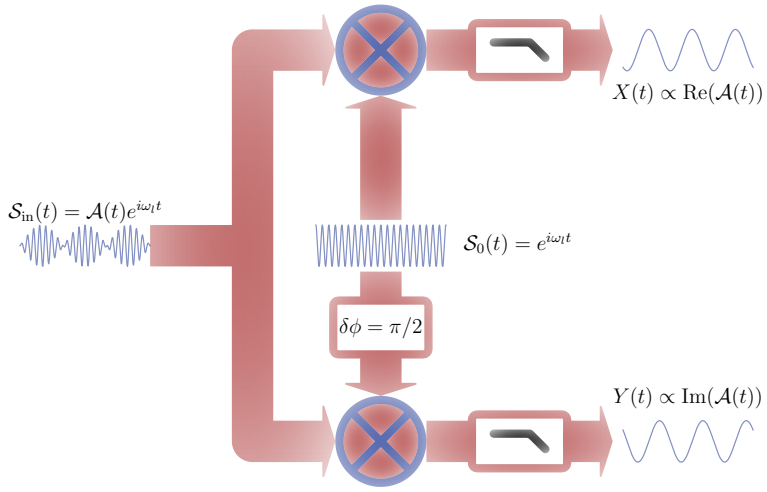

Figure II.8: Internal demodulation diagram of the signal analyzer, used for retrieving the two quadratures $X(t)$ and $Y(t)$ slowly varying around a carrier at frequency $\omega_l/2\pi$.(see section II.4.c.i for details).

where $x(t) \overset{\text{def}}{=} x_{\mathrm{ZPF}} \frac{\hat{b}(t)+\hat{b}^\dagger(t)}{\sqrt{2}}$ and $y(t) \overset{\text{def}}{=} x_{\mathrm{ZPF}} \frac{\hat{b}(t)-\hat{b}^\dagger(t)}{\sqrt{2}i}$ are the two quadratures of the mechanical oscillator position. After demodulation at a frequency $\Omega_0/2\pi$ close to the mechanical frequency, the resulting measured complex signal is proportional to:

$$X(t) + iY(t) = \frac{e^{-\Gamma_{\mathrm{m}} t/2}}{2} \left[x(0) + iy(0)\right] \left[\cos((\Omega_0 - \Omega_{\mathrm{m}})t) + i\sin(\Omega_0 - \Omega_{\mathrm{m}})t)\right], \quad \text{(II.4.9)}$$

which is a spiral, centered on zero, whose initial state is the initial state of the mechanical resonator. Retrieving its amplitude decay speed allows to measure the decay rate of the mechanical resonator. Moreover, the measurement of its dephasing rate is a measurement of the exact mechanical frequency (see figure II.9). The latter allows to fine tune the mechanical frequency between several measurements. Indeed, the mechanical frequency is dependent on the pressure and temperature, which can vary over time. The measurement of the decay rate allows to measure the quality factor of the resonator, which reads:

$$Q \overset{\text{def}}{=} \frac{\omega_{\mathrm{m}}}{\Gamma_{\mathrm{m}}}. \quad \text{(II.4.10)}$$

The measured mode was found to have quality factors in the range of the order of a million.

II.4.c.ii Radiation pressure excitation

The strong mechanical excitation can be performed by a piezoelectric actuator [TBPS17]. Alternatively, the optomechanical coupling can be used as a driving mechanism (see

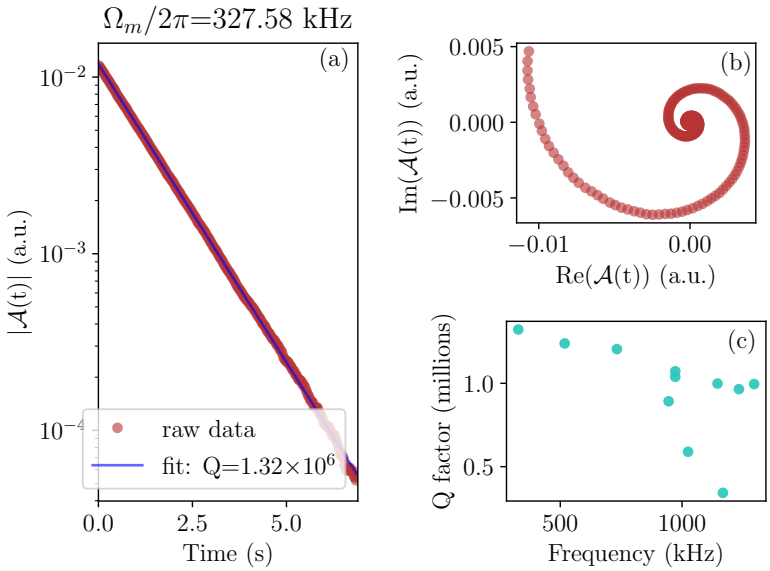

Figure II.9: (a) Modulus of the measured signal after a ringdown versus the time, for the fundamental mode of a square membrane with a thickness of 100nm. The measured quality factor is 1.3×10^6. (b) Smith chart of the data. (c) Measured Q factors of several modes of the same square membranes, versus their frequency.

section IV.1.b.ii). The scheme implemented here is based on a resonant radiation pressure modulation. Each photon reflected by the membrane experiences a change of momentum of:

$$\delta p = -2\frac{h}{\lambda}, \tag{II.4.11}$$

which leads to a force proportional to the light intensity I:

$$|\vec{F}| = R\left|\frac{d\vec{p}}{dt}\right| = R\frac{2I}{c}, \tag{II.4.12}$$

where c is the speed of light in vacuum and R is the reflectivity of the membrane. As a consequence, the modulation of the laser intensity induces a proportional mechanical excitation of the resonator. To perform the modulation, an Acousto-Optic Modulator (AOM) is used (see figure II.10). The latter consists in a crystal with a piezoelectric actuator and an acoustic absorber. Bragg reflection originates from sound waves traveling in the material perpendicularly to the light path. As the many diffracted orders have different output angles, a modulation of the intensity of the RF piezoelectric excitation leads to a modulation of the relative optical intensity between the zeroth order and the higher order diffracted modes.

The setup used for implementing this amplitude modulation is called a "double pass" setup [DHL+05]: the diffracted mode is reflected towards the AOM, while the zeroth order is blocked by a pinhole (see figure II.10. The diffracted beam is thus

scattered back in the input beam direction. Advantageously, this setup corrects the angle beam shift induced by the AOM such that it can be coupled efficiently to an optical fiber connected to the interferometer.

II.4.d: Mode shape measurement

To measure the mode shapes of the drum modes, the whole interferometer (see figure II.5 (a)) is placed on a 2 axis motorized translation stage, while the vacuum tank is fixed. The position of the laser beam on the membrane is controlled using the camera. Then, the interferometer is moved, and the height of the various thermal peaks in the noise spectrum, as well as the position of the laser beam, are measured again. By repeating those operations while scanning the beam position to cover the whole membrane, we reconstruct simultaneously the profile of the various mechanical modes. The result is in good agreement with finite element simulations (see figure II.11).

II.5: Conclusion

In this chapter, we have described the mechanical oscillators used in this work, along with some characterization tools. We were able to build high ($Q \sim 1 \times 10^6$) quality factor resonators at frequencies ranging from $\sim$ 300 kHz to $\sim$ 1 MHz. At room temperature, those resonators exhibit high ($n_\mathrm{B} \sim 12 \times 10^6$) mechanical occupation and are therefore behaving as classical oscillators. In the next chapters, we will describe the cryogenic setup used to reduce this occupation by a factor $\sim 10^3$, and from this point how we designed microwave resonator to reduce it further down by another similar factor.

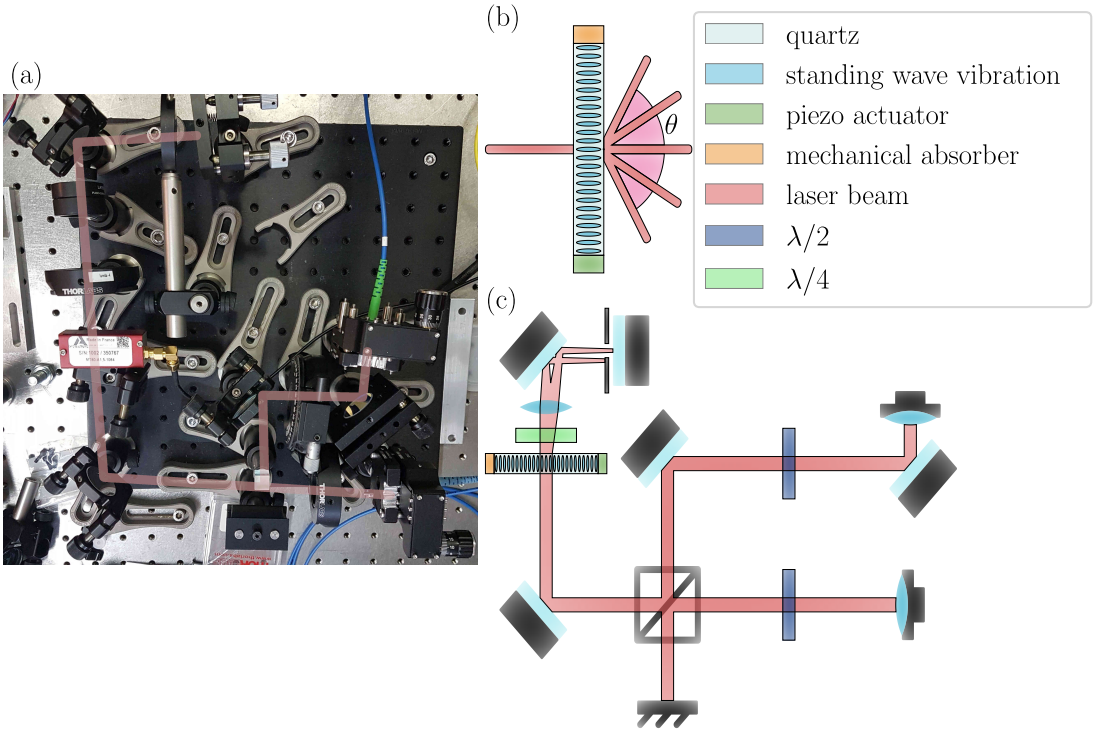

Figure II.10: (a) Picture of the optical setup. The light path is highlighted in light red. (b) Schematic of an Acousto-Optic Modulator. (c) Schematics of the amplitude modulation setup used to excite the mechanical resonator. For readability purpose, only the diffraction orders zero and one are represented

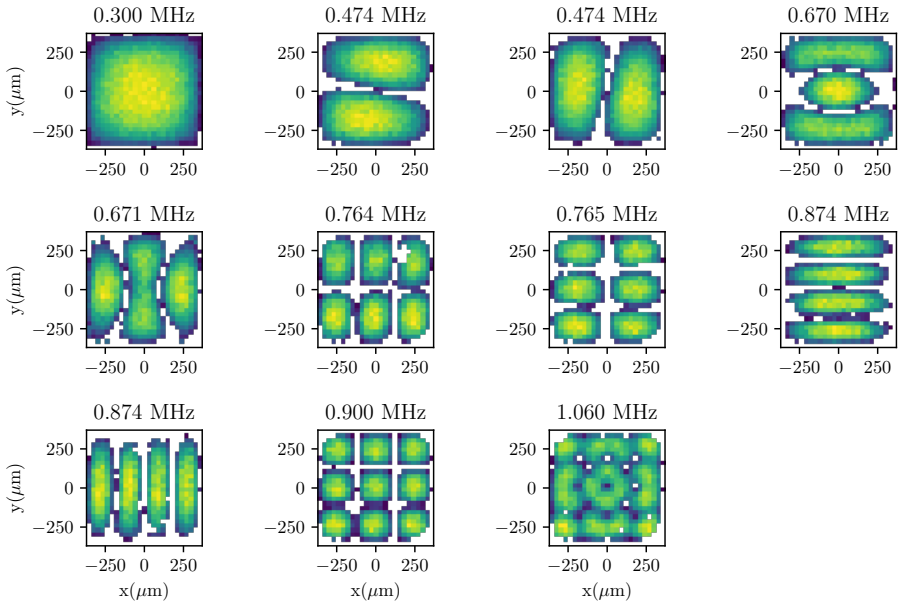

Figure II.11: Experimental measurement of the first mode shapes of a square membrane, together with the measured mechanical frequency.

Chapter III: Microwave electromechanics

To probe the quantum behavior of the mechanical resonators described in the previous section, it is required to couple them to a well controlled quantum system. Following the theoretical framework described in chapter I, the motion of those resonators were coupled to the microwave mode of a superconducting cavity. The design, fabrication and characterization of such superconducting resonators was an entirely new activity for the group in which I conducted this work. Therefore, I had to perform a careful step-by-step design of the microwave resonator, leading to an iterative optimization process of the sample designs, fabrication processes and low temperature characterizations.

Microwave cavities can perfectly be made as 3D cavities by machining a smooth parallelipedic shaped cavity inside a large piece of bulk superconductor, such as aluminum. [YSBS15, NYA$^+$16]. However, throughout this work we restrained ourselves to 2D lumped cavities, where the capacitive part of the circuit is spatially separated from its inductive part. Although those resonators are known to exhibit significantly lower microwave quality factors, their mode shapes usually show a much higher concentration of electric field in a small region around the capacitive part of the circuit. This feature allows to couple arbitrarily small mechanical resonators to the cavity with a good efficiency. In this work, we have investigated two kinds of 2D lumped cavities, differing by the nature of the capacitive element.

The first kind of resonator investigated consists of a Niobium meander inductor with an interdigitated capacitor. In this design, most of the electric field is located in the close vicinity of the interdigitated capacitor, with a strong electric field gradient that can in principle be exploited to couple the cavity to the motion of a nearby dielectric membrane [UWK09]. This coupling scheme doesn't require the metallization of the membrane, a process that we feared might jeopardize their exquisite mechanical properties. The thorough characterization of this design allowed the validation of most of the steps of the fabrication processes that are readily used for most 2D lumped cavities, such as the deposition of a high quality superconducting thin film, the lithography process, the cleaning recipes, etc. Also, this characterization validated the main features of the cryogenic setup, as well as the sample box design and the coupling scheme of the cavity to the waveguide.

Moreover, this characterization lead to the identification of a major loss mechanism in planar superconducting resonator which results from the coupling between the microwave mode and defects behaving as Two Level Systems (TLS) located mostly at material layer interfaces. In particular, we proposed and demonstrated an original pump-probe method to extract the maximum information about the microwave cavity non linear damping induced by the TLS bath [CFI+20] (This technique will be presented in details in chapter VI of this manuscript).

Unfortunately, the experimental demonstration of optomechanical coupling was not possible in this configuration. This was a consequence of several factors: the relative weakness of the purely dielectric coupling, the low microwave quality factor due to the presence of the TLS bath, and finally, as we realized at a later stage in this PhD, the membrane/resonator separation that exceeded the nominal one.

Consequently, we investigated a second class of resonators, where a metallic coating on the membrane plays the role of a moving electrode in a planar capacitor. In this geometry, the field doesn't penetrate in the silicon nitride membrane, thus mitigating the TLS induced losses. This change of design allowed the demonstration of optomechanical coupling. Surprisingly, we measured a remarkable improvement of mechanical properties at low temperature, leading for some of the devices tested to a record-high quality factors close to 300 millions (see chapter V). This clearly indicates that the metallization of silicon nitride membrane is fully compatible with extremely good mechanical properties.

In a first section, we will describe in details the aforementioned coupling schemes, with a particular emphasize on the strength of the electromechanical interaction expected in each scenario. In section III.2, we will present the low temperature setup that was developed specifically during this PhD for the characterization of these microwave-electromechanical devices. Finally, section III.3 will be dedicated to the delicate fabrication recipe employed to bring an ultrahigh-Q suspended membrane at a sub-micron distance from a superconducting circuit.

III.1: Various electromechanical coupling schemes

To couple the microwave cavity to the mechanical resonators presented in the previous chapter, we designed their capacitive part in such a way that their capacitance is changed with the mechanical resonator position. This problem has been addressed through various angles in the electromechanics community, including a parallel plate capacitance with a mechanically compliant electrode[TdL+11, TDCB+09], or a silicon nitride nanobeam in between two fixed electrodes of a capacitor [FKM+12]. Those two examples belong to two families of coupling mechanisms we investigated throughout this work: the electrostatic coupling and the gradient coupling.

III.1.a: Electrostatic and gradient force coupling

The two approaches that were initially envisionned to couple the membrane to a superconducting resonator are sketched in Fig III.1. In the first one, coined "gradient force coupling", the membrane oscillates in an electric field gradient generated by nearby

electrodes. In close analogy with a particle inside an optical tweezer, the force experienced by the membrane is due to the induced dipoles within the dielectric material, and it is proportionnal to the gradient of the squared modulus of the electric field [UWK09]:

$$\vec{F} = \epsilon \vec{E} \vec{\nabla} E, \tag{III.1.1}$$

where ϵ is the permittivity of the dielectric. To generate a strong electric field gradient along the direction of oscillation of the membrane, we employed a pair of interdigitated electrodes with a tooth spacing that is comparable to the membrane separation. Conversely, by moving in the close vicinity of the electrodes, the membrane modulates the capacitance between the interdigitated electrodes. To quantitatively assess the coupling expected in this scenario, we will derive approximate analytical expressions of the electric field generated by the interdigitated capacitor in the next section.

In the second approach (see Fig III.1 (b)), the membrane itself is coated with a metallic electrode, playing the role of a moving electrode in a plane - plane capacitor configuration. In this scenario, the charges accumulated on the metallic electrodes give rise to an electrostatic force attracting the membrane towards the circuit.

Irrespective of the details of the coupling mechanism, the electromechanical interaction is fully captured by the dependence $C(h)$ of the electrode capacitance with respect to the membrane displacement h. Indeed, the force can be derived by considering a fictitious experiment where the charges ± q on the electrodes remain constant such that no electrical energy is exchanged with an external circuit. In such a scenario, an energy conservation argument can be used to derive the force from the stored electrostatic energy U:

$$\vec{F} = -\vec{\nabla}(U) = -\frac{q^2}{2}\vec{\nabla}(1/C) = \frac{V^2}{2}\frac{dC}{dh}, \tag{III.1.2}$$

where V is the voltage across the electrodes. Unsurprisingly, we find a force proportional to the square of the voltage, or equivalently, to the energy stored in the capacitor. This quadratic force is the counterpart of radiation pressure in optomechanical systems operating in the optical domain. In microwave electromechanical experiments such as the ones pursued in this thesis, the capacitor is shunted by an inductor to form a LC resonator such that the microwave resonance frequency $\omega_c = 1/\sqrt{LC}$ also depends on h via:

$$\frac{d\omega_c}{dh} = \frac{-\omega_c}{2}\frac{1}{C}\frac{dC}{dh}. \tag{III.1.3}$$

In conjunction with the size of the zero-point fluctuations x_{zpf}, this parameter, denoted G in chapter 1 (see Eq. (I.3.9)), sets a definite value for the vacuum electromechanical coupling rate g_0 appearing in the Hamiltonian (I.3.10). This Hamiltonian description is a compact way of describing at the same time the effect of the mechanical oscillator on the electromagnetic degree of freedom (a position-dependent resonance frequency shift), and the effect of the field on the mechanical resonator (a force proportional to the energy stored in the electromagnetic cavity). In the next section, we will try to give quantitative estimates for the value of G achievable in each coupling scenario with our membrane geometry.

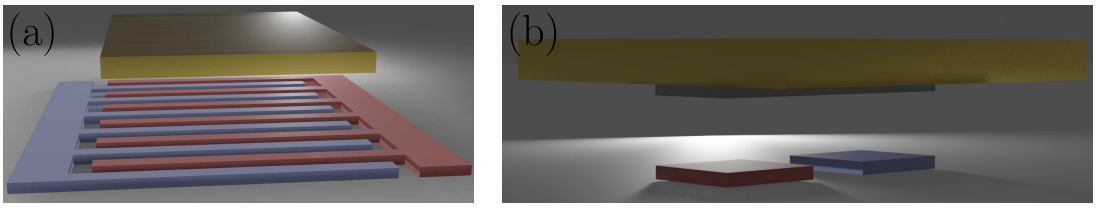

Figure III.1: (a) interdigitated capacitor and dielectric coupling. (b) metallic pads with a metallized membrane. The two electrodes are represented in red and blue, and the silicon nitride in yellow.

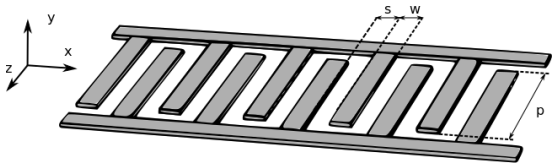

Figure III.2: Parametrization of the interdigitated capacitor for the analytical computation of the electric field.

III.1.b: Analytic estimates of the position-dependent capacitance

In practice, several geometric parameters influence the electromechanical coupling rate achieveable with each of the coupling schemes described above. To get a precise estimate of the parameter G, the most direct approach is to perform numerical simulations in which the membrane distance is systematically varied, and to infer the slope $\frac{d\omega_c}{dh}$ from these discrete set of points. However, this approach can be computationally intensive, and furthermore, it doesn't provide much intuition about the scaling of G with the various parameters. In this section, we will show that, under some reasonable approximations, an analytical expression of G can be obtained. The validity of this analytical expressions is finally checked by comparing the predicted frequencies $\omega_c(h)$ with the ones obtained from numerical simulations.

III.1.b.i Interdigitated capacitors

The first samples designed for this work were based on the gradient coupling scheme. Fingers of length p and width w belonging to one electrode are separated from the other electrode by a spacing s, this structure forming a periodic potential of half period $a = w + s$ in the x direction (see figure III.2). Under the assumptions of a large number of fingers, and a finger length p very large compared to the period $2a$, we can assume that the electrostatic potential is purely periodic in the x direction, and invariant in the z direction. Under these assumptions, it can be written as a Fourier series, leading to the following decomposition [DO02]:

$$V(x,y) = \sum_{n=1}^{\infty} \beta_n \sin(\alpha_n x) \exp(-\alpha_n |y|), \tag{III.1.4}$$

where:

$$\alpha_n = \frac{(2n-1)\pi}{a}. \tag{III.1.5}$$

The dependence along y has been chosen such that the potential fulfills the Laplace equations in the charge-free regions $y < 0$ and $y > 0$:

$$\Delta V = 0. \tag{III.1.6}$$

Moreover, the Fourier coefficients β_n are constrained by the boundary conditions imposed by the electrodes in the $y = 0$ plane:

$$\text{for } s < x < s + w, \qquad V(x) = +V_0/2 \tag{III.1.7}$$

$$\text{for } 0 < x < s, \qquad \sigma(x) = 0. \tag{III.1.8}$$

The first condition reflects the fact that the potential is uniform, with a value $\pm V_0/2$ in the region of the plane covered by the electrodes. The second equation imposes a vanishing charge density $\sigma(x)$ outside the electrode region. From the expression III.1.4 of the potential, we can derive the electric field:

$$\vec{E}(x,y) = -\vec{\nabla}V = \sum_{n=1}^{\infty} \alpha_n \beta_n \exp(-\alpha_n |y|) \begin{pmatrix} -\cos(\alpha_n x) \\ \sin(\alpha_n x)\mathrm{sgn}(y) \end{pmatrix}, \tag{III.1.9}$$

where $\mathrm{sgn}(y)$ is the sign of y. The discontinuity at $y = 0$ is due to a surface charge density $\sigma(x)$ which reads:

$$\sigma(x) = \epsilon_0 \frac{\partial V}{\partial y}(x, y = 0^+) + \epsilon_0 \epsilon_{\mathrm{r,Si}} \frac{\partial V}{\partial y}(x, y = 0^-) = \epsilon_0 \left(1 + \epsilon_{\mathrm{r,Si}}\right) \sum_{n=1}^{\infty} \alpha_n \beta_n \sin(\alpha_n x), \tag{III.1.10}$$

where ϵ_0 is the vacuum permittivity and $\epsilon_{\mathrm{r,Si}}$ is the relative permittivity of the substrate. Finding the right set of β_n such that Eq. III.1.4 and Eq. III.1.10 fulfill the boundary conditions III.1.7 and III.1.8 is a difficult mathematical problem, which, to our knowledge, doesn't have an analytical solution. However, Den Otter [DO02] proposed an approximate solution by equating the potential between the electrodes to the one created by two semi-infinite coplanar electrodes:

$$\beta_n = \frac{2V_0}{\alpha_n a} J_0 \left(\frac{(2n-1)\pi s}{2a} \right), \tag{III.1.11}$$

where J_0 is the zero order Bessel function of the first kind.

Figure III.3 shows the excellent agreement between this ansatz and the boundary conditions for both the potential (Fig III.3(a)) and the charge density in the $y = 0$ plane (Fig. III.3(b)). In principle, the capacitance can be obtained from this Ansatz by calculating the charge-to-voltage ratio:

$$C_{\mathrm{surface}} = \frac{1}{2V_0 pa} \left| \int_{s/2}^{s/2+w} \sigma(x) p dx \right| = \frac{\epsilon_0 (1 + \epsilon_{\mathrm{r,Si}})}{V_0 a} \sum_{n=1}^{\infty} (-1)^n \beta_n \sin\left(\frac{(2n-1)\pi w}{2a} \right), \tag{III.1.12}$$

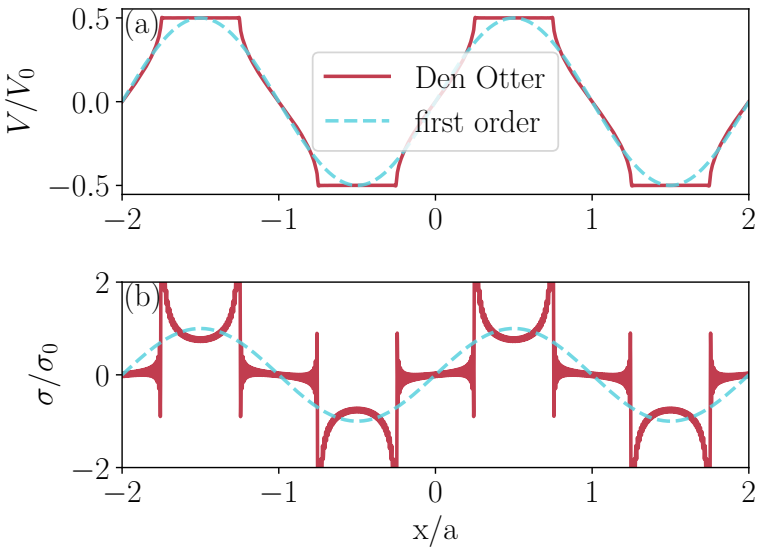

Figure III.3: Boundary conditions for various approximations of the interdigitated capacitor field: The potential (a) and the charge distribution (b) are plotted in the $y = 0$ plane for Den Otter's solution (Eq. III.1.4 with coefficients given by eq. III.1.11) and for the 1st order approximation (Eq. III.1.14) in red and blue respectively. The surface charge density is normalized by the maximum value $\sigma_0 \stackrel{\text{def}}{=} \frac{V_0\pi}{2a}\epsilon_0(1+\epsilon_{\text{r,Si}})$. Den Otter's solution has been calculated for $s/a = 1/2$, and 100 terms have been included in the summation.

Applying this formula for s/a = 1/2, which is close to the actual electrode geometry used in our experiments, one finds a capacitance per unit area $C_{\text{surface}} \approx 0.98\epsilon_0(1+\epsilon_r)/2a$. This value is also in very good agreement with numerical simulations conducted on a finite interdigitated electrode and presented in the next section.

Before attempting to derive the effect of a dielectric membrane on the interdigitated capacitance, we notice that this analytical model expresses the electric field generated by the interdigitated capacitor as a sum of evanescent components decreasing exponentially along y. In particular the square magnitude of the field only depends on the distance to the electrode plane y:

$$\vec{E}^2 = \sum_{n=1}^{\infty} \alpha_n^2 V_n^2 e^{-2\alpha_n |y|}. \tag{III.1.13}$$

The typical decay length α_n^{-1} is maximal for the first Fourier component $n = 1$, for which it takes the value $\alpha^{-1} = a/\pi$. Moreover, one can show that most of the electrostatic energy is contained in this first component: for instance, with $s/a = 1/2$, the energy in the first order mode accounts for approximately 93% of the total electrostatic energy. Since the electromechanical coupling results from the gradient of the field at the membrane location, which is situated in the "far-field", at a distance $h \gtrsim a$ from the electrodes, we will consider, for the sake of simplicity, a solution comprising only the 1st order evanescent component:

$$V_{\text{first order}}(x,y) = \frac{V_0}{2} \sin(\pi/ax) \exp(-\pi/a|y|) \tag{III.1.14}$$

In this approximation, one can show that the potential and the charge distribution in the $y = 0$ plane have a simple sinusoidal dependence:

$$V_{\text{first order}}(x,y=0) = \frac{V_0}{2} \sin(\pi/ax) \tag{III.1.15}$$

$$\sigma_{\text{first order}}(x) = \frac{\pi V_0 \epsilon_0}{2a} (1+\epsilon_{\text{r,Si}}) \sin(\pi/ax) \tag{III.1.16}$$

These expressions are only crude approximations of the real potential and charge distributions. In particular, we note that the boundary conditions Eq III.1.7 and III.1.8 are not fulfilled (see Fig. III.3(a) and III.3(b), dashed lines). However, one can interpret these quantities as the main Fourier component of the charge distribution in the electrode plane. We can thus extract a good approximation of the capacitance from this truncated expressions by integrating the charge density over the interval $[0, a]$:

$$C_{\text{surface,first order}} = \frac{1}{2V_0 a} \left| \int_0^a \sigma_{\text{first order}}(x) dx \right| = \frac{\epsilon_0(1+\epsilon_{\text{r,Si}})}{2a} \tag{III.1.17}$$

In spite of the rough approximations of the model, formula III.1.17 only deviates from the value derived in Eq III.1.12 by $\approx 2\%$.

Now that we have derived a simplified analytic expression for the electric field generated by the interdigitated capacitor, we will study the influence of the dielectric membrane on the electrode's capacitance. For this we will first show that the evanescent wave generated by the electrodes undergoes reflection and transmission when it encounters a dielectric interface, in close analogy with Fresnel laws for propagating waves.

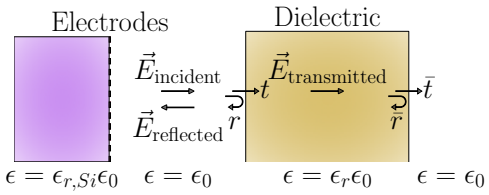

Figure III.4: reflection of the electric field of an interdigitated capacitor on a dielectric layer.

Reflection of an evanescent field on a dielectric interface A dielectric medium in presence of an external electric field exhibits a polarization $\vec{P}$ proportional to this field. This effect can be elegantly taken into account by introducing the displacement field vector $\vec{D}$:

$$\vec{D} = \epsilon_0\vec{E} + \vec{P} = \epsilon_r\vec{P}. \tag{III.1.18}$$

In an homogeneous dielectric medium, $\vec{D}$ fulfills the standard Maxwell's equations:

$$\vec{\nabla}\cdot\vec{D} = 0 \tag{III.1.19}$$

$$\vec{\nabla}\wedge\vec{D} = \vec{0}. \tag{III.1.20}$$

A field $\vec{D}$ that derives from a potential V automatically fulfills the rotational equation (Eq. III.1.20), and the divergence equation becomes the standard Laplace equation III.1.6. Moreover, at the interface between vacuum and a dielectric medium, the presence of surface charges imposes the following continuity relations:

$$\vec{D}_1\cdot\vec{n} = \vec{D}_2\cdot\vec{n} \tag{III.1.21}$$

$$\vec{E}_{t,1} = \vec{E}_{t,2}, \tag{III.1.22}$$

where $\vec{E}_t$ is the tangential component of the electric field, subscripts 1 and 2 are referring to the two regions the interface is delimiting, and $\vec{n}$ is a vector normal to the interface plane.

In other words, the field $\vec{E}_{\text{capacitor}}$ created by the electrodes gives rise to surface charges at the membrane surface, which in turn generates a new field $\vec{E}_{\text{dielectric}}$ fulfilling Maxwell's equation in the presence of charges. This field also fulfills the Laplace relation in both the dielectric and vacuum region. We can thus extend the well known description of reflection/refraction phenomena to the case of evanescent waves relevant here by looking for a solution of the form:

$$V_{\text{dielectric}}(y < h) = rV_{\text{capacitor}}(2h - y) \tag{III.1.23}$$

$$V_{\text{dielectric}}(y > h) = tV_{\text{capacitor}}(y). \tag{III.1.24}$$

The field is thus described as a superposition of three evanescent components. The incident field, decreasing exponentially with the electrode distance, is either reflected or transmitted at the vacuum/dielectric interface. The transmitted field keeps decreasing inside the dielectric material towards $y > 0$ while the reflected field decreases towards $y < 0$. Using the boundary conditions III.1.21 and III.1.22, we can show that the analogous of reflection and transmission coefficients r and t are given by:

$$r = \frac{1 - \epsilon_r}{1 + \epsilon_r} \tag{III.1.25}$$

$$t = \frac{2}{1 + \epsilon_r}. \tag{III.1.26}$$

In the same way, we can describe the reciprocal reflection/transmission coefficient from the inside of the membrane to vacuum

$$\bar{r} = \frac{\epsilon_r - 1}{1 + \epsilon_r} \tag{III.1.27}$$

$$\bar{t} = \frac{2\epsilon_r}{1 + \epsilon_r}. \tag{III.1.28}$$

Electrode capacitance in the presence of the dielectric membrane Thanks to the analogy with Fresnel reflection and transmission phenomena developed above, we are now equipped to study the effect of the membrane on the potential generated by the electrodes. The effective reflection coefficient of the membrane can be calculated by summing the fields reflected at the two ends of the membranes, in close analogy with a Fabry Perot cavity:

$$r_{\text{membrane}}(\tau) = r + t\bar{t}\bar{r} \sum_{n \in \mathbb{N}} \left(\bar{r}^2 \exp(-2\tau\pi/a) \right)^n \tag{III.1.29}$$

$$= r + t\bar{t}\bar{r} \frac{\exp(-2\tau\pi/a)}{1 + \bar{r}^2 \exp(-2\tau\pi/a))}, \tag{III.1.30}$$

with τ, the membrane thickness. Finally, the potential in the electrode plane can be derived by taking into account the successive reflections between the silicon substrate and the membrane:

$$V(x, y = 0) = \frac{V_0}{2} \sin(\pi/ax) \frac{1 + r_{\text{membrane}}(\tau) \exp(-2\pi h/a)}{1 - r_{\text{Si}} r_{\text{membrane}}(\tau) \exp(-2\pi h/a)}. \tag{III.1.31}$$

In this expression, $r_{\text{Si}} \overset{\text{def}}{=} \frac{1-\epsilon_{r,\text{Si}}}{1+\epsilon_{r,\text{Si}}}$ is the effective reflection coefficient between the silicon substrate and vacuum, and h is the distance between the membrane and the electrode plane. Eq. III.1.31 shows that the potential in the $y = 0$ plane is partially screened by the reflection of the evanescent wave emitted by the electrodes. In close analogy with the estimate derived earlier (see Eq. III.1.17), we can obtain the modified capacitance in the presence of the membrane by calculating the ratio between the

electrode charges (unmodified by the presence of the membrane), and the amplitude of oscillation of the potential in the electrode plane:

$$C_{\text{membrane}} \approx C_{\text{surface,first order}} \frac{1 - r_{\text{Si}} r_{\text{membrane}}(\tau) \exp(-2\pi h/a)}{1 + r_{\text{membrane}}(\tau) \exp(-2\pi h/a)}, \tag{III.1.32}$$

To verify the validity of this approximation, we have simulated an interdigitated capacitor in the presence of a thin dielectric membrane located at various heights h with the software Sonnet: a numerical electromagnetic solver using the method of moments to efficiently solve quasi-2 dimensional problems [Rau03]. The dependence C(h) predicted by Formula III.1.32 is compared to the result of the simulations in Fig. III.5 (a). Except for an $\approx 0.95\%$ global scaling, the simulations and the parameter-free analytical model show a remarkable agreement over the whole range of membrane heights (For the geometric parameter $2a = 1\ \mu m$ chosen in the simulation, the variation of the capacitance is mostly concentrated in the $1\,\text{nm} - 1\,\mu\text{m}$ region).

III.1.b.ii Electrostatic coupling

The sample design used for electrostatic coupling is depicted schematically in Fig. III.1 (b): the electrodes consists in two coplanar square pads which are separated by a given distance ξ, and are placed below the membrane. The rectangular region of the membrane directly facing the electrodes is metallized. To our knowledge, there is no exact analytical solution for this electrostatic problem. However, we propose a phenomenological description of the system by examining two limiting cases: when the membrane/electrode distance h is large compared to the electrode width, the capacitance has a fixed non zero value C_0 corresponding to the mutual capacitance of the two coplanar electrodes, but when $h \ll \xi$, the mutual capacitance between each electrode and the common metallic pad dominates, such that the circuit can be seen as two plane-plane capacitors in series, each with an area $\mathcal{A}$. We thus model the total capacitance between the coplanar electrodes by

$$C = \frac{\epsilon_0 \mathcal{A}}{2h} + C_0 \tag{III.1.33}$$

Although approximate [GBC+16, MBK14, UWK09] or exact [GGG+96] expressions are available in the literature for the capacitance of two coplanar microstrips, which is a similar geometry than two coplanar pads, they are not easily mappable to the case of squared electrodes. Consequently, we will consider C_0 as an adjustable parameter of the model, that we extract from finite element modeling. Fig. III.5 (b) represents the capacitance C(h) obtained with the Sonnet software for such a geometry, together with a model using formula III.1.33. C_0 is set to be equal to the simulated capacitance with the highest membrane height available. We observe an excellent agreement between the data and the fit justifying our model.

III.1.c: Microwave electromechanical resonators

So far, we have studied two possible implementations of a mechanically compliant capacitor. To probe and control the membrane motion in the quantum regime, our approach consists in coupling the mechanical degree of freedom to a microwave resonator

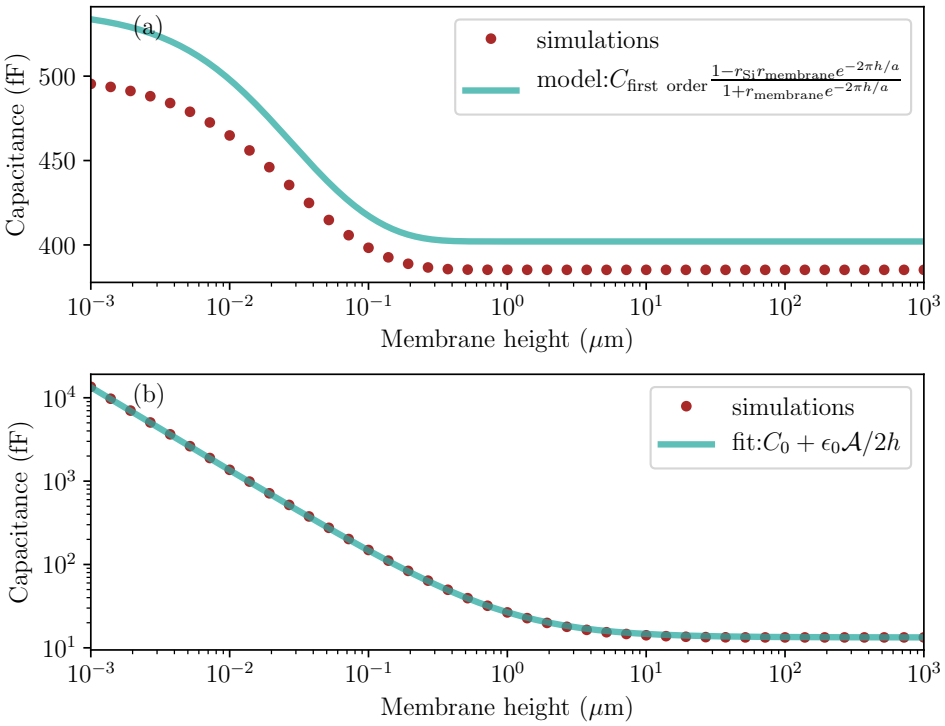

Figure III.5: Comparison between numerical simulations and approximate analytical formulas: (a) (dots) DC simulations using the software Sonnet of an interdigitated capacitance with a teeth period $2a = 1$ μm, teeth length $p = 80$ μm, and 44 teeth per electrode (see sketch in (c)). The membrane thickness is 100 nm. (line) Model using formula III.1.32. There are no free parameters. (b) (dots) simulations of a mechanically compliant capacitor with two squared electrodes of width 55 μm separated by a distance of 20 μm (see sketch in (d)). (line) Model using the formula III.1.33. The only free parameter is the parasitic capacitance C_0, which is set to be equal to the capacitance at the largest membrane height.

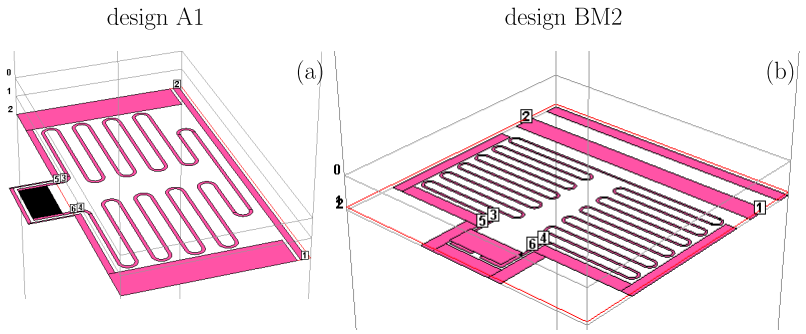

Figure III.6: (a) Simulated A1 design: a meander inductor with an interdigitated capacitor. (b) Simulated BM2 design: a meander inductor with a plane-plane capacitor.

by shunting this circuit element with an inductor. In the lumped-element approximation, where each component behaves as either a purely inductive or a purely capacitive element, the position-dependent resonance frequency is given by

$$\omega_{\mathrm{c,lump}}(h) = \frac{1}{\sqrt{LC(h)}}. \tag{III.1.34}$$

Several experimental considerations constrain the microwave resonance frequency. On the one hand, it should be large enough to fulfill $\hbar\omega_c > k_{\mathrm{B}}T$. This ensures that the microwave environment is free from thermal noise. For a cryostat at 300 mK, this corresponds to $\omega_c/2\pi > 5$ GHz. On the other hand, the price and availability of microwave components increases severely with frequency. In practice, the microwave measurement setup, described in more details in the next section, is limited to the 5-10 GHz band. Our initial estimate, was that the membrane distance from the electrodes would lie in the 50 - 500 nm range. With this assumption, the value of the capacitance in both the interdigitated and plane-plane capacitor geometries would be a few hundreds fF. Reaching 5 GHz $< \omega_c/2\pi <$ 10 GHz thus requires inductors of approximately 1 nH. In the initial design, this was realized with relatively small footprint by folding several times a long niobium strip to form a meander (see Fig. III.6). The resonator A1, represented in Fig. III.6(a), is an example of design for gradient force coupling experiment: it comprises an interdigitated capacitor shunted by an 700-μm meander inductor. The resonator BM2, represented in Fig. III.6(b), is an example of design for electrostatic coupling. The inductor is ~ 2 times longer to account for the smaller capacitance of the coplanar pads.

The resonance frequency predicted by Eq. III.1.34 is only valid in the lumped-element approximation, where each component behaves at all frequencies as a purely inductive or capacitive element. In fact, extrapolating at high frequency the impedance of the individual circuit elements based on their DC-capacitance or inductance can lead to significantly wrong resonance frequencies. To verify the validity of the lumped-element approximation, we have performed numerical simulations of the inductor and capacitor separately. Each component is modeled in Sonnet as a multi-port linear network, where port 1 and port 2 are the two electrodes of the component (see Fig. III.8 (d) and (e)). The linear network is fully characterized by its impedance matrix $Z_{ij}(\omega)$ which provides the link between the voltage and currents across the various

ports in the network:

$$U_i = \sum_j Z_{ij} I_j. \tag{III.1.35}$$

In this formula, U_i is the voltage across port i of the network, and I_j is the current flowing into port j. By symmetry of the problem, we are looking for solutions where the current and voltages are opposite in port 1 and port 2:

$$I_1 = -I_2 \stackrel{\text{def}}{=} I \tag{III.1.36}$$

$$U_1 = -U_2 \stackrel{\text{def}}{=} U/2, \tag{III.1.37}$$

such that the impedance of the component is defined by $Z_{\text{eq}} \stackrel{\text{def}}{=} U/I = Z_{11} + Z_{22} - Z_{12} - Z_{21}$. By performing Sonnet simulations of the "capacitor" and "inductor" circuit at various frequencies, we can extract the frequency dependent impedance matrix of each circuit element, and hence their characteristic impedance $Z_{\text{eq}}(\omega)$.

The results for circuit BM2 and A1 are presented in Fig. III.8 and III.7 respectively. The simulations have been performed with a very large electrode-membrane distance of 1 mm. If each component would behave as a pure capacitor (respectively a pure inductor), its impedance would be given by $Z_{\text{eq}} = \frac{1}{jC\omega}$ (respecitvely $Z_{\text{eq}} = jL\omega$). As visible on Fig. III.8 (b) and III.7 (b), this is correct in a very good approximation for the 2 capacitive elements studied in the previous section. On the other hand, the impedance of the meander inductances departs significantly from this ideal dependence. In particular, we observe a "self-resonance", around $\omega_l/2\pi \sim 24$ GHz for the short meander used in resonator A1 and $\omega_l/2\pi = 14$ GHz for the longer meander used with resonator BM2. This effect mainly results from the parasitic capacitance between successive meanders, that can be modeled as an extra capacitance $C_{0\text{L}}$ in parallel with the inductor. The impedance of the equivalent circuit (see Fig. III.8(d) and III.7(d)) is

$$Z_{\text{meander}} = \frac{jL\omega}{1 + (\omega/\omega_l)^2} \tag{III.1.38}$$

with:

$$\omega_l = 1/\sqrt{LC_{0\text{L}}}. \tag{III.1.39}$$

In practice, the "DC-values" C and L are extracted from the first point at frequency 0.1 GHz, and the parasitic capacitance $C_{0\text{L}}$ is extracted by inverting formula III.1.39. The impedance of the equivalent circuit (Eq. III.1.38), plotted as a full line in Fig. III.8 (b) and III.7 (b), is in excellent agreement with the simulated values. For comparison, the impedance $jL\omega$ of a pure inductor has been plotted in dashed line. Even in the 5 - 10 GHz interval, this DC-extrapolated impedance is significantly different from the simulated values, in particular for the longer meander of sample BM2.

The resonance frequency ω_c of the full circuit, composed of the meander and capacitor in series, reads:

$$Z_{\text{meander}}(\omega_c) + Z_{\text{capacitor}}(\omega_c) = 0. \tag{III.1.40}$$

To make the graphical resolution of this equation conspicuous, the values of $|Z_{\text{meander}}(\omega)|$ and $|Z_{\text{capacitor}}(\omega)|$ in Fig. III.7(b) and III.8(b) have been superimposed in the same

graph, with a blue color indicating a negative purely imaginary impedance, and a red color indicating a positive purely imaginary impedance. The x-value at the intersection between the red and the blue branches indicates the predicted resonance frequency. For consistency, we have also performed a simulation of the full circuit, and checked that the microwave resonance, witnessed by a sudden phase change in the waveguide transmission, is precisely superimposed with the predicted resonance condition (see Fig. III.7(c) and III.8(c)).

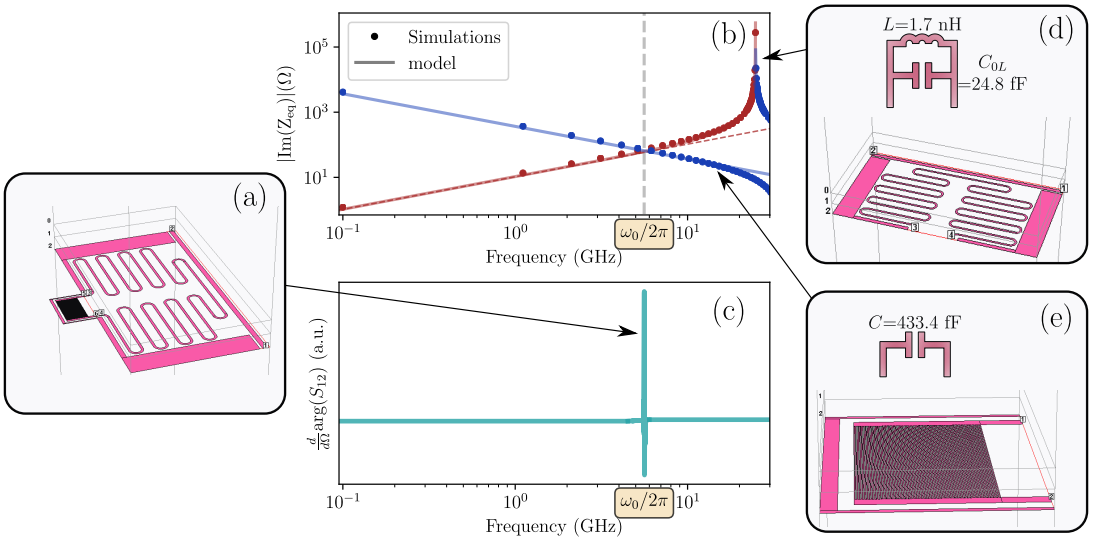

Figure III.7: RF modelization of the A1 design: the individual circuit elements represented in (d) and (e) are simulated independently with Sonnet. The simulated impedance $|Im(Z_{\mathrm{eq}})|$ of the meander and capacitor are overlayed in (b), where red dots indicate a positive imaginary part, and blue dots indicate a negative imaginary part. Each element is modeled by an equivalent lumped-element circuit: a pure capacitor C for the capacitive part of the circuit (see inset of (e)), and an inductor L in parallel with a capacitor $C_{0\mathrm{L}}$ for the meander circuit (inset of (d)). The corresponding impedances are represented as full lines in (b). The resonance condition $Z_{\mathrm{eq,meander}} + Z_{\mathrm{eq,inductor}} = 0$ is indicated by a vertical dashed line. The consistency between the simulation of individual circuit elements and the simulation of the full circuit is checked by simulating the waveguide transmission S_{12} for the full resonator represented in (a). The spike in the derivative of S_{12} plotted in (c), indicates the resonance condition for the full resonator simulation.

Finally, we plot on Fig. III.9(e) the electromechanical coupling rate $G = d\omega_c/dh$ obtained by deriving the analytical fomula III.1.34. Based on this quantitative analysis, we discuss in the following the specificities of the different coupling schemes, and the reasons why we think we couldn't observe the signatures of electromechanical coupling with gradient force coupling schemes such as that pursued with sample A1.

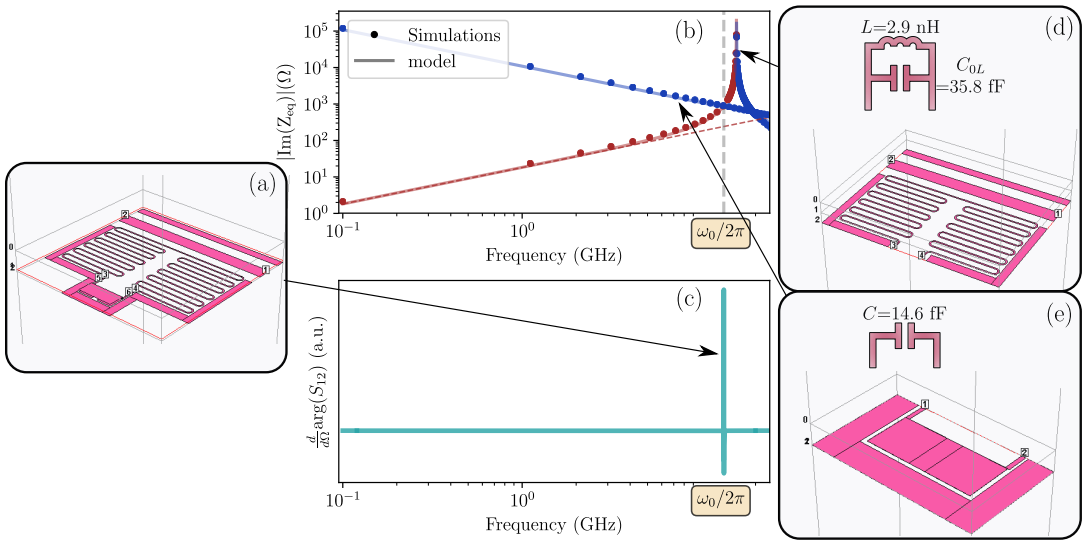

Figure III.8: Same analysis as figure III.7 but for the BM2 design

III.1.d: Discussion

A crucial difference between the gradient coupling and electrostatic coupling schemes described in the previous sections resides in the shape of the height-dependent capacitance $C(h)$: on the one hand, in the electrostatic coupling scheme, $C(h)$ varies with an hyperbolic dependence over a large range of distances h. On the other hand, in the gradient force coupling scheme, $C(h)$ has a short-range exponential dependence due to the nature of the evanescent modes generated by the interdigitated capacitors. In practice, for a given value of h, the typical decay length of the evanescent field should be matched by choosing a value of the interdigitated teeth period $2a \approx 2\pi h$.

Furthermore, the efficiency of the evanescent coupling scheme decreases strongly when the membrane thickness is small compared to the typical decay length of the evanescent field (as visible in Eq. III.1.29). In the particular example of A1 studied above, the maximal value of the electromechanical coupling scheme is a factor ~ 16 below the value obtained at the same distance with a metallized membrane (see Fig. III.9(e)).

Unfortunately, we have realized during the course of this thesis that the membrane/electrode distance was difficult to control experimentally. For instance, we have observed that, without extra precautions, the membrane could easily end up at a distance exceeding 1 micron from the electrodes, in a region where the interdigitated electrode is insensitive to the membrane motion. This experimental difficulty strongly plays against the dielectric gradient scheme, and it is only when we have switched to the electrostatic coupling scheme that we have been able to observe signatures of the electromechanical coupling.

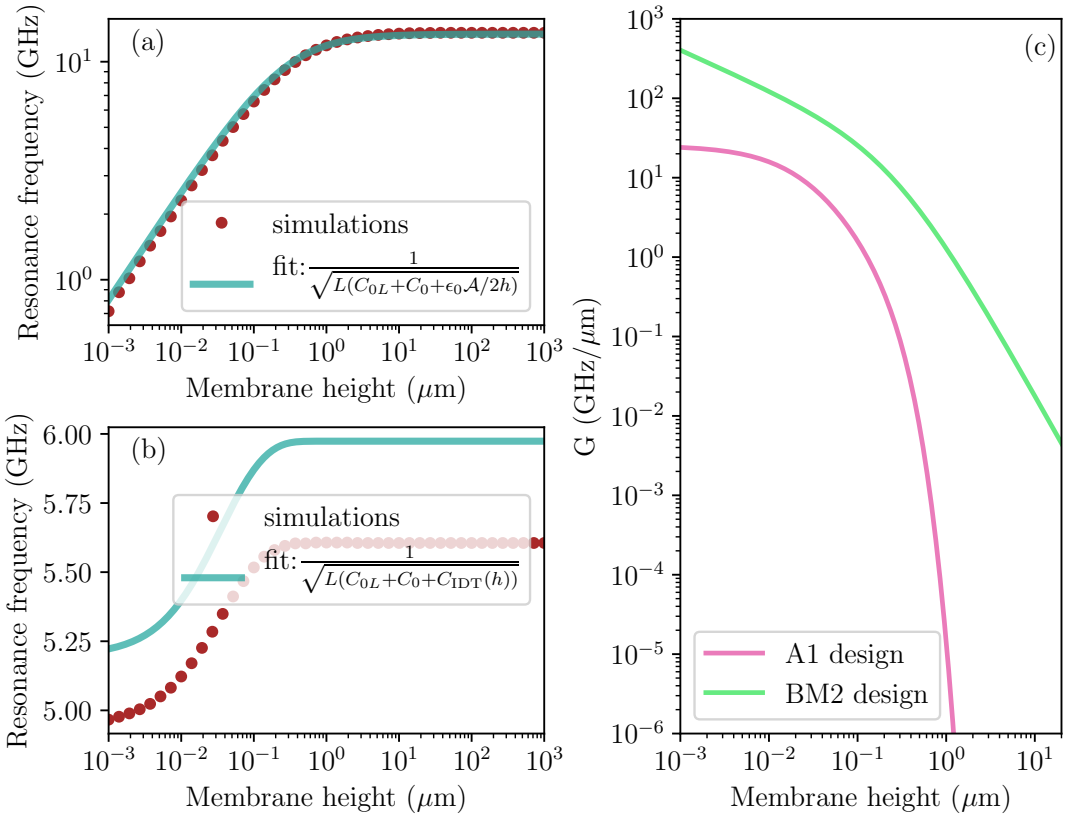

Figure III.9: Membrane height-dependent frequency of A1 and BM2: resonators A1 (sketched in (a) for reference) and BM2 (sketched in (b)) are simulated for various membrane heights. The resonance frequency extracted from the waveguide transmission are represented as dots in (c) and (d) respectively. The prediction of formula III.1.40, with the values of L and $C_{0\mathrm{L}}$ extracted from Fig. III.7 and III.8, and the values of C(h) given by the analytical formulas III.1.32 and III.1.33 are plotted as blue lines. The parameter $G = d\omega_c/dh$ obtained by deriving the later analytical expression is plotted in pink (resp. green) for the sample A1 (resp. BM2) in (e).

III.2: Low temperature measurement setup

One of the prerequisites of most experiments performed in this work was to use "cold" electromagnetic resonator, *i.e.* where the temperature is such that $k_{\mathrm{B}}T \ll \hbar\omega_c$, with $\omega_c/2\pi$ being the cavity frequency. Whereas the optical frequency range allows to access this regime at room temperature, as explained in the previous section, the cavity frequencies that were chosen for this work are in the microwave range, typically between 5 to 10 GHz. At this frequency, the characteristic temperature needed for adding one thermal photon to the cavity is:

$$T_{\mathrm{lim,opt}} \overset{\mathrm{def}}{=} \hbar\omega_c/k_{\mathrm{B}} \approx 360 \text{ mK}. \tag{III.2.1}$$

Moreover, the use of a superconducting material for the cavity imposes to work at temperatures significantly low in front of its critical temperature (for example for

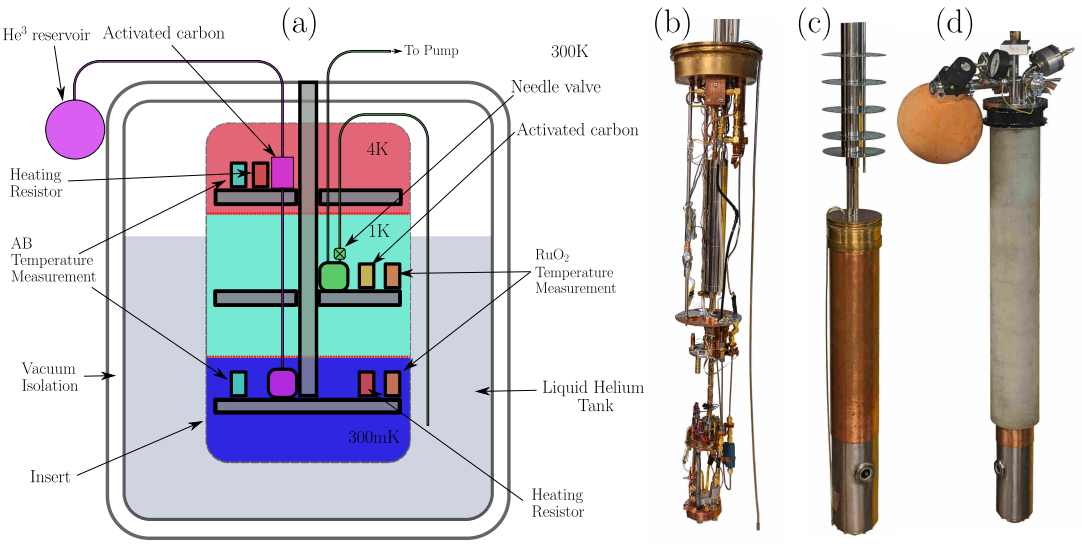

Figure III.10: (a) Schematics of the He^3 cryostat. In light blue is the liquid Helium Tank, in green the 1K-pot circuit, and in pink is the He^3 circuit. (b) Picture of the opened insert. (c) Picture of the closed insert. (d) Picture of the closed insert with its exterior seal (see main text for details).

Niobium, $T_c \approx 9.2$ K). In consequence, the use of a cryogenic setup is mandatory for all the experiments carried out in this work. The measurements were performed in two different cryogenic setups: one of them is a "wet" He^3 IceOxford fridge without dilution, the other one is a BlueFors "dry" dilution fridge with pulse tube, for the use of which we would like to thank the group of Zaki Leghtas at LPENS. Both setups were quite similar, and we will describe in details the He^3 cryostat in this section.

III.2.a: The He^3 cryostat

The use of a He^3 cryostat has several advantages compared to dilution fridges. Its relatively short cycle duration ($\sim$ 5 h from room temperature to $\sim$ 330 mK) allows to perform quick tests at low temperature, a useful feature to characterize several samples successively. Moreover, the relative affordability of such technology makes it available to a research group with a budget comparable to a typical french Agence Nationale de la Recherche (ANR) grant. The He^3 cryostat was bought at the same time I arrived in the lab. Consequently, the first months of this PhD were dedicated to the learning of the different skills necessary to work with this instrument. Indeed, contrary to other kinds of cryogenic systems, such as modern dilution cryostats that are fully automatized, the cooldown cycle of the He^3 cryostat requires to perform a number of manual steps that are described in section III.2.a.ii.

III.2.a.i Description of the different components

A schematic of this cryostat is represented in figure III.10 (a). It comprises three cryogenic stages. The first one consists in a $\sim$ 60 L liquid He^4 tank, isolated from the

room temperature environment by an isolation vacuum. This tank is filled with He^4 gas at atmospheric pressure, so the temperature of the liquid is equal to 4.2 K.

The rest of the experiment lies in a removable compartment, which will be referred to as the "insert" thereafter (see figure III.10 (b), (c)). It is composed of three distinct stages of decreasing nominal temperature. The first stage, colored in red in Fig. III.10 is in thermal contact with the surrounding liquid helium bath, and it has thus a nominal temperature of 4.2 K. It can dissipate a large heating power and it hosts the microwave amplifiers used in our experiments.

The second stage consists in an independent helium circuit, which will be referred to as the "1K-pot" thereafter. It is colored in green in figure III.10 and is composed of a small ($\sim$ 10 cL) buffer connected to the liquid He^4 tank on one hand and an external pumping line emerging atop of the insert on the other hand, with a precise needle valve allowing to manually control the section for the connection between the buffer and the tank. After the needle valve lies a root pump, allowing to maintain a low pressure downstream the needle valve, while at the same time evacuating a continuous gaseous flow of approximately 15 m^3/h. This corresponds to the realization of a Joule-Thompson expansion, which generates a cooling power in the 1K-pot corresponding to the latent heat of vaporization of the constant helium flow through the needle valve. In reaction, the temperature is lowered down to $\sim$ 1.5 K.

The third stage consists in a closed He^3 circuit, colored in pink in figure III.10 (a). When not used the gas lies in a spherical exterior reservoir, linked to a small ($\sim$ 10 cL) buffer thermalized with the baseplate of the cryostat. It is only when the 1K-pot reaches its nominal temperature ($\approx 1.5\,K$) that the helium 3 liquefies in the bottom stage of the cryostat. The principle of operation of the lower cryogenic stage is simple: once most of the helium 3 is liquefied in the buffer, the pressure of the bath is reduced to displace the working point on the vapor-liquid equilibrium curve, such that the final temperature decreases transiently below the 1K-pot temperature[1].

The cryostat remains at low temperature until all the liquid helium 3 is evaporated in the process. Pumping of the helium 3 with an external mechanical pump would be inconvenient given the price of such a gas ($\approx$ 2000 euros/L), and the risks of a leak in the external pumping circuit. Instead, a sorption pump—referred to as the "sorb" in the following—is used. This device is based on an activated carbon which can adsorb some gas, and whose adsorbtion rate is reduced when the temperature is increased. The sorb is installed in loose thermal contact with the 1K-pot and it can be effectively switched on or off thanks to a heating resistor.

Several temperature sensors have been pre-installed in the cryostat to monitor the good operation of these various cryogenic circuits: two Allen Bradley (AB) resistors, sensitive in the 4 - 300 K range are disposed in close thermal contact with the helium 3 "sorb" and the 1K-pot respectively. In addition, two Rhutenium-Oxyde (RuO_2) sensors, sensitive in the 10 mK - 4 K range are mounted on the helium 3 buffer stage and 1K-pot respectively. We have also installed a home-made temperature-controlled platform with a RuO_2 sensor and a 50 Ω terminator used in DC as a heater for precise temperature control and calibration experiments (see section III.2.b.ii). Finally, a superconducting sensor is used to monitor the level of liquid helium in the

[1]Helium 3 is preferred over helium 4 because it has a lower boiling temperature (3.19 K instead of 4.2 at ambient pressure)

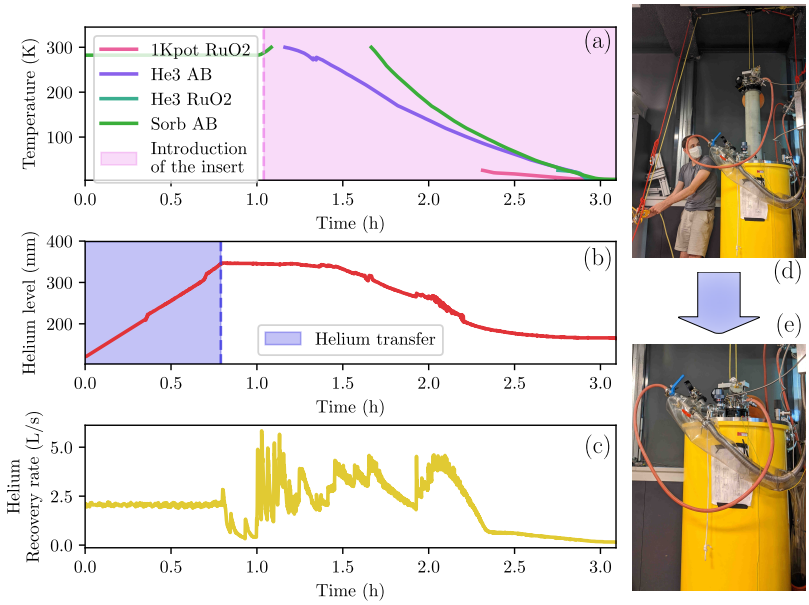

Figure III.11: First step of a cooldown in the He^3 cryostat. (a) Temperature versus time. The period where the insert is inside the tank is highlighted in light red. (b) Helium level versus time. A Helium transfer is highlighted in blue. (c) Evaporation rate of the Helium. (d) Picture of the lowering mechanism, at the start of the insertion of the insert. (e) Picture of the cryostat after the insertion of the insert is complete.

main reservoir, and a digital counter has been installed on the recovery line to monitor the rate of evaporation within the bath.

In the following we will describe the main steps that are required to operate this cryostat down to base temperature.

III.2.a.ii Cooldown procedure

Preparation of the insert The first step of a cooldown consists in closing the insert and pumping it thoroughly. The seal between the interior part of the insert and its exterior shield is made by a simple metal-on-metal contact on a slightly conical surface (see figure III.10 (b)) homogeneously covered in vacuum grease. The two pieces are manually brought into contact before starting the pumping. The sole vacuum is then holding the insert closed. Consequently, after the pressure has been reduced down to $\sim 5 \times 10^{-5}$ mbar, a leak detection is performed to check that there is no risk of a sudden opening of the insert after having turned off the pump. Then, a small quantity of He^4 gas is introduced in the insert as an exchange gas. This exchange gas is used to help thermalize the inner part of the insert with the surrounding helium 4 bath.

The insert is then fixed to its exterior seal (see figure III.10 (d)), which aims at slowly inserting it in the tank without losing Helium in the room. The 1K-pot circuit is then meticulously purged with He^4 such that nothing freezes inside during the cooldown, which might lead to an obstruction. Before inserting the insert in the helium reservoir, the good circulation of He^4 in the 1K-pot circuitry is checked by

immersing the tip of the helium pickup in an isopropanol basin, which results in the production of a stream of bubbles under normal operating conditions.

Insertion of the insert in the tank Let us first note that contrary to the case of a closed cycle fridge, the tank has to be filled manually and regularly. This operation is done by transferring Helium from a liquid helium dewar. To that end, a transfer tube, which is isolated from the room temperature by an isolation vacuum, is inserted in both the container and the cryostat tank. Then, a heating resistor is inserted in the container and $\sim$ 5 W of electrical power is used to evaporate the Helium. The increase of pressure then triggers the Helium transfer. If several cooling cycles are repeated over a short period of time, for instance when several samples need to be characterized successively, it is usually advantageous to maintain the reservoir at low-temperature between the successive insert cooldowns by performing regular helium transfers. In practice, thanks to the good thermal isolation and large volume of the reservoir, the cryostat has an autonomy of approximately 5 days. Since the cooldown of the insert leads to a significant evaporation in the bath, it is preferable to start the procedure described below when the level of liquid helium in the bath, as indicated by the superconducting sensor, exceeds 300 mm.

The insertion phase is performed while carefully monitoring the recovery rate, indicative of the helium 4 evaporation in the main reservoir while the insert is dipped inside the bath. To reduce the helium consumption during this phase, we try to maintain this value between 2.5 and 5 L/s. After $\sim$ 2 h, the temperature of the 1K-pot and "sorb" Allen Bradleys should be around 4.2 K, and the Rhutinum Oxyde sensors on the helium 3 stage and 1K-pot should be within the valid measurement range (see Fig. III.11). A dedicated activated carbon is thermalized with the 1K-pot stage. Consequently, most of the exchange gas is adsorb after this step. It is indeed mandatory to reduce the thermal contact between the surrounding liquid helium bath and the various parts of the insert (sorb, 1K-pot, He^3 buffer) in order to proceed successfully with the next step. In particular, a too large thermal contact between the sorb and the 1K-pot prevents to reach the conditions required for helium 3 condensation (see next step). In this case, the insert can be evacuated in-place by connecting it for several hours to a turbo-pump. The pump can be disconnected and the normal procedure can be resumed when the residual helium 4 pressure reaches the 10^{-6} mbar level.

He^3 condensation and cooldown to base temperature The He^4 balloon in the input of the circuit is then replaced by a primary pump, and the needle valve opening is adjusted to admit a constant helium flow through the 1K-pot. In practice, a too small opening of the needle valve results in the "drying" of the 1K-pot: the flow of helium 4 is too small to compensate the thermal load on the 1K-pot, such that eventually, no more liquid remains in the 1K-pot. This situation is visible as a sudden rise of the 1K-pot temperature. On the other hand, a too large opening results in a large flow of liquid helium through the 1K-pot, bringing its temperature close to 4 K. When the good setting is found, the temperature quickly settles close to 1.8 K. (see figure III.12 (a)).

A current is then injected through the heating resistor of the He^3 activated carbon in order to reach a temperature > 48 K for approximately 30 minutes (see figure III.12

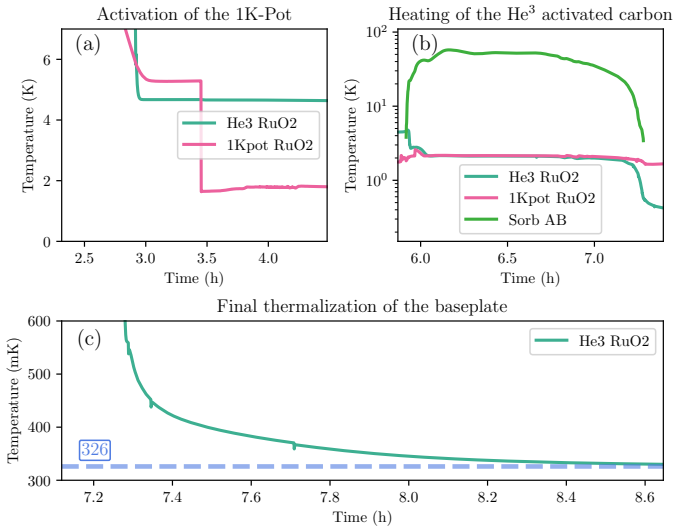

Figure III.12: Evolution of the different temperatures in the last cooling steps. (a) Activation of the 1K-pot. (b) Manual heating of the He^3 activated carbon. (c) Condensation of the He^3 leading to the baseplate temperature of ~ 326 mK.

(b)). This provokes the desorption of the He^3 from the activated carbon to the buffer. During this step, it is crucial that the 1K-pot stays below ~ 2.8 K, such that the He^3 condensates at the contact of the buffer. After this step, the buffer is full of liquid He^3, and the system is ready to reach its base temperature. For this purpose, the sorb temperature is decreased below 4 K to reduce the pressure of the helium 3 bath. The temperature of the helium 3 stage immediately starts to decrease, reaching ≈ 330 mK in approximately 2 hours (see Fig. III.12 (c)).

In this configuration, the autonomy at low temperature is a few days. Eventually, the He^3 buffer runs out of liquid and needs to be refilled. This is done by repeating the condensation cycle. Of course, the He^4 reservoir needs to be regularly refilled during the cryostat operation.

III.2.b: Measurement setup

The microwave experiments we performed in the cryostat have certain requirements, such as not adding noise to the system while injecting strong microwave pulses at low temperature and reading very small signals. It is also very important for the various DC and RF connections used to preserve the thermal isolation of the different stages of the cryostat. In a first section, we will describe the different wiring and thermalization techniques employed to fulfill those requirements. In a second section, we will focus on the microwave measurement setup.

III.2.b.i Wiring and thermalization

Coaxial lines The RF signals used throughout this work are carried via semi rigid coaxial cables in the cryostat. The choice of the material used for those lines is important, as the descent line and the output line have quite different requirements. For

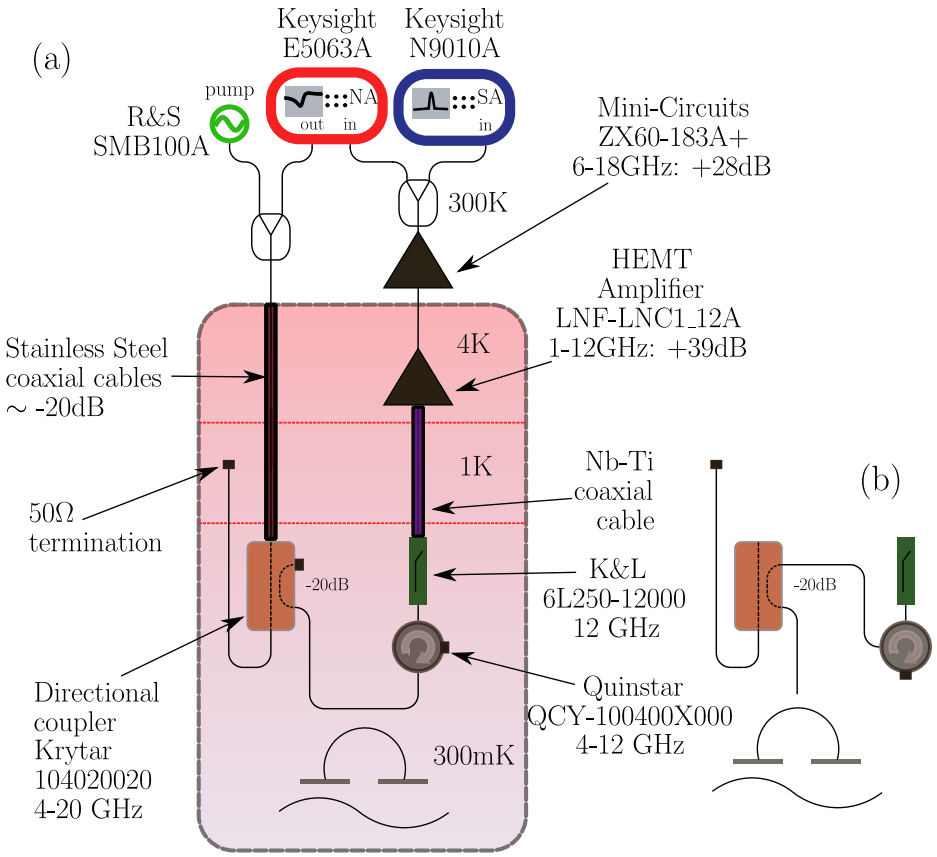

Figure III.13: (a) RF wiring used in the He^3 cryostat. NA: Network Analyzer. SA: Signal Analyzer. See main text for details. Triangles represent amplification. This wiring corresponds to the "hanger" cavity coupling. (b) Variation of the wiring corresponding to the reflection cavity configuration. The part not represented stays the same.

the descent line, we used stainless steel cables: their low thermal conductivity ensures a good isolation between the different cryogenic stages, while, as we will see in section III.2.b.ii, their low electrical conductivity is used for dissipating the room temperature Johnson Nyquist noise. For the output line, the baseplate of the cryostat has been connected to the 4K stage by a superconducting Niobium-Titanium cable, which combines the benefits of a very low RF loss and a very low thermal conductivity. Finally, the part of the output line connecting the 4K stage to the room temperature environment is made in Beryllium Copper, as it also exhibits very low RF loss rate[SDZ$^+$12], and that its higher thermal conductivity is less critical for this part of the circuit. Those cables were thermalized with the different cryogenic stages using extra copper wires pressing the coaxial cables in contact with a copper cylinder thermalized with the desired stage (see figure III.14 (a)).

RF component thermalization The signals going in the output line were amplified with a High Electron Mobility Transistor (HEMT) amplifier (see section III.2.b.ii). To thermalize it properly, a dedicated copper L-shaped piece has been designed, which is tightly screwed to both the 4 K stage of the insert and the amplifier (see figure III.14 (f)). We used essentially commercial RF components, which are thermalized to their respective stages with thin copper plate (see figure III.14)(e). Finally, some 50 Ω termination connectors had also to be thermalized properly, which by pressing them between two thick parallel copper plates (see figure III.14(b))

Temperature measurements As explained in section III.2.a.i, the temperatures are monitored by measuring the resistance of dedicated temperature dependent resistors. This measurement is performed by a 4-wires measurement: two wires are connected at each end of the resistor. The first pair is used for injecting a known current, while the second pair is used for measuring the voltage. Advantageously, in such configuration, there is no voltage drop associated with a current flowing in the voltage measurement pair. The DC wires used for this temperature measurement are very thin (diameter of 100 μm) copper wires, with a resistivity of $\sim 10\ \Omega/m$. They are protected from short circuits by a thin insulating layer. By using very long wires, we decrease the thermal conductivity between the cryogenic stages. To make sure that both ends of the wire are properly thermalized with the corresponding cryogenic stage, we wrap a large number of times the wires around a copper cylinder thermalized with the cryogenic stage. The wire is efficiently thermalized with the cylinder by coating the roll with Varnish (see figure III.14 (c) and (d)). The DC-wires running from stage to stage are maintained in place by small linen wires to prevent them from touching the surface of the insert, and thus avoiding unwanted thermal bridges.

Temperature stabilized stage Some of the experiment performed requires to be able to set the temperature at a given value instead of simply reaching the lowest temperature possible. To that end, a small temperature stabilized stage has been set up with a heating resistor, made with a 50 Ω termination connector, and a RuO_2 temperature sensitive resistor. Consequently, this stage requires 6 wires to be operated: 4 wires for the temperature measurement, and 2 wires for the heating resistor. Those two resistors are thermalized by pressing two thick copper plates with screws and nuts

on their edges, similarly to the thermalization of other 50 Ω resistors (see figure III.14 (b)).

III.2.b.ii Microwave measurement setup

line and noise thermalization Any signal generated in an environment at temperature T_1 carries a Johnson-Nyquist noise. For a small bandwidth around the central frequency ω, these random fluctuations are well approximated by a white noise:

$$\langle \hat{a}^\dagger(t)\hat{a}(t')\rangle = \delta(t-t')n_{\mathrm{B}}(T_1,\omega), \tag{III.2.2}$$

where $\hat{a}$ is the bosonic lowering operatror for the field in the transmission line, and $n_{\mathrm{B}} = \frac{1}{e^{\hbar\omega/k_{\mathrm{B}}T}-1}$ is the Bose-Einstein factor. Since microwave sources are located at room-temperature, all generated signals comprise a large thermal occupation $n_B(T_1,\omega) \gg 1$. This noise needs to be suppressed before letting the signal interact with the low-temperature system. This is achieved by attenuating the signal with dissipative elements placed at a lower temperature T_2. In close analogy with a beam-splitter in quantum optics, the attenuator output is the sum of two terms:

$$\hat{a}_{\mathrm{out}} \overset{\mathrm{def}}{=} \sqrt{A}\hat{a}_{\mathrm{in}} + \sqrt{1-A}\hat{b}_{\mathrm{in}} \tag{III.2.3}$$

where A is is the power attenuation of the dissipative element, and $\hat{b}_{\mathrm{in}}$ is a Johnson-Nyquist noise at the temperature of the attenuator. As a result, the output occupation reads:

$$N_{\mathrm{out}} = An_{\mathrm{B}}(T_1,\omega) + (1-A)n_{\mathrm{B}}(T_2,\omega), \tag{III.2.4}$$

Formula III.2.4 shows that the output noise is reduced as long as the dissipative element is at a lower temperature than the source. An estimate of the attenuation needed for a proper thermalization between a stage at temperature T_1 and a stage at temperature T_2 is $A = T_2/T_1$, in the limit of a high occupation at both temperatures and $T_2 \ll T_1$. This corresponds to approximately 30 dB in the He^3 cryostat, and approximately 45 dB in the case of the dilution fridge. Note that the unused output port of this effective beam splitter corresponds, for a purely dissipative element, to power dissipated through Joule effect. This will set up a higher limit to the input power that can be sustained in the cryostat: when the dissipated power overcomes the cooling power of the cryostat, the temperature starts to rise significantly.

Instead of a purely dissipative element, a way to rise up this power limit is to use a directional coupler, (see figure III.13 and III.14(e)): this element, equivalent to two transmission lines evanescently coupled to each other, allows to experimentally access the four ports of the effective beam splitter. With a 20 dB coupler, the coupling between the two transmission line is such that 99 % of the power injected emerges in the transmitted port of the coupler. In our setup, this port is connected to a 50 Ω termination thermalized with a higher cryogenic stage, such that the microwave power dissipated can be efficiently sinked away (see Fig. III.14 (b)). On the other hand, the coupled port is connected to the experiment, such that the noise and drives from the source are attenuated by 20 dB. Finally, the unused port of the coupler needs to be terminated by a 50 Ω load placed at the lowest possible temperature, since it is directly

coupled to the experimental port. The advantage of this setup is that the noise seen by the experiment is equivalent to that obtained with a 20 dB attenuator, but the heat generated by the 20 dB absorption of the drive is produced at a higher cryogenic stage where the available cooling power is greater.

On top of those lumped element dissipators, the material used for the coaxial cables in this input line is a lossy material (Stainless steel in our case), aiming at providing approximately 20 dB of loss at cryogenic temperatures and at the range of frequencies we are interested in (i.e. between 5 and 10 GHz).

Sample box To shield the sample from the thermal radiation from the exterior part of the cryostat, as well as from any electromagnetic perturbation, it is required to put it in a metallic box. In this thesis, we measured samples in aluminum or copper boxes, both of those materials having different qualities: as a superconductor, aluminum is a very good electromagnetic shield at low temperature, while copper exhibits a higher thermal conductivity. In practice, we did not notice any difference between experiments performed in different boxes. The dimensions of the box should be large enough to contain the sample. However, such a box inevitably behaves as a microwave resonator with a discrete number of resonant modes. Each of those modes could couple to the modes of interest of our samples and perturb the experiment. It is therefore crucial to design the box such that the first resonance frequency is above any experimentally frequency of interest.

The modes of a rectangular box of width L_x, length L_y and height L_z have the following resonance frequencies:

$$f_{mnl} \overset{\text{def}}{=} \frac{c}{2\epsilon_r \mu_r} \sqrt{\left(\frac{m}{L_x}\right)^2 + \left(\frac{n}{L_y}\right)^2 + \left(\frac{l}{L_z}\right)^2}. \tag{III.2.5}$$

In this expression, m, n and l are natural integers characterizing the number of nodes in the x, y, and z directions respectively. At least two of these parameters need to be different from 0 to describe a non-zero electric field mode profile. The lowest frequency box mode is thus determined by the two largest dimensions of the box. Moreover, the formula III.2.5 is only strictly correct when the box is filled with a uniform dielectric material of permittivity ϵ_r. In the relevant case where the box contains a silicon chip of height h_{Si} below a uniform vacuum layer of height h_{vac}, the lowest resonance frequency is approximately obtained by taking $\epsilon_r = (h_{\text{Si}}\epsilon_{\text{r,Si}} + h_{\text{vac}})/(h_{\text{vac}} + h_{\text{Si}})$. It is thus useful to chose a dimension L_z as close as possible from the other dimensions of the box to reduce ϵ_r.

We designed our box (see figure III.15 (a) and (b)) with dimensions L_x =15 mm, L_y = 18 mm and L_z =13 mm. Therefore, the lowest mechanical frequency of our box is $f_{110} \sim 13$ GHz, which is indeed above the highest microwave frequencies we intend to use in our experiments ($\sim$ 10 GHz).

The RF signals are carried throughout the measurement setup in SMA connectors, while on the sample chip the waveguides are either coplanar waveguides or striplines (see section IV.2.b). To connect those, we file the SMA connector tips from a cylindrical shape to a semi-cylindrical shape (see figure III.15 (c)) and we solder small aluminum wires, called wirebounds, to the coplanar waveguide or stripline conductor

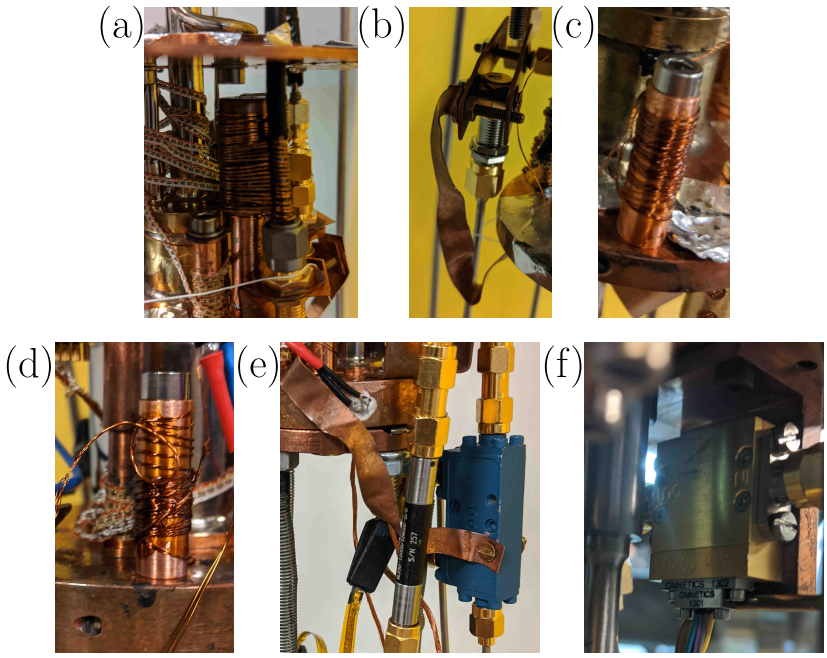

Figure III.14: (a) Thermalization of a RF cable (b) Thermalization of the 50Ω resistor at the end of the chimney to the 1K-pot. (c) Thermalization of a DC wire to the 1K-pot. (d) Thermalization of a DC wire to the baseplate: the wire is rolled around a copper cylinder and coated with Varnish. (e) Thermalization of the directional coupler to the baseplate of the cryostat. (f) Thermalization of the Hemt amplifier.

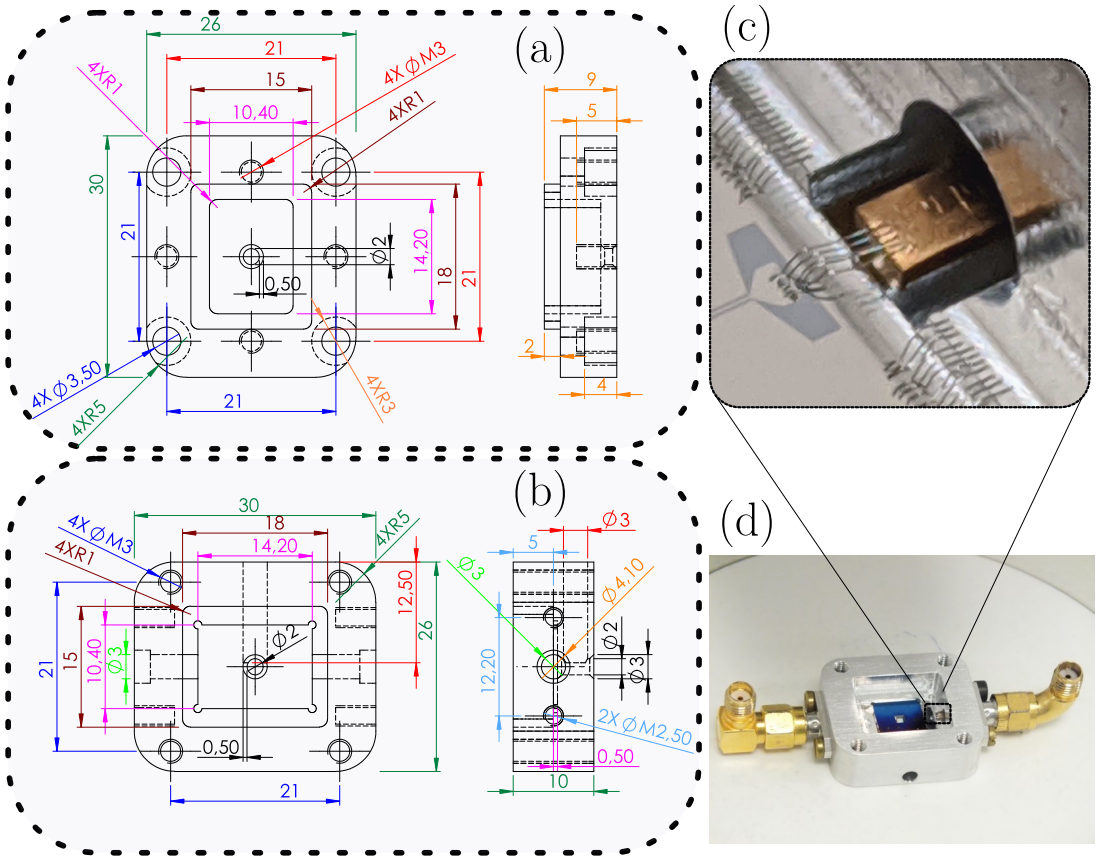

Figure III.15: (a) Mechanical plans of the bottom part of our sample box. Dimensions are in mm. (b) Mechanical plans of the top part of our sample box. (c) Pictures of a filed SMA connector tip wirebounded to a stripline waveguide on a sample chip. (d) Picture of a wirebounded optomechanical cavity in the bottom part of the sample box, before closing the box.

line. The soldering is performed with a dedicated "wirebounding" machine, using ultrasonic excitations. It is necessary to put several wirebounds in parallel to reduce the impedance mismatch of the connection.

Amplification We have already seen that the drive signals need to be attenuated to suppress the Johnson Nyquist noise generated at room temperature. In contrast, the signals originating from the sample need to be amplified to overcome the noise that is inevitably added by the measurement apparatus located at room temperature. To this end, we use a High Electron Mobility Transistor (HEMT) commercial amplifier from Low Noise Factory (LNF-LNC1_12A) (see a picture in Fig. III.14(f)).

As explained in section I.4.c.i, any amplification comes at the cost of added noise, with a lower bound set by quantum mechanics and corresponding to half a quantum of noise. HEMT amplifiers are currently the most efficient commercial microwave amplifiers. When operated in a cryogenic environment, the LNF-LNC1_12A provides a gain G_1 of ~ 30 dB over a large (1-12 GHz) bandwidth and exhibits a noise temperature of approximately ~ 4 K (or equivalently an added noise of ~ 10 quantas). Before being fed into the measurement apparatus, the signal is further amplified at room temperature by a $G_2 = 28$ dB gain amplifier ZX60-183A+. The input equivalent noise added by a chain of two amplifiers of gain G_1 and G_2 and input equivalent noise N_1 and N_2 is given by:

$$N_{\text{out}} = N_1 + N_2/G_1. \tag{III.2.6}$$

In other words, provided the first amplifier in the chain has a sufficient gain, the effective noise of the chain is dominated by the first amplifier noise. In practice, we have measured an input equivalent noise for the whole amplification chain of 4.4 K, very close to the specifications of the HEMT amplifier (see next section).

Calibration of the lines As explained in the previous paragraphs, the RF descent line used to drive the circuit, and the readout amplification chain used to retrieve the signals from the sample are composed of various coaxial lines, attenuators, and amplifiers, whose properties can vary significantly between room temperature and cryogenic conditions. It is thus hazardous to measure independently the attenuation of the descent line and the amplification of the readout chain. However, these are very important quantities that are needed to calibrate the amplitude of the signals *at the sample location* in absolute terms.

One way of calibrating the gain G of the amplification chain *in-situ* is to use the known Johnson Nyquist noise of a 50-Ohm terminator, placed in the cryostat at the fourth port of the directional coupler, such that most of the noise generated by the terminator reaches the amplification chain (see Fig. III.16). The terminator is placed on the temperature controlled stage described in section III.2.b.i, and its temperature T is varied systematically between 400 and 500 mK, a range that is easily accessible by the temperature controlled platform.

The total noise spectral density measured by a spectrum analyzer at room temperature is given by

$$S(\omega, T) = G\hbar\omega_c(n_{\text{B}}(T, \omega) + N_{\text{add}}), \tag{III.2.7}$$

where the first term is due to the Johnson-Nyquist noise of the 50-Ohm termination, and the second term is the added noise of the measurement chain, expressed in added photons. For a central frequency $\omega/2\pi \approx 7$ GHz, the Nyquist noise $n_{\rm B}(T,\omega)$ is expected to vary from 0.76 photons, to 1.04 photons when the temperature spans the interval [400 mK, 500 mK]. The added noise of the amplifier ($\approx$ 10 photons) thus strongly dominates over the Nyquist noise. However, both of these random signals being white noises, the total noise spectral density can be measured very precisely by integrating the signal over a large bandwidth. In practice, the temperature is cycled up and down with a 5 minutes thermalization time for each value, and the spectrum is averaged over a 500 MHz bandwidth around 7 GHz. To track small drifts of the gain over the course of the measurements, we have added a calibration tone and rescaled each spectrum to maintain the height of this peak constant.

The average power spectral density is plotted in Fig. III.16 as a function of temperature. To make sure that the measurement is not affected by a thermal lag of the platform temperature, we plot separately the points acquired during the ramp up of the temperature (in red) and the points acquired during the ramp down (in blue). As expected, we observe a nearly linear dependence of the spectral density as a function of T.

$$\mathcal{S}[\omega,T] \approx \alpha T + \beta. \tag{III.2.8}$$

In the regime where $n_{\rm B}(\omega,T) \approx k_{\rm B}T/\hbar\omega$, the slope α and offset β of the line are directly linked to the gain G and added noise N of the amplification chain via

$$G = \alpha/k_{\rm B} \tag{III.2.9}$$

$$N_{\rm add} = (k_{\rm B}/\hbar\omega)(\beta/\alpha). \tag{III.2.10}$$

In this particular experiment, we find G $\sim 1.5\times10^6$ (= 61.8 dB), and $N_{\rm add} \sim 13 = k_{\rm B}\times 4.4$ K, a value that is in very good agreement with the specification of the HEMT amplifier.

Measuring the probe amplitude at the output of the setup allows to retrieve the total gain of the input and output lines of the cryostat:

$$\mathcal{T} \stackrel{\rm def}{=} \mathcal{A} + G \sim 9 \text{ dB}, \tag{III.2.11}$$

where $\mathcal{A}$ is the attenuation of the descent line. Therefore, we have:

$$\mathcal{A} = \mathcal{T} - G \sim -52 \text{ dB}. \tag{III.2.12}$$

A similar calibration has been performed for the dilution fridge.

III.3: Nanofabrication of the electromechanical resonators

The electromechanical resonators described in section III.1 are composed of two distinct elements: a superconducting circuit located on a first silicon chip, and a suspended membrane placed in regard. As discussed in part III.1.b and III.1.c, the distance separating the superconducting electrodes and the vibrating membrane is a crucial parameter as it directly impacts the electromechanical coupling rate G. The full resonator,

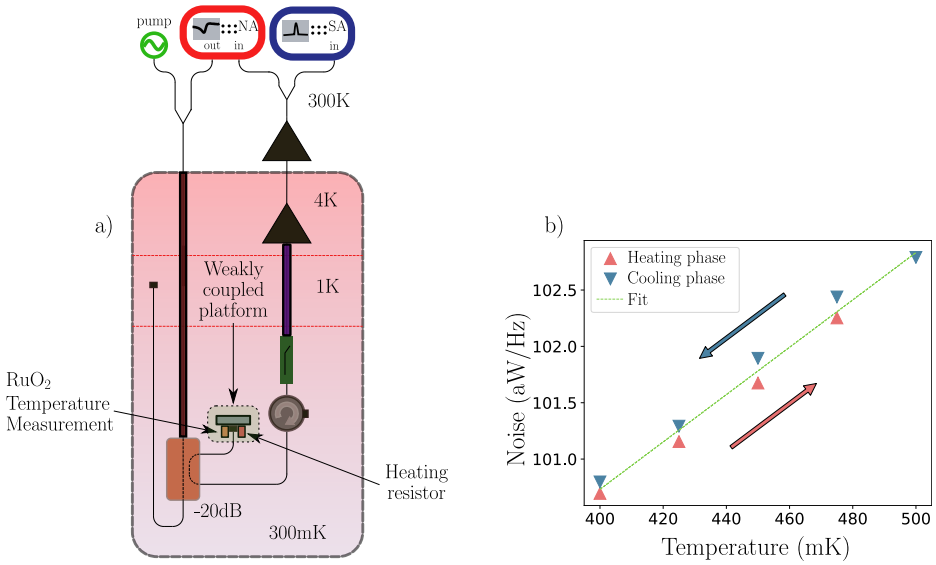

Figure III.16: (a) Setup used for the calibration of the amplification and attenuation chain in the ^{3}He cryostat. SA, spectrum analyzer. (b) Experimental results, for increasing and decreasing temperatures, with added fit.

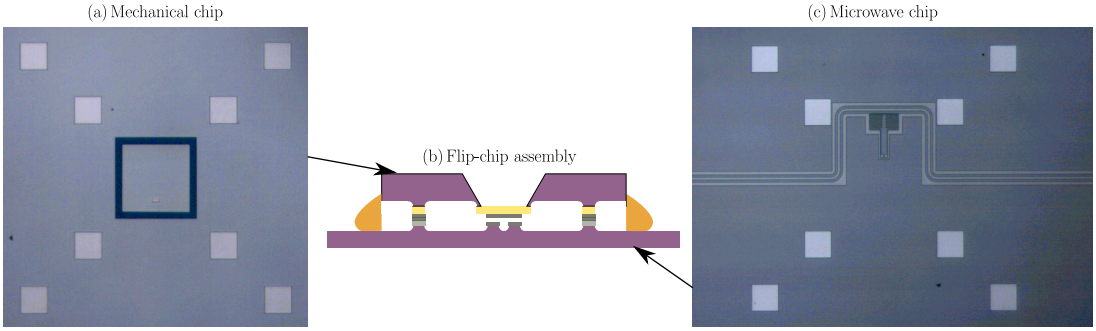

Figure III.17: Schematic view of the electromechanical sample: the mechanical sample (a) and the microwave chip (c) are assembled together with a flip-chip assembly technique. The nominal distance between the 2 chips ($\sim$ 300 nm) is defined by the thickness 8 metallic spacers in regards, visible on both samples.

represented schematically in Fig. III.17, is obtained by assembling two independently fabricated samples with a "flip-chip" technique. The fabrication of the suspended membranes has already been described in section II.3. However, an additional metallization step is required before the membrane can be used in an electromechanical resonator. This step is used to pattern a superconducting electrode on the membrane itself. Moreover, we had to develop from scratch the microfabrication process for the "microwave chip" hosting the rest of the superconducting circuit, and the flip-chip assembly procedure.

As explained in the introduction of this chapter, we have first developed microwave resonators based on interdigitated capacitors. The microwave properties of these resonators were first characterized in the absence of a vibrating membrane. These experiments, described in section IV.1.a, have been useful to validate the microfabrication process, the measurement setup described in III.2.b, and they have led to a new experimental technique for the characterization of the TLS bath limiting the quality factor of planar superconducting resontarors [CFI+20] (see chapter VI). However, electromechanical coupling was only observed with the electrostatic coupling scenario involving a metallized membrane.

In the following, we describe the main microfabrication steps for the development of electromechanical resonators. In section III.3.a.i, we describe the fabrication of the "microwave chip", underlining the specificities of the resonators based on interdigitated capacitors and coplanar pads. In section III.3.b, we describe the steps involved for the metallization of the membranes. Finally, in section III.3.c, we describe the flip-chip technique developed to bring the "microwave-chip" and the suspended membranes at a sub-micron distance.

III.3.a: Microwave chips

The recipe for microwave resonators with interdigitated capacitors we present below is a simple one that does not include spacers to integrate it in a flip chip assembly. Indeed, those resonators were first used for microwave characterization purpose. In the second section, however, we describe a recipe for microwave resonators with a coplanar pad capacitor which includes those spacers.

III.3.a.i Interdigitated capacitors

We fabricated resonators on 3 different substrates:

- a 250 μm thick substrate of float-zone (FZ) grown (100) intrinsic silicon, with a resistivity of more than 10 000 Ω.cm (substrate referred to as Si),

- a 500 μm thick substrate of FZ grown (100) P-doped type-n silicon, with a resistivity of more than 10 000 Ω.cm, with 2 μm of SiO_2 from thermal oxidation (substrate referred to as Si/SiO_2),

- a 650 μm thick substrate of Czochralski (CZ) grown (100) silicon, with P/boron doping and a resistivity of 1-30 Ω cm, with 200 nm of Si_3N_4 deposited through low-pressure chemical vapor deposition (substrate referred to as Si/Si_3N_4).

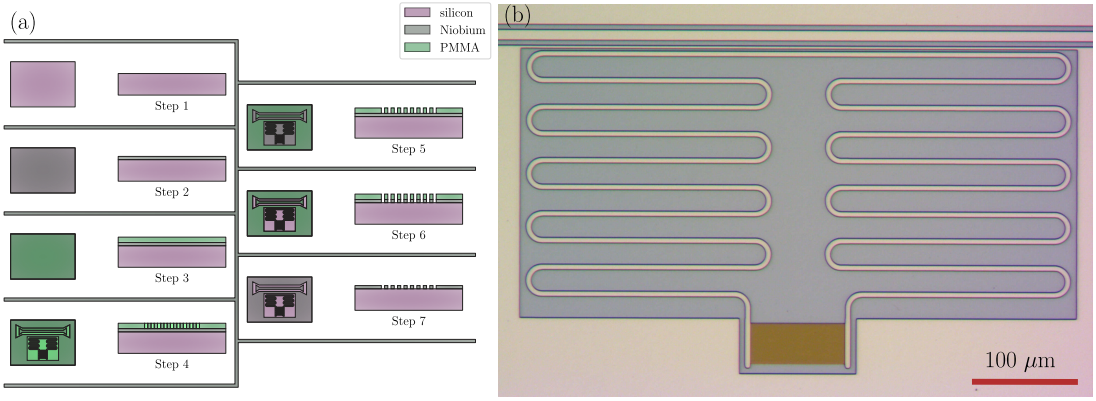

Figure III.18: (a) Detailed recipe for the nanofabrication of interdigitated capacitors based resonators. (b) Picture of a fabricated interdigitated resonator.

The design retained for this contained sharp features: teeth width and spacing were made as small as ~ 250 nm, which precludes the use of optical lithography. Instead, we developed a recipe based on e-beam technology, using a 30 kV Raith "e-line" e-beam machine. This recipe is decomposed as follows (see fig. III.18):

- Step 1: a 10 mm x 14 mm sample of the desired substrate is cleaned, with a 10 minute Acetone bath at 50°C with ultrasounds, followed by a 20 s rinsing in Isopropanol (IPA) and a drying with a nitrogen Gun

- Step 2: In a Plassys evaporator, the sample is pumped until reaching a vacuum of approximately $\sim 5\times10^{-10}$ mBar, and then 100 nm of Niobium are evaporated.

- Step 3: After a new cleaning, the sample is covered by 300 nm of PMMA. To reach this thickness, a spin coating machine is used at at speed of 4000 rpm, and acceleration of 4000 rpm.s^{-1}, and a duration of 30 s, starting from the relevant dilution of PMMA with Anisole. After the spinning, a 15 min bake at 160°C is performed.

- Step 4: In the e-beam machine, the sharp features, such as the teeth, are made in a 10 μm aperture with a dose of 215 μC/cm^2, while the large features, such as the inductor and the waveguide, are made in a 120 μm aperture and a dose of 320 μC/cm^2.

- Step 5: The development is done in a MIBK 1:3 IPA solution and lasts 70 s. After that, a rinsing is done in IPA, followed by a drying with the Nitrogen gun.

- Step 6: The Niobium is etched in a Reactive Ion Etching (RIE) Corial machine, in a 7 mTorr and 70 W SF6 plasma for approximately 1 minute.

- Step 7: A last cleaning is done for the removal of the resist.

Note that in e-beam lithography, some electrons sent by the machine are not interacting with the resist but instead are scattered by the substrate, generating secondary electrons which are in turn interacting with the resist. In practice, this leads to an insulated area larger than the area exposed to the primary electrons. This has to be dealt with for sharp features by adjusting carefully the dose used and by insulating a region smaller than desired. For example, for generating a tooth spacing of 250 nm for teeth spacing of 250 nm, it is necessary to expose the area between the teeth on a width of ~ 200 nm.

The choice of a hanger configuration allowed that for each substrate, 10 resonators have been multiplexed on the same coupling waveguide and their resonance frequency was staggered by incrementing the capacitor's area by steps of ≈ 2.5 %. The coupling-limited quality factor was designed to be $\approx 2 \times 10^4$.

III.3.a.ii Coplanar pads capacitors

We now describe the fabrication of microwave resonators with coplanar pads capacitors. The recipe described here is for a resonator coupled to a stripline waveguide (see section IV.2.b), but the fabrication steps are not significantly different from a resonator coupled to a coplanar waveguide. A processflow is represented scematically in Fig. III.19.

The fabrication starts with 2" $\langle 100 \rangle$ high resistivity FZ grown single side polished silicon wafers of thickness 270 μm. A first and important task is to remove most of the natural silicon oxyde layer covering any bare silicon substrate, prior to a metal deposition (Step 1). Indeed, as will be explained in section VI, in those amorphous layers lies some defects limiting the quality factor of the microwave cavities. To fulfill this prerequisite, a standard cleaning process routinely used in the industry is the so called RCA cleaning process [Ker90]. The key step aiming at removing oxides is the last one: an immersion in dilute HF. We therefore kept this step in our cleaning recipe, which reads:

- 10 min bath in RBS with ultrasounds,
- rinsing in DI water for 1 min, then drying with nitrogen gun,
- 10 min bath in Acetone with ultrasounds, then drying with nitrogen gun,
- 10 min bath in Isopropanol with ultrasounds, then drying with nitrogen gun,
- 10 min of O_2 plasma,
- 10 min in 1:1 piranha bath with ultrasounds,
- rinsing in DI water,
- 30 s in 4 % dilute HF.

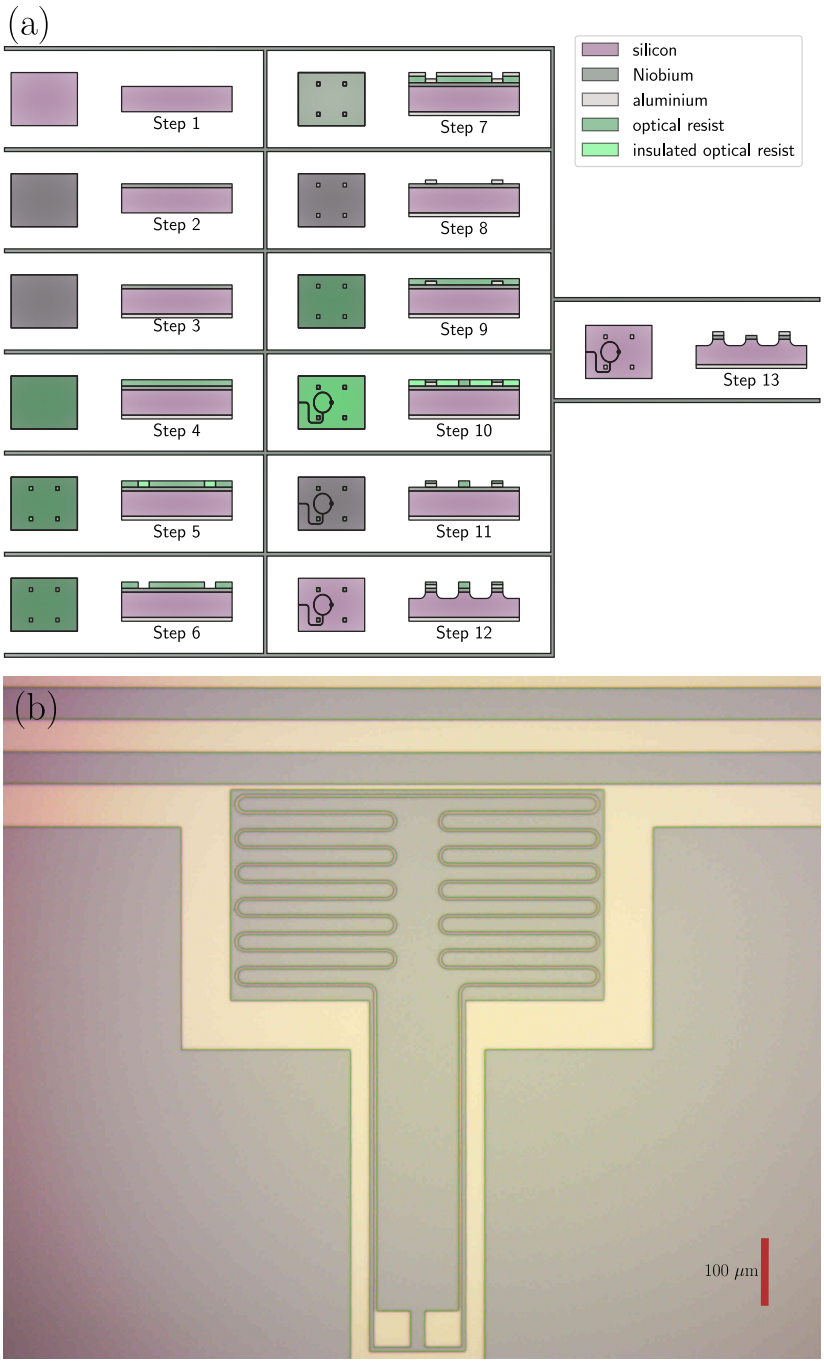

Figure III.19: (a) Nanofabrication process for making a microwave cavity. This recipe is valid for a stripline resonator. (b) Picture of a fabricated microwave cavity.

The wafer is then immediately pumped in a Plassys stutterer, to deposit a 100 nm thick Niobium film at a pressure of 0.01 mbar, a power of 600 W and a time of 40 s (Step 2). Prior to the deposition, the wafer is further cleaned by a RF argon plasma inside the vacuum chamber. Interestingly, note that we tried to replace our cleaning recipe by a simple acetone+IPA cleaning, before the same sputtering deposition, and obtained the same quality factors, probably limited by the quality of the metal deposition and the argon plasma. As a consequence, we believe that the thorough and complicated cleaning we used at first, which is used in the industry, is not relevant, and that the argon cleaning plasma inside the sputtering chamber is enough for a proper removal of the natural oxide silicon layer.

The wafer is then diced in 14 mm*10 mm rectangular samples: this rectangular shape is needed for allowing to stamp a 10x10 mm membrane substrate and still being able to wirebound this sample to our sample box. The ground plane of the stripline is then first defined by a back evaporation of $\sim$ 300 nm of Aluminum (Step 3). To do that, the metallic part of the sample is protected with a layer of thick optical resist, and inserted upside down in an evaporator.

The smallest features of this design being larger than a few microns, there is no need to define the patterns using e-beam lithography. Instead, the resonator design was defined using laser lithography. The spacers, whose goal are to impose a well-defined distance between the two chips, are defined using a lift off technique: AZ5214 resist is spun at 4000 rpm, with an acceleration of 4000 rpm/s and a duration of 30 s, followed by a 1 min 30 s hot plate bake at 110 °C (step 4) and a positive laser lithography is performed to create the corresponding openings in the resist (step 5 and 6). The shapes of these spacers are typically 500 mum x 500 μm squares. The sample is then placed in an evaporator where a layer of $\sim$ 100 nm of aluminum is deposited (step 7). The thickness of this layer needs to be well controlled since it defines the nominal separation between the electrodes and the membrane. The edges of the sample, which are usually imperfectly covered with photoresist are protected by standard tape during this evaporation step. The leftover resist is then removed in a hot acetone bath without ultrasounds for 20 minutes (Step 8).

The resonator is then defined by a second laser lithography using the recipe described above (steps 9 and 10). The etching recipe then starts with the etching of the Niobium layer in the Corial RIE machine, in a SF6 plasma with a pressure of 7 mTorr and a power of 70 W for 1 minute (Step 11). After that, a stronger program is used to etch a few microns of silicon (Step 12) : a 100 W plasma at 80 mTorr, CHF_3 (15 sccm) + SF_6 (25 sccm) + O_2(4 sccm) for 2 min 30 s. Then the same program we use for etching the Niobium is used for 30 s, followed by another strong etch for 2 min 30 s.

The etched profile of the resonator can be seen in figure III.20. The samples are then cleaned in a hot Acetone bath with ultrasounds for 5 minutes, rinsed in Isopropanol for 20 s and dried with a nitrogen gun. The result can be seen in figure IV.8(b) and IV.10(a).

III.3.b: Membrane metallization

The fabrication of mechanically compliant capacitors imposed the metallization of the membrane. The corresponding recipe is presented in figure III.21 (a) To do so, we

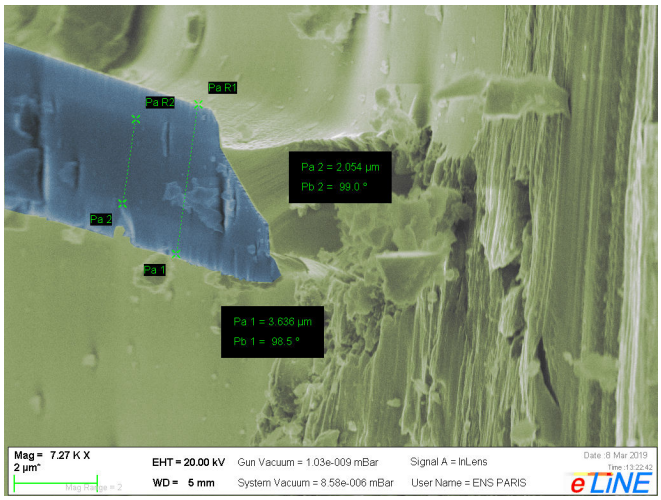

Figure III.20: Scanning Electron Microscope angle view in false color of the deep etching of silicon. Niobium is represented in blue, and silicon in green. The etch depth is approximately 2.5 μm, and we can see the undercut due to the isotropy of this etching technique. A dummy sample was etched and intentionally broken perpendicularly to the Niobium wire direction to realize this image. This breaking explains the quite irregular shape of the Niobium film, and the level of dirt in the picture.

start from the square membranes presented in section II.3. After a thorough cleaning (Step 1), the sample is inserted in a Plassys sputterer. 50 nm of Niobium are then deposited (Step 2), in a 0.01 mbar 500 W plasma for 33 s. To make sure the substrate is clean before the deposition, the sputtering is preceded by a 30 s, 50 W AC argon plasma at 0.01 mbar. The base of the sample is then protected with a clean room compatible blue tape in order to not break the membrane with the vacuum suck of the spin coating machine. AZ5214 resist is then spun at 4000 rpm, with an acceleration of 4000 rpm/s and a duration of 30 s, followed by a 1 min 30 s hot plate bake at 110 °C (Step 3).

The purpose of the following lithographic step is to define the metallic pad on the membrane along with 8 metallic spacers that will be perfectly aligned in regards with the spacers previously patterned on the microwave-chip. For this, we use a positive laser lithography using a LW405C, at a dose of 200 μC/cm^2 (Step 4). We make sure that this lithography is perfectly aligned with the membrane by using alignment marks that were imprinted during the etch of the square membrane openings (see section II.3). Since these marks are located on the opposite side of the sample, we use a back camera of the laser lithography machine, allowing for double face alignment. The lithography is followed by the same development than before: 50 s in AZ726MIF and rinsing in DI water, then drying using a nitrogen gun (Step 5).

The niobium is then etched in a RIE SF_6 25 sccm 70 W plasma for 1 min at 7 mTorr (Step 6). The leftover resist is removed in a hot (50°C) acetone bath without ultrasounds for 15 minutes, followed by a rinsing in isopropanol and a nitrogen gun drying (Step 7). A third lithography is then performed, following an identical than the previous lithography, but the pattern left protected by the resist here corresponds to

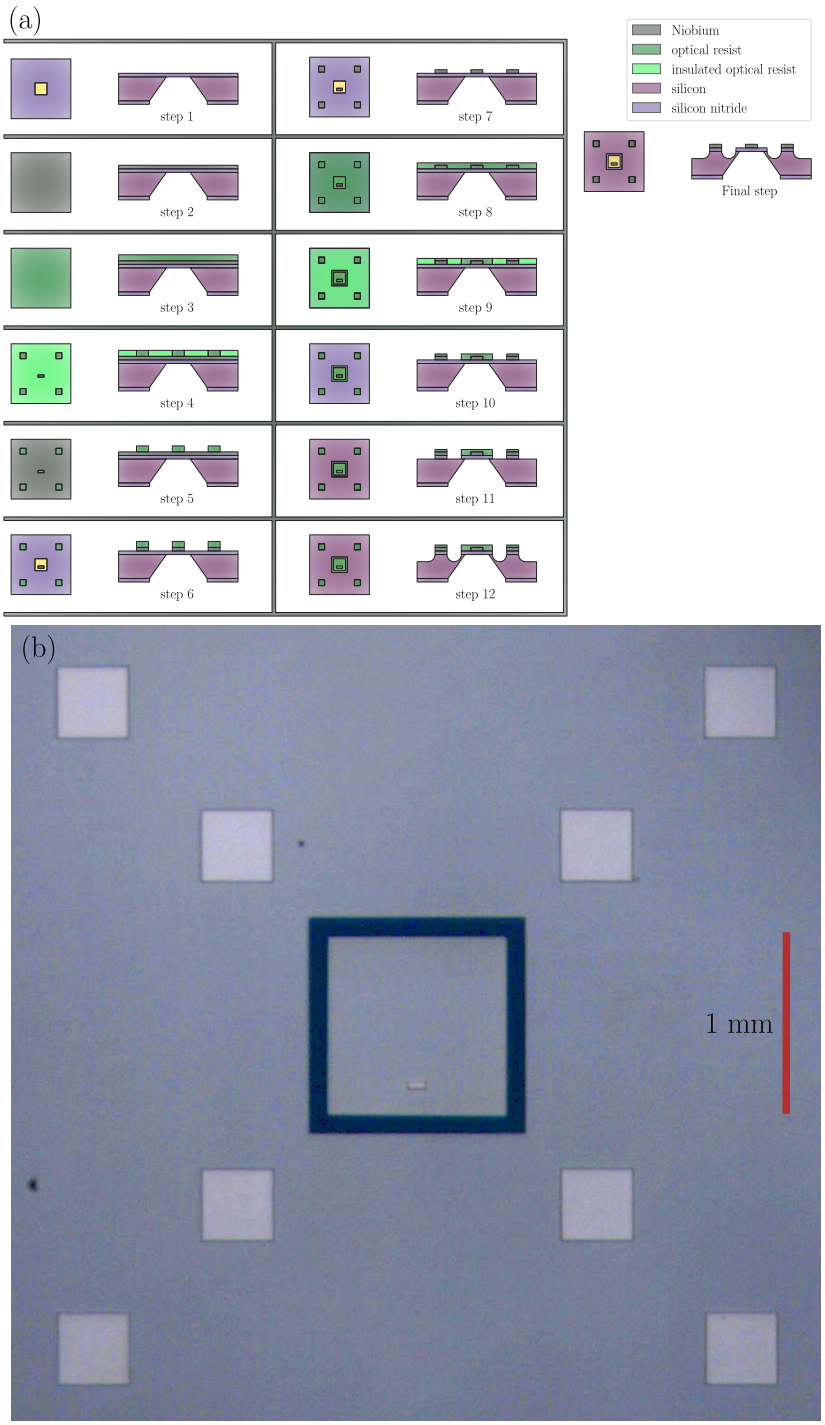

Figure III.21: (a) Nanofabrication process for making the metallization of a square membrane. (b) Picture of a metallized membrane.

a square a little bit larger than the membrane, and 8 squares slightly larger than the spacers. This corresponds to the steps 8 to 10.

The silicon nitride is removed using the same RIE program than the first lithography (Step 11) : CHF_3 (50 sccm) + O_2 (6 sccm) for a 70 W plasma at 20 mTorr for 3 min30s. Then the silicon etching program described in the previous section is used. The leftover resist is then removed in a hot (50 °C) Acetone bath without ultrasound for 10 min, followed by a rinsing in Isopropanol and a drying with a nitrogen gun (Final step). The result can be seen in the bottom right part of figure III.21 (b).

III.3.c: Flip-chip assembly

The technique used for the stamping of the mechanical resonator to the microwave sample is described in figure III.22. The process starts from the two samples thoroughly cleaned: 30 min in 1:3 piranha bath in a homemade holder followed by a rinsing in DI water, then in IPA for the membrane side, or 10 min in a 50 °C Acetone bath with ultrasounds followed by a rinsing in IPA for the microwave side.

The stamping itself is made on a MJB4 mask aligner, for which we use a homemade mask holder. The purpose of this holder is to maintain the membrane from the top by vacuum suction, while at the same time leaving an optical access to see through the membrane for alignment. The mask holder is thus designed to suck the membrane chip only on its external silicon part, where the membrane is not liberated (see a schematic of the vacuum circuit directly machined inside the holder on Fig. III.22 (b), (c), and (d)). Furthermore, two large apertures have been machined on the sides of the holder, such that enough space is available to manually bring epoxy glue once a satisfying alignment has been obtained.

The first step consists in positioning the mask aligner upside down next to the MJB4 and to bring the membrane, the liberated silicon nitride facing upwards, on top of the trenches connected to the vacuum sucking, the latter being not connected. Then we connect the vacuum suck, such that the membrane is safely affixed to the holder as visible on Fig. III.22 (a) (the membrane is located on the central beam of the holder, and a vacuum tube is visible at the bottom of the picture). The mask holder is then carefully flipped such that the membrane faces downwards, and the former is inserted into the MJB4 (see Fig III.22 (b)). At this point, it is possible to use the microscope objective of the MJB4 to check carefully that the back face of the membrane sample is clean enough. It is important to abort the procedure at this stage in case the sample is found dirty, as dust particles on the membrane usually lead to degraded quality factors, and even worst, they can enter in contact with the microwave chip once the samples have been stamped.

The microwave sample, placed on a microscope glass, is then inserted below the sucked membrane and the alignment is made, first by approaching the two samples in the z direction close enough to be able to see the features of the two samples in the field depth of the microscope objective, then by aligning the angle between the two samples using straight features such as the side of the membrane, the extra membranes used for reflectometry measurements, or straight parts of the coupling lines or the inductive part of the sample. Then the x-y alignment is made so that the capacitive part of the circuit matches the metallic part of the membrane. The two chips are then

slowly approached in the z direction, with small corrections of the x-y alignment if necessary. After contact has been made, an extra pressure is added to make sure that the alignment will not be broken upon any contact, and rapid (5 min) Araldite epoxy glue drops are place on at least two corners of the membrane, at the interface between the two chips. A thin wire is used as a pencil to reach those spots. The system stays then still for 30 min such that the glue properly dries off. The vacuum is then turned off, and the chip assembly is then slowly lowered. Using the microscope objective, we can see that this step is relaxing the membrane chip towards a position farther from the microwave sample chip.

At this point, the sample can be glued to the bottom part of its sample box, using conductive Ag glue. After the glue dried off (which takes approximately 15 minutes), the sample is wire bounded in a dedicated machine. To protect the liberated part of the membrane from possible projections of aluminum wire sections, an unused silicon chunk is placed on top of the membrane chip during wirebounding. The bounding is made between the coupling wires and the SMA connectors, whose central parts have been filed into a flat, smooth tip. At least three bounds are made for the connection. In the case of a coplanar waveguide microwave sample design, the ground plane is also wirebounded to the bottom part of the sample box, with as much bounds as possible, regularly spaced. After that, a multimeter check allows to measure the resistivity between the central part and the ground plane, and between the two ports, if two ports are used. For instance, a resistance in the range of at least a few kΩ is nominal, depending on the geometry, between the central part and the ground plane. This last check allows to spot any short circuit, and to assess the resistivity of silicon, which should be high enough to indicate that intrinsic silicon is used. the top of the box is then installed, and the sample is then ready for a cooldown.

Conclusion In this chapter we have presented the design and fabrication recipe of microwave cavities that can be efficiently coupled to the mechanical resonators presented in the previous chapter. We also described in details the low temperature measurement setup used for their measurement and characterization at low temperature. In the next chapter, we will describe the characterization techniques employed to measure the microwave, and electromechanical properties of these samples.

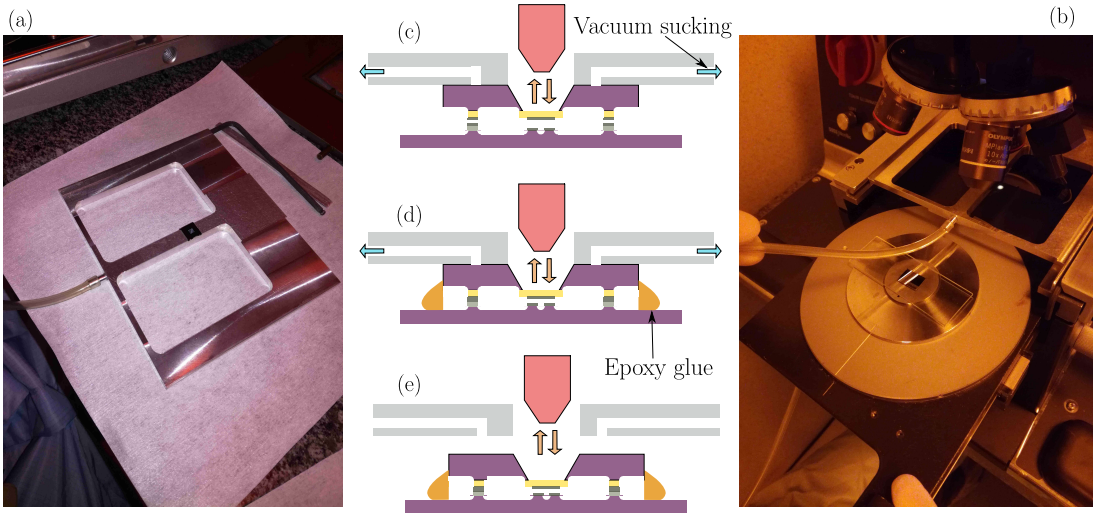

Figure III.22: Stamping technique used for assembling the mechanical oscillator and the microwave cavities. (a): Homemade mask holder: the plastic tube used for sucking the membrane is connected to a primary pump that is not visible in the picture. The sample is the blue chip on the central beam of the mask holder. (b) Insertion of the microwave sample in the MJB4 mask aligner. The homemade mask holder, in place below the MJB4 microscope, is also visible in the picture. where the homemade mask is maintaining the membrane. (c) Alignment of the two samples is performed while imaging them through the membrane with the MJB4 microscope. (d) Once the alignment is satisfying, the two samples are pressed together and several drops of Araldite epoxy glue are applied at the corners of the membrane chip. (e) The vacuum suck is disconnected and the mask holder can be removed once the glue has dried off.

Chapter IV: Characterization and optimization of the electromechanical coupling

In this chapter, we will describe how to use the low temperature measurement setup described in the previous chapter to characterize and optimize the sample design. In particular, we demonstrated the coupling between a microwave resonator and a mechanical resonator with a very high quality factor ($\approx 300 \times 10^6$) at low temperature.

IV.1: Characterization

A prerequisite to the coupling between mechanical and microwave resonators is the characterization of the microwave cavity. In this section we explain how the microwave resonance is characterized. The setup used for the A1 design will be shown. However, the technique is similar for other designs (BM2, and further optimizations).

IV.1.a: Microwave cavity resonance

The characterization of the microwave resonance is performed by a Virtual Network Analyzer (VNA): a low power probe is sent to the sample through the cryogenic setup and the transmitted signal is demodulated at the probe frequency. The complex transmission coefficient of the cavity is obtained by comparison between the input probe and the transmission. This operation is repeated at different frequencies around the resonator resonance frequency. Note that the resonance profile predicted by the equation (I.3.4) has a perfectly symmetric lorentzian profile. However, the experimentally measured spectra are usually not symmetric. This is due to reflections at the ports of the sample box and in the coupling waveguide. This phenomenon still allows to fit the resulting lorentzian by introducing an extra phase in the formula [GSE+12]:

$$\mathcal{T} \overset{\text{def}}{=} 1 + \frac{\eta e^{i\delta}}{\frac{2i\Delta}{\kappa} - 1}. \tag{IV.1.1}$$

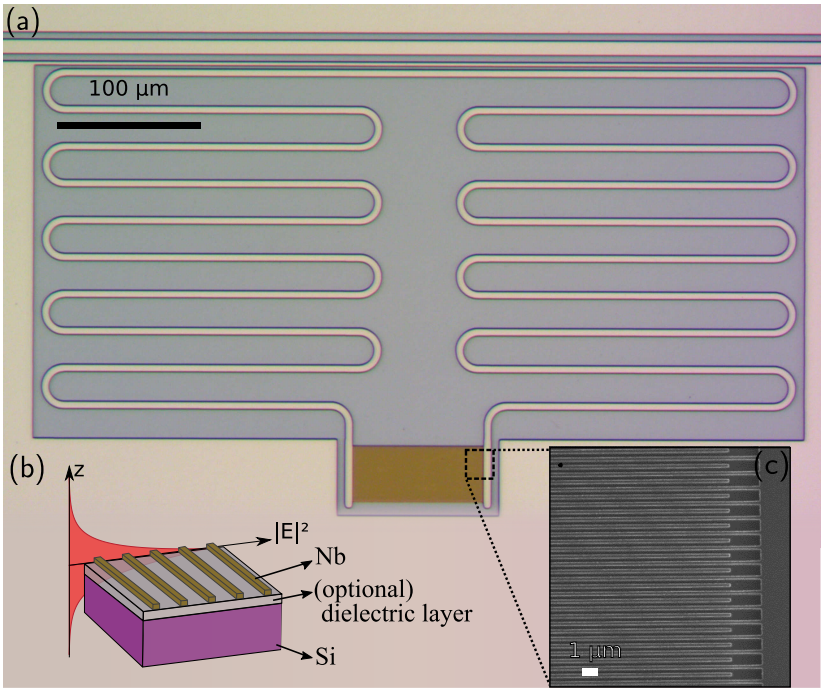

Figure IV.1: (a) Optical micrograph of the microwave cavity. (b) The dielectric environment of the capacitor and the profile of the electric field mode profile (magnitude square), which exhibits in good approximation an exponentially decaying z-dependence. Silicon is represented in purple, niobium is represented in grey, and the optional (SiO_2 or Si_3N_4) amorphous dielectric layer is represented in green. (c) view of the capacitor using electron microscopy.

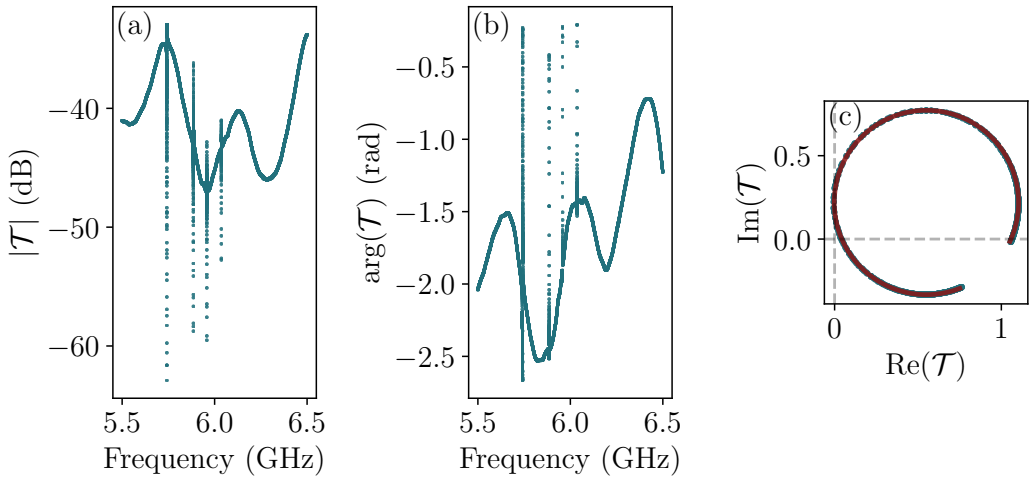

Figure IV.2: modulus (a) and phase (b) of the measured transmission of a sample with several resonators. Four resonances are shown. (c) Smith plot of the transmission close to the first resonance, with a fit using equation IV.1.1. The extracted parameters are $\omega_0/2\pi = 5.74$GHz, $\kappa/2\pi = 574$kHz. κ_0 was too small with respect to κ_c, and could not be measured.

This equation is a circle in the complex plane, centered on $1 - \frac{\eta e^{i\delta}}{2}$ and with a $\frac{\eta}{2}$ radius. Note that the extra phase does not modify the shape and the radius of the circle. However, it slightly shifts its center (see figure IV.2 (c)). Fitting eq. IV.1.1 to the data provides the resonance frequency $\omega_0/2\pi$, the coupling rate between the microwave cavity and the feedline $\kappa_c/2\pi$, and the intrinsic loss rate of the microwave cavity $\kappa_0/2\pi$.

Note that the value of $\kappa_c/2\pi$ is determined by the geometry. For example, in a hanger configuration, moving the resonator away from the feedline or reducing the length of the inductor that is evanescently coupled to the feedline decreases its value. It is possible to assess it quantitatively using Finite Element Modeling. In a first time, to see clearly the resonance and to assess the value of κ_0, it is useful to design a resonator with a rather high value of κ_c. In a second time, another sample is fabricated with $\kappa_c \approx \kappa_0$. Indeed, this configuration is the best compromise between on one hand the minimization of $\kappa = \kappa_c + \kappa_0$ to engineer a well isolated microwave resonator, and on the other hand the need to retrieve a large proportion of the signal in the cavity by maximizing $\eta = \kappa_c/\kappa$. More precisely, looking at equation I.3.33, we see that the optomechanical gain $|\mathcal{G}|^2 \propto \eta C \propto \left(\frac{1}{\kappa_0}\eta(1-\eta)\right)^2$. Therefore, the situation where $\kappa_c \approx \kappa_0$ is maximizing the optomechanical gain.

IV.1.b: Electromechanical coupling

As explained in the previous chapter, the development of the BM2 design allowed the measurement of optomechanical coupling. In this section, we will describe two experimental characterization techniques that were used on those samples. In particular, we

will see that the metallization of the membrane does not affect its exquisite mechanical properties: quality factors of ~ 300 millions were measured with such membranes.

IV.1.b.i Optomechanically induced transparency

In close analogy with atomic EIT[IH89], an interference effect between two optical excitation pathways leads to a dramatic modification of the complex probe amplitude transmission when a particular resonance condition is met (the frequency difference between the probe and the pump needs to match the mechanical resonance frequency). In certain configurations, the pump tone can be used to switch on or off a narrow transparency window for the probe, hence the name Optomechanicaly Induced Transparency[WRD+10]. Moreover, as we will demonstrate it shortly, the precise dependence of the probe transmission with pump power provides quantitative informations about various parameters of the system: for instance, the mechanical linewidth $\Gamma_{\rm m}$ and the pump power dependent cooperativity C.

Theroretical derivation This problem can be quantitatively addressed through the following Langevin equations in Fourier space, where the coherent evolution is derived from the Hamiltonian (I.4.6), and we neglected the quantum noises:

$$(-i(\Omega+\tilde{\Delta}_c)+\kappa/2)\hat{\tilde{\mathbf{a}}}(\Omega) = -ig_0\alpha\hat{\tilde{\mathbf{b}}}(\Omega)+\sqrt{\frac{\kappa_c}{2}}\alpha_{\rm in} \tag{IV.1.2}$$

$$(-i(\Omega-\Omega_{\rm m})+\Gamma_{\rm m}/2)\hat{\tilde{\mathbf{b}}}(\Omega) = -ig_0\alpha^*\hat{\tilde{\mathbf{a}}}(\Omega). \tag{IV.1.3}$$

In the previous equations, $\alpha_{\rm in}$ is the amplitude of the incoming coherent probe: $\hat{a}_{\rm in} \stackrel{\rm def}{=} \alpha_{\rm in}e^{-i\Omega t}$, $\Omega \stackrel{\rm def}{=} \omega_{\rm probe}-\omega_l$, with ω_l the pump frequency, and α is the complex amplitude of the intracavity pump beam. Moreover, a hanger configuration (see Fig. I.2) has been assumed, and will be during this derivation. The solution of this system then reads for the mechanical equation IV.1.3:

$$(-i(\Omega-\Omega_{\rm eff})+\Gamma_{\rm eff}/2)\hat{\tilde{\mathbf{b}}}(\Omega) = \frac{-ig_0\alpha^*\sqrt{\frac{\kappa_c}{2}}\alpha_{\rm in}}{-i(\Omega_{\rm m}+\tilde{\Delta}_c)+\kappa/2}. \tag{IV.1.4}$$

We recognize on the left-hand side of the equation the optomechanically induced modified susceptibility, represented by the effective mechanical frequency $\Omega_{\rm eff}/2\pi$ and linewidth $\Gamma_{\rm eff}/2\pi$. Moreover, we see that the mechanical resonator is coherently driven by the beatnote between the source and the probe (term proportional to $\alpha^*\alpha_{\rm in}$ on the right-hand side) whenever the frequency difference is sufficiently close to the mechanical frequency: $|\Omega-\Omega_{\rm eff}| \ll \Gamma_{\rm eff}$. Injecting back this result in (IV.1.2) we have:

$$(-i(\Omega+\tilde{\Delta}_c)+\kappa/2)\hat{\tilde{\mathbf{a}}}(\Omega) = \left(1-\frac{g_0^2|\alpha|^2}{\left[-i(\Omega_{\rm m}+\tilde{\Delta}_c)+\kappa/2\right]\left[-i(\Omega-\Omega_{\rm eff})+\Gamma_{\rm eff}/2\right]}\right)\sqrt{\frac{\kappa_c}{2}}\alpha_{\rm in}. \tag{IV.1.5}$$

We see that in return, by modulating the cavity frequency at the frequency Ω, the mechanical oscillations scatter optical photons from the pump tone at frequency ω_l

to the probe frequency $\omega_{\text{probe}} = \omega_l + \Omega$. At this frequency, we therefore observe an interference phenomenon between the photons directly created by the probe (term proportional to 1 in the right-hand side parenthesis) and the photons indirectly scattered after a conversion to mechanical excitations (second term in the right-hand-side parentheses). In the canonical situation described above ($\Delta_c = -\Omega_{\text{m}}$, $\Omega_{\text{eff}} \approx \Omega_{\text{m}}$, $\Omega \sim \Omega_{\text{m}}$), the interference is destructive and the intracavity probe field amplitude is strongly suppressed due to the presence of the second excitation pathway. The exact consequences of this intracavity interference effect on the output field depends on the precise coupling configuration. For instance, in the assumed hanger configuration, the input-output relation reads: $\hat{a}_{\text{out}} = \hat{a}_{\text{in}} - \sqrt{\frac{\kappa_c}{2}}\hat{a}$. We thus obtain the complex reflection coefficient:

$$t(\Omega) \overset{\text{def}}{=} \frac{\tilde{\hat{a}}_{\text{out}}(\Omega)}{\tilde{\hat{a}}_{\text{in}}(\Omega)} = 1 - \frac{\eta}{1 - i\frac{\Omega+\tilde{\Delta}_c}{\kappa/2}} \left(1 - \frac{C}{1+C}\frac{1}{1 - i\frac{\Omega-\Omega_{\text{eff}}}{\Gamma_{\text{eff}}/2}}\right), \tag{IV.1.6}$$

where $\tilde{\Delta}_c + \Omega_{\text{m}} \ll \kappa/2$ is assumed. We remind the definition of the optomechanical cooperativity $C = \frac{4g_0^2|\alpha|^2}{\kappa\Gamma_{\text{m}}}$, calculated here for the pump beam amplitude α. We retrieve the Lorentzian resonance of the cavity, of typical width κ, superimposed with a sharp spectral feature occurring precisely at the mechanical resonance condition $\Omega = \Omega_{\text{m}}$. Indeed, we notice that close to this resonance condition, Eq. IV.1.6 can be approximated by a Lorentzian of width $\Gamma_{\text{eff}} = \Gamma_{\text{m}}(1 + C)$ and amplitude $\eta\frac{C}{1+C}$:

$$t(\Omega) \approx (1 - \eta) + \eta\frac{C}{1+C}\frac{1}{1 - i\frac{\Omega-\Omega_{\text{eff}}}{\Gamma_{\text{eff}}/2}} \qquad \text{for } |\Omega - \Omega_{\text{m}}| \ll \kappa. \tag{IV.1.7}$$

This approximation holds as long as $\Gamma_{\text{eff}} \ll \kappa$, which is always the case throughout this work.

Measurement setup The experimental setup (see figure III.13) is composed of a microwave source used for generating the strong pump and a network analyzer used to generate the weak probe field. The output of those two instruments is combined by a microwave power splitter before being routed to the input of the sample box via the descent line of the cryostat. The output signal, amplified and filtered by the measurement line of the cryostat is then routed towards the readout port of the network analyzer, in order to retrieve the complex amplitude transmission for the probe field.

Experimental Results A typical experimental result, obtained on sample BM2, is shown on Fig. IV.3. On all subplots, the probe transmission is plotted with a color corresponding to the varying pump power. The magnitude of the transmission is plotted close to the resonance condition $\Omega \sim \omega_l$ in Figure IV.3(a). We clearly see a linewidth increase with larger pump powers. Furthermore the complex probe transmission is plotted in a Smith chart, in the absence (Fig. IV.3(b)), or in the presence (Fig. IV.3(c)) of a pump field. In the absence of the pump field, the probe transmission describes a circle in the complex plane. Indeed, we have

$$\left[\text{Re}(t(\Omega)) - \left(1 - \frac{\eta}{2}\right)\right]^2 + [\text{Im}(t(\Omega))]^2 \approx \left[\frac{\eta}{2}\right]^2, \tag{IV.1.8}$$

which is the equation of a circle of center $(1-\frac{\eta}{2},0)$ and of radius $\frac{\eta}{2}$ in the complex plane. In the presence of the pump, the sharp OMIT feature appears in the smith chart as a second circle of varying amplitude. Indeed, for $|\Omega-\Omega_{\mathrm{m}}| \ll \Gamma_{\mathrm{eff}}$, we have:

$$\left[\mathrm{Re}(t(\Omega)) - \left(1-\eta+\frac{\eta}{2}\frac{C}{C+1}\right)\right]^2 + [\mathrm{Im}(t(\Omega))]^2 \approx \left[\frac{\eta}{2}\frac{C}{C+1}\right]^2, \tag{IV.1.9}$$

which is the equation of a circle of center $\left(1-\eta+\frac{\eta}{2}\frac{C}{C+1},0\right)$ and of radius $\frac{\eta}{2}\frac{C}{C+1}$ in the complex plane. At lower power, this shape is distorted. This corresponds to situations where the sweep time is small compared to the lifetime of a phonon inside the mechanical resonator: the permanent regime is not reached and the shape of the resonance is not Lorentzian anymore. In this regime, extracting informations is quite complicated, and thus for low cooperativity we will prefer to perform ringdown experiments as presented below. If we place ourselves in a quasi-static regime, we can fit the Lorentzian responses, and plot the width Γ and magnitude $\mathcal{M}$ of the OMIT signal as a function of pump power (see Fig. IV.4). From Eq. IV.1.6, we know that these quantities should scale as $\Gamma = \Gamma_{\mathrm{m}}(1+C)$ and $\mathcal{M} = \eta C/(1+C)$. We thus perform a global fit to the model

$$\Gamma = \Gamma_{\mathrm{m}}(1+\xi P) \tag{IV.1.10}$$

$$\mathcal{M} = \eta\xi P/(1+\xi), \tag{IV.1.11}$$

where Γ_{m}, ξ, η are fit parameters, and P is the pump power. The fit (full lines in Fig. IV.4) matches very well with the measurements. In this particular instance, we find $(\Gamma_{\mathrm{m}}/2\pi,\ -10\mathrm{log10}(P_0\xi),\ \eta) = (46\text{ mHz},\ -26\text{ dBm},\ 0.65)$. The second parameter corresponds to the pump power required to reach a cooperativity of 1, while $P_0 = 1$ mW.

IV.1.b.ii Microwave ringdowns

Another useful tool used for optomechanical devices is the ringdown technique. The goal of this experiment is to probe, this time in the temporal domain, the rate of energy decay in the mechanical oscillator, and to do so at different optomechanical coupling rates. To this end, we need to drive the resonator with a coherent amplitude way above the thermal noise. While the use of external piezoelectic excitation is routinely done in other experiments [TBPS17], we chose instead to use radiation pressure from the cavity itself. The experimental sequence is thus divided into a first *excitation phase*, during which the mechanical resonator is driven out of equilibrium by a series of microwave pulses, and a second *readout phase*, during which the cavity is driven on the red sideband and the decay of the mechanical amplitude is monitored by demodulating the outgoing microwave signal at the frequency Ω_{m}.

Excitation phase The excitation sequence is composed of two distinct steps: in the first one, the resonator is cooled close to a displaced vacuum state, and then starting from this initial state, an unstable dynamics is briefly used to amplify the mechanical quadratures way above the thermal noise (see figure IV.5).

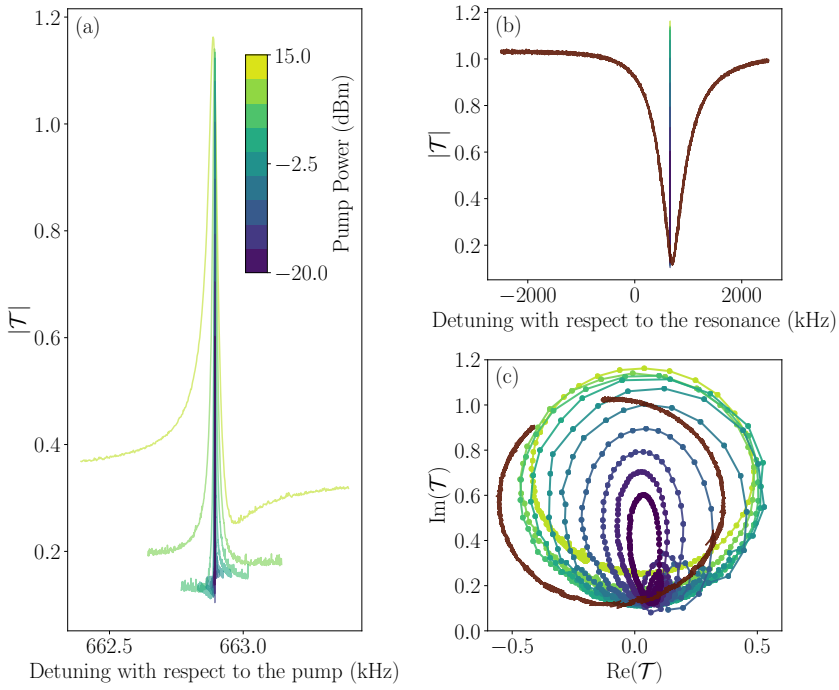

Figure IV.3: Optomechanically induced transparency experiments made with varying power. Left : magnitude of the transmission, zoomed in the OMIT signal. Top-right : magnitude of the transmission in a large scan, with the transmission of the microwave cavity in dark red. Bottom-right : Smith chart of the data.

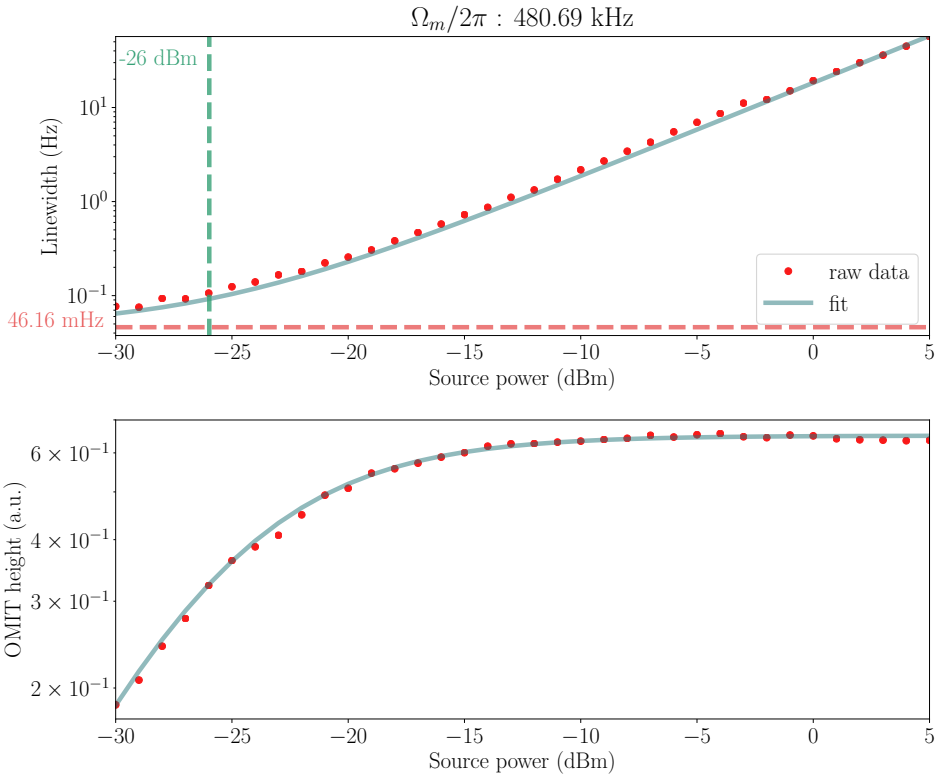

Figure IV.4: Optomechanically induced transparency experiments made with varying power. Top : linewidth of the OMIT peak. Bottom : height of the OMIT peak. Both were extracted with a Lorentzian fit, then fitted together (solid line) to extract the natural linewidth of the mechanical resonator, as well as the power required to have a cooperativity of one (dashed lines)

In the first step, the source frequency is set to the red sideband ($\Delta = -\Omega_\mathrm{m}$), and modulated at the mechanical frequency in order to generate a sideband resonant with the cavity. In a frame rotating at the carrier frequency, the drive thus writes:

$$\alpha_d(t) = \alpha + \alpha_\mathrm{in} e^{-i\Omega_\mathrm{m} t} \tag{IV.1.12}$$

This microwave drive, equivalent to the one undergone by the system during an OMIT sequence has two effects: first, it drives the mechanical oscillator to a displaced equilibrium amplitude

$$\hat{b}_\mathrm{prep}(t) = \frac{-4ig_0\alpha^*\sqrt{\kappa_c}\alpha_\mathrm{in}}{\kappa\Gamma_\mathrm{m}} e^{-i\Omega_\mathrm{m} t}. \tag{IV.1.13}$$

Furthermore, it reduces the variance around this mean value by a factor $\frac{1}{1+C}$, where $C = 4\frac{g_0^2|\alpha|^2}{\kappa\Gamma_\mathrm{m}}$ is the cooperativity of the pump tone. In other words, the mechanical resonator is "cooled" towards the displaced vacuum state $\hat{b}_\mathrm{prep}(t)$. In principle, this displaced vacuum state could be used as the starting point of the readout phase, however, the maximal amplitude $\hat{b}_\mathrm{prep}(t)$ being limited by practical considerations (such as the maximum microwave power that can be injected in the cryogenic setup), the signal-to-noise ratio during the readout phase would not be sufficient to observe the decay of the mechanical amplitude over more than a few decades.

Consequently, during the second step of the excitation, the system is briefly driven into instability by a microwave drive on the blue electromechanical sideband. In such configuration, the relevant quantum Langevin equations are (see section I.4.c:

$$\frac{d}{dt}\hat{a} = -\kappa/2\hat{a} - ig_0\alpha\hat{b}^\dagger + \sqrt{\kappa}\hat{a}_\mathrm{in} \tag{IV.1.14}$$

$$\frac{d}{dt}\hat{b}^\dagger = (i\delta - \Gamma_\mathrm{m}/2)\hat{b}^\dagger + ig_0\alpha^*\hat{a} + \sqrt{\Gamma_\mathrm{m}}\hat{b}^\dagger_\mathrm{in}. \tag{IV.1.15}$$

These equation are written in an interaction picture with respect to $\hat{H}_0 = -\hbar\Delta_c\hat{a}^\dagger\hat{a} + \hbar(\Omega_\mathrm{m}+\delta)\hat{b}^\dagger\hat{b}$, with Δ_c the pump detuning, δ a small error in the mechanical frequency estimation, and α the intracavity pump amplitude. The adiabatic elimination is then performed by considering that when we are interested in the evolution of the mechanical oscillator, the optical resonator is in its steady state, because $\kappa \gg \Gamma_\mathrm{m}$, and thus we have $\frac{d}{dt}\hat{a} \approx 0$. We can then formally integrate this system to get:

$$\hat{b}^\dagger(t) = \hat{b}^\dagger(0)h_b(t) + (h_b \circledast \mathcal{N})(t), \tag{IV.1.16}$$

where $\Gamma_b \overset{\mathrm{def}}{=} C\Gamma_\mathrm{m}$, $h_b(t) \overset{\mathrm{def}}{=} e^{i\delta t}e^{(\Gamma_b-\Gamma_\mathrm{m})t/2}$, and $\mathcal{N}(t) \overset{\mathrm{def}}{=} \sqrt{\Gamma_b}e^{i\Psi_b}\hat{a}_\mathrm{in}(t) + \sqrt{\Gamma_\mathrm{m}}\hat{b}^\dagger_\mathrm{in}(t)$, Ψ_b is such that $-i\alpha^* = |\alpha|e^{i\Psi_b}$ and $\circledast$ is the convolution product. We see that, when the condition $\Gamma_b > \Gamma_\mathrm{m}$, or equivalently $C > 1$, is fulfilled, the mechanical position operator undergoes an exponential growth, that is only limited by non linear behavior at very high amplitude. We exploit this regime to "amplify" the initial mechanical amplitude $\hat{b}_\mathrm{prep}(t)$ by a large factor. In practice, we typically use a cooperativity $C \sim 1000$ and a duration $t_\mathrm{blue} \sim 5 \times 10^{-3}/\Gamma_\mathrm{m}$, corresponding to an amplification by a factor ~ 150.

To illustrate this experimental sequence, Fig. IV.5 (f) and (g) shows the evolution of the mechanical amplitude during the 2 steps of the excitation sequence. The initial

state is drawn from a random thermal distribution, and the exact dynamics is obtained by solving the Langevin equations. Each line represents a random trajectory, such that the variance of the mechanical amplitude can be inferred visually by looking at the spread of the various lines. To underline the importance of the first "cooling" step, we compare the trajectories obtained in step 2 when starting from the "cold" distribution resulting from step 1 (blue trajectories in Fig. IV.5 (f)) and the trajectories that would be obtained if we directly applied step 2 on a thermal distribution (red trajectories in Fig. IV.5 (f)). The very large spread of the final excitation amplitude in the second case would be inconvenient: some ringdown trajectories would start with a limited initial amplitude, and some would exceed the non-linearity threshold. Furthermore, let's note that given the very long lifetime of our resonators, waiting for the system to equilibrate in the absence of a cooling pulse would be very time-consuming.

Readout phase Once the resonator has been excited with an amplitude $\hat{b}(0)$ largely exceeding the thermal noise, we apply a pulse on the red sideband to imprint the decaying mechanical amplitude on the outgoing signal. A calculation similar to the one performed above shows that during this readout phase, the mechanical amplitude evolves according to:

$$\hat{b}(t) = \hat{b}(0)h_r(t) + (h_r \circledast \mathcal{N})(t), \tag{IV.1.17}$$

where $\Gamma_r \overset{\text{def}}{=} C\Gamma_\text{m}$, $h_r(t) \overset{\text{def}}{=} e^{i\delta t}e^{-(\Gamma_r+\Gamma_\text{m})t/2}$, and $\mathcal{N}(t) \overset{\text{def}}{=} \sqrt{\Gamma_r}e^{i\Psi_r}\hat{a}_\text{in}(t) + \sqrt{\Gamma_\text{m}}\hat{b}_\text{in}(t)$, Ψ_r is such that $-i\alpha^* = |\alpha|e^{i\Psi_r}$ and $\circledast$ is the convolution product. Furthermore, we can derive the outgoing field amplitude by applying the input-output relation. For instance, assuming a cavity in reflection, we have:

$$\hat{a}_\text{out}(t) = -\sqrt{\eta\Gamma_r}e^{-i\Psi_r}\left[\hat{b}(0)h_r(t) + (h_r \circledast \mathcal{N})(t)\right] + (2\sqrt{\eta} - 1)\hat{a}_\text{in}, \tag{IV.1.18}$$

For a large amplitude b(0), the first term is dominating over the two noise terms, at least in the beginning of the the evolution. Indeed, this exponentially decaying amplitude is a faithful readout of the mechanical amplitude IV.1.17. For low drive power, ($\Gamma_r \ll \Gamma_\text{m}$, or equivalently $C \ll 1$) the decay rate $\Gamma_\text{m} + \Gamma_r$ is dominated by the intrinsic mechanical decay Γ_m. In other words, the natural damping exceeds the electromechanical damping. On the other hand, at higher drive power where $\Gamma_r \gg \Gamma_\text{m}$, or equivalently $C \gg 1$, the total decay rate is dominated by the electromechanical cooling rate.

Experimental setup The experimental setup is similar to the one used for the OMIT experiments (figure III.13), except that the network analyzer is not used for ringdowns. Instead the two tones required for the first excitation step are generated by the microwave source: the source is set to "amplitude modulation" mode, the carrier frequency is set to the lower electromechanical sideband, and the modulation frequency is set to Ω_m such that one of the modulation sidebands is resonant with the cavity. During the readout phase, the microwave field amplitude is demodulated around the frequency ω_c by the signal analyzer and the slowly varying quadratures X(t) and Y (t) are extracted in a similar way than what was explained in section II.4.c for the room

temperature ringdowns. Let's note that there is no well defined phase relationship between the source and the signal analyzer, such that the phase of the demodulated signal varies from realization to realization of the experiment. However, given the large amplitude of the mechanical excitation, the signal-to-noise ratio is sufficient with a single-shot realization of the experiment, and there is no need to average several traces together.

Experimental results A typical experimental result is presented in figure IV.5. This result was obtain on sample BM2 : the amplitude decay allows to retrieve the loss rate, while the phase variation of the signal allows to correct the mechanical frequency estimation. Similarly to the OMIT experiments described above, we can then perform ringdown series, as shown in figure IV.6, where the readout power is varied and the linewidth is extracted by fitting the different ringdowns. Fitting this curve to the same model ($\Gamma = \Gamma_{\mathrm{m}}(1 + \xi P)$, where P is the input power), we are also able to extract the intrinsic linewidth of the resonator, and the power required to have a cooperativity of 1, and therefore the cooperativity as a function of the input source power. In this particular instance, we find the linewidth of ~ 2.1 mHz corresponds to a Q-factor of $\sim 3.2 \times 10^8$, a nearly two orders of magnitude improvement compared to room temperature measurements. In agreement with other experimental observations performed in Delft [YCS15], we have noticed a dramatic improvement between 330 mK and 10 mK, most of the measured quality factors exceeding 50 millions (we typically measured the first 4 mechanical modes of the membranes with this method).

Discussion While the ringdown method may seem to bring a redundant information compared to the OMIT experiment, they are in fact complementary. In particular, OMIT is useful to find the mechanical frequency when it is not precisely known in advance. Indeed, the amplitude of the OMIT peak is equal to one at high cooperativity, and its linewidth is large, making it very easy to notice while sweeping a large range of possible mechanical frequencies. Then, reducing the power of the pump gradually around the assumed mechanical frequency allows to gain more precision. At low power, however, the use of the OMIT technique is getting more tedious: as explained above, the probe sweep speed needs to be slower than the decay rate of the mechanical oscillator in order to avoid a ringdown during the OMIT, which makes the fit of a Lorentzian quite complex. Therefore, when the mechanical frequency is well inferred by this technique, it is usually more efficient to perform ringdown measurements at low power. Interestingly, those measurements are also able to correct the mechanical frequency estimation, by retrieving the phase of the data. This is particularly useful when this frequency is showing some slow and unpredictable drifts of more than one mechanical linewidth, a situation that is more likely to happen when the mechanical linewidth is close to its intrinsic linewidth.

We have used the characterization methods described above to characterize various samples. Furthermore, as we gathered more information about the fabricated samples, we have gradually improved the design and fabrication techniques. Some of these improvements are described in the following sections.

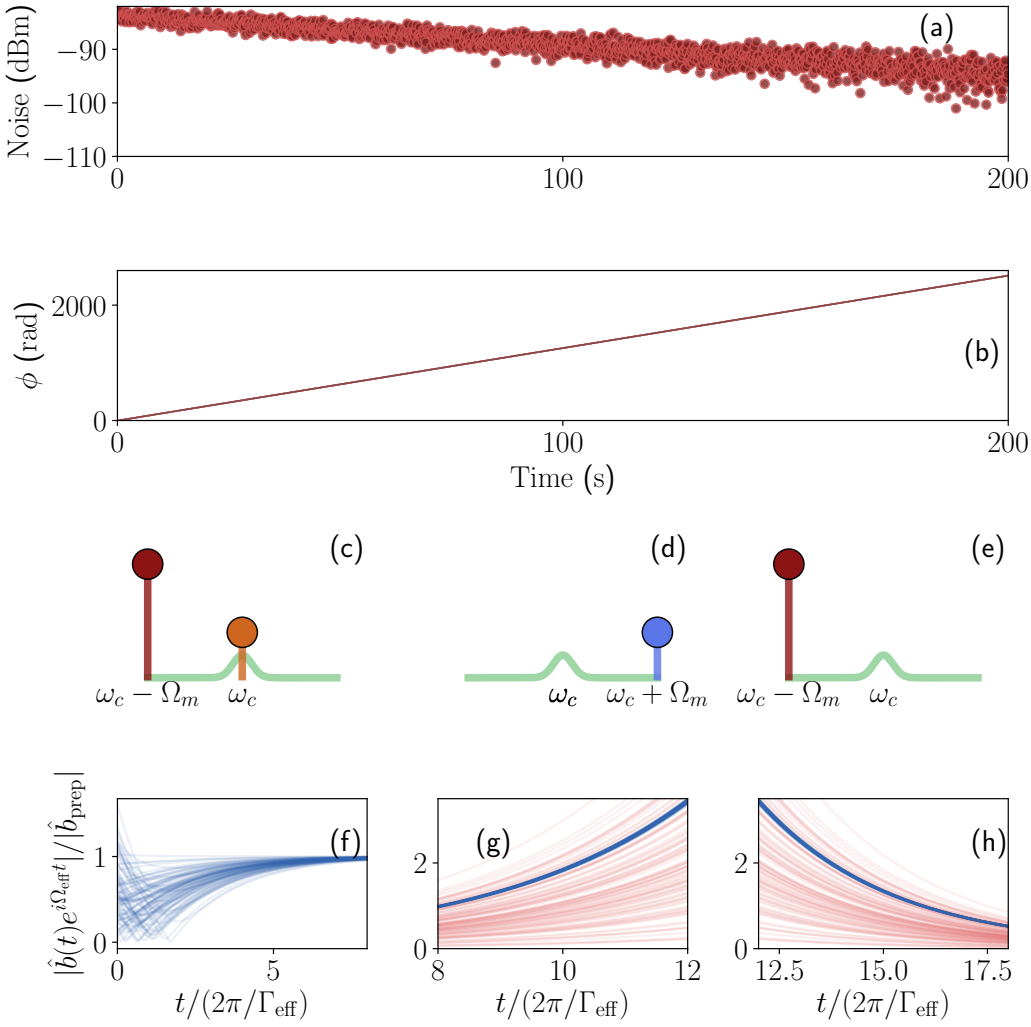

Figure IV.5: (top) Experimental result for a ringdown measurement, showing the exponential decay of the amplitude demodulated noise (a), here at a power sufficiently low to avoid any back action.(b) Argument of the amplitude demodulated noise. ((c) (d) and (e)) Sequence used for a ringdown, in the Fourier space. (bottom line) temporal evolution of the amplitude of the anihilation operator $\hat{b}$ for several randomly drawn initial conditions representing a thermal state. (f) : the oscillator is driven by a pump on the red sideband, and an internally generated modulation sideband detuned from the cavity by the mechanical frequency $\Omega_{\rm m}$. We extract the amplitude of the noise at the cavity frequency using a signal analyzer, with an AM demodulation at the pump frequency. (g) The resonator's motion is amplified using a *blue-detuned* sideband of the same pump. (h) We set up a red detuned pump and we retrieve the exponential decay of the two quadratures X(t) and Y(t) of the mechanical noise upconverted in the microwave domain through the optomechanical interaction and demodulated in a signal analyzer. On the bottom line, in red are presented the same trajectories without performing the first step of the sequence.

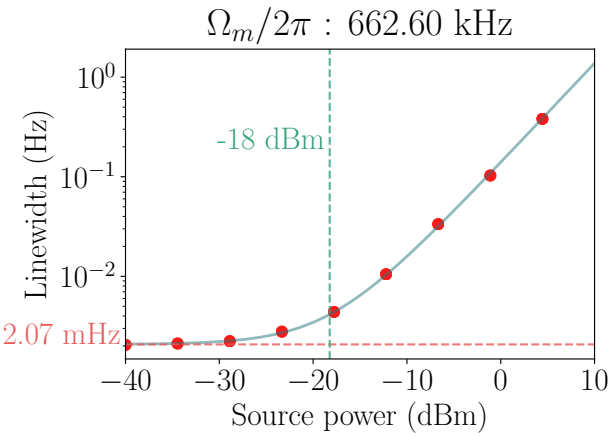

Figure IV.6: Ringdown serie made on the resonator BM2 while varying the readout power and extracting the linewidth. Raw data are circular red dots, while a fit (in blue) allows two parameters to be extracted : the intrinsic linewidth and the power required for the cooperativity to be equal to 1.

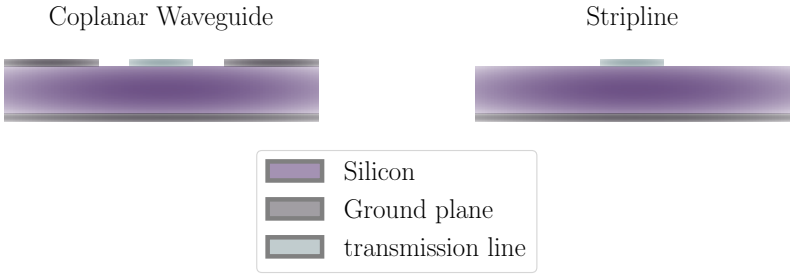

Figure IV.7: Principle of a Coplanar Waveguide (left) and a Stripline (right) transmission line

IV.2: Optimization

In this section we present the main optimization steps of the microwave cavity.

IV.2.a: From A1 to BM2

As explained in the previous chapter, following our inability to measure optomechanical coupling with the design A1, we developed a different coupling scheme, based on electrostatic coupling with a metallized membrane used as a moving electrode in the capacitive part of the circuit. This design is denoted by BM2 (see figure IV.8). In this design, a capacitive element is composed of two metallic pads brought directly below the membrane metallic pad. The inductor consists in a meander placed far away from the capacitor. Similarly to the design A1, the membrane motion induces a shift of the circuit capacitance, and thus of its resonance frequency.

IV.2.b: From coplanar waveguide to stripline

The first design implementing the electrostatic coupling was coupled to a coplanar waveguide, whose principle is presented in figure IV.7 (left): a central conductor sits on a (silicon) dielectric insulator. Two ground planes surround it at a constant distance. The main problem caused by this ground plane is that it needs to be very large to be properly defined, and that it prevents from overetching silicon on a large area (which is required, for a dust not to increase the distance between the two chips). Furthermore, to avoid spurious modes, the two parts of the ground plane should be at the same potential. This is usually ensured by "bridge" wirebonds [JWYY18, YBE$^+$11, LEBB12]. However, this solution does not work in our case, since wirebounds would collide with the membrane chip located in the immediate proximity of the microwave sample. As a result, the two halves of the ground plane, on either part of the waveguide were only loosely connected with each other in the outermost part of the sample. This led to a number of spurious "waveguide" modes, appearing as random peaks in figure IV.9 (a) and (b). To solve this issue, we switched the coupling line from a coplanar waveguide to a stripline (see figure IV.7). In this configuration, the ground plane is on the back side of the chip, such that the field lies mostly in the silicon. As can be seen in figure IV.9 (a) and (c), it suppressed all the spurious modes appearing in the previous design.

IV.2.c: From the "hanger" configuration to the reflection configuration

The coupling between the coplanar waveguide and the resonator was first made in a "hanger" geometry, discussed in section I.3.a.i. Although this configuration allows to couple several resonators at different frequencies on the same line (see for instance figure IV.2), it comes with the flaw of having an unmeasured port: half of the signal that comes out of the resonator is scattered in the mode propagating towards the input port, which is not measured by the output line. As a result, all this information is lost. We modified the coupling scheme from a "hanger" configuration to a reflection configuration. In a reflection configuration, only one port of the sample box is wirebounded

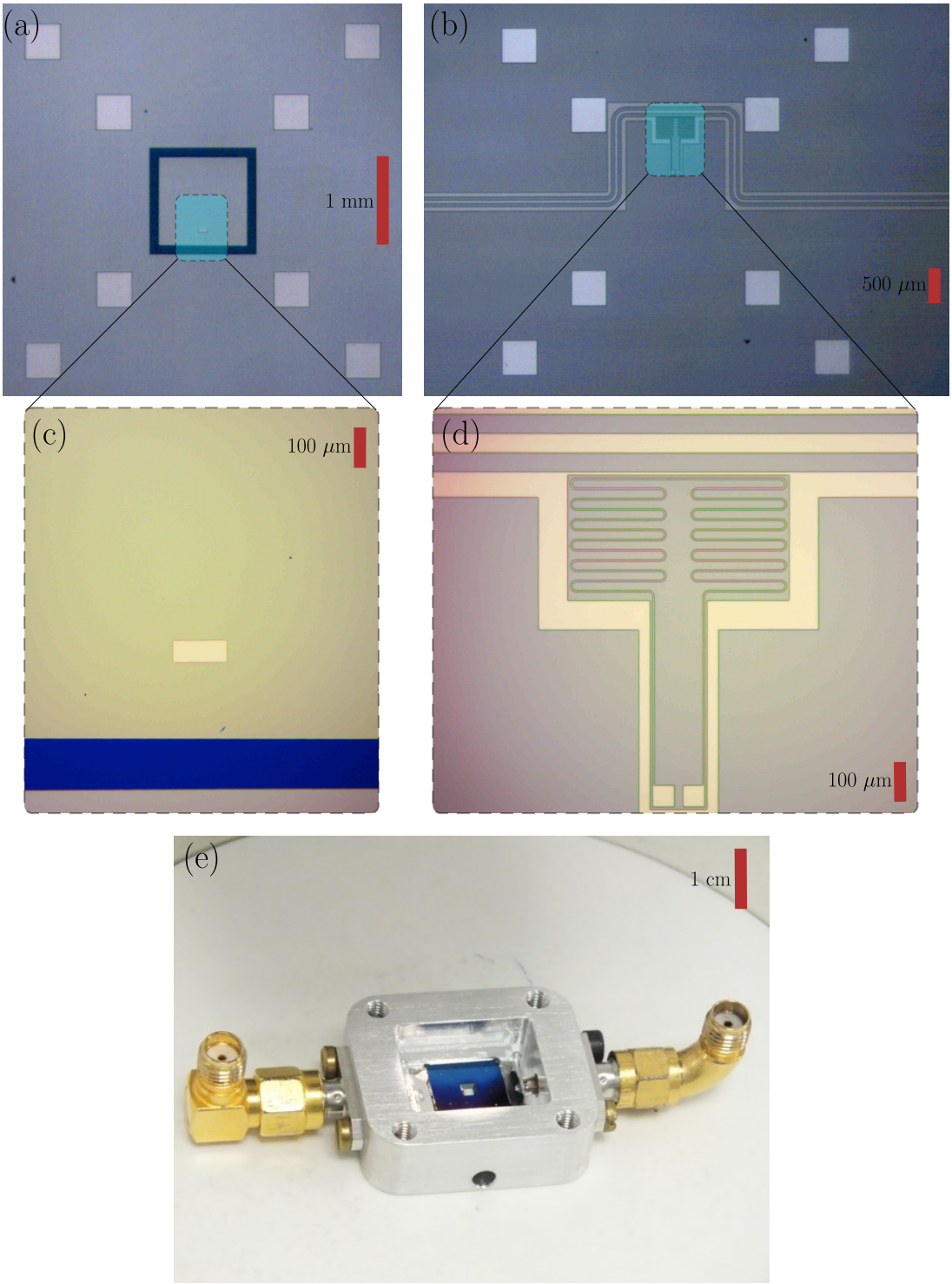

Figure IV.8: Photographs of the microwave sample. (a) large photo of the membrane sample. (b) large photo of the microwave sample. (c) zoom on the metallic pad of the membrane. (d) zoom on the microwave resonator. (e) stamped and wirebounded sample ready for being cooled down.

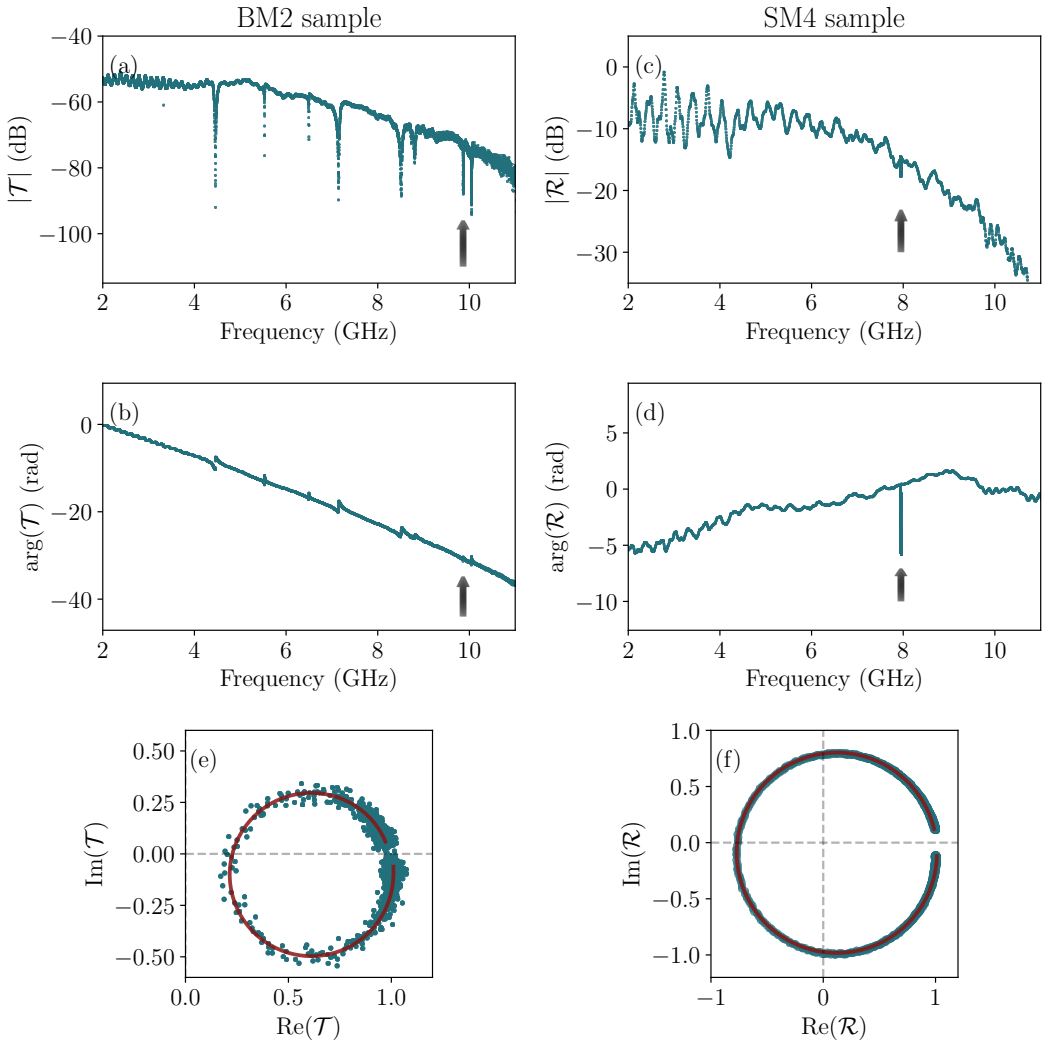

Figure IV.9: Comparizon of the large VNA scans, showing the amplitude (top) and angle (bottom) of the reflection (after design optimization, on the right) or transmission (before design optimization, on the left) of the sample. The angular drift is due to a delay corresponding to the time a signal needs to travel through he whole transmission lines. The resonance frequency is each time indicated with a black arrow. (e) Smith chart of the data close to the resonance for a resonator before design optimization. Data are represented by blue dots and a fit is represented in red. The extracted parameters are $\omega_c/2\pi \approx 9.86$ GHz, $\eta \approx 0.79$, $\kappa/2\pi \approx 792$ kHz, and $\kappa_0/2\pi \approx 166$ kHz. (f) Smith chart of the data close to the resonance of a resonator after design optimization. Data are represented by blue dots and a fit is represented in red. The extracted parameters are $\omega_c/2\pi \approx 7.95$ GHz, $\eta \approx 0.89$, $\kappa/2\pi \approx 1.36$ MHz, and $\kappa_0/2\pi \approx 150$ kHz.

to the sample and connected to the input line of the cryostat. A directional coupler and a circulator are used for ensuring the reflected signal to follow the output line. The corresponding reflection is given by eq.I.3.5. In this configuration, no signal is lost. As a consequence, the radius of the circle drawn by the resonance in the complex plane is a factor 2 larger than the one of a similar resonator in a hanger configuration (see figure IV.9 (e) and (f)).

IV.2.d: From a meander inductor to a circular wire inductor

For debugging purposes, we temporarily designed the circuit in such a way that the resonance frequency approximately spans the accessible measurement range (5 to 10 GHz) as the membrane distance varies from ~ 100 nm, to $+\infty$. In this way, one can expect to observe a measurable microwave resonance over the whole range of possible membrane distances. Very importantly, this allows to witness a resonance in a microwave cavity even in the absence of a metallized moving membrane.

Moreover, we have decided to switch from a meander-shaped inductor to a large (~ 2 mm diameter) circular inductor. We expect this geometry to minimize the stray capacitance for a given value of the inductance. This design, named SM4, was carefully simulated using Sonnet, following the same protocol than for the previous designs (see section III.1.c for further details). The circular inductor has a value $L \sim 6.1$ nH, more than a factor 2 larger than the value of the meander inductor used in BM2. On the other hand, the parasitic capacitance $C_{0L} \sim 53$ fF, is only multiplied by a factor ~ 1.5 compared to BM2. These values lead to a self-resonance $\omega_l = 1/\sqrt{LC_{0L}} \sim 2\pi \times 8.8$ GHz (see Fig. IV.11). As desired, the resonance frequency varies in the interval [4.25 GHz to 7.87 GHz] when the membrane distance is varied between 100 nm and $+\infty$ (see figure IV.12).

Conclusion

In this chapter we showed that we were able to probe the motion of the mechanical resonators presented in chapter II by interfacing them with the microwave cavities described in chapter III. Although the presented method imposed the metallization of the membranes, we experimentally demonstrated exceptionally high quality factors at low temperature (> 300 millions), which paves the way towards the use of the optical field to cool down the mechanical resonator, which will be presented in the following chapter.

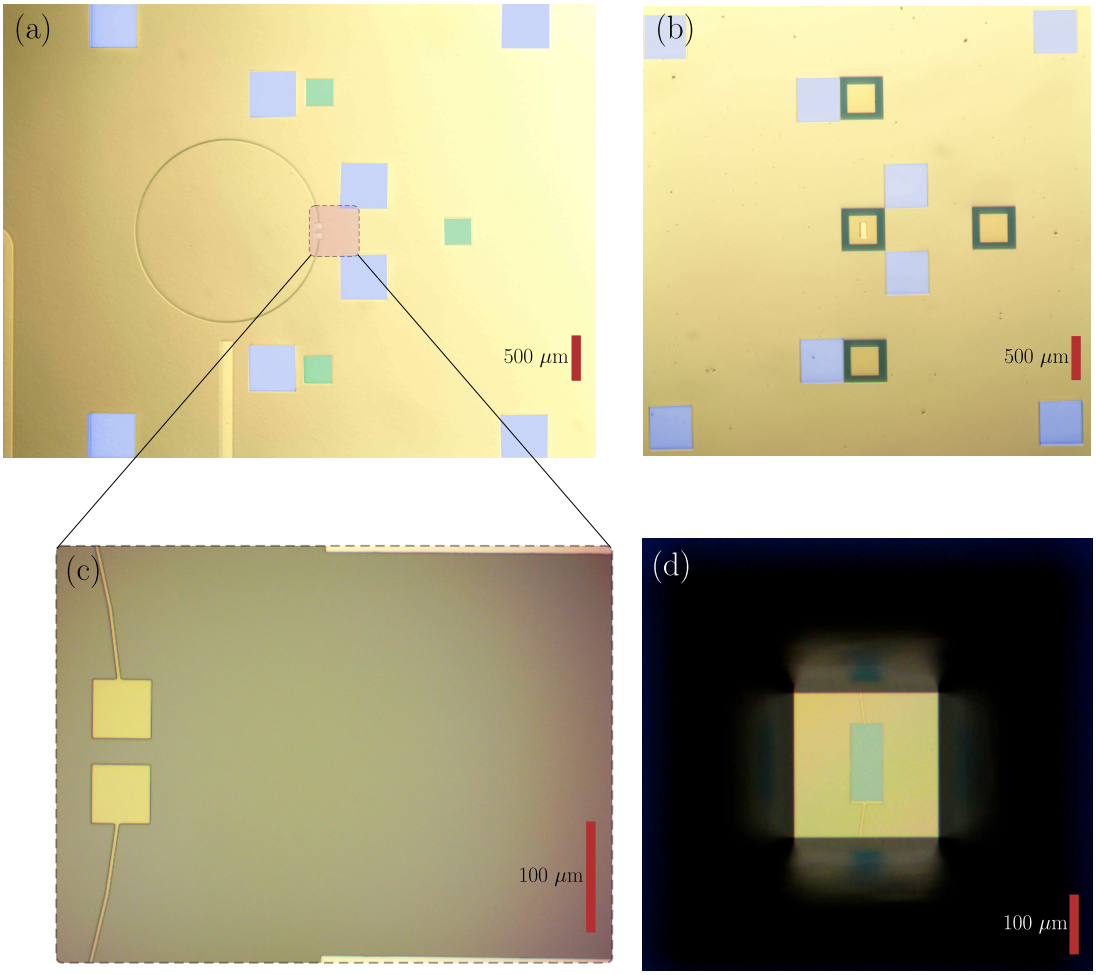

Figure IV.10: Photographs of the SM4 sample. (a) large photo of the microwave sample. False blue color has been used to highlight the 8 Aluminum spacers, and false green color has been used for highlighting the three areas that were used for distance measurement (b) large photo of the membrane sample. False blue color has been used to highlight the 8 Aluminum spacers positions, supposed to be at the same height as the metallic pad of the membrane (c) zoom on the capacitive part of the microwave circuit. (d) pictures taken after stamping, from above the chip assembly.

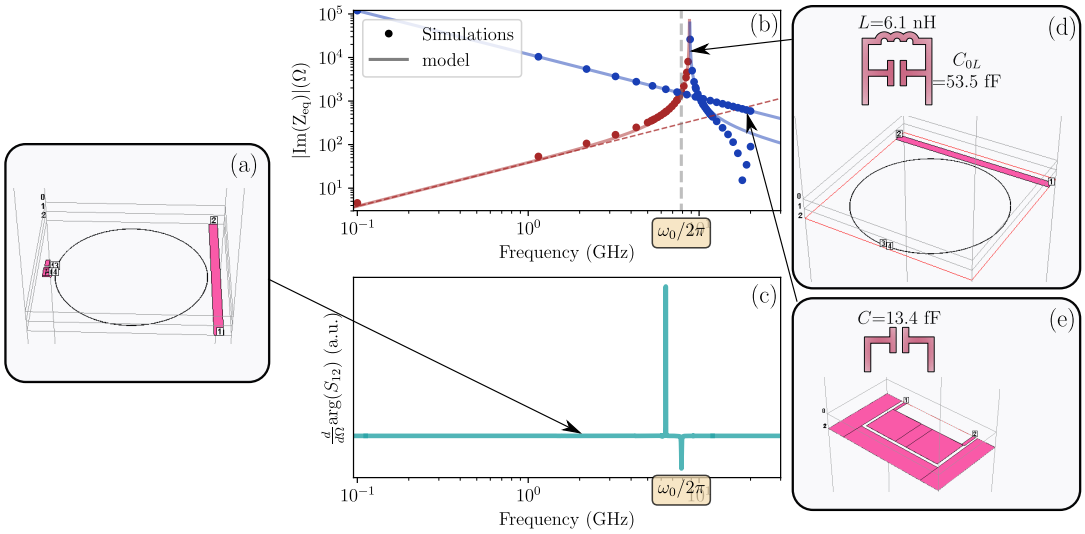

Figure IV.11: Same data than for the fig. III.7, but for the SM4 design.

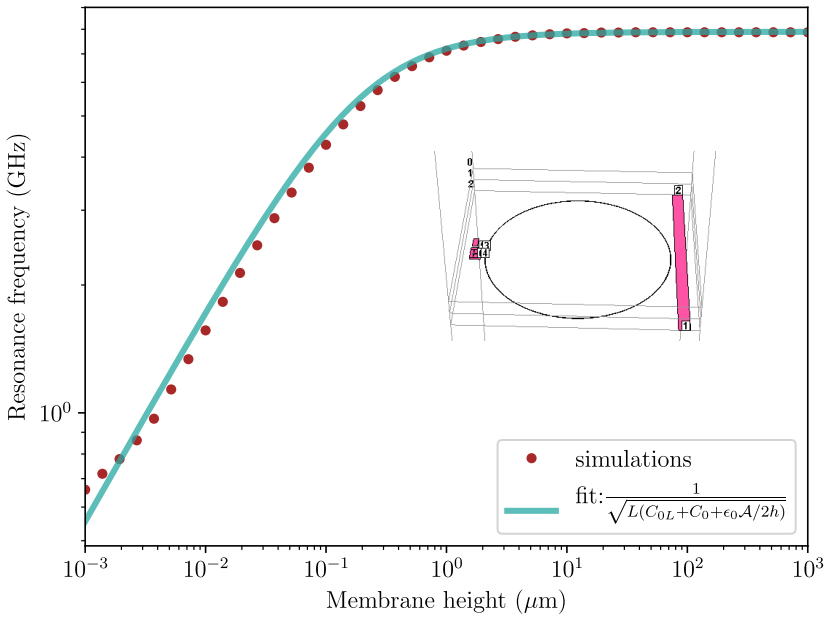

Figure IV.12: Membrane height dependance of the frequency of the SM4 design (the simulated design is sketched in inset). See the caption of figure III.9 for further details.

Chapter V: Cooling a mechanical oscillator close to its quantum ground state

One of the prerequisites of most quantum mechanics experiments involving harmonic oscillators such as the mechanical oscillators presented in the previous chapters is to operate in a regime where the occupation number of those oscillators are small compared to 1. Indeed, in this regime, the predictions of quantum mechanics differ from the classical physics. While the latter describes a mechanical oscillator's position variance Δx^2 that evolves linearly with the temperature and therefore can be arbitrarily small, the former stands that respecting the Heisenberg inequality imposes a minimum position variance (see figure I.1). Consequently, reaching this regime allows to prove to some extents the validity of quantum mechanics at low temperature. Furthermore, this regime opens the path towards the exploitation of exquisite properties of mechanical oscillators. Among them is the relatively long time this system can evolve without interacting with any thermal phonons. For example, patterned membranes modes has been observed exhibiting quality factors of the order of 1×10^9 for mechanical frequency close to 1 MHz [CRMS20]. Thermalized with the baseplate of a typical dilution fridge reaching temperatures of approximately 10mK, this system can live for approximately $\sim$ 5 s with no interactions with its environment. This incredibly long time makes these kind of devices a good candidate for several applications, including for instance quantum memories[SE15]. Another incredible property exhibited by mechanical oscillators in this regime is its mesoscopic scale with a very large number of atoms. As such, it represents an intermediate scale between individual atoms where quantum mechanics is routinely observed and macroscopic objects almost exclusively governed by classical physics, and therefore is an ideal platform for exploring the complex and not well known decoherence mechanisms separating those two regimes. Finally, as a large system experiencing gravity, it can be an ideal platform for studying the quantum mechanical description of gravity[BBG$^+$19].

The low frequency of the mechanical oscillators makes the inequality $k_B T < \hbar\omega$, signature of being closed to the ground state, hard to achieve. For instance, for a $\omega = 2\pi \times 1$MHz the resonator needs to be cooled down to a temperature below 50μK.

Reaching such a low temperature usually requires to combine direct cryogenic techniques and alternative cooling effects. Alternatively, the coupling to an external optical degree of freedom, as described in the previous chapter, allows to benefit from the high frequency and therefore low occupation of this optical mode to actively cool down the mechanical oscillator. The first experimental observation of a mechanical oscillator in its motional ground state has been performed in 2011[TdL$^+$11].

In this chapter, we first present the sideband cooling result from the optomechanical cavity described in the previous chapter. Then we present two optimizations that will in principle pave the way towards reaching the motional ground state. The first is aiming at increasing the coupling factor, and the second at improving its isolation from the mechanical noise of the cryostat.

V.1: Resolved sideband cooling

To approach the mechanical ground state, we perform a sideband cooling experiment, as detailed in section I.4.b. A strong detuned pump ($\Delta_c = -\Omega_\mathrm{m}$) is used to enhance the anti-Stokes process in the optomechanical linearized hamiltonian, resulting in the scattering of phonons into photons in the microwave cavity, which has a much smaller lifetime, and ideally, an environmental occupation close to 0. If we denote n_m the mechanical occupation number, the final occupation number $n_\mathrm{m,f}$ is given by:

$$n_\mathrm{m,f} = \frac{n_\mathrm{m}}{1+C}, \tag{V.1.1}$$

where C is the cooperativity. The occupation number of the resonator is directly related to the total displacement noise of the resonator, that is to say to the full area of $S^\mathrm{meas}_{\hat{x}\hat{x}}$. The experimental difficulty is to precisely know the conversion factor between the measured microwave spectrum and the inferred mechanical spectrum. Therefore, the measured power has to be divided by the optomechanical gain:

$$\mathcal{S}^\mathrm{meas}_{\hat{x}\hat{x}}/(\Gamma_\mathrm{m} x^2_\mathrm{ZPF}) = \mathcal{S}_{\hat{X}\hat{X}}\frac{4}{G\eta C\Gamma_\mathrm{m}}, \tag{V.1.2}$$

where G is the gain of the amplification chain, calibrated in section III.2.b.ii, and where $\mathcal{S}_{\hat{X}\hat{X}}$ is the measured optical power spectrum. The following measurements were conducted in the ^{3}He fridge (see figure V.1), at $\sim$ 330mK, with the sample presented in figure IV.8. The parameters are the following:

Mechanical resonator		Microwave cavity	
$\Omega_\mathrm{m}/2\pi$	481 kHz	$\omega_c/2\pi$	9.82 GHz
$\Gamma_\mathrm{m}/2\pi$	83 mHz	$\kappa/2\pi$	792 kHz
width of the membrane	1 mm	$\Delta_c/2\pi$	-481 kHz
thickness of the membrane	100 nm	η	0.79
		T_base	330 mK
$g_0/2\pi$		0.6 Hz	

We observe the linear increase of the linewidth of the Lorentzian spectrum with the pump power, accounting for the smaller phonon lifetime due to the optomechanical interaction. To compute the area under those peaks, we fit the spectrum with a Voigt

profile which corresponds to the convolution of a Gaussian function and a Lorentzian function. Indeed the expected profile is the Lorentzian mechanical response of the resonator monitored by a signal analyzer with a Gaussian filter of a fixed bandwidth. Usually the bandwidth of the analyzer can be ignored but in our case the linewidth of the mechanical resonance is small ($\sim$ 83 mHz) compared to the resolution bandwidth (500 mHz) of the measurement. The fitting function has 4 degrees of freedom, $\Omega_{\rm m}/2\pi$, $\Gamma_{\rm m}/2\pi$, the height of the peak, plus a flat noise level. When the pump power is increased from -50 dBm to 5 dBm the linewidth of the Brownian motion is increased while the height is reduced as expected. The overall area under the peak of noise is decreased, corresponding to a reduction of the occupation number from $n \sim 65000$ ($T \sim 1.5$ K) to a minimum $n_{\rm m,f}$ =274 ($T \sim 5$ mK). This last value is still far from the ground state and two problems precluded us from reaching this milestone. The first one is the relatively low value of g_0. A successful technique to increase it will be described in the previous section. The second one is that we measured a mechanical noise that was not Brownian limited, due to mechanical vibrations from our cryostat. As a result, the mechanical mode effective temperature at low cooperativity was still significantly higher than the baseplate temperature (1.5 K$\gg$ 330 mK). In the ^{3}He cryostat, we identify the cryostat mechanical vibrations as the result of 1K pot helium boiling. A successful technique to mitigate this extra mechanical noise will be presented in section V.2.c.

V.2: Experimental optimization

V.2.a: Phase noise of the source

We already mentioned in section III.2.b.ii that the maximum pump power we can inject in the cryostat is limited by its cooling power. Indeed, the noise thermalization imposes that most of the input power should be dissipated in the different cyogenic stages. This sets a maximum power ($\sim$ 5 dBm at the input of the cryostat) that can be injected and as a consequence limits the cooperativity for a given device.

Another cause of limitation for the input power an experiment can use is the quality of the microwave source. Indeed, any source carries a classical noise whose amplitude is proportional to the input power. This noise is a measure of the discrepancy between the signal generated and a perfect sinusoidal signal. Such spurious noise can be seen in figure V.2, where a direct measurement of the microwave source noise is performed with a signal analyzer. At fixed power, there is an excess of classical noise close to the pump, but this noise reaches an asymptotic value far away from the pump. Although at the frequency those experiments were performed the asymptotic value is not perfectly reached, there is not that much noise reduction that can be provided by an increase in frequency.

V.2.b: Optimization of the optomechanical coupling

The cooling factor we are able to provide to a mechanical oscillator using resolved sideband cooling is $1 + C$, C being the cooperativity. While the latter is proportional to the optical intensity used to pump the system, several problems precludes the use

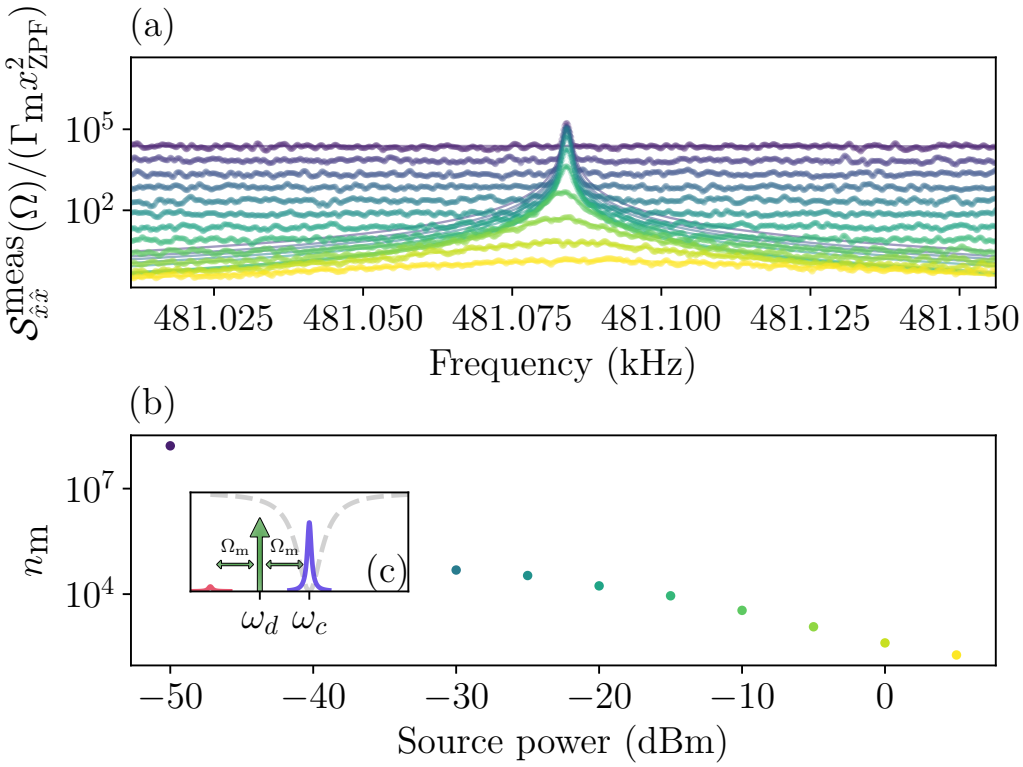

Figure V.1: Sideband cooling experiment results. (a) Measured mechanical spectrum inferred from the measured microwave spectrum, for different powers. Each time, data are plotted in dots while a Voigt profile fit is plotted as a line (b) Mechanical occupation, extracted from the area under the peak for each plot in figure (a). The minimal occupation is ~ 274, while the maximal occupation is ~ 65000. (c) Schematic of the experiment. The light grey dashed line represents the transmission of the cavity, the arrow represents the drive at an angular frequency $\omega_d = \omega_c - \Omega_{\mathrm{m}}$. The two sidebands are represented as Lorentzian peaks.

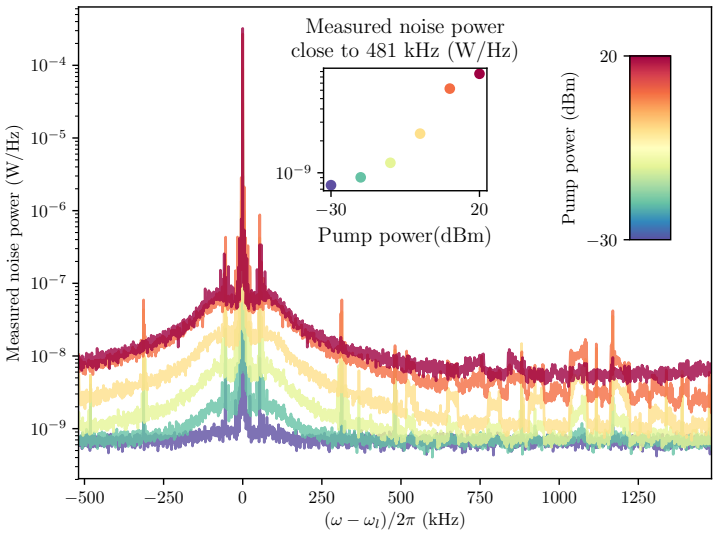

Figure V.2: Direct measurement, for different pump powers, of the noise of the microwave source using a signal analyzer. Inset: noise value around 481 kHz of positive detuning (one of the mode of BM2) versus the power

of an infinite optical intensity (see section III.2.b.ii). Alternatively, the cooperativity exhibits a squared dependence in another parameter, g_0, that needs to be measured and optimized.

V.2.b.i Optomechanical coupling measurement

The informations gathered by the experiments described in the previous chapter are however not sufficient to measure g_0. Indeed, the knowledge of the cooperativity $C = \frac{4g_0^2|\alpha|^2}{\kappa\Gamma_\mathrm{m}}$, along with the optical (mechanical) linewidths κ (Γ_m) is not sufficient to unambiguously determine the values of g_0 and $|\alpha|$. If $|\alpha|$ can be determined from the calibrated measure of the amplification gain G presented in section III.2.b.ii, this gain can change for instance when a cable is replaced or an RF component in introduces. Therefore, it is always useful to dispose of an indepandant measurement of g_0. The method we propose is the following: we experimentally compare the Brownian motion of our resonator to a well known calibration tone[GSA+10] generated by a frequency modulation of our microwave source, which is tuned on the red sideband.

Indeed, a small (amplitude $\delta_f \ll \Omega_\mathrm{m}/2\pi$) frequency modulation of our source at a frequency $\Omega_\mathrm{mod}/2\pi$ will generate a signal:

$$\hat{a}_\mathrm{in}(t) = \hat{a}_\mathrm{in}\left(1 - \frac{i\pi\delta_f}{\Omega_\mathrm{m}}\left(e^{i\Omega_\mathrm{mod}t} + e^{-i\Omega_\mathrm{mod}t}\right)\right), \tag{V.2.1}$$

and we can then compute the spectrums $S_{PP}(\Omega)$ with $P \overset{\mathrm{def}}{=} \hbar\omega_l|\hat{a}_\mathrm{out}|^2$ for both the modulation and the Brownian motion transducted by the optomechanical setup. Interestingly, although both processes are not equivalent, we find the same proportionality con-

stant between the output and input noise, as long as we fulfill $\kappa \gg |\Omega_{\rm mod} - \Omega_{\rm m}| \gg \Gamma_{\rm m}$, in the case of an amplitude demodulation of the output power with a signal analyzer:

$$S_{PP}(|\Omega - \Omega_{\rm m}| \ll \kappa) \approx P_{\rm in}^2 \mathcal{K}(\Omega_{\rm m}) \mathcal{F}(\Omega) \circledast \Big\{ (2\pi\delta_f/\Omega_{\rm mod})^2 \delta(\Omega - \Omega_{\rm mod}) \tag{V.2.2}$$

$$+ (G/\Omega_{\rm m})^2 \mathcal{S}^s_{\hat{x}\hat{x}}(\Omega) \Big\}, \tag{V.2.3}$$

with $\mathcal{K}(\Omega_{\rm m})$ a dimentionless number depending on the the gains and attenuations of the microwave lines as well as on the cavity parameters, $P_{\rm in} \overset{\rm def}{=} \hbar\omega_l |\hat{a}_{\rm in}|^2$, $\circledast$ the convolution product, $\mathcal{F}$ the filter function of our signal analyzer, which has a centered Gaussian profile with a known equivalent noise bandwidth $ENBW$, and $\mathcal{S}^s_{\hat{x}\hat{x}}(\Omega)$ is the symmetrized spectrum of the mechanical resonator. The measured spectrum $S_{PP}(|\Omega - \Omega_{\rm m}| \ll \kappa)$ then presents two peaks: the first one, due to the phase modulation is a Gaussian of width $ENBW$ and area $\mathcal{A}_{\rm mod} \overset{\rm def}{=} P_{\rm in}^2 \mathcal{K}(\Omega_{\rm m})(2\pi\delta_f/\Omega_{\rm mod})^2$. The second one, due to the Brownian motion of the mechanical resonator, has a Voigt profile, convolution of a Lorentzian and a Gaussian for the Brownian motion of the mechanical resonator, with an area $\mathcal{A}_{\rm mech} \overset{\rm def}{=} P_{\rm in}^2 \mathcal{K}(\Omega_{\rm m}) g_0^2 \times 4n_{\rm B}/\Omega_{\rm m}^2$. Finally we have the formula:

$$g_0^2 = \frac{\mathcal{A}_{\rm mech}}{\mathcal{A}_{\rm mod}} \frac{\pi^2 \delta_f^2}{n_{\rm B}}. \tag{V.2.4}$$

While this may seem to be enough for a measurement of g_0, an experimental difficulty lies in the mechanical noise source. As explained in section V.1, the Brownian peak we measure is not only due to the natural thermal environment of the mechanical resonator, but mainly to another mechanical noise coming from the boiling of ^{4}He in the 1KPot. Luckily, we managed to temporarily shut down this noise source by replacing the pump on the 1K pot by a balloon of ^{4}He. While this technique worked perfectly fine for this measurement, it cannot be routinely exported to long experiment since after a certain amount of time (in the order of 15 minutes in our case), the 1KPot is out of liquid helium and the temperature of the cryostat rises significantly. In particular, the sideband cooling experiment described in section V.1 cannot benefit from this trick, since long integration times with stable parameters are needed at each pump power. To be sure that we are indeed measuring Brownian motion in those conditions, we varied the base temperature of our cryostat from 400 to 800 mK. At each temperature, we stabilized the temperature using a PID, and we took in average ~ 60 spectrums, each with 3 averages and a bandwidth of 1 Hz. We then extract g_0 by performing a linear fit on the temperature dependence of the ratios of the curves (see figure V.3). The measured value for g_0 of this sample was ~ 0.6 Hz.

V.2.b.ii Measurement of the distance between the membrane and the capacitor

When considering the design presented in section III.1.c, it appears that g_0 can be increased by reducing the distance h between the two capacitor plates. The system developed to vary the distance h is described in the next section. In this section,

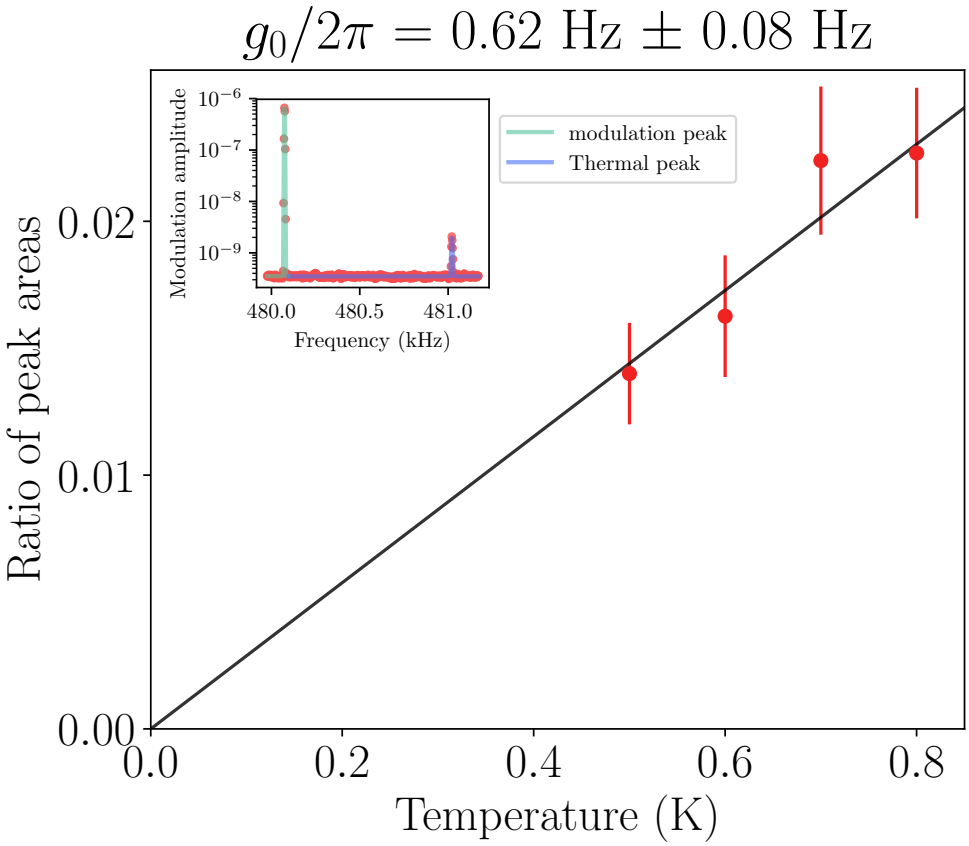

Figure V.3: Measurement of g_0 using a calibration peak, for the BM2 sample. The two measured peaks are shown in the inset for a temperature of 600 mK, with a modulation frequency $\Omega_{\mathrm{mod}}/2\pi = \Omega_{\mathrm{m}}/2\pi - 1$ kHz. The ratio of peak areas is plotted versus the base temperature of the cryostat, and a linear fit allows the measurement of g_0. The errorbars are computed using a bootstrap technique, with repeated measurements of the ratio of peak areas for each temperature.

we describe the techniques that we used to measure h. We performed two kinds of measurements. The first one is a qualitative measurement using a microscope objective: when the distance between the chips becomes comparable to the wavelength used for the illumination, the color is changing. Such a measurement allows to spot places where the two chips are stuck together, but also to see an angle between the two chips, and to detect the presence of a dust. The second one is a quantitative measurement using a Nanocalc thin film reflectometer. This device contains a broadband white light source, covering wavelengths from ~ 400 nm to ~ 1 μm. Using an optical fiber, it sheds light with a normal incidence on a small spot of the sample. The reflected light is is fed back into the same fiber and then spectrally resolved by the reflectometer.

Let us consider a one-dimensional problem where a plane wave amplitude can be decomposed in a sum of a right-propagating term E_+ and a left propagating term E_-:

$$\mathrm{E}(z) \stackrel{\text{def}}{=} \mathrm{E}_+(z) + \mathrm{E}_-(z). \tag{V.2.5}$$

Two elements are modifying the values of those fields, as presented in figure V.4: the first one is an interface between two dielectrics, of optical indices n_1 and n_2. Taking the notations of the figure, we have:

$$\begin{pmatrix} \mathrm{E}_{+,1} \\ \mathrm{E}_{-,1} \end{pmatrix} = \frac{1}{t} \begin{pmatrix} 1 & r \\ r & 1 \end{pmatrix} \begin{pmatrix} \mathrm{E}_{+,2} \\ \mathrm{E}_{-,2} \end{pmatrix}, \tag{V.2.6}$$

where $t \stackrel{\text{def}}{=} \frac{2n_2}{n_1+n_2}$ and $r \stackrel{\text{def}}{=} \frac{n_2-n_1}{n_1+n_2}$ are the Fresnel coefficients. The second type of element is the propagation in a dielectric of thickness z_0 and of optical index n. We have:

$$\begin{pmatrix} \mathrm{E}_{+,1} \\ \mathrm{E}_{-,1} \end{pmatrix} = \begin{pmatrix} e^{iknz_0} & 0 \\ 0 & e^{-iknz_0} \end{pmatrix} \begin{pmatrix} \mathrm{E}_{+,2} \\ \mathrm{E}_{-,2} \end{pmatrix}. \tag{V.2.7}$$

The problem we are interested in consists in finding the reflection coefficient of a stack of dielectrics composed by a silicon nitride layer and a vacuum layer representing the gap between the membrane and the silicon, and a Niobium film (see figure V.4). Indeed, the description used here can be extended to the case of a metallic film for which we can measure the optical constants n and k. Quantitatively, we derive the value of $R \stackrel{\text{def}}{=} \left|\frac{\mathrm{E}_{-,1}}{\mathrm{E}_{+,1}}\right|^2$ by setting $\mathrm{E}_{-,2} = 0$.

This model fitted to the experimental data is shown on figure V.5, for which a very high distance (~ 1.9 μm) has been obtained. Note that to perform the distance measurements, one needs to be able to see through the membrane, so the region exactly under the metallic pad of the membrane cannot be measured. Furthermore, as explained in section III.3.a.ii and as can be seen in figure III.20, a few microns of silicon has been etched everywhere except on the resonator and coupling wires. Therefore, a distance measurement around the membrane is possible only above the part of the inductor wire that is below the liberated part of the membrane sample. This corresponds to a very small area, and the NanoCalc device is not precise enough to resolve such details. To circumvent this problem, we modified the two samples by adding three auxiliary square membranes, as shown in figure IV.10(b), at positions far enough from both the resonator and the coupling lines such that their behavior is not modified. On the microwave sample, the areas facing the liberated part of those membranes were not etched.

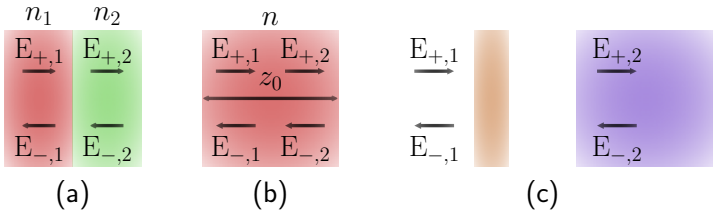

Figure V.4: Schematics of the model used to retrieve the chips distance from the measured reflection. (a) Interface between two dielectrics, with optical indices n_1 and n_2. (b) propagation inside a dielectric of optical index n and thickness z_0. (c) The problem to solve: a Silicon nitride membrane on top of a Niobium film

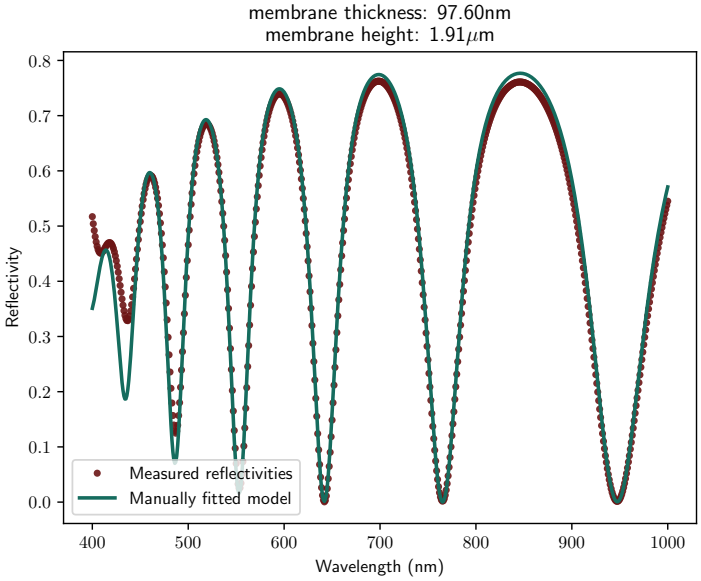

Figure V.5: Measured reflection for a wide range of wavelengths, and matching manual fit. The extracted membrane height is approximately 1.9 μm.

V.2.b.iii Increasing g_0 with the "pushing top"

To cool the resonator as much as possible, it is necessary to reach a cooperativity as high as possible. Even if the cooperativity is proportional to the input pump power, the limitation presented in the previous section precludes to reach an infinite cooperativity based solely on this parameter. It is therefore of utmost importance to design optomechanical cavities exhibiting a large g_0 value. To that end, we describe in this subsection an original technique that we called "pushing top".

In principle, for the designs used in this thesis, the thickness of the spacers should be proportional to the final distance between the two chips around the metallic pad of the membrane. However, due to the bending of the chips, which is not reproducible, the distance actually measured after a stamping is much higher (typically between ~ 600 nm and 3 μm). The use of a Directive Reactive Ion Etching (DRIE) machine has been reported to achieve lower values of h in a reproducible way [APP+14]. However, the unavailability of such machine in all cleanrooms of Paris and most cleanrooms of Paris suburban area pushed us to develop another approach: after the initial stamping (see section III.3.c), the top of the sample box is replaced by a modified one designed to mechanically push the membrane on the microwave sample, as represented in figure V.6. A large hole on the top allows to look at the sample during the pushing with a "Super Long Working Distance" microscope objective or a reflectometer to control the distance between the chips: it is important that the two electrodes of the capacitor do not come into contact with each other. In order to push, four copper tips, protected by a thin (~ 120 μm) piece of Kepton tape, are pressed against the back of the membrane chip. A set of four setscrews (in blue in figure V.6) are there to set up a limit on the position of the "pushing top". A set of four other screws (in green in figure V.6), mounted on a few turns of small springs, are here to push it.

The effect of a push on the distance between the chips is monitored using the reflectometry technique presented in the previous section. The effect of the pushing can be seen in figure V.7. Note that even a poor data quality can be used for extracting an estimate of the distance.

The effect of the pushing on the optomechanical system characteristics has been first measured by performing three cooldowns with increasing pushing strength, as shown in figure V.8. For each three membrane height, ringdown experiments(see section IV.1.b.ii) are performed to measure the mechanical linewidth of the membrane at different input power. As we see, the power required for a cooperativity of 1 (*i.e.* such that $\Gamma_{\text{eff}} = 2\Gamma_{\text{m}}$), is reduced as expected if g_0 is increased when the two chips are getting closer. Equivalently, for a given input power, the cooperativity is increased. Note that the mechanical quality factor is not reduced due to the pushing. As suggested by figure V.8, it even seem that the mechanical quality factor is increasing, but experimentally we found that it varies quite randomly between cooldowns, probably due to different dust contaminations or temperature cycles for instance.

A direct measurement of g_0 for a sample after being pushed can be seen in figure V.9. The protocol, described in section V.2.b.i, has been followed before and after an increase of pushing strength. We found and increase by a factor ~ 10 of $g_0/2\pi$, which goes from ~ 0.6 Hz to ~ 5.5 Hz.

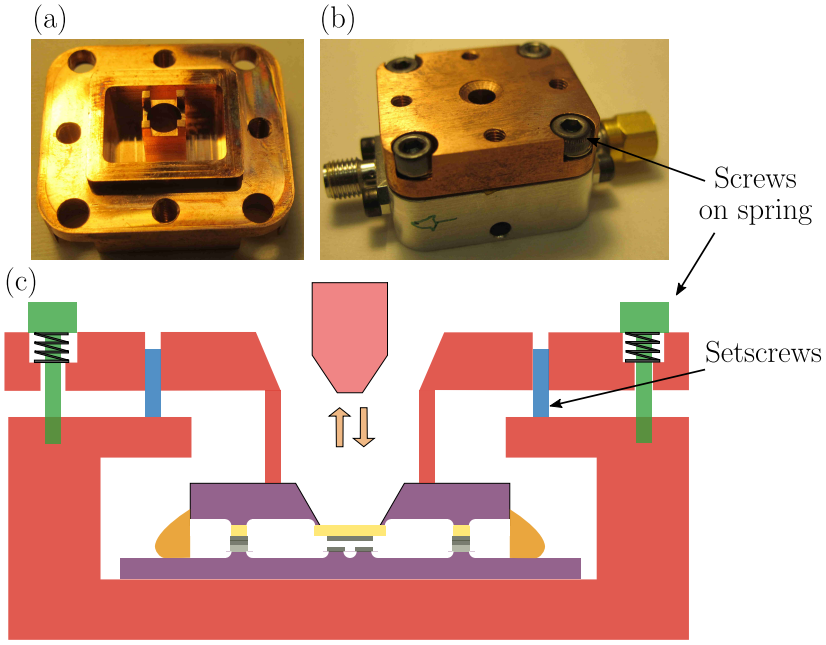

Figure V.6: (a) Picture of the pushing top (b) Picture of a closed sample box with pushing top (c) Scheme of the pushing technique to reduce the distance between the membrane and the microwave chip. The silicon is colored in purple, the copper in red, the silicon nitride in yellow, the Niobium and aluminum in dark and light grey, respectively. The epoxy glue is colored in orange. The set screws are presented in blue, while the pushing screws are presented in green.

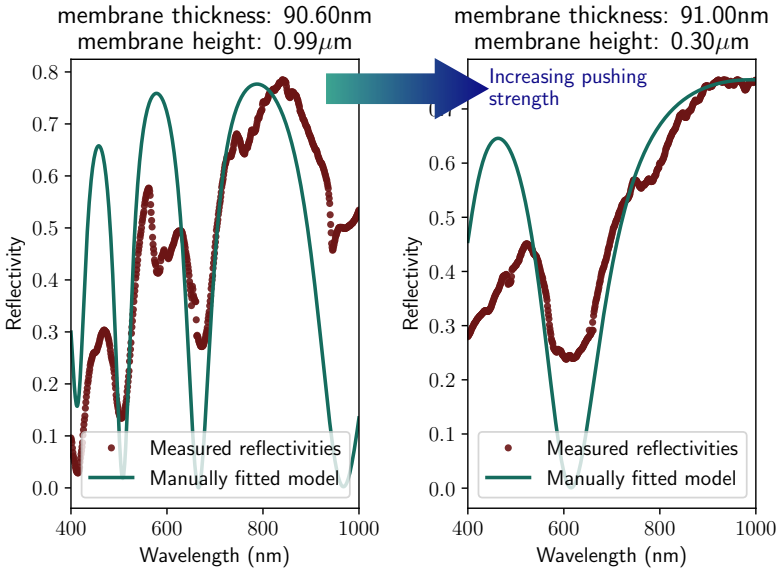

Figure V.7: Effect of the pushing top on the distance between two chips, measured using the refletometry technique described in section V.2.b.ii. Raw reflection is represented with dots, a manual fit is represented as a straight line. Left: before the push, the measured distance is ~ 1 μm. Right: after the push, the measured distance is ~ 300 nm.

V.2.c: Isolation of the mechanical system

To cool down the resonator and reach the quantum ground state, we need to eliminate or reduce all the sources of noise identified in section V.2.b.i. Otherwise, most of the sideband cooling will only serve at removing these extra noises and we will reach the technical limits of our setup before reaching the ground state as it was the case in the first attempt in section V.1. For example, in the latter, the extra mechanical noise from the 1KPot ^{4}He boiling set up an initial occupation of ~ 65000, which corresponds to an effective temperature of ~ 1.5 K. It is thus reasonable to assume that we would benefit from a factor of $\sim 1.5/0.33 \approx 4.5$ simply by using a mechanical isolation.

V.2.c.i Principle of the mechanical isolator

To passively isolate the sample from those spurious noise sources, we thus developed a simple mechanical isolator whose principle relies on the same idea than the attenuators used for instance by the gravitational wave community [Col05]. A simple model for this device consists in a unidimentional system in which the test mass to be isolated is represented by a point mass m at coordinate x_2 and is connected to a moving plate of coordinate x_1 with a spring/dissipator ensemble of stiffness k, relaxed length l_0 and dissipative coefficient α (see figure V.10). In the Fourier domain, the transfer function expressing the amplitude of $\tilde{x}_2(\Omega)$ as a function of the amplitude of $\tilde{x}_1(\Omega)$ reads:

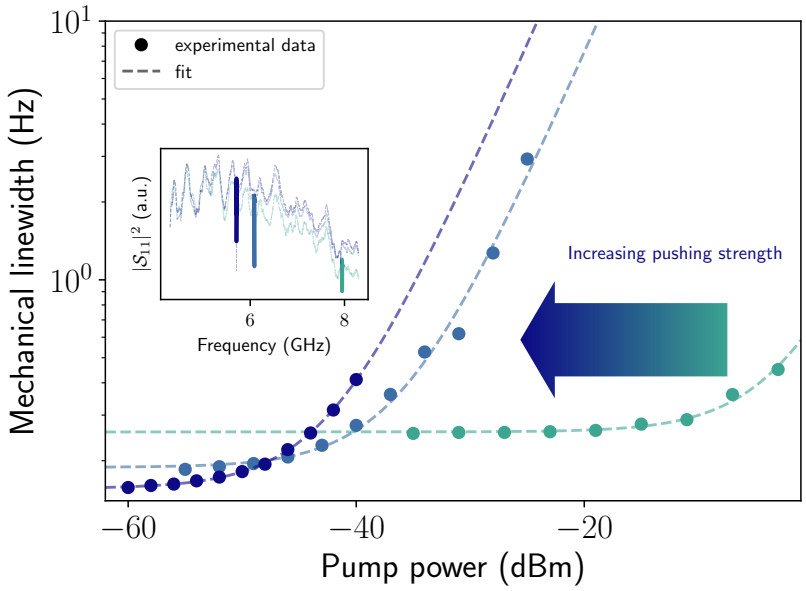

Figure V.8: Effect of the pushing top on the ringdown measurements presented in section IV.1.b.ii, for the SM4 sample. Three cooldowns have been made, each with a different pushing strength. For a given input pump power, the cooperativity is much higher each time the strength is increased. Inset: corresponding transmission of the microwave cavity probed by a VNA. The resonance is highlighted in blue. When the distance is reduced, the capacitance is increased and thus the frequency goes down.

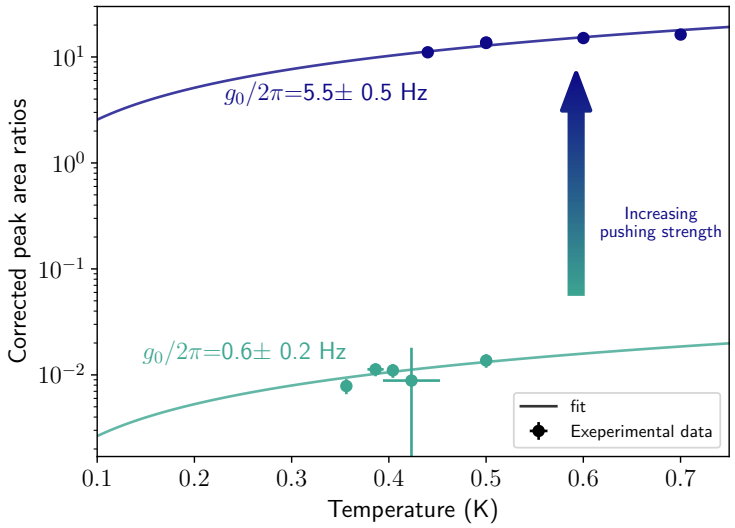

Figure V.9: Comparison of two g_0 measurements following the protocol described in section V.2.b.i, for the BM2 sample. Between the two cooldowns, the pushing strength has been increased.

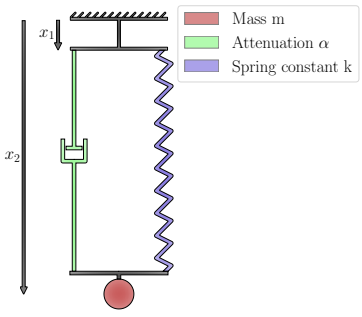

Figure V.10: Schematics of the isolator model

$$H(\Omega) \stackrel{\text{def}}{=} \frac{\tilde{x}_2(\Omega)}{\tilde{x}_1(\Omega)} = \frac{\Omega_0^2 + j\Omega\frac{\Omega_0}{Q}}{\Omega_0^2 - \Omega^2 + j\Omega\frac{\Omega_0}{Q}}, \tag{V.2.8}$$

where $\Omega_0 \stackrel{\text{def}}{=} \sqrt{\frac{k}{m}}$ is the angular resonance frequency of the system, while $Q \stackrel{\text{def}}{=} \frac{\Omega_0}{\Delta\Omega}$ is the quality factor of the resonator. In this last expression, $\Delta\Omega/2\pi$ is the linewidth of the resonance, that depends among other on the dissipative coefficient α. The result is the sum of a second order lowpass filter with a cutoff frequency $\Omega_0/2\pi$ and a second order bandpass filter with a frequency $\Omega_0/2\pi$ and a quality factor Q. Note that this system has to fulfill $\Omega_\mathrm{m} \gg \Omega_0$ to access the maximum attenuation at $\Omega \approx \Omega_\mathrm{m}$, which lies between $\approx 2\pi \times 300$ kHz and $\approx 2\pi \times 1$ MHz.

V.2.c.ii Realization and room temperature characterization of the isolator

To realize the isolator, we fixed the sample to a large copper mass suspended by three soft and long (~ 15 cm) springs. This configuration ensures the lowest mechanical resonance frequency possible. Three loose copper wires are used for the thermalization of the lower stage, while the RF signal is transmitted from the RF lines of the cryostat to the sample using a CryoFlex cable, which is a flexible (thus ensuring lower mechanical conductivity) SMA connector exhibiting low thermal conductivity but low RF losses.

The isolator was first characterized in a homemade test bench at room temperature in air, which can be seen in figure V.11 (a) and (b). The upper stage of the isolator is suspended to a loudspeaker in order to excite it with a known frequency, amplitude and phase. Then, a diverging laser diode, together with a lens, generates a large ~ 1 cm collimated beam, aligned such that a significant part is clipped by the upper stage of the isolator. On the other side, another lens is used to collect the clipped beam and to focus it on a photodiode. As a consequence, the resulting signal, when demodulated at the mechanical excitation frequency, is proportional to the stage displacement amplitude. An identical setup is used to measure the lower stage position, and the ratio of the two demodulated signals gives the attenuation. To stay in the linear regime of the springs while maximizing the sensitivity of the characterization bench at each frequency, the excitation amplitude was dynamically adjusted: when the lower stage measured amplitude is high (*i.e.* near the resonance frequency of the isolator $\omega_0/2\pi$), the excitation amplitude is reduced, whereas when it is low, the latter is increased. The results are presented in figure V.11 (c), where the grey shaded area represents a regime where the attenuation is so strong that the lower stage displacement amplitude was hidden in noise. Together with the raw data appearing as red dots, this figure shows a fit to the model of eq (V.2.8), showing a good agreement. The resulting resonance frequency was ~ 3 Hz, and we measured attenuations as strong as ~ 35 dB for $\Omega/2\pi \sim 30$ Hz.

V.2.c.iii Low temperature characterization

The characterization the isolator at low temperature in “real" conditions is performed by cooling down a sample once with and once without the isolator. Each time we reproduce the optomechanical coupling measurement experiment described in section V.2.b.i, and measure at low temperature the Brownian motion peak in two conditions:

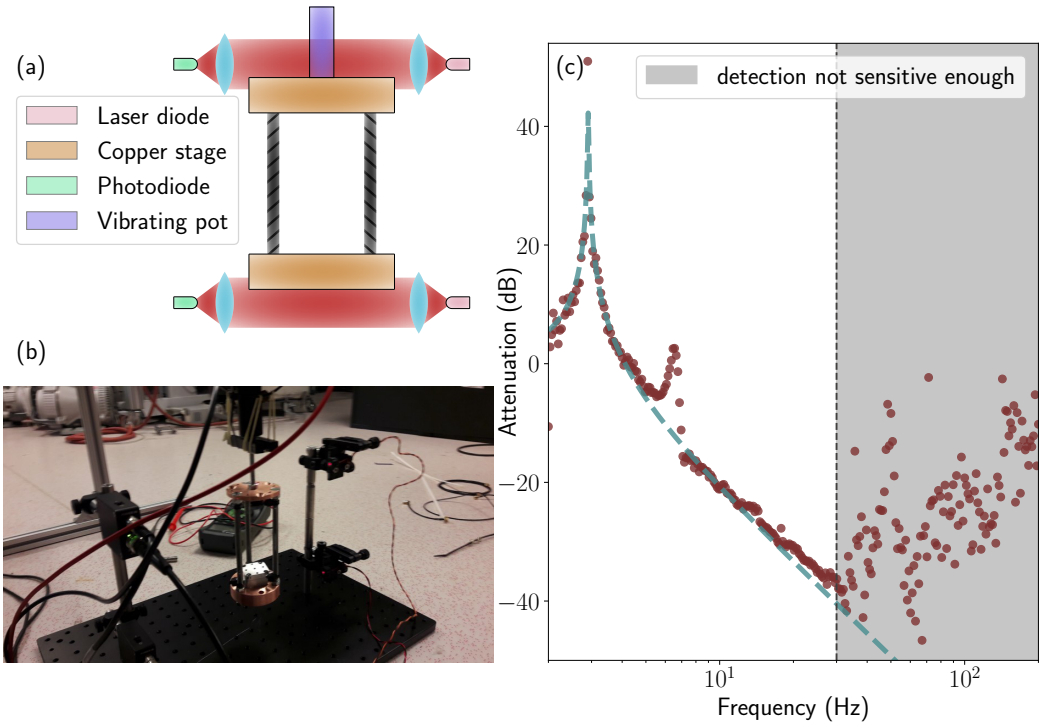

Figure V.11: (a) Schematics of the setup: a vibrating pot is holding the whole system, while a laser diode coupled to a photodiode is measuring the amplitude of motion of the upper stage of the isolator, and another laser diode coupled to a photodiode is measuring the amplitude of the lower stage of the isolator, on which the sample box is fixed. (b) Photo of the characterization setup. (c) Measured attenuation between the first and the second stage of the isolator. The shaded area corresponds to a regime where the lower motion was so small that it was not possible to measure it. The dashed blue line corresponds to a fit to the model (V.2.8).

one with the 1KPot pump turned on, the other with the 1KPot pump turned off, the latter being a regime where the Brownian motion overcomes any other mechanical noise source, as already demonstrated by the measured temperature dependence in figure V.3. The area below those peaks is directly proportional to the effective mechanical occupation of the environment. Therefore, the ratio between the area with and without the noise source turned on, in the regime where the Brownian motion is not dominating, is proportional to the spurious noise occupation. Thus, the ratio of this quantity with and without the attenuator is a measurement of the attenuation provided by the isolator. This scheme allowed us to measure an attenuation of$\sim$ 40 dB at $\sim$ 870 kHz, which is less than expected, given that eq. (V.2.8) predicts an attenuation proportional to Ω^{-2} and that we measured at room temperature an attenuation of $\sim$ 35dB for $\Omega \sim$ 30Hz. We can attribute this discrepancy to a change of mechanical properties of the isolator parts at low temperatures, or mechanical noise transferred through the thermalization cables or the flexible SMA cable. Even though the contribution from cryostat vibrations in the resonator noise is still visible in the total spectrum, the more than 33 dB reduction provided by the attenuator bring us in a regime where it is only marginally larger than the thermal motion.

V.3: Conclusion

In this chapter, we have presented a sideband cooling experiment that brought the mechanical resonator from an occupation of $\sim$ 65000 phonons to an occupation of $\sim$ 274 phonons. If we did not succeed in reaching the motional ground state in this experiment, we identified, designed and demonstrated two optimization techniques that would help us to reach this regime. The first one is the implementation of the pushing top technique presented in section V.2.b.iii, aiming at reducing the distance between the two chips by a mechanical pressure. The second one is the mechanical isolation of the whole system, mitigating the mechanical noise produced by the cryostat. In the next chapter, we will describe in details a technique we used to probe the microwave losses induced by substrate defects behaving as Two Level Systems. Finally, in a last chapter, we will introduce a few long term prospects this project is paving the way to, and are currently in development.

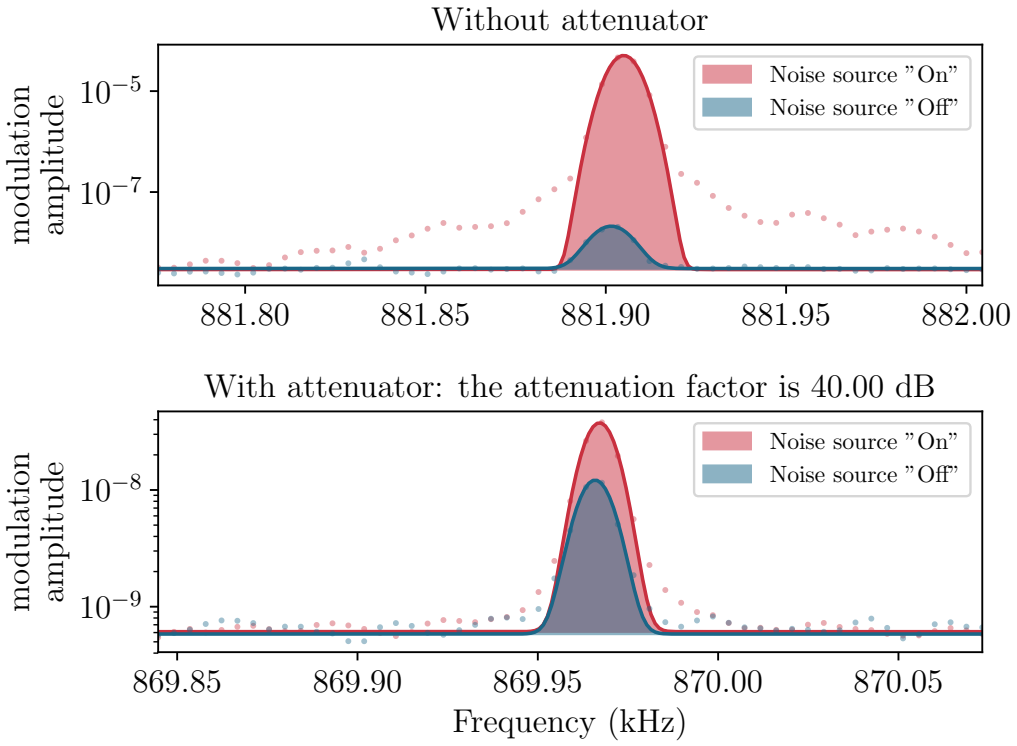

Figure V.12: Zoom on the thermal peak at low temperature when performing the experiment detailed in section V.2.b.i. Bottom (Top): the sample is measured with (without) the isolator. Red: the noise source, identified to be the 1KPot bubbling, is turned on. Blue: the pump is replaced by a ^{4}He balloon to suppress the extra noise. Data are represented by dots, while Gaussian fit are represented in straight lines.

Chapter VI: Characterization of the TLS bath with interdigitated capacitor resonators

Owing to the very low resistivity of superconducting materials, combined with advanced electromagnetic engineering to reduce radiation losses, the dominant loss channel of microwave superconducting resonators such as the ones used in this work is the dielectric loss due to the presence of a two-level system (TLS) bath in amorphous materials [WHW+09]. A salient feature of this loss mechanism is its non-linear nature. Indeed, the damping of TLS-limited cavities was shown to depend on resonator occupancy, originating from thermal fluctuations [GDM+08], from resonant excitation [LHC+09, SKW+15], or from non-degenerate resonant mode occupancy [SBO+11, KSB+17]. The characterization of the microscopic properties of individual TLSs probed under stress [LGM+15] or DC voltage bias [SRB+16] is an active field of research, and considerable experimental efforts have been devoted to the characterization [OAB+08, KWO11, VKG+12] and mitigation [PO10, WBB+11, QMC+14, BLA+15, CMW+18] of TLS-related losses for superconducting resonators in the single photon regime.

In the configuration in which those cavities were operated throughout this work however, the off-resonant microwave tone responsible for the saturation of the TLS bath is spectrally distinct from the resonant mode subjected to the losses, simultaneously giving rise to a shift of the resonance frequency and a modification of the population dependence of the quality factor.

In this chapter, we present the content of the reference [CFI+20]. We propose a scheme to probe the energy relaxation and frequency shift properties of an off-resonantly-driven microwave cavity due to the presence of a TLS bath. A semi-classical model that describes the modified susceptibility is derived and compared to experimental data obtained on several resonators fabricated on different substrates. Contrary to earlier works where a pump tone was injected at resonance with specifically engineered cavity modes [SBO+11, KSB+17], our technique is readily applicable to any kind of resonator, which makes it a versatile approach to identify a TLS loss mechanism, and quantify its contribution to the total resonator loss, a key capability for the design

and optimization of high-Q cavities. Moreover, the ability to continuously scan the pump detuning allows us to determine the average dephasing rate of the TLS bath by relating it to a well-controlled experimental parameter.

VI.1: Pump probe characterization

Each sample is placed in the base plate of the He^3 cryostat, and probed by a two-tone excitation (see Fig. VI.1(a) and Fig. III.13): a strong pump with a fixed detuning in an interval spanning from several linewidths below to several linewidths above the cavity resonance, saturates the TLS bath and a weak probe is used to measure the resonance frequency $\omega_c/2\pi$ and damping $\kappa/2\pi$ of the resonator (See Fig. VI.1(b)). An example of the complex probe transmission $\mathcal{T}$ recorded for various pump power is represented in Fig. VI.1(b). Fitting those transmissions to the fit formula IV.1.1 allows to separate the contributions of the coupling waveguide κ_{ext} and internal damping κ_{int} in the total cavity linewidth $\kappa = \kappa_{\text{int}} + \kappa_{\text{ext}}$.

Figure VI.2(a) shows the frequency shift $\Delta\omega_c/2\pi$ and internal damping $\kappa_{\text{int}}/2\pi$ measured by the probe for various pump powers and detunings Δ. Even with the large pump detuning, we observe a decrease of the resonator losses for increasing pump power. This effect can be attributed to the saturation of the TLS bath by the intracavity pump tone. To deconvolve the filtering of the detuned incoming pump tone by the cavity linewidth, the pump power is converted into intracavity photon number $\bar{n}$ via the formula $\bar{n} = 2\kappa_{\text{ext}}|a_{\text{in}}|^2/(\kappa^2 + 4\Delta^2)$, where $|a_{\text{in}}|^2$ is the incoming photon flux in photon/s as determined by an independent calibration experiment (see section III.2.b.ii). Furthermore, to measure the correct intrinsic damping at low power, the probe beam was ensured to be sufficiently weak to prevent it from saturating the TLS bath.

A noticeable feature of this pump-probe experiment is the pump-dependent frequency shift observed in Fig. VI.2(a). This result is in contrast with single-tone experiments where the interaction with the TLS bath is only affecting the resonator damping. Moreover, the observed frequency shift has a non-monotonous behavior, with a maximum (respectively minimum) resonator frequency observed for a given pump power at positive (resp. negative) pump detuning Δ.

In the next section, we give a detailed theoretical description of the pump-probe experiment, and we propose an analytical model that can be used to link the previous experimental signatures with various properties of the bath, such as the average TLS dephasing rate.

VI.2: Theoretical Analysis

Here, we derive analytical formulas for the frequency shift and damping induced by an ideal bath of TLSs. These are characterized by a uniform frequency distribution of density $P_0/2\pi$ (in Hz^{-1}), a coupling g to the resonator assumed to be identical for all TLSs in the distribution, and a damping (dephasing) rate Γ_1 (Γ_2). This is a simplifying assumption since the real TLS population has some statistical variation in these parameters (for instance, the coupling g of individual TLSs to the resonator

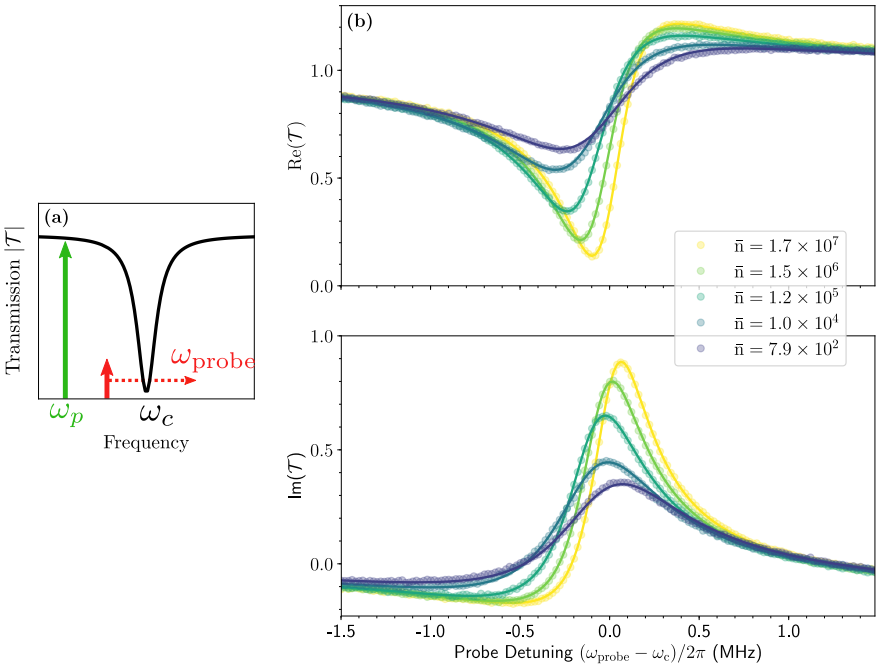

Figure VI.1: (a) Experimental protocol: a strong pump field is applied with a given detuning from a microwave cavity resonance, while a weak probe field is swept across the cavity resonance to measure its transmission spectrum $\mathcal{T}$. (b) Real (top) and imaginary part (bottom) of the probe transmission for a pump detuning of 4 MHz at various (pump) intracavity photon numbers.

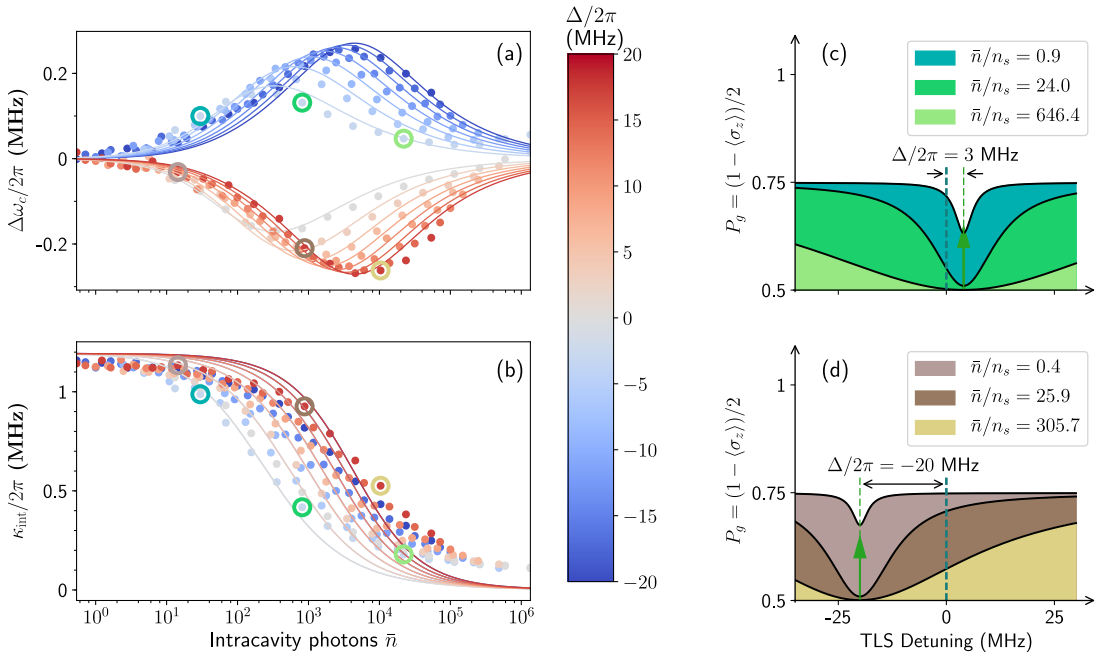

Figure VI.2: (a) Frequency shift and (b) damping of the resonator, versus the number of intracavity photons. Each color corresponds to a different pump detuning ranging from -20 MHz to $+20$ MHz (color bar). Points correspond to experimental data, while solid lines correspond to fits by the model (Eq. (VI.2.3) and (VI.2.4)). (c) and (d) are the ground state population distribution of the TLSs versus their frequency detuning $\omega_q - \omega_c$ calculated with Eq. (VI.2.1). The various curves have been calculated for various intracavity pump photon numbers and the related points in (a) and (b) are highlighted with the corresponding color-circles. This measurement was performed on a Si/SiO_2 sample, with $\omega_c/2\pi = 7.521$ GHz (see circled point in Fig. VI.4).

depends on the value and orientation of the electric field at the TLS location). However, by neglecting these effects, we can provide analytical formulas, which are numerically verified in section VI.3 with a more realistic TLS bath, and found to be in good agreement provided the fitted parameters are interpreted as averaged values over the TLS distribution.

VI.2.a: Analytic formula for a uniform TLS bath

As the weak probe has a negligible effect on the TLS bath, the pump affects the population imbalance $\langle \boldsymbol{\sigma_z}(\omega_\mathrm{q})\rangle$ according to the saturation law for a TLS at frequency $\omega_\mathrm{q}/2\pi$

$$\langle \boldsymbol{\sigma_z}(\omega_q)\rangle = \langle \boldsymbol{\sigma_z}\rangle_\mathrm{th}\left(1 - \frac{\Gamma_2^2\bar{n}/n_\mathrm{s}}{(\omega_\mathrm{q}-\omega_\mathrm{p})^2 + \Gamma_2^2(1+\bar{n}/n_\mathrm{s})}\right), \tag{VI.2.1}$$

where $\langle \boldsymbol{\sigma_z}\rangle_\mathrm{th} = -\tanh(\hbar\omega_\mathrm{q}/2k_\mathrm{B}T) \approx -0.52$ is the thermal imbalance resulting from the Fermi-Dirac distribution at the base temperature $T = 330$ mK of our ^{3}He cryostat, Γ_2 (Γ_1) the TLS dephasing (energy relaxation) rate, g the coupling rate, $\bar{n}$ the number of intracavity photons, $n_\mathrm{s} = \Gamma_1\Gamma_2/4g^2$ the number of photons required to saturate the TLS transition. In turn, the population imbalance $\langle \boldsymbol{\sigma_z}(\omega_\mathrm{q})\rangle$ of a single TLS induces a shift of the complex cavity frequency [KSB+17]

$$\delta\omega_c = \frac{g^2\langle \boldsymbol{\sigma_z}(\omega_\mathrm{q})\rangle}{\omega_\mathrm{q} - \omega_\mathrm{c} + i\Gamma_2}. \tag{VI.2.2}$$

The frequency shift and damping, as measured by the probe beam, are related to the real and imaginary parts of $\delta\omega_c$. The total frequency shift and damping are obtained by integrating the contribution of individual TLS, assuming a flat spectral distribution of density P_0, uniform coupling rate g, and no interaction between individual TLSs, leading to (see Appendix B)

$$\Delta\omega_\mathrm{c} = -\frac{\Gamma_0}{2}\frac{(\Delta/\Gamma_2)\,(\bar{n}/n_\mathrm{s})}{\sqrt{1+\bar{n}/n_\mathrm{s}}\left[(\Delta/\Gamma_2)^2 + \left(1+\sqrt{1+\bar{n}/n_\mathrm{s}}\right)^2\right]}, \tag{VI.2.3}$$

$$\kappa_\mathrm{int} = \Gamma_0\left[1 - \frac{\bar{n}/n_\mathrm{s}}{\sqrt{1+\bar{n}/n_\mathrm{s}}}\frac{1+\sqrt{1+\bar{n}/n_\mathrm{s}}}{(\Delta/\Gamma_2)^2 + \left(1+\sqrt{1+\bar{n}/n_\mathrm{s}}\right)^2}\right]. \tag{VI.2.4}$$

In these formulas, in addition to the dephasing rate Γ_2, the TLS bath is described by two characteristic parameters: $\Gamma_0 = P_0 g^2\,|\langle \boldsymbol{\sigma_z}\rangle_\mathrm{th}|$, the maximum damping produced by the TLS bath at the temperature T, that acts as a scaling factor on the curves $\Delta\omega_c(\bar{n},\Delta)$ and $\kappa_\mathrm{int}(\bar{n},\Delta)$, and n_s, that corresponds to a scaling of the curves with respect to the axis $\bar{n}$.

Eq. (VI.2.3) and (VI.2.4) agree well with the experimental observations of the previous section. The solid lines in Fig. VI.2(a) and (b) are a simultaneous fit of the experimental points to Eq. (VI.2.3) and (VI.2.4) with Γ_0, Γ_2, and n_s as free parameters. The small ($\sim 5\%$) discrepancy between the measured damping and the fits at low pump power is attributed to the residual saturation of the TLS bath by the probe

tone. We also observe a residual loss at high pump power, that represents $\sim 10\%$ of the low power value and that is attributed to a loss mechanism unrelated to the TLS bath. The smaller overall variation of the measured damping cannot be captured by the model since we perform a common fit on both damping and detuning points. We have nonetheless observed a decrease of this discrepancy as the probe power is weakened, consistent with the hypothesis of a residual saturation of the bath by the probe field. Since the detuning curve is not affected by these artifacts, we attribute a 90 % weighting to the detuning data in the global fit, and ignore these effects in our model for simplicity. In the following sections, we give a qualitative explanation of the phenomena captured by our model and derive simple formulas in two limiting cases.

VI.2.b: Small detuning limit

When the pump detuning is small compared to the TLS dephasing rate ($\Delta \ll \Gamma_2$), the TLSs that are affected by the pump are the same as in a single-tone experiment. In particular, since an equal number of TLSs are excited by the pump on either side of the cavity, the frequency shift vanishes in this regime:

$$\Delta\omega_c = 0, \tag{VI.2.5}$$

$$\kappa_{\text{int}} = \frac{\Gamma_0}{\sqrt{1+\bar{n}/n_{\text{s}}}}. \tag{VI.2.6}$$

Eq. (VI.2.6) is the well known power-dependent absorption of the TLS bath derived in the context of single-tone experiments [Phi87].

VI.2.c: Large detuning limit

In the large detuning limit ($\Delta \gg \Gamma_2$), the effect of the pump field on the TLS distribution is more subtle: as the intracavity field resonates at a frequency ω_p that is significantly different from ω_c, a depletion in population imbalance $\langle \boldsymbol{\sigma_z}(\omega_{\text{q}})\rangle$ occurs for TLSs that have a frequency ω_q close to ω_p. More quantitatively, the width of this Lorentzian dip is given by the generalized Rabi frequency $\Gamma_2\sqrt{1+\bar{n}/n_{\text{s}}}$. Consequently, the frequency pull exerted by TLSs that are above the cavity frequency will not be perfectly compensated by those that are below, resulting in a net shift of the cavity resonance. At even larger pump power, the width of the dip in population imbalance exceeds the pump detuning, such that the asymmetry decreases. Qualitatively, the maximum cavity frequency shift occurs when the pump creates a depletion of population imbalance $\langle \boldsymbol{\sigma_z}(\omega_{\text{q}})\rangle$ of spectral width Δ. In the current limit, this occurs when $\bar{n} \approx n_s\,(\Delta/\Gamma_2)^2$. This effect is illustrated in Fig. VI.2(c) and (d), where the ground state population has been calculated using Eq. (VI.2.1) for two different pump detunings, and various pump powers spreading below and above this value.

Further, we can note that Eqs. (VI.2.3) and (VI.2.4) can be approximated in the large detuning limit by:

$$\Delta\omega_c = -\frac{\Gamma_0}{2}\frac{\delta}{\delta^2+1} \tag{VI.2.7}$$

$$\kappa_{\text{int}} = \Gamma_0\frac{\delta^2}{1+\delta^2} \tag{VI.2.8}$$

with the dimensionless parameter $\delta = \sqrt{n_s/\bar{n}}\Delta/\Gamma_2$. Hence, in the regime $\Delta \gg \Gamma_2$, the curves $\Delta\omega_c(\bar{n}, \Delta)$ are invariant under the transformation $(\bar{n}, \Delta) \to (\sqrt{\alpha}\bar{n}, \Delta/\alpha)$, where α is an arbitrary positive number. In particular, the maximum frequency shift and damping are independent of the pump detuning provided it greatly exceeds the dephasing rate Γ_2 of the bath and their ratio is a non-adjustable prediction of the model:

$$\frac{\Delta\omega_c(\delta = 1)}{\kappa_{\text{int}}(\bar{n} = 0)} = 1/4. \tag{VI.2.9}$$

We find experimentally $\max(\Delta\omega_c)/\max(\kappa_{\text{int}}) \approx 0.23$ with the data presented in Fig. VI.2(a) and (b).

By capturing the transition between these two distinct regimes, the fit with the full Eqs. (VI.2.3) and (VI.2.4) performs a direct comparison between the TLS bath dephasing rate Γ_2, and the known pump detuning Δ. The two-tone experiments therefore give direct experimental access to Γ_2, a parameter that is elusive to the single-tone probing of a TLS bath.

VI.3: Effect of the non-uniform TLS distribution

VI.3.a: Monte Carlo simulations

The model derived in the previous section is based on the assumption that the bath is composed of a large number of TLSs with identical properties. In this section, we study numerically how a non-uniform distribution of TLS parameters affects the previous findings. We perform a Monte Carlo simulation where we randomly pick an ensemble of N TLSs characterized by the parameters $\{\omega_{q,i}, g_i, \Gamma_{1,i}, \Gamma_{2,i}\}_{i\in[1..N]}$. The individual TLS frequencies $\omega_{q,i}$ are drawn from a uniform distribution of density P_0. The couplings g_i are chosen randomly in a uniform distribution on the intervals $[0, g_{\max}]$: this distribution would be rigorously justified for a bath of TLSs with random orientations in a uniform electric field. The energy damping and dephasing rates $\Gamma_{1,i}$ and $\Gamma_{2,i}$ are drawn from a log-normal distribution, where the standard-deviation of the variable's logarithm is fixed to 1/2.

The TLS spectral density P_0 is not constrained by our model, we thus choose a starting value $P_0/2\pi = 1$ kHz^{-1} large enough to ensure that the numerical results are insensitive to the sampling noise associated with the random realization of TLSs. In practice, we choose 10^6 TLSs in a 1 GHz interval around the cavity frequency. Moreover we choose the mean values of the probability distributions such that $\bar{\Gamma}_0 = |\langle\boldsymbol{\sigma_z}\rangle_{\text{th}}|\, P_0\langle g_i^2\rangle$, $\bar{\Gamma}_2 = \langle\Gamma_{2,i}\rangle$, and $\overline{n_s^{-1}} = \langle\frac{4g_i^2}{\Gamma_{1,i}\Gamma_{2,i}}\rangle$ match the values fitted with our model on the experimental data of Fig. VI.2.

The expected frequency shift and damping are then computed on a regular grid of pump detuning and intracavity power by summing the contribution of individual TLSs using Eq. (VI.2.2). The resulting graph is represented in Fig. VI.3, together with a fit using the analytic Eqs. (VI.2.3) and (VI.2.4). We observe a very good agreement between the fits and the values calculated with the simulations; the fitted values of Γ_0, Γ_2 and n_s^{-1} match to within 15 % the average values $\bar{\Gamma}_0, \bar{\Gamma}_2$ and $\overline{n_s^{-1}}$ of the distributions sampled in the Monte Carlo simulation. This indicates that although the

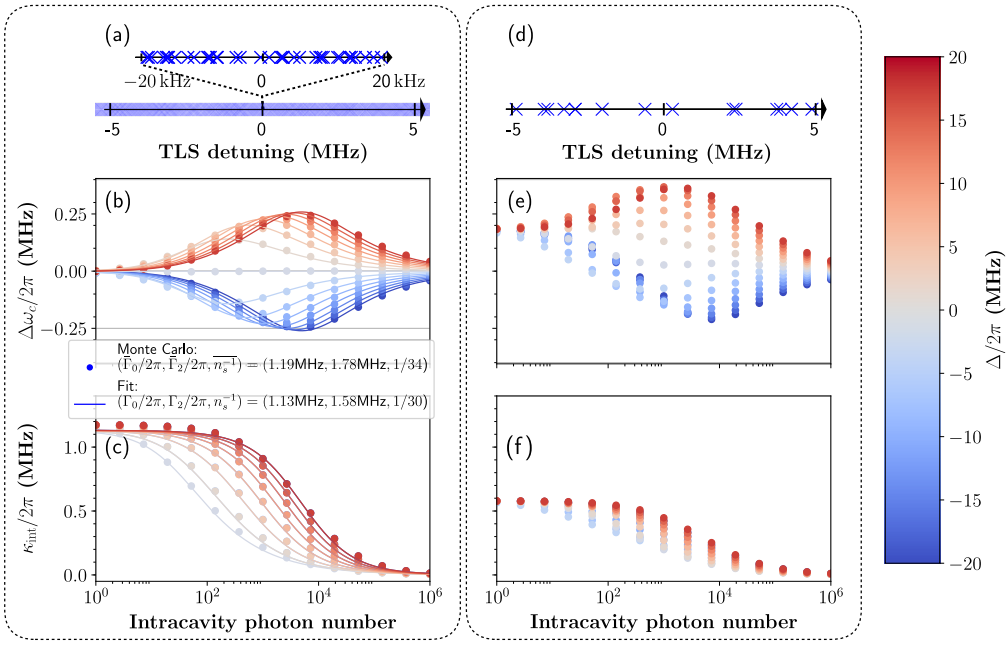

Figure VI.3: (Left) Numerical validation of the model: the points in (b) and (c) are the frequency shifts and dampings calculated with a Monte Carlo simulation for various pump power and detuning. The TLS frequencies are sampled from a flat distribution of density $P_0/2\pi = 1\,\text{kHz}^{-1}$. A 10 MHz fragment of the sampled TLS frequencies is visible as a collection of blue crosses in (a), as well as a zoom on a 40 kHz-wide region. The average values $(\bar{\Gamma}_0, \bar{\Gamma}_2, \overline{n_s^{-1}})$ of the sampled population (see legend) match the values obtained with the experimental fit of Figure VI.2. The full lines are fits with Eqs. (VI.2.3) and (VI.2.4) (fitted parameters are also indicated in the legend). (Right) Random sampling effects at low TLS density: the points in (e) and (f) are the typical Monte Carlo results for the same parameters as in (b) and (c), except for a lower spectral density $P_0/2\pi = 1\,\text{MHz}^{-1}$. In this particular realization, the reduced damping and positive frequency shift at low pump power results from a deficit of TLSs on the low frequency side of the cavity (see sampled TLS frequencies over a 10 MHz-fragment in (d)).

Eqs. (VI.2.3) and (VI.2.4) were rigorously derived with the assumption of a unique value of g^2, Γ_1 and Γ_2, they well describe the effect of a non-uniform TLS bath, provided the fitted values are interpreted as average values over the TLS distribution.

VI.3.b: Effect of random sampling

Our model is insensitive to the spectral density of TLSs: the scaling $(P_0, g, \Gamma_1) \rightarrow (\alpha P_0, \alpha^{-1/2} g, \alpha\Gamma_1)$ with α an arbitrary positive number, leaves the parameters Γ_0, Γ_2, n_s unchanged. However, the smaller the density P_0, the smaller the number of resonant TLSs that will contribute to the complex frequency pull. When only a handful of TLSs contribute to the effect, we observe the signatures of the random sampling in the Monte Carlo simulation. Fig. VI.3 (e), (f) shows the typical shape of $\Delta\omega_c(\bar{n}, \Delta)$ and $\kappa_{\text{int}}(\bar{n}, \Delta)$ for a TLS density as low as 1 MHz^{-1}. We observe an asymmetry in the frequency shift of the resonator: at low pump power, the frequency shift is mainly governed by the few TLSs that are located within a frequency difference Γ_2 from the resonator. An excess on one side of the cavity leads to a constant shift of the cavity frequency. On the other hand, in the large pump power limit, the cavity recovers its unshifted frequency since all the TLSs in a large frequency span around the cavity are saturated. Depending on the particular frequencies of the TLSs close to the cavity resonance, the low-power shift can be either towards low or high frequency. These effects have not been observed in our experiments, and we thus conclude that the TLS density $P_0/2\pi \gg 1$ MHz^{-1}. This result is consistent with other work from the literature [BFL16], that found a typical surface density for resonant TLS of $\sim 1\,\mu\text{m}^{-2}$ (resonant TLSs are those with a detuning $|\omega_{\text{q},i} - \omega_c| \lesssim \Gamma_2$, that contribute significantly to the low-power damping effect). With this estimate, we can infer that approximately 5000 TLSs contribute to the resonator shifts, or equivalently, a frequency density $P_0/2\pi$ in the kHz range.

VI.4: Measurement results

To evaluate the dispersion in the parameters estimated by our technique, we have repeated the fit presented in Fig. VI.2 on various resonators. Out of the 10 resonators fabricated on each of the Si/SiO_2, Si/Si_3N_4, and Si substrates, we have observed 3, 4, and 6 resonances respectively. We attribute the missing resonances to the presence of short circuits in the interdigitated capacitors.

The 3 parameters $(\Gamma_0, \Gamma_2, n_s)$ extracted from the fit of each operative resonator are represented as a point in the (Γ_2,Γ_0) and (n_s,Γ_0) planes in Fig. VI.4(a) and (b) respectively. The resonators fabricated on Si/SiO_2, Si/Si_3N_4 and Si substrates are represented in red, green, and blue points respectively. For a given substrate, the standard deviation of each parameter is represented as an error bar on the corresponding plot. Table VI.1 also summarizes the values extracted and the corresponding standard deviations for the different substrate types. The large dispersion of the parameter n_s, in particular for the Si/SiO_2 and Si/Si_3N_4 substrates, is likely due to systematic errors in the calibration of $\bar{n}$. Indeed, the determination of κ_{ext} is difficult for these largely undercoupled resonators (for some resonators, we have found a contribution of the coupling to the waveguide as low as ~ 3 % of the total damping). However, since this

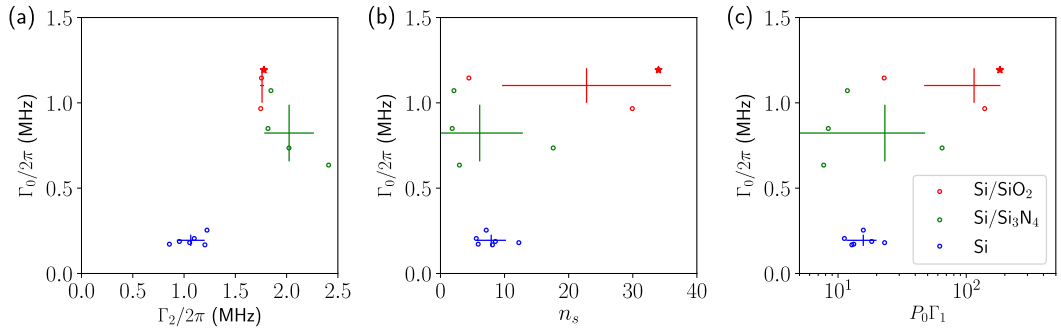

Figure VI.4: Fit results: each point in the scatter plots represents the result of a fit similar to that in Fig. VI.2(a), (b). Resonators fabricated on a Si/SiO_2, Si/Si_3N_4, and Si substrates are represented by red, green, and blue points respectively. The coordinates (Γ_0, Γ_2) and (Γ_0, n_s) extracted on each sample are represented in (a) and (b) respectively. The same data-points are represented in the $(P_0\Gamma_1, \Gamma_0)$ plane in (c), see text for details. The mean and standard deviation of each ensemble is represented as thick crosses in each of the plots. The starred data point is the result of the fit presented in Fig. VI.2(a) and (b).

effect only corresponds to a global shift of the curves $\Delta\omega_c(\bar{n}, \Delta)$, $\kappa_{\rm int}(\bar{n}, \Delta)$ towards lower occupancies $\bar{n}$, the determination of Γ_0 and Γ_2 is not affected by this inaccurate calibration. The losses Γ_0 are typically higher by a factor 5 with the Si/Si_3N_4 and Si/SiO_2 substrates as compared to Si. This indicates that most of the TLSs are indeed located in the amorphous layers SiO_2 and Si_3N_4. Moreover, we find a dephasing rate $\Gamma_2/2\pi$ in the MHz range for the 3 kinds of substrate, with a consistent variation from 1.07 ± 0.13 MHz for Si substrates, 1.76 ± 0.013 MHz for the SiO_2 substrates, and 2.02 ± 0.24 MHz for the Si_3N_4 layers. This points towards different TLS microscopic nature in the various materials. Even though the TLS spectral density P_0 cannot be resolved by our technique, a *normalized* TLS spectral density $P_0\Gamma_1 = 4\Gamma_0 n_{\rm s}/\Gamma_2 |\langle \boldsymbol{\sigma_z} \rangle_{\rm th}|$ can be calculated from the fitted parameters $(\Gamma_0, \Gamma_2, n_{\rm s})$. Fig. VI.4(c) represents the same experimental points as in Fig. VI.4(a) and (b) in the $(P_0\Gamma_1,\ \Gamma_0)$ plane. For the three substrate types the normalized TLS spectral density is comprised between $\sim$10 and $\sim$ 200 TLSs per intrinsic linewidth. As for the parameter $n_{\rm s}$, the relatively large scatter observed for the Si/Si_3N_4 and Si/SiO_2 substrates results from the poor determination of $\kappa_{\rm ext}$ for these resonators. The lowest values are found on the Si and Si/Si_3N_4 substrates and the largest values on the Si/SiO_2 substrates. The low spectral density of TLSs on the Si/Si_3N_4 (comparable to the bare Si substrate) is likely due to the small thickness of the amorphous Si_3N_4 layer on these samples: the TLSs contributing to the damping are relatively rare, but strongly coupled to the resonator due to their proximity to the interdigitated capacitor.

The low-power internal quality factor $Q(330\,{\rm mK}) = \omega_c/\Gamma_0$, and the quality factor extrapolated at zero temperature and zero pump power $Q(0\,{\rm K}) = Q(330\,{\rm mK})\,|\langle \boldsymbol{\sigma_z} \rangle_{\rm th}|$ is also presented in separate columns. The relatively low value of $\sim 10^4$ even for the samples fabricated on Si is likely due to the unusually small pitch of the interdigitated capacitors studied here [GSE+12], along with the absence of a chemical surface

treatment prior to metal deposition [BLA$^+$15].

Wafer	$\Gamma_0/2\pi$ (MHz)	$\Gamma_2/2\pi$ (MHz)	n_s (ph)	$P_0\Gamma_1$	Q(330 mK)	Q(0 K)
Si/SiO_2	1.1 ± 0.098	1.76 ± 0.013	22.8 ± 13	115 ± 68	6800 ± 400	3300 ± 100
Si/Si_3N_4	0.823 ± 0.16	2.02 ± 0.24	6.12 ± 6.6	23.2 ± 24	7400 ± 1300	3000 ± 500
Si	0.194 ± 0.029	1.07 ± 0.13	7.92 ± 2.2	15.7 ± 4	27500 ± 3000	10000 ± 900

Table VI.1: Extracted parameters of the TLS bath for the three types of substrates. The confidence intervals are the standard deviation of the measurement clusters.

Although recent experiments conducted on state-of-the art high-Q resonators have seen evidence of TLS-TLS interactions in the spectrum of resonator frequency fluctuations [BFW$^+$14, FI15], or on the power-dependence of the damping rate in single-tone experiments [BFL16], we haven't observed such signatures in our experiments. In particular, the generalized tunneling model proposed in [FI12] predicts a logarithmic dependence of the resonator damping as a function of $\bar{n}$. The absence of such signature in the samples fabricated on amorphous substrates such as Si/SiO_2 or Si/Si_3N_4 is not surprising as the density of TLSs in bulk amorphous material is too low to induce strong coupling between neighboring TLSs [FI12]. On the other hand, the dominating TLSs for the Si substrates are likely located at the oxide interface layers and should thus induce the same non-trivial power-dependence of the damping rate. The discrepancy between our experiment and these recent works is probably due to the lack of chemical surface treatment prior to metal deposition in our sample processing. However, extending our simple model to the case of interacting TLSs could provide useful insight on the physics of these complex systems. In particular, the two-tone experiment demonstrated here may be useful to test some of the underlying hypotheses of the generalized tunneling model, such as a temperature dependent dephasing rate of the TLSs [FI12].

VI.5: Conclusion

In conclusion, we have presented an experimental method to characterize the non-linear properties of a TLS bath—the dominant loss channel of planar superconducting resonators. The method has been applied to lumped-element resonators that have been specifically optimized to confine the electric field in a small region around the substrate surface. By selectively saturating a fraction of the TLSs that are resonant with a detuned-pump field, and simultaneously measuring the cavity spectrum with a weak probe field, we have observed clear signatures of "spectral hole burning" in the TLS frequency distribution. The details of the evolution of the resonance frequencies and damping as a function of the pump detuning can be used to infer physical properties of the bath, such as its average dephasing rate Γ_2. This technique requires only standard microwave equipment and it is readily applicable to a large range of microwave resonators. Beyond their interest for the investigation of amorphous materials, the experimental signatures reported in this work can be used as a method to unambiguously identify the precise contribution of the TLS-bath to the total resonator loss, and thus

gives a useful insight into the design and optimization of superconducting cavities.

Furthermore, the physical situation considered here is ubiquitous in parametrically coupled systems where a particular interaction is activated by a strong pump field detuned with respect to the resonant mode frequency. This is notably the case in reservoir engineering, where the mode of interest inherits a non-trivial dissipation mechanism from the parametric coupling to an intentionally low-Q microwave mode [Kap17]. In this regime, the coupled dynamics of the resonant mode and TLS bath have to be carefully studied since pump photons can be scattered to the resonator via the interaction with TLSs, leading to an effective heating process. This phenomenon is currently under theoretical investigation [FSC$^+$18] and its characterization, which requires a quantum limited read-out to resolve the associated fluctuations, will be the subject of future work.

Chapter VII: Prospects

Although this work was not able to experimentally demonstrate the ground state cooling of a mechanical oscillator, it succeeded in approaching this regime, as well as proposing and experimentally demonstrating several optimization directions that would eventually lead to this milestone. In the first section of this chapter, we present the next optimization we developed for improving this experiment. In the second section, we propose and successfully demonstrate a method to extract informations on the mechanical oscillator despite the noise of the HEMT. Finally, in the third section, we propose a possible experiment which aims at generating nonclassical state of motion. This last experiment would require first to reach the ground state of the mechanical oscillator beforehand, and second to dispose of a single microwave photon detector. We here demonstrate experimental results of the characterization of such a detector, with unprecedentedly low dark count rate.

VII.1: Patterned membranes

The experimental investigations described in the previous chapters demonstrated several limitations inherent to the use of the square membranes presented in section II. Among those, their relatively low frequency is a concern, as the microwave source noise is getting higher as we work closer to the frequency of the pump. This reduces the maximum source power that can be injected at the input of our electromechanical cavity. We also believe this low frequency to be among the causes of the extra mechanical noise we measure at low temperature. Indeed, other experiments working at higher frequencies are not measuring such effects[TdL+11], and it is reasonable to assume that most physical systems behave as lowpass filters for phonons. Furthermore, although the mechanical quality factors that we observed were exceptionally high, reaching higher values is always desirable, as the lowest mechanical occupation a sideband cooling experiment can reach scales with the mechanical loss rate. As explained in chapter II, the two main loss channels for the thin highly stressed resonators we are using are clamping losses and intrinsic losses. To the latter is associated the quality factor (see section II.2):

$$Q_{\text{int}}^{-1} = \frac{\sin(\phi)}{1-\nu^2}\left(\lambda + \frac{\pi^2}{4}\lambda^2(n^2+m^2)\right), \tag{VII.1.1}$$

where ϕ is the loss angle of the silicon nitride, ν its Poisson ratio, $\lambda \stackrel{\text{def}}{=} \sqrt{\frac{Eh^2}{3\sigma a^2}}$, E is the Young modulus, σ the stress, h the thickness and a the side length of the membrane. In this expression, we see that, since λ is very small, the dominant term is the first one, which originates from the extra bending the rigid edge clamping imposes at the edge of the membrane.

This observation led to the development of the concept of *soft-clamping* [TBPS17, RFAmca+19], aiming at having "soft" boundary conditions. The principle is as follows: a honeycomb periodic pattern of holes is etched through a large square ($\sim$ 3 mm) membrane made with a thin ($\sim$ 100 nm) pre stressed silicon nitride film. Crucially, at the center of the membrane, some holes are displaced to create a defect and to localize a mechanical mode. The geometrical dimensions of those structures are chosen for this localized mode frequency to lie in the quasi-bandgap created by the periodic pattern.

This geometry has several advantages when compared to a simple square membrane. First, the motion of the mode is exponentially suppressed by the quasi-bandgap structure, making it very difficult for phonons to be scattered from the frame of the resonator to the mechanical mode. This considerably reduces the sensitivity to clamping losses, and we hope that it will also prevent mechanical noise from the cryostat to considerably excite the mechanical resonator. Second, this exponential suppression of the motion produces a smoother bending than the square membrane rigid clamps, greatly reducing the bending losses and opening the path to new quality factor regimes. Finally, those designs allow to increase the mechanical frequency to work in the MHz range.

In this section, we will present nanofabrication recipes we developed to make those patterned membranes, with a geometry similar to the one used in Tsaturyan and al. [TBPS17], as well as the mechanical characterization we performed at room temperature on those devices.

VII.1.a: Nanofabrication

The fabrication of patterned membranes follows a similar line, presented in figure VII.2 than the fabrication of unpatterned membranes, presented in figure II.3. The first difference is the size: while the size of unpatterned membranes is directly linked to their mechanical frequency, leading in our case to the realization of small (1 mm and 300 μm large) membranes to benefit from rather large mechanical frequencies, the mechanical frequencies of patterned membranes is set by the size of the central defect of this pattern, and the bandgap central frequency by the period of the pattern. A large number of repetitions of the pattern between the defect and the frame of the membrane is however favorable for a good isolation of the mechanical mode. This leads to the realization of larger (3 mm) membranes.

In addition, the presence of holes inevitably leads to different fabrication techniques. Along with an additional lithography (step 8 to 12), the KOH etching steps (step 13 to 15) and the metallization steps (step 16 to 18) presents strong modifications. For the former, after several tries and errors, we converged towards the use of a commercial KOH resistant Protek PSB coating for protecting the patterned side of the sample during the etching, together with a simple vertical holder (see figure VII.1), ensuring the liquid pressure on both sides of the sample to be the same during the etching, at

Figure VII.1: Picture of the KOH etching holder used for the patterned membrane recipe with Protek.

the cost of a small etching of the edges of the sample.

As for the metallization, we chose to use a *shadow mask* technique: the use of a physical mask precludes the metal to be deposited everywhere except on the central pad and the spacers. This technique allows to circumvent the problems arising when performing a lithography on a surface presenting holes. Indeed, such a geometry, due to surface tension, prevents to spin coat a homogeneous layer of optical resist, which would exhibit edge effects. Close to a hole, the thickness will be larger than the required thickness for a proper bake and insulation. As a result, a lithography in those conditions is particularly tedious.

VII.1.b: Shadow mask

The fabrication of this shadow mask is presented in figure VII.4. We circumvented the impossibility of using a DRIE machine by using KOH etching with similar techniques than the ones used for the patterned membrane recipe: starting with the same wafers, and after having cut them in 3 cm×3 cm samples, we open on the backside 9 square openings that are large enough for the front pattern to be on the liberated membrane after the KOH etching. Then, we draw the desired pattern for the deposition on the front side of the sample. After these steps, the recipe is identical with the one for patterned membrane: we protect the front face of the shadow mask with Protek PSB coating, and we etch the silicon in KOH before removing the resist and proceeding to further cleaning. This technique prevents us from depositing arbitrary metallic shape: basically, only rectangles and rounds, perhaps ellipses, are allowed, and their sizes could not be much smaller than a few tenth of microns. We chose a design with a simple round pad with a diameter of 100 μm, and used the mask to define also height square pads that would eventually be facing the aluminium spacers of the microwave sample. The result is presented in figure VII.5 (a).

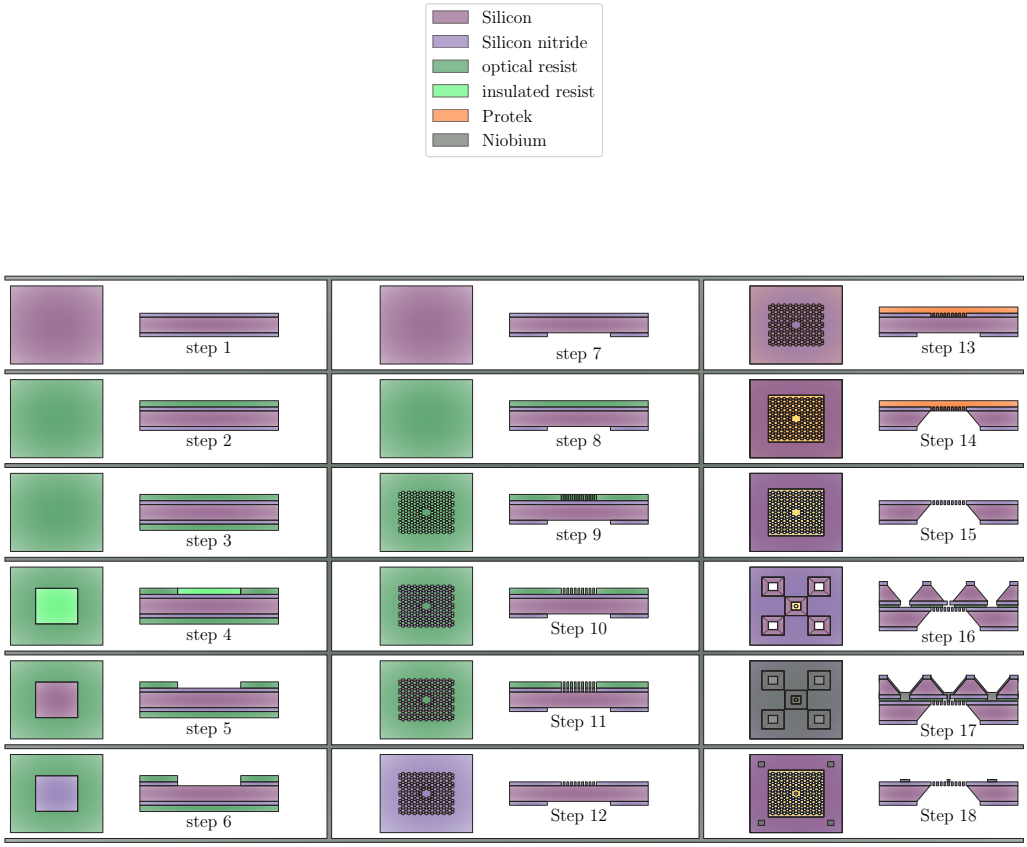

Figure VII.2: Fabrication recipe of a metallized patterned membrane

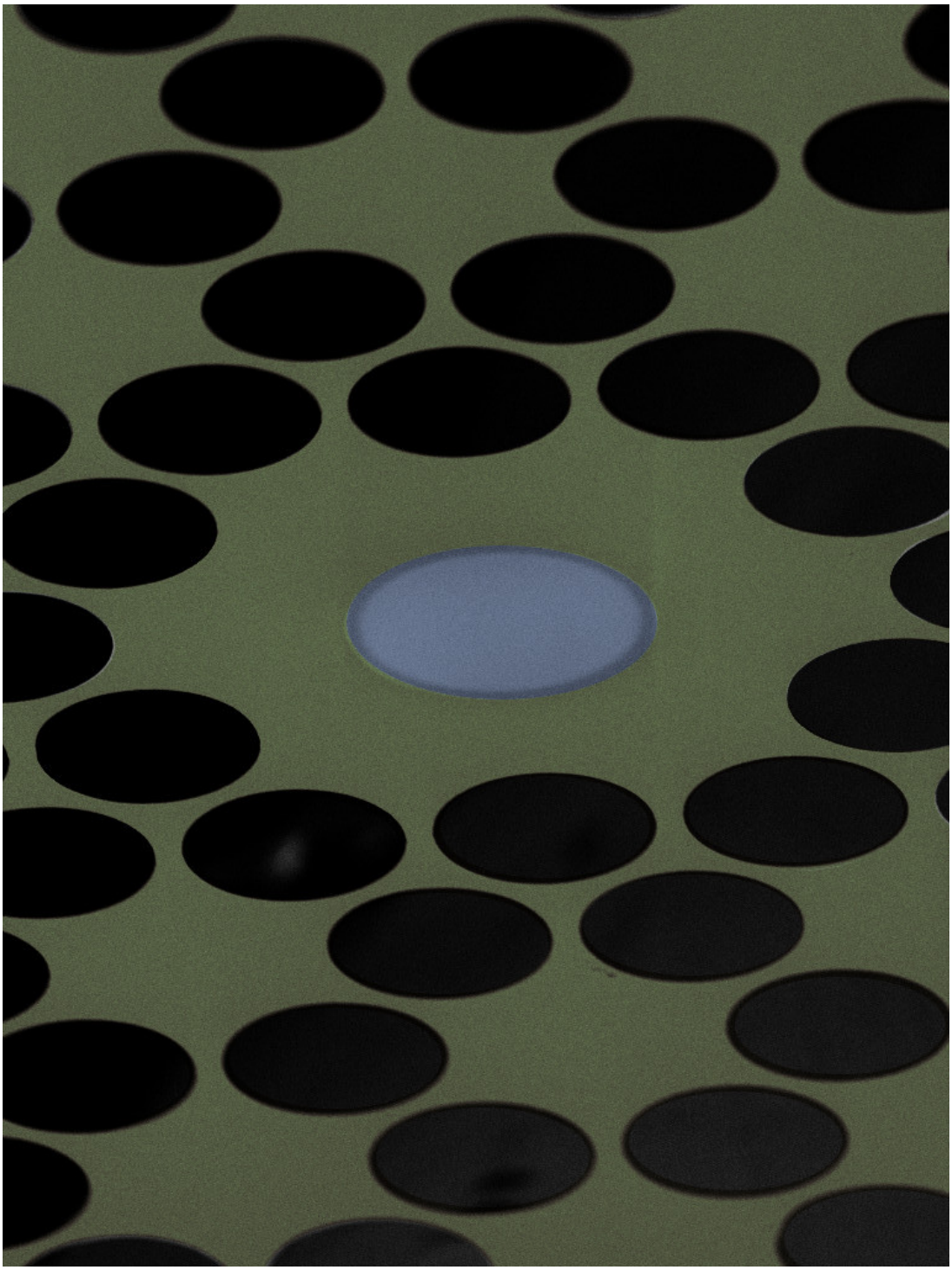

Figure VII.3: Scanning Electron Microscope angle view in false color of a metallized patterned membrane made following the recipe of figure VII.2. Silicon nitride is represented in green, while Niobium is represented in blue.

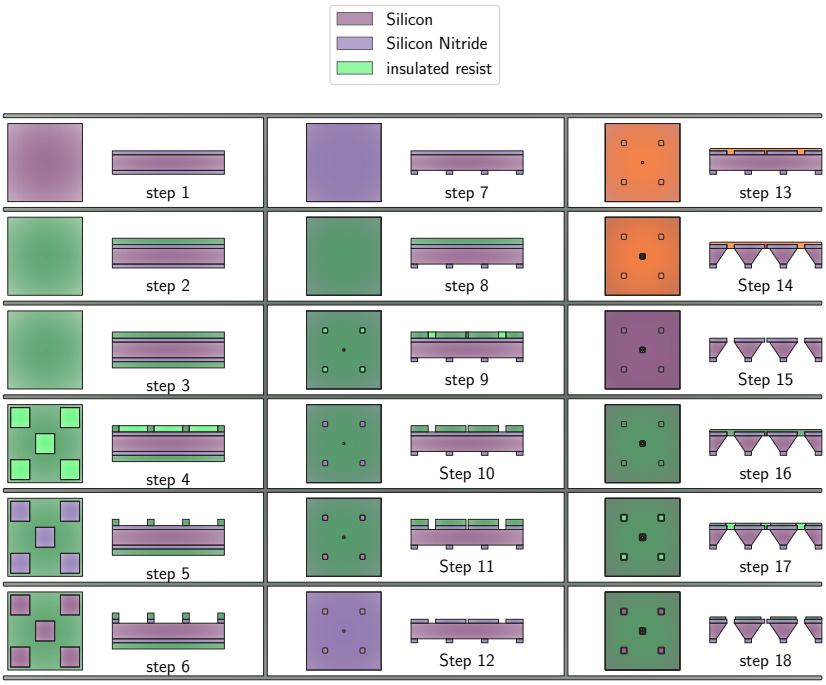

Figure VII.4: Fabrication recipe of a shadow mask

The stamping of a shadow mask (step 16 of figure VII.2) is done as follows: after a 30 min 1:3 piranha bath cleaning using a homemade PTFE holder to manipulate the samples, followed by a DI water bath and an IPA bath, the samples are dried and the shadow mask is prepared for a spin coating with the use of a cleanroom blue tape on its back side. Then, small droplets of optical resist are deposited at positions where the spreading of those droplets after spin coating would not cover any holes made for deposition. This deposition is made using a micropipette. After a spin coating at 4000 rpm, 4000 rpm/s, 30 s, the stamping is then performed in a MJB4 mask aligner, as shown in figure VII.5, with a homemade mask holder allowing to vacuum suck the membrane without jeopardizing the liberated part of the sample.

The mask holder allows to see through the membrane with the microscope objective of the MJB4, thus allowing to control the alignment of the shadow mask with respect to the membrane. Pictures of the mask and mask aligner used for a stamping, along with more details on the process, can be found in section III.3.c. Indeed, the technique for assembling the shadow mask and the membrane is to some degree identical to the technique used for assembling a microwave sample and a mechanical sample.

The assembly is made with the shadow mask facing upwards while the membrane is vacuum sucked, facing downwards during the alignment. Using the transparency of the membrane for this step, instead of looking through the shadow mask, allows first to benefit from the large (3 mm) membrane to align more precisely the two samples, and second to reuse the shadow mask several times. Indeed, after the Niobium has been sputtered, the shadow mask becomes opaque everywhere apart in the holes, making it nearly impossible to align properly with another sample if we would try to see through it during the alignment step. Once the alignment is made, the two chips are pressed against each other, then a 1 min 30 s 110 °C bake is performed for maintaining them together.

In the sputterer, however, the shadow mask has to face downwards towards the Nb target, while the membrane has to be stuck on the wafer holder. To that end, the use of metallic clamps, routinely used in such machines for maintaining wafers in place, is prohibited: it would immediately disassemble and misalign the two chips. We found an alternative with a carbon tape bounding: a small piece of this adhesive is placed on the wafer holder of the sputterer, which is softly approached towards the membrane from above it. The chip assembly is then stuck on the wafer holder. Additional aluminum film pieces are added around the shadow mask such that they cover the parts of the membrane that are not properly covered by the shadow mask. The wafer holder is then placed in the sputtered, which is pumped to achieve a vacuum of $\sim 1.10^{-7}$ mbar, then a ~ 50 nm Nb film is deposited.

After the deposition, the extra aluminum film protecting the edges is removed, and the sample with the shadow mask is unstuck from the wafer holder. The shadow mask is then separated with a 15min 50°C Acetone bath, followed by a rinsing in IPA.

VII.1.c: Characterization

If we have not yet succeed in coupling those mechanical resonators to a microwave circuit, various characterization techniques were used to assess the mechanical parameters of the patterned membranes. We present the obtained results in this section.

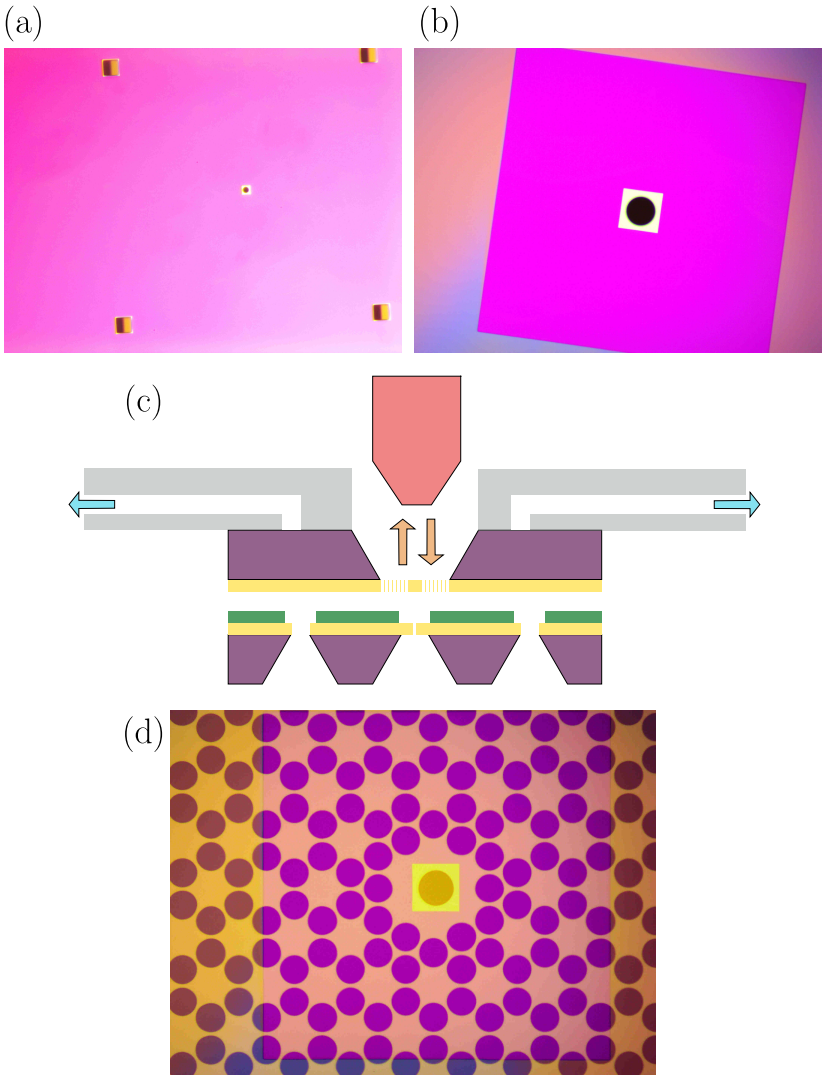

Figure VII.5: (a) Picture of the front side of a shadow mask made following the recipe presented in figure VII.4 (b) The shadow mask after deposition of AZ5214 optical resist. (c) Principle of stamping of a shadow mask. The shadow mask is facing upwards while the membrane is vacuum sucked using a dedicated homemade aluminum mask holder. The latter allows to optically see through the transparent membrane for aligning the two samples. The AZ5214 optical resist, used for maintaining the two samples together, is represented in green. (d) Picture of the membrane after stamping of the shadow mask.

VII.1.c.i Spectrum

We started by comparing finite element simulations to the measurements conducted in the interferometer described in section II.4.a. To simulate the band structure of the hexagonal periodic pattern, we define its unit cell (see figure VII.6(c)) from which we can generate an infinite pattern by performing translations following the directions:

$$\forall (i,j) \in \mathbb{Z}^2, \vec{t}_{ij} = i\vec{a}_1 + j\vec{a}_2, \tag{VII.1.2}$$

where:

$$\vec{a}_1 \overset{\text{def}}{=} \frac{a}{2}\left(-\frac{1}{2}\vec{e}_x - \frac{\sqrt{3}}{2}\vec{e}_y\right) \tag{VII.1.3}$$

$$\vec{a}_2 \overset{\text{def}}{=} \frac{a}{2}\left(\frac{1}{2}\vec{e}_x - \frac{\sqrt{3}}{2}\vec{e}_y\right). \tag{VII.1.4}$$

In such a structure, all function characterizing the material properties are periodic in space and can therefore be expanded as Fourier series. For instance, the transverse displacement field reads:

$$\vec{u}(\vec{r}) = \sum_{\vec{G}\in\mathcal{G}} \vec{u}_{\vec{G}}(\omega,\vec{k}) e^{i(\omega t - \vec{k}\cdot\vec{r} - \vec{G}\cdot\vec{r})}. \tag{VII.1.5}$$

In the above expression, $\mathcal{G}$ corresponds to the reciprocal lattice vectors, which is defined by:

$$\mathcal{G} = \{n_1\vec{b}_1 + n_2\vec{b}_2, (n_1,n_2) \in \mathbb{N}^2\}. \tag{VII.1.6}$$

The reciprocal basis vectors are defined by:

$$\vec{b}_1 \overset{\text{def}}{=} \frac{\vec{a}_2 \wedge \vec{e}_z}{\vec{a}_1 \cdot (\vec{a}_2 \wedge \vec{e}_z)} \tag{VII.1.7}$$

$$\vec{b}_2 \overset{\text{def}}{=} \frac{\vec{e}_z \wedge \vec{a}_1}{\vec{a}_1 \cdot (\vec{a}_2 \wedge \vec{e}_z)}. \tag{VII.1.8}$$

To compute the band diagram, we impose Floquet boundary conditions at the edges of the unit cell, which means that a displacement from one side of the unit cell to the other will multiply the displacement field by the phase factor:

$$e^{i\vec{r}_0 \cdot \vec{k}}, \tag{VII.1.9}$$

where $\vec{r}_0$ is the translation from one edge to the other, and $\vec{k}$ is a given wavevector of the reciprocal space. For each $\vec{k}$ we compute the eigenfrequencies of the problem. Scanning the value of $\vec{k}$ allows to access the band diagram (see figure VII.6 (b)) Using symmetry and periodicity considerations, it is possible to show that the smallest region of the reciprocal space we need to cover when scanning the value of $\vec{k}$ corresponds to the edges of the region appearing in red in figure VII.6 (d). It is called the irreducible Brillouin Zone. The band diagram of such a structure presents a quasi-bandgap, where the propagation of plane waves is forbidden, apart from high phase velocity modes that are usually not relevant experimentally. Note that for thicker structures, it is possible to achieve a complete bandgap.

The measurement of the spectrum is performed in the Michelson interferometer with a balanced detection described in section II.4.a. The experimental result is presented in figure VII.6 (a), where the bandgap appears as a region with much less noise. Crucially, in this phononic crystal, some holes are displaced in the center of the structure to localize some mechanical modes, which therefore are well isolated from their environment.

VII.1.c.ii Ringdowns

We then performed ringdown measurements as presented in section II.4.c (see figure VII.7) The measured Q factor was here $\sim 8.48 \times 10^6$. The increase of quality factor compared to the square membrane case is due partly to the good isolation of the mode, which strongly attenuates the clamping losses, and partly to the reduction of the edge bending those localized modes exhibit compared to square membranes [TBPS17].

VII.1.c.iii Mode reconstruction

Finally, we performed mode reconstruction, as detailed in section II.4.d. The results are presented in figure VII.8, where a good agreement with simulations is shown.

To conclude, we demonstrated the fabrication, characterization and metallization of high quality factor patterned membranes with frequencies in the MHz range. We did not yet succeed in coupling them to a microwave cavity, however this milestone seems to be relatively straightforward to achieve. It would be quite interesting to measure the sensitivity of such well isolated membranes to the mechanical noise in the cryostat.

VII.2: Parametric amplification

The optimization techniques presented in chapter V.2, together with the implementation of the patterned membranes presented in the previous section, are likely to bridge the gap towards the ground state cooling of a mechanical oscillator. However, even if this milestone is reached, our current experimental setup will have to overcome a serious difficulty to prove it. Indeed, as explained in section III.2.b.ii, the added gain of our amplification line is approximately equal to the added noise of our first amplifier, a High Electron Mobility Transistor (HEMT), which is not quantum limited but is exhibiting a noise temperature of $\sim$ 4K, or equivalently $\sim$ 10 noise photons. As a result, the noise of a mechanical oscillator in its motional ground state would be blurred by a noise whose amplitude is one order of magnitude superior. Although most electromechanical experiments are using parametric amplifiers such as the JPA[DRAL19, TdL$^+$11] or a TWPA to overcome this problem, those devices are not commercially available and can be complicated to use. For instance, a JPA has a small bandwidth that should match the frequency of the electromechanical cavity, and those devices are known to exhibit saturation at lower input powers than HEMT amplifiers.

Alternatively, we here propose a scheme to use the electromechanical cavity itself to transiently amplify the mechanical noise above the noise level of the HEMT, as detailed in section I.4.c. We will show how this technique can be used to measured

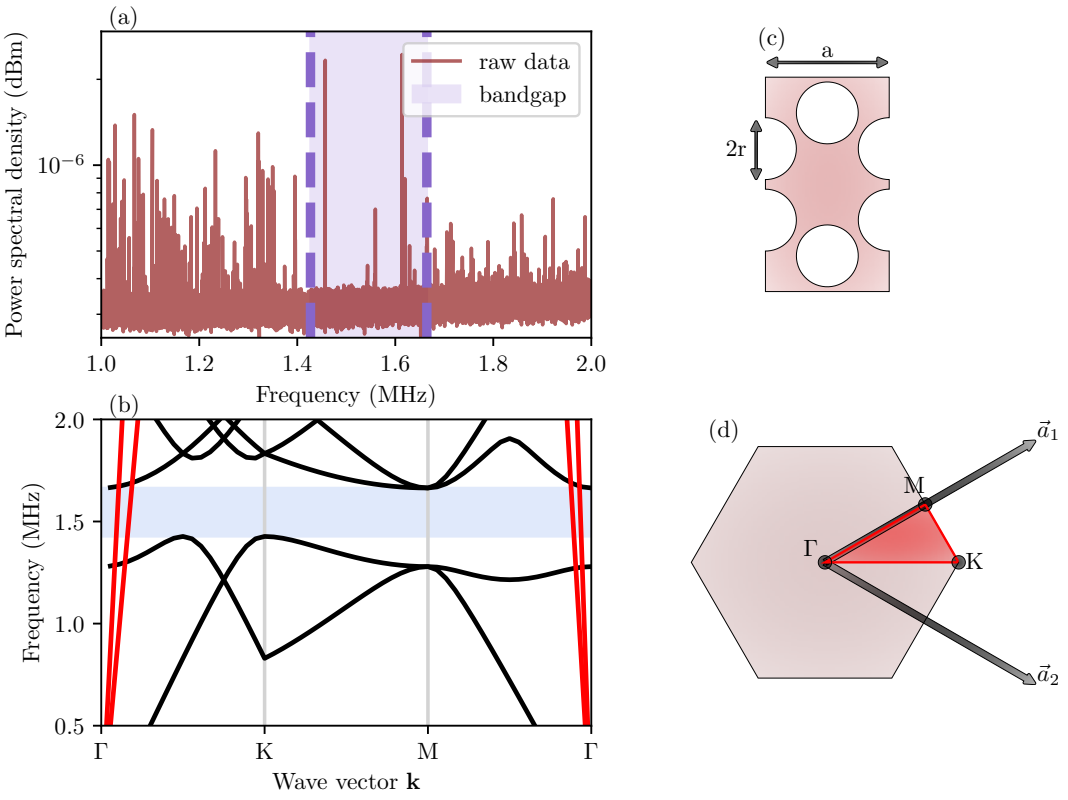

Figure VII.6: (a) Measured spectrum of a patterned membrane in the interferometer presented in section II.4.a probing the motion of the defect. The light blue shaded area is the simulated bandgap. (b) Simulated band diagram. The light blue shaded area is the simulated bandgap. Colored in red are the edge modes. (c) Geometry of the simulated cell for the computation of the band structure. The unit cell defined by VII.1.3 and VII.1.4 is the subcell inside the hexagon.(d) Irreducible Brillouin Zone corresponding to the unit cell (in red). The two base vectors of the reciprocal space are represented as arrows.

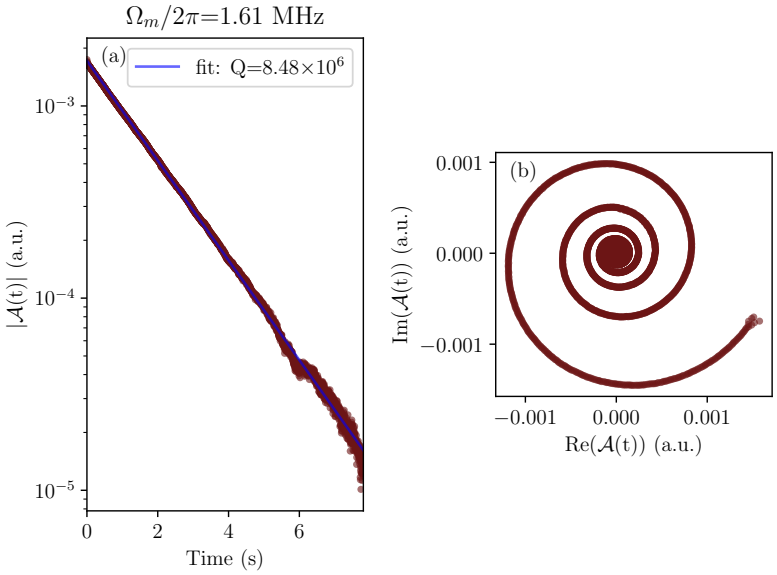

Figure VII.7: (a) Modulus of the measured signal versus time during a ringdown measurement. The measured quality factor is 8.48×10^6. (b) Smith chart of the data.

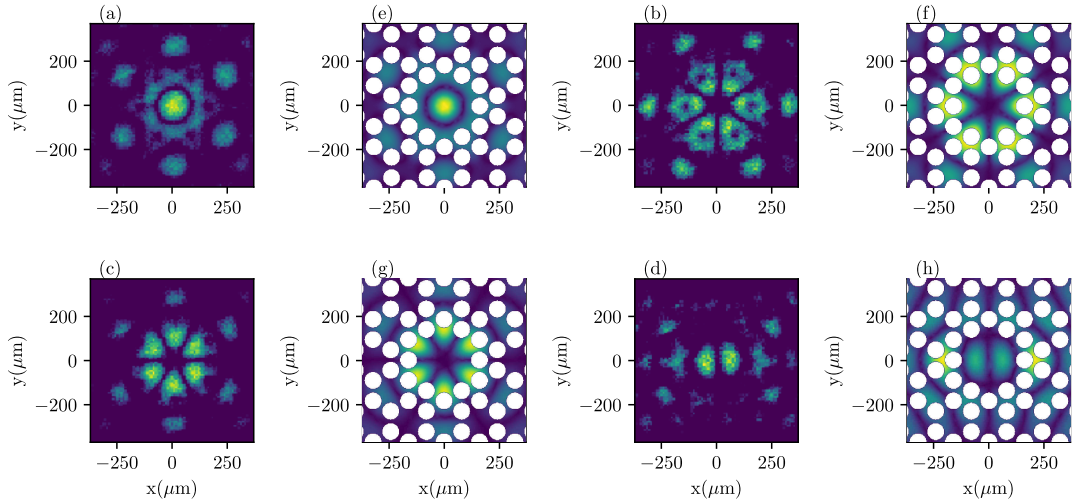

Figure VII.8: (left) Experimental measurement of the mode shapes. (Right) Corresponding simulated mode

the thermal occupation of the mechanical oscillator. The principle is presented in figure VII.9: a strong pump with a frequency on the blue sideband ($\omega_d = \omega_c + \Omega_\mathrm{m}$) is applied for a short time t_b. If the intensity of this pump is strong enough to induce a cooperativity $C > 1$, the mechanical motion amplitude undergoes an exponential increase. After a time t_b, this pulse is stopped, and another pulse is sent on the red sideband ($\omega_d = \omega_c - \Omega_\mathrm{m}$) for a time t_r. After that, a time t_wait is spent without any pump driving the system.

During these steps, the output signal is demodulated at the cavity frequency ($\omega_c/2\pi \sim 9.8$ GHz) in a Signal Analyzer (see section II.4.c for details) to recover its time trace. The span and the bandwidth are adjusted such that the time trace comprises a significant part of both the blue pulse and the red pulse. Note that if a different cooperativity is used for the blue pulse and the red pulse, we expect the measured traces to show a discontinuity at the transition between them (see fig. VII.9 (a)), as the output signal amplitude is proportional to the cooperativity.

The experiment is repeated a large ($N = 100$) number of times. Equation I.4.31 describes the shape of the time trace: the initial value $\hat{x}(0)$ is a random variable with a distribution imposed by the thermal state, and is exponentially increased. Some errors in the exact assessment of Ω_m lead to a phase shift during this exponential increase. Therefore, it is necessary to extract the exact waveform from this collection of traces. We do that by computing the matrix:

$$\mathcal{K} \overset{\text{def}}{=} \sum_i \mathcal{M}_i, \tag{VII.2.1}$$

where the matrices $\mathcal{M}_i$ are defined by:

$$(\mathcal{M}_i)_{kl} \overset{\text{def}}{=} \mathcal{T}_i(k)^* \mathcal{T}_i(l), \tag{VII.2.2}$$

and $\mathcal{T}_i(k)$ is the k-th value of the i-th trace. It can be shown [MFL13] that the waveform we need for computing the variance is the eigenvector of the matrix $\mathcal{K}$ with the largest eigenvalue. If we call this waveform $\mathcal{W}$, we can plot, as in figure VII.10 (b), the scalar product of each trace with the waveform:

$$P_i \overset{\text{def}}{=} \sum_k \mathcal{W}(k)\mathcal{T}_i(k), \tag{VII.2.3}$$

from which we obtain the amplitude variance $\mathrm{Var}(t_\mathrm{wait})$, which is proportional to the initial mechanical occupation $n_\mathrm{m}(0)$. The evolution of this quantity with t_wait is presented in figure VII.10 (c), together with an exponential fit. For $t_\mathrm{wait} \ll \frac{1}{\Gamma_\mathrm{m}}$, the initial mechanical state correspond to a thermal state that has been amplified by the previous blue pulse and cooled down by the following red pulse. Neglecting the microwave input noise in the equations I.4.21 and I.4.22, the evolution of the occupation during a blue pulse reads:

$$n_\mathrm{m}(t) = n_\mathrm{m}(0)e^{\Gamma_\mathrm{m}(C_b-1)t} + \frac{n_\mathrm{th}}{C_b - 1}\left(e^{\Gamma_\mathrm{m}(C_b-1)t} - 1\right), \tag{VII.2.4}$$

and similarly during a red pulse starting at $t = t_b$:

$$n_\mathrm{m}(t) = n_\mathrm{m}(t_b)e^{-\Gamma_\mathrm{m}(C_r+1)(t-t_b)} + \frac{n_\mathrm{th}}{C_r + 1}\left(1 - e^{-\Gamma_\mathrm{m}(C_r+1)(t-t_b)}\right). \tag{VII.2.5}$$

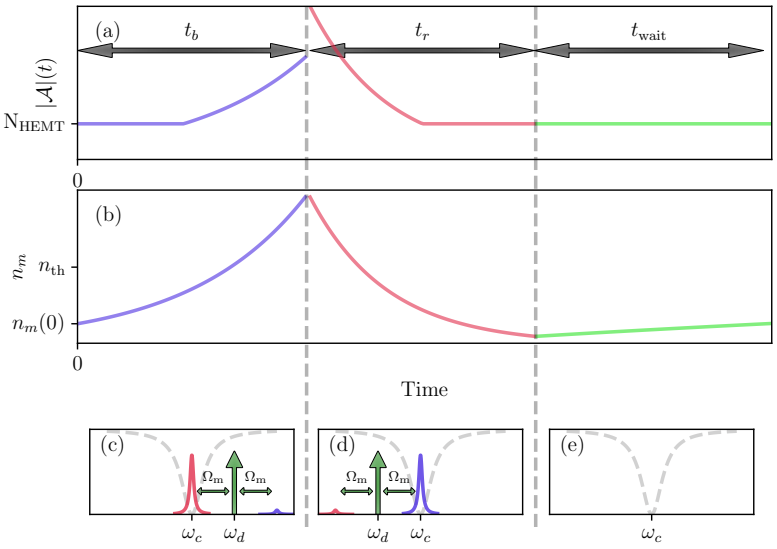

Figure VII.9: (a) Typical evolution of the measured amplitude $|\mathcal{A}|(t)$ over one realization of the experiment. The value N_{HEMT} corresponds to the limiting noise of the experiment, which is in our case the noise from the HEMT amplifier.(b) Corresponding evolution of the mechanical occupation $n_{\text{m}}(t)$. n_{th} corresponds to the occupation of the resonator thermalized with the environment. (c) First part of the sequence : a strong blue pulse is applied by setting $\omega_d = \omega_c + \Omega_{\text{m}}$ for a time t_b.(d) Second part: a strong red pulse is applied by setting $\omega_d = \omega_c - \Omega_{\text{m}}$ for a time t_r. (e) Last part: no pulse is sent for a time t_{wait}.

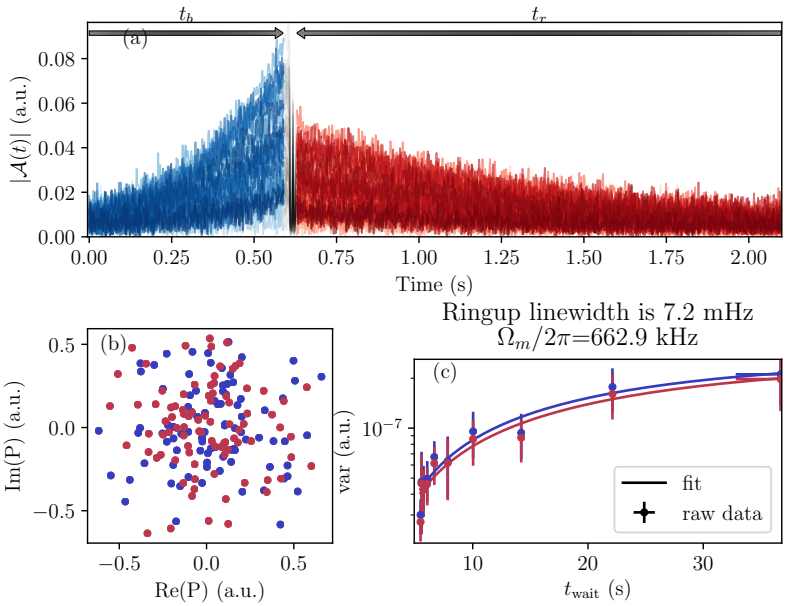

Figure VII.10: (a) For the parameters $t_{\text{wait}} = 0.1$s, $t_b = 0.7$ s and $t_r = 4.5$ s, a few experimental time traces are presented, taken from the BM2 sample. From those traces the waveform is inferred using the method proposed in [MFL13]. In blue (red) are presented the part of the time trace that is used to produce the blue (red) dots of (b) and (c). (b) complex representation of the scalar products of each trace with the inferred waveform. (c) Variance of the scalar products for different value of t_{wait}, together with an exponential fit. The inferred linewidth is ~ 7 mHz

In the previous equations, C_b (C_r) represents the cooperativity during the blue (red) pulse. Those two quantities, along with Γ_m, are already known precisely from previous ringdown serie measurements. From those equations, it is possible to compute the occupation when this cycle is reproduced for a time long enough, by solving the equation $n_\mathrm{m}(t_b + t_r) = n_\mathrm{m}(0)$. We obtain:

$$\frac{n_\mathrm{m}(0)}{n_\mathrm{th}} = \frac{1}{1 - e^{\Gamma_\mathrm{m}((C_b-1)t_b-(C_r+1)t_r)}}\Big[\frac{1}{C_b-1}\left(e^{\Gamma_\mathrm{m}(C_b-1)t_b}-1\right)e^{-\Gamma_\mathrm{m}(C_r+1)t_r} + \frac{1}{C_r+1}\left(1-e^{-\Gamma_\mathrm{m}(C_r+1)t_r}\right)\Big] \quad \text{(VII.2.6)}$$

In the dataset presented in figure VII.10, this cooling factor was equal to $\frac{n_\mathrm{m}(0)}{n_\mathrm{th}} \sim 0.142$ when extracted from the blue pulse, or $\frac{n_\mathrm{m}(0)}{n_\mathrm{th}} \sim 0.138$ when extracted from the red pulse. This results agrees fairly well with the formula VII.2.6, which predicts $\frac{n_\mathrm{m}(0)}{n_\mathrm{th}} \sim 0.146$.

For $t_\mathrm{wait} \gg \frac{1}{\Gamma_\mathrm{m}}$, the mechanical state has time to thermalize with its environment, and the variance is therefore proportional to the natural occupation of the mechanical resonator. The variance is fitted with an exponential formula:

$$\mathrm{Var}(t_\mathrm{wait}) = A + B\exp(-\Gamma_\mathrm{m} t_\mathrm{wait}). \quad \text{(VII.2.7)}$$

and the linewidth is retrieved. The measured value, $\Gamma_\mathrm{m}/2\pi \sim 7.7$mHz, is on the same order of magnitude than the values measured more precisely using ringdown techniques ($\Gamma_\mathrm{m}/2\pi \sim 36$mHz).

Note that for a higher pump power, the results obtained from the red pulse and the blue pulse does not agree anymore (see figure VII.11). In particular, the time trace amplitude does not agree with the theoretical predictions. Indeed, when the cooperativity is increased, the exponential characteristic time of the time trace is reduced as expected, but the time trace is also supposed to be proportional to the cooperativity. In figure VII.11(a), it is clearly not the case. Although we do not know the precise mechanism that creates those discrepancies in our case, discrepancies between the informations gathered in the red and blue pulse have been reported in more elaborated experiments, where two pulses are used simultaneously, one of them on the blue sideband, the other on the red sideband [DRAL19, SYS$^+$19]. The extra phase noise the pump exhibits at extreme powers (see section V.2.a) may also be the cause of such phenomenon. Finally, it could also be linked to thermal effects the high pump powers induces on the cyostat.

To conclude, we presented in this section a technique which uses the optomechanical interaction to amplify the microwave signals well above the HEMT noise limit, and to retrieve the initial mechanical oscillator occupation. This technique might help to provide the first electromechanical experiment in the ground state performing thermometry without quantum limited amplifier such as Josephson Parametric Amplifiers or Traveling Wave Parametric Amplifiers. In the next section, we will present an application such a mechanical oscillator brought in its motional ground state through sideband resolved cooling could lead to.

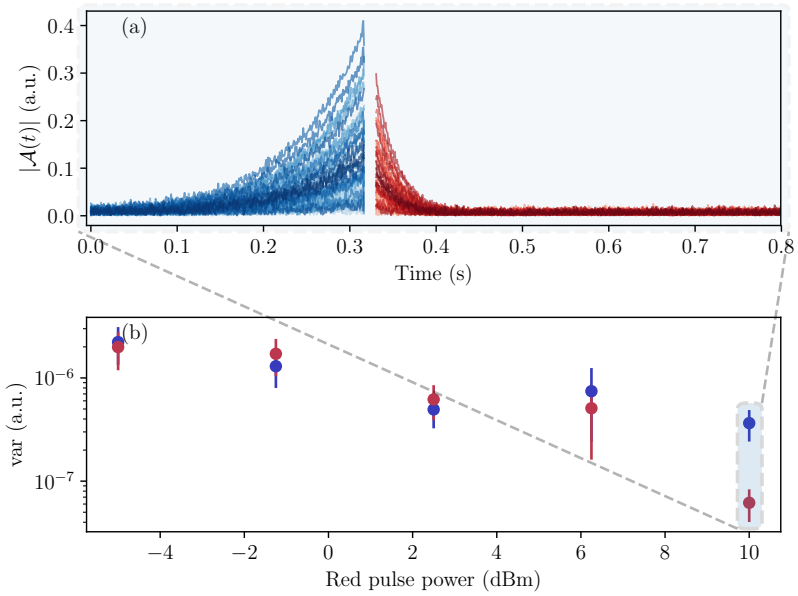

Figure VII.11: (a) Same results than figure VII.10(a), for a very high red pulse power ($P_{\mathrm{r,in}} = 10\mathrm{dBm}$), and blue power ($P_{\mathrm{b,in}} = 5\mathrm{dBm}$). t_{wait} is set to 0.(b) Variation of the measured variance on the blue pulse and the red pulse for various pump powers.

VII.3: Generating non Gaussian states of motion

Close to its motional quantum ground state, a mechanical oscillator behavior cannot be described by classical physics. However, the scope of quantum mechanics goes far beyond the family of gaussian states, and being able to prepare a mechanical oscillator exhibiting negative Wigner functions is a milestone that has drawn increasing attention in the past years[RMT$^+$17, SMVL19].

First, such a result would be a prerequisite in the making of a hybrid optomechanical transducer that transforms microwave into optical quantum information[APP$^+$14]. This application would benefit from the maturity of the techniques used in the circuit Quantum Electro-Dynamics (cQED) community to create and manipulate easily quantum information along with the ability to transport quantum information at room temperature on very long distances that exists in the optical domain.

Moreover, being able to build quantum superpositions of different mechanical states and probing their decoherence would enable the testing of certain theories regarding the influence of gravity on quantum mechanics[AH14].

In this section, we propose a scheme to generate single phonon Fock states in a mechanical resonator, based on a heralding experiment which relies on a single microwave photons detector. We then present the principle of a single microwave photon detector that was developed in the group of Zaki Leghtas at LPENS [LDA$^+$20].

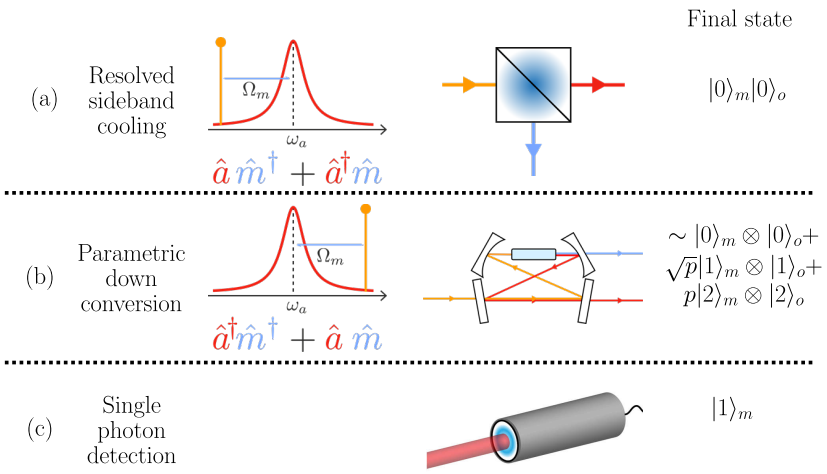

Figure VII.12: The three steps of the proposed heralding scheme: (a) sideband resolved cooling of a mechanical oscillator to its ground state. (b) Parametric down conversion using a blue detuned drive on the optomechanical cavity. (c) Detection of a single photon, which projects the mechanical state to the Fock state with 1 phonon.

VII.3.a: Heralding scheme

As seen in the previous chapters, an optomechanical system is a powerful tool to manipulate the state of a mechanical oscillator. However, if some observations have been performed of optomechanical systems operating in a nonlinear regime [BVL+16, LLGF+17], the optomechanical Hamiltonian is a purely linear interaction in the regime we are usually working with. This precludes the generation of non-Gaussian states with a Gaussian state (which are the initial thermal states of the mechanical and optical system) at the input: a nonlinear element has to be introduced.

Although we may use a non classical state at the electromagnetic input of the system, by using for instance a single photon source —which is then the nonlinear element— [RMT+17], the scheme we propose here is based on a very different approach, that was pioneered in the optical domain by the group of Simon Gröblacher [RSN+16] (see figure VII.12).

When an optomechanical system in the sideband resolved regime is pumped on its blue sideband ($\omega_d = \omega_c + \Omega_\mathrm{m}$), the linearized optomechanical Hamiltonian reads (see section I.4.c):

$$H_\mathrm{int} = \hbar g_0 \left(\alpha \hat{a}^\dagger \hat{b}^\dagger + \alpha^* \hat{a}\hat{b}\right), \tag{VII.3.1}$$

where g_0 is the optomechanical coupling rate, α the average number of photons in the cavity due to the strong pump, and $\hat{a}$ ($\hat{b}$) is the optical (mechanical) annihilation operator. Under such interaction, a system initially in its optical and mechanical ground state (which was previously reached by sideband cooling for instance) reaches after a short time the state:

$$|\Psi\rangle \approx |0\rangle_\mathrm{m} \otimes |0\rangle_o + \sqrt{p}|1\rangle_\mathrm{m} \otimes |1\rangle_o + p|2\rangle_\mathrm{m} \otimes |2\rangle_o, \tag{VII.3.2}$$

where p is the probability for a Stokes scattering to happen, and m (n) subscripts refer to the mechanical (optical) mode. This state is a two mode squeezed state. However, it

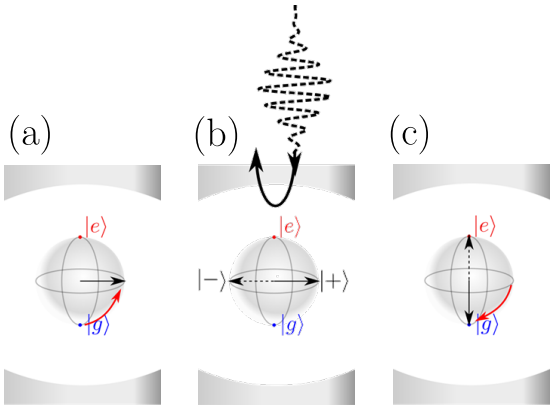

Figure VII.13: (a) Initialization of the qubit with a $\pi/2$ pulse. (b) Detection window: the evolution of the qubit is dependant of the presence or not of a photon in the cavity. (c) Another $\pi/2$ pulse project the qubit in a given state depending on the presence or absence of a photon during the detection window.

is still a Gaussian state and has a positive Wigner function. Nonetheless, if we place at the output of the electromagnetic cavity a single photon resolved detector, it is possible to post-select (or *herald*) the experiments where this detector detects a photon. Indeed, at each detection, the state of the mechanical oscillator is projected into the 1 photon Fock state, which is a highly nonclassical sate. Crucially, this protocol, if used with a low number of false positive detection or "dark count", allows to circumvent the loss inevitably present in the circuits connecting the various components of the setup.

One of the experimental difficulties of such experiment is to design a detector able to resolve the energy of a single photon. This is particularly challenging in the microwave domain, where the low energy of the latter precluded until recently [ILK+16, LDA+20] to reach this milestone with a sufficiently low dark count for this proposal. In the following subsection, we will present the results obtained by Zaki Leghtas's group at LPENS in succeeding to build a single photon microwave detector.

VII.3.b: Single microwave photon detector

The detection of single microwave photons has first been performed using Ramsey interferometry in the atomic physics community [GKG+07, NRO+99], and later on in the circuit Quantum Electro-Dynamics (cQED) community[SHS+07, BGC+18].

The principle is as follows (see figure VII.13): a qubit is set in a state:

$$|\phi\rangle = \frac{1}{\sqrt{2}}\left(|0\rangle + |1\rangle\right), \tag{VII.3.3}$$

where $|0\rangle$ and $|1\rangle$ stands for the ground state and the excited state of the qubit, respectively. This operation is done through a $\pi/2$ pulse: a microwave tone is sent a the frequency corresponding to the level splitting of the qubit, for a time long enough for performing a quarter of a Rabbi oscillation. Then, for a given measurement time, small compared to the decoherence time of the qubit, we let the qubit evolve. If a single photon appears, this evolution will differ from the case where no photon appears. For

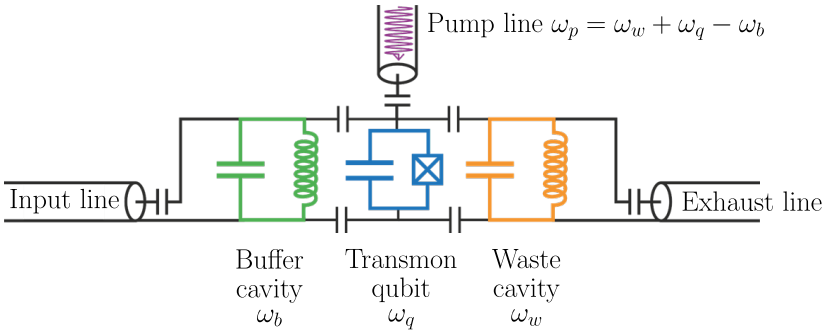

Figure VII.14: Schematics of the Single Photon Microwave Detector.

instance, if there is a detuning $\delta/2\pi$ between the qubit and the cavity frequencies, the superposition acquires a phase, which can be tuned to π for one photon by playing on the parameter δ.

This information is retrieved by first sending another $\pi/2$ pulse. If the qubit is still in the state $|\phi\rangle$, it will be transformed into the state $|0\rangle$. However, if the qubit has evolved due to an interaction with a microwave photon such that it is now in the state:

$$|\psi\rangle = \frac{1}{\sqrt{2}}\left(|0\rangle - |1\rangle\right), \tag{VII.3.4}$$

it will be projected in the state $|1\rangle$. The state of the qubit is then read by measuring its frequency. Measuring a $|1\rangle$ corresponds to a "click". If this scheme is producing detections of single microwave photons with high efficiencies, the fact that it encodes the information of the presence or absence of a photon in the phase of a quantum superposition makes it really sensitive to decoherence mechanisms. Consequently, when the measurement time is longer than the T_2 of the qubit, the dark count rate rises significantly. For example, in Besse et al. [BGC$^+$18], if the efficiency is approximately 60%, the dark count after 2μs of integration is as high as $\sim 40\%$. In a heralding scheme such as the one proposed here, a low efficiency reduces the number of events with a phononic Fock state. This only increases the time needed for acquiring some data. However, a high dark count reduces the quality of those states, since events where the mechanical oscillator is in fact not in a Fock state will be mixed with events where it is.

Alternatively, the method proposed for detecting single microwave photons is here based on a "reservoir engineering" technique to drive the system by dissipation towards the desired state, thus avoiding decoherence effects.

The design is the following (see figure VII.14): it comprises three cavities. The first one, called the buffer cavity, with a frequency $\omega_b/2\pi \sim 5.77$ GHz, is strongly coupled to the input line from which we want to count the microwave photons. The second one is a transmon qubit: a microwave cavity with a nonlinear inductance which allows to address two internal levels with their frequency difference $\omega_q/2\pi \sim 4.53$GHz. The third cavity is a waste cavity, whose frequency is $\omega_w/2\pi \sim 5.50$GHz. This last cavity is strongly coupled to a RF line we will refer to as the exhaust line. The transmon qubit is coupled to the two other cavities, as well as a pump line. The Hamiltonian of such system is highly nonlinear. However, in close analogy with the linearization

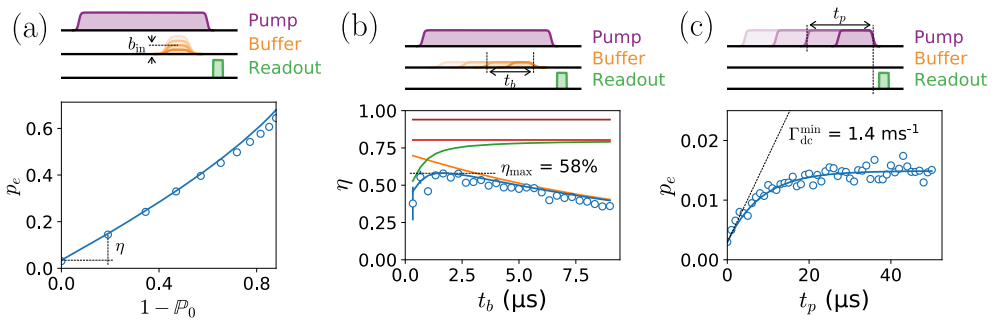

Figure VII.15: Characterization of the detector (See main text for details) (a) The amplitude b_in is varied and the probability to measure the qubit in the excited state is ploted versus the 1 minus the probability for the buffer cavity to be in the vacuum. The slope at small amplitude is a measure of η, the efficiency, and the y value for low amplitude is a measure of the dark count. (b) Variation of the efficiency η with the duration of the input pulse (dots). (Straight line): model taking into account three contributions to this efficiency. First, the orange curve corresponds to the T_1 limitation of the qubit. Second, the green curve correspond to the bandwidth limitation of the buffer cavity. Finally, the red curve corresponds to the value predicted by equation VII.3.8.(c) Without any photons at the input, the dark count is measured for different detection window time t_d.

which is operated in optomechanics (see section I.3.b), a strong pump can be used to "select" the right terms in this Hamiltonian by looking at small displacements around the state of the system displaced by the pump. For instance, under a strong pump at the frequency:

$$\omega_p = \omega_w + \omega_q - \omega_b, \tag{VII.3.5}$$

its Hamiltonian reads[LDA+20]:

$$\hat{H} = \chi \hat{b}\hat{\sigma}^\dagger \hat{w}^\dagger + \chi^* \hat{b}^\dagger \hat{\sigma} \hat{w}. \tag{VII.3.6}$$

In eq. VII.3.6, $\hat{b}$ ($\hat{w}$) represents the annihilation operator of a photon in the buffer (waste) cavity, $\hat{\sigma}^\dagger$ is the operator that creates an excitation in the qubit, and χ is a rate proportional to the pump amplitude. The first term in the Hamiltonian corresponds to the destruction of a photon in the buffer cavity together with the creation of an excitation in the qubit and a photon in the waste cavity. This encodes the presence of a single photon in an excitation of the qubit. The readout of the qubit is then performed by a measurement of the frequency of the waste cavity while the pump is turned off.

Crucially, the reverse process, corresponding to the second term of the Hamiltonian, is never happening. Indeed, due to the strong coupling between the waste cavity and the exhaust line, the waste cavity is almost always empty of photons. Note that this reverse process can be manually triggered by sending a strong pulse to the exhaust line directly, while the pump is turned on. This operation performs a reset of the system after a readout.

It is possible to derive the irreversible dynamics of the buffer-qubit subsystem by adiabatically eliminating the waste mode[LDA+20]. The dynamics is then described

by a single loss operator:

$$\hat{L} = \sqrt{\kappa_{nl}}\hat{b}\hat{\sigma}^{\dagger}, \tag{VII.3.7}$$

where $\kappa_{nl} \overset{\text{def}}{=} 4\frac{|\chi|^2}{\kappa_w}$ and κ_w is the coupling rate between the waste and the exhaust line. Consequently, from the buffer-qubit subsystem perspective, photons are entering at a rate κ_b, the coupling rate between the buffer and the input line, and are dissipated to the desired output state at a rate κ_{nl}. The resulting efficiency η, defined as the probability to have a click when there is a single photon at the input, reads, for input photons inside the bandwidth $(\kappa_{nl} + \kappa_b)/2\pi$:

$$\eta = 4\frac{\kappa_{nl}\kappa_w}{(\kappa_{nl} + \kappa_w)^2}. \tag{VII.3.8}$$

The characterization of the system has been performed as follows (see figure VII.15): the pump is turned on for a time t_p, and a coherent field with small amplitude b_{in} is presented at the input line for a time t_b. After this, the pump is turned off and a readout of the qubit is performed. First, the amplitude b_{in} is varied and the probability to count a click is plotted versus the probability for the input state to be in the vacuum. The slope at origin is a measure of η, and the probability of having a click with no photon at the input is the measure of the dark count. Then, η is measured for different time t_b.

The value predicted by eq. VII.3.8 has to be corrected by two other effects. First, for t_b superior to or comparable to the T_1 of the qubit, the excitation due to the click can disappear before the readout, thus limiting the efficiency. Then, for t_b smaller than the inverse of the bandwidth of the cavity $\frac{1}{\kappa_{nl}+\kappa_b}$, the input wavepacket is partly reflected by the cavity, also reducing η. Those two effects are taken into account in figure VII.15(b) with a remarkably good agreement with measured data. The maximum measured efficiency is $\eta \approx 58\%$, which is comparable to Ramsey interferometry experiments.

Finally, The dark count is measured with no photon at the input line for various times t_p. The measured value saturates quickly at $\approx 1.5\%$, even after 40μs. At low time, the measured value of the dark count is:

$$p_e = 0.003 + \Gamma_{dc} \times t_p, \tag{VII.3.9}$$

with a minimum value of Γ_{dc} close to $\sim 1.4(ms)^{-1}$. This value is lower by one order of magnitude to values previously reported in the literature [ILK+16, NSH+16, BGC+18].

To conclude, in this section we described a proposal to generate mechanical Fock state using the optomechanical cavity described in the previous chapters, previously cooled down to the motional ground state of the mechanical resonator, and using heralded projection based on measurements with a single photon detector. We also demonstrated a microwave single photon detector with high efficiency and an all time low dark count rate, which is a critical parameter in the proposed scheme. Although some technical difficulties are still under investigation —such as the filtering of the microwave pump between the optomechanical cavity and the single photon detector— most of the basic elements of this proposal have been demonstrated.

Conclusion

In this work, we presented in a first chapter the theoretical framework of cavity optomechanics. In a second chapter, we described the fabrication and room temperature characterization of high quality factor mechanical resonators which are optimized for being cooled down to their motional ground state using sideband resolved cooling. Those resonators were highly stressed thin square membranes of Silicon Nitride. In the third chapter, we presented the different coupling mechanisms we studied for reaching this milestone. First of all, we studied microwave resonators based on interdigitated capacitors, at the vicinity of which the purely dielectric membranes presented in the previous chapter are dielectrically coupled. Unfortunately, we have not succeeded in observing this coupling experimentally. Nonetheless, we used those resonators to validate numerous fabrication and characterization recipes, and to understand an important loss mechanism of most microwave resonators, the Two Level System Losses. This study resulted in a publication[CFI+20], which is presented in details in chapter VI.

Then, we shifted our approach towards the use of mechanically compliant capacitors. In this configuration, we observed optomechanical coupling. The characterization techniques we performed on our systems are presented in chapter IV. In the same chapter, we also described several optimizations of our design we perfomed. Although this evolution required the metallization of the membranes, we were able to demonstrate extremely high quality factors ($Q > 300 \times 10^6$) at low temperature.

In chapter V, we cooled the mechanical oscillators to an occupation of ~ 274 phonons. Although the ground state was not reached, we identified the main limitations of our system, which corresponds to a low optomechanical coupling, and extra mechanical noise coming from the cryostat. We proposed and experimentally demonstrated otpimizations to address those problems. The first one is a new sample box that pushes down the membrane to the microwave resonator, resulting in an increase of the optomechanical coupling of one order of magnitude. The second optimization is a mechanical isolator, which mitigates the noise of the cryostat by a factor ~ 40dB. We believe those two optimizations might lead to the milestone of ground state cooling.

Finally, in chapter VII, we described three future directions of this project, together with preliminary data. In a first section, we proposed to implement patterned membranes in lieu of the square membranes presented in chapter II. Indeed, those membranes exhibit higher mechanical frequencies, which is beneficial when working

with noisy microwave sources, as well as with the mitigation of the extra noise of the cryostat. Furthermore, those membranes exhibits considerably larger mechanical quality factors. We developed nanofabrication recipes and were able to characterize those membrane at room temperature. We measured an increase of quality factor by a factor of ~ 6 compared with square membranes.

In a second section, we proposed and successfully demonstrate a technique which aims at circumventing the noise of HEMT amplifier in electromechanics setup. To this ens, the electromechanical cavity itself is used as a quantum limited amplifier, by pumping it on the blue sideband for a short time. We experimentally demonstrated a scheme to extract some informations on the mechanical resonator with this technique.

Finally, in the last section, we proposed a scheme to set the mechanical resonator in a single phonon Fock state, which is highly non classical and is of high interest in many fundamental physics experiment. This scheme requires to reach the ground state beforehand, and is based on heralded measurements with a single photon detectors. This kind of detector did not exist until recently in the microwave domain with low enough dark count to operate this scheme successfully. However, Zaki Leghtas's group at LPENS developed such a detector[LDA$^+$20], and its characterization is presented in the last part of this section.

Appendices

Chapter A: MAXWELL-BLOCH EQUATIONS IN THE PRESENCE OF DEPHASING

The interaction of a single TLS with a cavity is described by the Jaynes-Cummings Hamiltonian (in a frame rotating at the pump frequency ω_p):

$$H = \hbar(\omega_\mathrm{p} - \omega_\mathrm{c})\hat{a}^\dagger\hat{a} + \frac{\hbar(\omega_\mathrm{p} - \omega_\mathrm{q})}{2}\boldsymbol{\sigma_z} \tag{I.0.1}$$

$$+ i\hbar g(\hat{a}^\dagger\boldsymbol{\sigma} - \hat{a}\boldsymbol{\sigma}^\dagger) + i\hbar J\left(\hat{a}^\dagger - \hat{a}\right), \tag{I.0.2}$$

where $J = a_\mathrm{in}\kappa_\mathrm{ext}/\sqrt{2}$ is supposed to be real without loss of generality (the factor $\sqrt{2}$ accounts for a "hanger-type" waveguide coupling). The dissipation is described by the Lindblad equation:

$$\frac{d\rho}{dt} = -\frac{i}{\hbar}[\boldsymbol{H}, \rho] + \Gamma_{\uparrow\downarrow}(n_\mathrm{th} + 1)\mathcal{D}_{\boldsymbol{\sigma}}(\rho) + \frac{\Gamma_\phi}{2}\mathcal{D}_{\boldsymbol{\sigma_z}}(\rho) \tag{I.0.3}$$

$$+ \Gamma_{\uparrow\downarrow} n_\mathrm{th}\mathcal{D}_{\boldsymbol{\sigma}^\dagger}(\rho) + \kappa_\mathrm{ext}\mathcal{D}_{\hat{a}}(\rho), \tag{I.0.4}$$

with $n_\mathrm{th} = \frac{1}{e^{\hbar\omega/kT}-1}$ the occupation number of the TLS, κ_ext the damping of the cavity in the absence of TLS, Γ_ϕ the eventual TLS dephasing rate, $\Gamma_{\uparrow\downarrow}$ its energy loss rate at zero temperature, and

$$\mathcal{D}_{\boldsymbol{A}}(\rho) = \boldsymbol{A}\rho\boldsymbol{A}^\dagger - \frac{1}{2}(\boldsymbol{A}^\dagger\boldsymbol{A}\rho + \rho\boldsymbol{A}^\dagger\boldsymbol{A}).$$

Using the formulas $\langle\boldsymbol{A}\rangle = \mathrm{tr}(\boldsymbol{A}\rho)$ and $\frac{d}{dt}\langle\boldsymbol{A}\rangle = \mathrm{tr}\Big(\boldsymbol{A}\frac{d}{dt}\rho\Big)$, one can compute the Maxwell-Bloch equations

$$\frac{d\langle\hat{a}\rangle}{dt} = (-i\Delta - \frac{\kappa_\mathrm{ext}}{2})\langle\hat{a}\rangle + g\langle\boldsymbol{\sigma}\rangle + J \tag{I.0.5}$$

$$\frac{d\langle\boldsymbol{\sigma}\rangle}{dt} = (-i(\omega_\mathrm{p} - \omega_\mathrm{q}) - \Gamma_2)\langle\boldsymbol{\sigma}\rangle + g\langle\hat{a}\boldsymbol{\sigma_z}\rangle \tag{I.0.6}$$

$$\frac{d\langle\boldsymbol{\sigma_z}\rangle}{dt} = -2g(\langle\hat{a}^\dagger\boldsymbol{\sigma}\rangle + \langle\hat{a}\boldsymbol{\sigma}^\dagger\rangle) - \Gamma_1\left(\langle\boldsymbol{\sigma_z}\rangle - \langle\boldsymbol{\sigma_z}\rangle_\mathrm{th}\right), \tag{I.0.7}$$

where we defined $\Gamma_2 = \frac{\Gamma_{\uparrow\downarrow}}{2}(1+2n_{\rm th})+\Gamma_\phi$, $\Gamma_1 = \Gamma_{\uparrow\downarrow}(1+2n_{\rm th})$, $\langle\boldsymbol{\sigma_z}\rangle_{\rm th} = -1/(1+2n_{\rm th}) = -\tanh(\hbar\omega/2k_{\rm B}T)$ and $\Delta = \omega_{\rm p} - \omega_{\rm c}$.

Chapter B: APPENDIX B: FULL DERIVATION OF THE TWO LEVEL SYSTEMS INDUCED LOSSES MODEL

To transform this system ((I.0.5), (I.0.6), and (I.0.7)) into a closed set of equations, we neglect the correlations and factorize the products $\langle \hat{a}\boldsymbol{\sigma_z}\rangle = \langle \hat{a}\rangle\langle\boldsymbol{\sigma_z}\rangle$, $\langle \hat{a}^\dagger\boldsymbol{\sigma}\rangle = \langle \hat{a}^\dagger\rangle\langle\boldsymbol{\sigma}\rangle$ and $\langle \hat{a}\boldsymbol{\sigma}^\dagger\rangle = \langle \hat{a}\rangle\langle\boldsymbol{\sigma}^\dagger\rangle$. Moreover, we decompose the mean values into semi-classical stationary and modulated components $\langle \hat{a}\rangle = \alpha + \delta\alpha(t)e^{-i\Delta t}$, $\langle\boldsymbol{\sigma}\rangle = \sigma_0 + \delta\sigma(t)e^{-i\Delta t}$, $\langle\boldsymbol{\sigma_z}\rangle = \sigma_{z0}$, and with $\delta\alpha(t)$ and $\delta\sigma(t)$ slowly varying complex functions. The equations for the stationary components then read:

$$0 = (-i\Delta - \kappa_{\text{ext}}/2)\alpha + g\sigma_0 + J \tag{II.0.1}$$

$$0 = (-i(\omega_p - \omega_q) - \Gamma_2)\sigma_0 + g\alpha\sigma_{\text{z0}} \tag{II.0.2}$$

$$0 = -2g(\alpha^*\sigma_0 + \alpha\sigma_0^*) - \Gamma_1(\sigma_{\text{z0}} - \langle\boldsymbol{\sigma_z}\rangle_{\text{th}}), \tag{II.0.3}$$

From Eq. (II.0.2), we get:

$$\sigma_0 = \frac{g\alpha\sigma_{\text{z0}}}{i(\omega_{\text{p}} - \omega_{\text{q}}) + \Gamma_2}. \tag{II.0.4}$$

and from Eq. (II.0.3), we obtain the population imbalance resulting from the saturation of the transition by the pump field

$$\sigma_{z0} = \langle\boldsymbol{\sigma_z}\rangle_{\text{th}}\left(1 - \frac{\Gamma_2^2\bar{n}/n_{\text{s}}}{(\omega_{\text{q}} - \omega_{\text{p}})^2 + \Gamma_2^2(1 + \bar{n}/n_{\text{s}})}\right), \tag{II.0.5}$$

where $\bar{n} = |\alpha|^2$ is the mean photon number in the cavity and $n_{\text{s}}^{-1} = 4g^2/\Gamma_1\Gamma_2$ the number of photons required to saturate the TLS transition. We then solve for the modulated parts by adiabatically eliminating the TLS dynamic ($\text{d}\delta\sigma/\text{d}t = 0$). From Eq. (I.0.5), we obtain

$$\dot{\delta\alpha} = -\kappa_{\text{ext}}\delta\alpha/2 + g\delta\sigma, \tag{II.0.6}$$

and from Eq. (I.0.6)

$$\delta\sigma = \frac{g\sigma_{z0}\delta\alpha}{-i(\omega_c - \omega_q) - \Gamma_2}. \tag{II.0.7}$$

By substituting Eq. (II.0.7) into Eq. (II.0.6), we obtain

$$\dot{\delta\alpha} = \left(-\kappa_{ext}/2 + \frac{g^2\sigma_{z0}}{i(\omega_c - \omega_q) + \Gamma_2}\right)\delta\alpha. \tag{II.0.8}$$

Hence, the complex frequency pull is given by

$$\delta\omega = \frac{g^2\sigma_{z0}}{(\omega_q - \omega_c) + i\Gamma_2}. \tag{II.0.9}$$

In turn, the population difference $\langle\boldsymbol{\sigma_z}(\omega_q)\rangle$ of a single TLS induces a shift of the complex cavity frequency [KSB+17]

$$\delta\omega = \frac{g^2\langle\boldsymbol{\sigma_z}(\omega_q)\rangle}{\omega_q - \omega_c + i\Gamma_2}. \tag{II.0.10}$$

We also compute the total frequency shift and damping by summing the individual contributions of all the TLSs. If we assume a homogeneous distribution of frequencies of the TLS, with a density P_0, we have the following

$$\delta\omega_c = \int_{-\infty}^{\infty} d\omega_q \frac{P_0}{2\pi}\frac{g^2\sigma_{z0}}{\omega_q - \omega_c + i\Gamma_2} \tag{II.0.11}$$

$$= \int \langle\boldsymbol{\sigma_z}\rangle_{th}\left(1 - \frac{\Gamma_2^2\bar{n}/n_s}{(\omega_q - \omega_p)^2 + \Gamma_2^2(1 + \bar{n}/n_s)}\right) \tag{II.0.12}$$

$$\times \frac{P_0 g^2}{(\omega_q - \omega_c) + i\Gamma_2}\frac{d\omega_q}{2\pi}. \tag{II.0.13}$$

This integral can be interpreted as the convolution product

$$\delta\omega_c(\Delta) = \langle\boldsymbol{\sigma_z}\rangle_{th} P_0 g^2 \times \tag{II.0.14}$$

$$\left[\left(1 - \frac{\Gamma_2^2\bar{n}/n_s}{\omega^2 + \Gamma_2^2(1 + \bar{n}/n_s)}\right) \otimes \frac{1}{\omega + i\Gamma_2}\right](\Delta). \tag{II.0.15}$$

Using standard Fourier transforms and the convolution theorem, we derive the expression

$$\delta\omega_c = -P_0 g^2\langle\boldsymbol{\sigma_z}\rangle_{th}/2 \times \tag{II.0.16}$$

$$\left(i + \frac{\bar{n}/n_s}{\sqrt{1 + \bar{n}/n_s}}\frac{1}{\Delta/\Gamma_2 + i(1 + \sqrt{1 + \bar{n}/n_s})}\right). \tag{II.0.17}$$

The real and double-imaginary parts of this expression, given by formula (VI.2.3) and (VI.2.4), correspond to the frequency shift and damping induced by the TLS bath.

Bibliography

[AAWW+19] Patricio Arrangoiz-Arriola, E. Alex Wollack, Zhaoyou Wang, Marek Pechal, Wentao Jiang, Timothy P. McKenna, Jeremy D. Witmer, Raphaël Van Laer, and Amir H. Safavi-Naeini. Resolving the energy levels of a nanomechanical oscillator. *Nature*, 571:537–540, 2019. 35

[AH14] Markus Arndt and Klaus Hornberger. Testing the limits of quantum mechanical superpositions. *Nature Physics*, 10:271–277, 2014. 159

[APP+14] R. W. Andrews, R. W. Peterson, T. P. Purdy, K. Cicak, R. W. Simmonds, C. A. Regal, and K. W. Lehnert. Bidirectional and efficient conversion between microwave and optical light. *Nature Physics*, 10:321–326, 2014. 5, 122, 159

[Ash78] A. Ashkin. Trapping of atoms by resonance radiation pressure. *Phys. Rev. Lett.*, 40:729–732, Mar 1978. 3

[BBG+19] P. A. Bushev, J. Bourhill, M. Goryachev, N. Kukharchyk, E. Ivanov, S. Galliou, M. E. Tobar, and S. Danilishin. Testing the generalized uncertainty principle with macroscopic mechanical oscillators and pendulums. *Phys. Rev. D*, 100:066020, Sep 2019. 113

[BFL16] J Burnett, L Faoro, and T Lindström. Analysis of high quality superconducting resonators: consequences for TLS properties in amorphous oxides. *Superconductor Science and Technology*, 29(4):044008, mar 2016. 139, 141

[BFW+14] J Burnett, L Faoro, I Wisby, V L Gurtovoi, A V Chernykh, G M Mikhailov, V A Tulin, R Shaikhaidarov, V Antonov, P J Meeson, and T Lindstro. Evidence for interacting two-level systems from the 1/ f noise of a superconducting resonator. *Nature communications*, 5(May):4119, 2014. 141

[BGC+18] Jean-Claude Besse, Simone Gasparinetti, Michele C. Collodo, Theo Walter, Philipp Kurpiers, Marek Pechal, Christopher Eichler, and Andreas Wallraff. Single-shot quantum nondemolition detection of individual itinerant microwave photons. *Phys. Rev. X*, 8:021003, Apr 2018. 161, 162, 164

[BLA+15] A Bruno, G De Lange, S Asaad, K L Van Der Enden, N K Langford, and L Dicarlo. Reducing intrinsic loss in superconducting resonators by surface treatment and deep etching of silicon substrates. *Appl. Phys. Lett.*, 182601(May):4–8, 2015. 131, 141

[BM67] V. B Braginski and A. B. Manuskin. Ponderomotive effects of electromagnetic radiation. *SOVIET PHYSICS JETP*, 25, 1967. 3

[BMT70] V. B Braginski, A. B. Manuskin, and M. Yu Tikhonov. Ponderomotive effects of electromagnetic radiation. *SOVIET PHYSICS JETP*, 31, 1970. 3

[BVL+16] G. A. Brawley, M R. Vanner, P. E. Larsen, S. Schmid, A. Boisen, and W. P. Bowen. *Nature Communications*, 7:10988, 2016. 160

[CAL+19] Jonathan Cripe, Nancy Aggarwal, Robert Lanza, Adam Libson, Robinjeet Singh, Paula Heu, David Follman, Garret D. Cole, Nergis Mavalvala, and Thomas Corbitt. Measurement of quantum back action in the audio band at room temperature. *Nature*, 568:364–367, 2019. 23

[CASN+11] Jasper Chan, T. P. Mayer Alegre, Amir H. Safavi-Naeini, Jeff T. Hill, Alex Krause, Simon Gröblacher, Markus Aspelmeyer, and Oskar Painter. Laser cooling of a nanomechanical oscillator into its quantum ground state. *Nature*, 478:89–92, 2011. 4, 35

[Cav81] Carlton M. Caves. Quantum-mechanical noise in an interferometer. *Phys. Rev. D*, 23:1693–1708, Apr 1981. 4

[CC16] LIGO Scientific Collaboration and Virgo Collaboration. Observation of gravitational waves from a binary black hole merger. *Phys. Rev. Lett.*, 116:061102, Feb 2016. 4

[CDG+10] A. A. Clerk, M. H. Devoret, S. M. Girvin, F. Marquardt, and R. J. Schoelkopf. Introduction to quantum noise, measurement and amplification. *Review of Modern Physics*, 82:1155–1208, 2010. 9, 11, 30

[CFI+20] Thibault Capelle, Emmanuel Flurin, Edouard Ivanov, Jose Palomo, Michael Rosticher, Sheon Chua, Tristan Briant, Pierre-Fran çois Cohadon, Antoine Heidmann, Thibaut Jacqmin, and Samuel Deléglise. Probing a two-level system bath via the frequency shift of an off-resonantly driven cavity. *Phys. Rev. Applied*, 13:034022, Mar 2020. 6, 54, 83, 131, 165

[CKY+18] Yiwen Chu, Prashanta Kharel, Taekwan Yoon, Luigi Frunzio, Peter T. Rakich, and Robert J. Schoelkopf. Creation and control of multi-phonon fock states in a bulk acoustic-wave resonator. *Nature*, 563:666–670, 2018. 5, 35

[CMW+18] G. Calusine, A. Melville, W. Woods, R. Das, C. Stull, V. Bolkhovsky, D. Braje, D. Hover, D. K. Kim, X. Miloshi, D. Rosenberg, A. Sevi, J. L.

Yoder, E. Dauler, and W. D. Oliver. Analysis and mitigation of interface losses in trenched superconducting coplanar waveguide resonators. *Appl. Phys. Lett.*, 112(6):062601, 2018. 131

[Col05] Virgo Collaboration. Measurement of the seismic attenuation performance of the virgo superattenuator. *Astroparticle Physics*, 23(6):557 – 565, 2005. 124

[CRMS20] Junxin Chen, Massimiliano Rossi, David Mason, and Albert Schliesser. Entanglement of propagating optical modes via a mechanical interface. *Nature Communications*, 11, 2020. 113

[CtBF18] C. Cohen-tannoudji, Diu B., and Laloë F. *Quantum mechanics*, volume 1. 2018. 7

[CtDRG97] C. Cohen-tannoudji, J. Dupont-Roc, and G. Grynberg. *Photons and atoms. Introduction to quantum electrodynamics.* 1997. 11

[DBS+10] Lu Ding, Christophe Baker, Pascale Senellart, Aristide Lemaitre, Sara Ducci, Giuseppe Leo, and Ivan Favero. High frequency gaas nano-optomechanical disk resonator. *Phys. Rev. Lett.*, 105:263903, Dec 2010. 35

[DHL+05] E. A. Donley, T. P. Heavner, F. Levi, M. O. Tataw, and S. R. Jefferts. Double-pass acousto-optic modulator system. *Review of Scientific Instruments*, 76(6):063112, 2005. 49

[DMM+83] A. Dorsel, J. D. McCullen, P. Meystre, E. Vignes, and H. Walther. Optical bistability and mirror confinement induced by radiation pressure. *Phys. Rev. Lett.*, 51:1550–1553, Oct 1983. 16

[DO02] MW Den Otter. Approximate expressions for the capacitance and electrostatic potential of interdigitated electrodes. *Sensors and Actuators, A*, 96:140–144, 2002. 56, 57

[DRAL19] R. D. Delaney, A. P. Reed, R. W. Andrews, and K. W. Lehnert. Measurement of motion beyond the quantum limit by transient amplification. *Phys. Rev. Lett.*, 123:183603, Oct 2019. 11, 152, 158

[DRD+20] Uroš Delić, Manuel Reisenbauer, Kahan Dare, David Grass, Vladan Vuletić, Nikolai Kiesel, and Markus Aspelmeyer. Cooling of a levitated nanoparticle to the motional quantum ground state. *Science*, 367(6480):892–895, 2020. 35

[FEG+19] S. A. Fedorov, N. J. Engelsen, A. H. Ghadimi, M. J. Bereyhi, R. Schilling, D. J. Wilson, and T. J. Kippenberg. Generalized dissipation dilution in strained mechanical resonators. *Phys. Rev. B*, 99:054107, Feb 2019. 35

[FI12] Lara Faoro and Lev B Ioffe. Internal Loss of Superconducting Resonators Induced by Interacting Two-Level Systems. *Phys. Rev. Lett.*, 109(157005):1–5, 2012. 141

[FI15] Lara Faoro and Lev B Ioffe. Interacting tunneling model for two-level systems in amorphous materials and its predictions for their dephasing and noise in superconducting microresonators. *Physical Review B*, 014201(91):1–11, 2015. 141

[FKM+12] T. Faust, P. Krenn, S. Manus, J.P. Kotthaus, and E.M. Weig. Microwave cavity-enhanced transduction for plug and play nanomechanics at room temperature. *Nature Communications*, 3:728, 2012. 36, 54

[FMR+19] R Fischer, D P McNally, C Reetz, G G T Assumpção, T Knief, Y Lin, and C A Regal. Spin detection with a micromechanical trampoline: towards magnetic resonance microscopy harnessing cavity optomechanics. *New Journal of Physics*, 21(4):043049, apr 2019. 5

[FSC+18] Paolo Forni, Alain Sarlette, Thibault Capelle, Emmanuel Flurin, Samuel Deleglise, and Pierre Rouchon. Adiabatic elimination for multipartite open quantum systems with non-trivial zero-order dynamics. In *57th IEEE Conference on Decision and Control, CDC 2018, Miami, FL, USA, December 17-19, 2018*, pages 6614–6619, 2018. 142

[GBC+16] J. Guo, T. Bamber, M Chamberlain, L. Justham, and M. Jackson. Optimization and experimental verification of coplanar interdigital electroadhesives. *Journal of Physics D: Applied Physics*, 49(415304), 2016. 62

[GDM+08] Jiansong Gao, Miguel Daal, John M. Martinis, Anastasios Vayonakis, Jonas Zmuidzinas, Bernard Sadoulet, Benjamin A. Mazin, Peter K. Day, and Henry G. Leduc. A semiempirical model for two-level system noise in superconducting microresonators. *Appl. Phys. Lett.*, 92(21):212504, 2008. 131

[GDS15] K. E. Grutter, M. Davanço, and K. Srinivasan. Si_3n_4 nanobeam optomechanical crystals. *IEEE Journal of Selected Topics in Quantum Electronics*, 21(4):61–71, 2015. 36

[GFE+18] A. H. Ghadimi, S. A. Fedorov, N. J. Engelsen, M. J. Bereyhi, R. Schilling, D. J. Wilson, and T. J. Kippenberg. Elastic strain engineering for ultralow mechanical dissipation. *Science*, 360(6390):764–768, 2018. 36

[GGG+96] K.C. Gupta, K.C. Gupta, R. Garg, I. Bahl, and P. Bhartia. *Microstrip Lines and Slotlines*. ARTECH HOUSE ANTENNAS AND PROPAGATION LIBRARY. Artech House, 1996. 62

[GKG+07] Sébastien Gleizes, Stefan Kuhr, Christine Guerlin, Julien Bernu, Samuel Deléglise, Ulrich Busk Hoff, Michel Brune, Jean-Michel Raimond, and

Serge Haroche. Quantum jumps of light recording the birth and death of a photon in a cavity. *Nature*, 446:297–300, 2007. 161

[GSA+10] M. L. Gorodetksy, A. Schliesser, G. Anetsberger, S. Deleglise, and T. J. Kippenberg. Determination of the vacuum optomechanical coupling rate using frequency noise calibration. *Opt. Express*, 18(22):23236–23246, Oct 2010. 117

[GSE+12] K. Geerlings, S. Shankar, E. Edwards, L. Frunzio, R. J. Schoelkopf, and M. H. Devoret. Improving the quality factor of microwave compact resonators by optimizing their geometrical parameters. *Appl. Phys. Lett.*, 100(19):192601, 2012. 93, 140

[IH89] A. Imamoğlu and S. E. Harris. Lasers without inversion: interference of dressed lifetime-broadened states. *Optics Letters*, 14:1344–1346, 1989. 96

[ILK+16] Kunihiro Inomata, Zhirong Lin, Kazuki Koshino, William D. Oliver, Jaw-Shen Tsai, Tsuyoshi Yamamoto, and Yasunobu Nakamura. Single microwave-photon detector using an artificial λ-type three-level system. *Nature Communications*, 7:12303, 2016. 161, 164

[JWYY18] Zhen-Chuan Jin, Hai-Teng Wu, Hai-Feng Yu, and Yang Yu. Fabrication of al air-bridge on coplanar waveguide. *Chinese Phys. B*, 27(100310), 2018. 106

[Kap17] Eliot Kapit. The upside of noise: engineered dissipation as a resource in superconducting circuits. *Quantum Science and Technology*, 2(3):033002, aug 2017. 142

[Kep19] Johannes Kepler. *De Cometis libelli tres.* 1619. 3

[Ker90] Werner Kern. The evolution of silicon wafer cleaning technology. *Journal of The Electrochemical Society*, 137(6):1887, 1990. 85

[KHK+19] Prashanta Kharel, Glen I. Harris, Eric A. Kittlaus, William H. Renninger, Nils T. Otterstrom, Jack G. E. Harris, and Peter T. Rakich. High-frequency cavity optomechanics using bulk acoustic phonons. *Science Advances*, 5(4), 2019. 35

[KMY+12] Farid Ya. Khalili, Haixing Miao, Huan Yang, Amir H. Safavi-Naeini, Oskar Painter, and Yanbei Chen. Quantum back-action in measurements of zero-point mechanical oscillations. *Phys. Rev. A*, 86:033840, Sep 2012. 21, 33

[KPJ+08] Dustin Kleckner, Igor Pikovski, Evan Jeffrey, Luuk Ament, Eric Eliel, Jeroen van den Brink, and Dirk Bouwmeester. Creating and verifying a quantum superposition in a micro-optomechanical system. *New Journal of Physics*, 10(9):095020, sep 2008. 4

[KSB+17] Naftali Kirsh, Elisha Svetitsky, Alexander L. Burin, Moshe Schechter, and Nadav Katz. Revealing the nonlinear response of a tunneling two-level system ensemble using coupled modes. *Phys. Rev. Materials*, 1:012601, Jun 2017. 131, 135, 172

[KWO11] M. S. Khalil, F. C. Wellstood, and K. D. Osborn. Loss dependence on geometry and applied power in superconducting coplanar resonators. *IEEE Transactions on Applied Superconductivity*, 21(3):879–882, June 2011. 131

[LDA+20] Raphaël Lescanne, Samuel Deléglise, Emanuele Albertinale, Ulysse Réglade, Thibault Capelle, Edouard Ivanov, Thibaut Jacqmin, Zaki Leghtas, and Emmanuel Flurin. Irreversible qubit-photon coupling for the detection of itinerant microwave photons. *Phys. Rev. X*, 10:021038, May 2020. 159, 161, 163, 166

[LEBB12] Y. J. Y. Landkwarden, A. Endo, J. J. A. Baselmans, and M. P. Bruijn. Development of nbtin-al direct antenna coupled kinetic inductance detectors. *Journal of Low Temperature Physics*, 167:367–372, 2012. 106

[LGM+15] Jürgen Lisenfeld, Grigorij J Grabovskij, Clemens Müller, Jared H Cole, Georg Weiss, and Alexey V Ustinov. Observation of directly interacting coherent two-level systems in an amorphous material. *Nature communications*, 6:6182, 2015. 131

[LHC+09] T. Lindström, J. E. Healey, M. S. Colclough, C. M. Muirhead, and A. Ya. Tzalenchuk. Properties of superconducting planar resonators at millikelvin temperatures. *Phys. Rev. B*, 80:132501, Oct 2009. 131

[LLGF+17] Rick Leijssen, Giada R. La Gala, Lars Freisem, Juha T. Muhonen, and Ewold Verhagen. Nonlinear cavity optomechanics with nanomechanical thermal fluctuations. *Nature Communications*, 8, 2017. 160

[Max73] J. C. Maxwell. *A Treatise on Electricity and Magnetism*. Clarendon Press, 1873. 3

[MBK14] John M. Martinis, Rami Barends, and Alexander N. Korotkov. Calculation of coupling capacitance in planar electrodes, 2014. 62

[MFL13] Olivier Morin, Claude Fabre, and Julien Laurat. Experimentally accessing the optimal temporal mode of traveling quantum light states. *Phys. Rev. Lett.*, 111:213602, Nov 2013. 155, 157

[MKP+17] Riccardo Manenti, Anton F. Kockum, Andrew Patterson, Tanja Behrle, Joseph Rahamim, Giovanna Tancredi, Franco Nori, and Peter J. Leek. Circuit quantum acoustodynamics with surface acoustic waves. *Nature Communications*, 8, 2017. 35

[MWG+20] L. McCuller, C. Whittle, D. Ganapathy, K. Komori, M. Tse, A. Fernandez-Galiana, L. Barsotti, P. Fritschel, M. MacInnis,

F. Matichard, K. Mason, N. Mavalvala, R. Mittleman, Haocun Yu, M. E. Zucker, and M. Evans. Frequency-dependent squeezing for advanced ligo. *Phys. Rev. Lett.*, 124:171102, Apr 2020. 4

[NH01] E. F. Nichols and G. F. Hull. A preliminary communication on the pressure of heat and light radiation. *Phys. Rev. (Series I)*, 13:307–320, Nov 1901. 3

[NRO+99] G. Nogues, A. Rauschenbeutel, S. Osnaghi, M. Bruno, J. M. Raimond, and S. Haroche. Seeing a single photon without destroying it. *Nature*, 400:239–242, 1999. 161

[NSH+16] A. Narla, S. Shankar, M. Hatridge, Z. Leghtas, K. M. Sliwa, E. Zalys-Geller, S. O. Mundhada, W. Pfaff, L. Frunzio, R. J. Schoelkopf, and M. H. Devoret. Robust concurrent remote entanglement between two superconducting qubits. *Phys. Rev. X*, 6:031036, Sep 2016. 164

[NTM+17] William Hvidtfelt Padkær Nielsen, Yeghishe Tsaturyan, Christoffer Bo Møller, Eugene S. Polzik, and Albert Schliesser. Multimode optomechanical system in the quantum regime. *Proceedings of the National Academy of Sciences*, 114(1):62–66, 2017. 4

[NYA+16] Atsushi Noguchi, Rekishu Yamazaki, Manabu Ataka, Hiroyuki Fujita, Yutaka Tabuchi, Toyofumi Ishikawa, Koji Usami, and Yasunobu Nakamura. Ground state cooling of a quantum electromechanical system with a silicon nitride membrane in a 3d loop-gap cavity. *New Journal of Physics*, 18(10):103036, oct 2016. 53

[OAB+08] Aaron D. O'Connell, M. Ansmann, R. C. Bialczak, M. Hofheinz, N. Katz, Erik Lucero, C. McKenney, M. Neeley, H. Wang, E. M. Weig, A. N. Cleland, and J. M. Martinis. Microwave dielectric loss at single photon energies and millikelvin temperatures. *Appl. Phys. Lett.*, 92(11):112903, 2008. 131

[OHA+10] A. D. O'Connell, M. Hofheinz, M. Ansmann, Radoslaw C. Bialczak, M. Lenander, Erik Lucero, M. Neeley, D. Sank, H. Wang, M. Weides, J. Wenner, John M. Martinis, and A. N. Cleland. Quantum ground state and single-phonon control of a mechanical resonator. *Nature*, 464:697–703, 2010. 4, 35

[OKDP+18] C. F. Ockeloen-Korppi, E. Damskägg, J.-M. Pirkkalainen, M. Asjad, A. A. Clerk, F. Massel, M. J. Wooley, and M. A. Sillanpää. Stabilized entanglement of massive mechanical oscillators. *Nature*, 556:478–482, 2018. 4

[Pen14] Roger Penrose. On the gravitization of quantum mechanics 1: Quantum state reduction. *Foundations of Physics*, 44:557–575, 2014. 4

[Phi87] W.A. Phillips. Two-level states in glasses. *Reports on Progress in Physics*, 50:1657–1708, December 1987. 136

[PO10] Hanhee Paik and Kevin D. Osborn. Reducing quantum-regime dielectric loss of silicon nitride for superconducting quantum circuits. *Appl. Phys. Lett.*, 96(7):072505, 2010. 131

[PSL+13] P. Paulitschke, N. Seltner, A. Lebedev, H. Lorenz, and E. M. Weig. Size-independent young's modulus of inverted conical gaas nanowire resonators. *Applied Physics Letters*, 103(26):261901, 2013. 35

[PTSL13] T. A. Palomaki, J. D. Teufel, R. W. Simmonds, and K. W. Lehnert. Entangling mechanical motion with microwave fields. *Science*, 342(6159):710–713, 2013. 4

[QMC+14] C. M. Quintana, A. Megrant, Z. Chen, A. Dunsworth, B. Chiaro, R. Barends, B. Campbell, Yu Chen, I.-C. Hoi, E. Jeffrey, J. Kelly, J. Y. Mutus, P. J. J. O'Malley, C. Neill, P. Roushan, D. Sank, A. Vainsencher, J. Wenner, T. C. White, A. N. Cleland, and John M. Martinis. Characterization and reduction of microfabrication-induced decoherence in superconducting quantum circuits. *Appl. Phys. Lett.*, 105(6):062601, 2014. 131

[Rau03] James C. Rautio. Planar electromagnetic analysis. *IEEE Microwave Magazine*, 4:35–45, 2003. 62

[RBMC04] D. Rugar, R. Budakian, H. J. Mamin, and B. W. Chui. Single spin detection by magnetic resonance force microscopy. *Nature*, 430:329–332, 2004. 5

[RFAmca+19] C. Reetz, R. Fischer, G.G.T. Assump ç ao, D.P. McNally, P.S. Burns, J.C. Sankey, and C.A. Regal. Analysis of membrane phononic crystals with wide band gaps and low-mass defects. *Phys. Rev. Applied*, 12:044027, Oct 2019. 36, 144

[RMBS16] Christoph Reinhardt, Tina Müller, Alexandre Bourassa, and Jack C. Sankey. Ultralow-noise sin trampoline resonators for sensing and optomechanics. *Phys. Rev. X*, 6:021001, Apr 2016. 36

[RMT+17] A. P. Reed, K. H. Mayer, J. D. Teufel, L. D. Burkhart, W. Pfaff, M. Reagor, L. Sletten, R. J. Ma, X. ad Schoelkopf, E. Knill, and K. W. Lehnert. Faithful conversion of propagating quantum information to mechanical motion. *Nature Physics*, 13:1163–1167, 2017. 159, 160

[RSN+16] Ralf Riedinger, Hong Sungkun, Richard A. Norte, Joshua A. Slater, Juying Shang, Alexander G. Krause, Vikas Anant, Markus Aspelmeyer, and Simon Gröblacher. Non-classical correlations between single photons and phonons from a mechanical oscillator. *Nature*, 530:313–316, 2016. 160

[SBO+11] Jeremy M Sage, Vladimir Bolkhovsky, William D Oliver, Benjamin Turek, and Paul B Welander. Study of loss in superconducting coplanar

waveguide resonators. *Journal of Applied Physics*, 109(6):063915, 2011. 131

[SDZ+12] E. Smith, R. De Alba, N. Zhelev, R. Bennett, V.P. Adiga, H.S. Solanki, V. Singh, M.M. Deshmukh, and J.M. Parpia. Compact, inexpensive coaxial terminations and wiring for low temperature rf applications. *Cryogenics*, 52(10):461 – 464, 2012. 75

[SE15] Eyob A. Sete and H. Eleuch. High-efficiency quantum state transfer and quantum memory using a mechanical oscillator. *Phys. Rev. A*, 91:032309, Mar 2015. 113

[SGB+95] J. A. Sidles, J. L. Garbini, K. J. Bruland, D. Rugar, O. Züger, S. Hoen, and C. S. Yannoni. Magnetic resonance force microscopy. *Rev. Mod. Phys.*, 67:249–265, Jan 1995. 5

[SHS+07] D. I. Schuster, A. A. Houck, J. A. Schreier, A. Wallraff, J. M. Gambetta, A. Blais, L. Frunzio, J. Majer, B. Johnson, M. H. Devoret, S. M. Girvin, and R. J. Schoelkopf. Resolving photon number states in a superconducting circuit. *Nature*, 445:515–518, 2007. 161

[SKB+19] A. B. Shkarin, A. D. Kashkanova, C. D. Brown, S. Garcia, K. Ott, J. Reichel, and J. G. E. Harris. Quantum optomechanics in a liquid. *Phys. Rev. Lett.*, 122:153601, Apr 2019. 35

[SKW+15] Sebastian T Skacel, Ch Kaiser, S Wuensch, Hannes Rotzinger, Alexander Lukashenko, Markus Jerger, Georg Weiss, Michael Siegel, and Alexey V Ustinov. Probing the density of states of two-level tunneling systems in silicon oxide films using superconducting lumped element resonators. *Appl. Phys. Lett.*, 106(2):022603, 2015. 131

[SMB+18] E. Serra, B. Morana, A. Borrielli, F. Marin, G. Pandraud, A. Pontin, G. A. Prodi, P. M. Sarro, and M. Bonaldi. Silicon nitride moms oscillator for room temperature quantum optomechanics. *Journal of Microelectromechanical Systems*, 27(6):1193–1203, 2018. 35

[SMVL19] L. R. Sletten, B. A. Moores, J. J. Viennot, and K. W. Lehnert. Resolving phonon fock states in a multimode cavity with a double-slit qubit. *Phys. Rev. X*, 9:021056, Jun 2019. 159

[SNCH+12] Amir H. Safavi-Naeini, Jasper Chan, Jeff T. Hill, Thiago P. Mayer Alegre, Alex Krause, and Oskar Painter. Observation of quantum motion of a nanomechanical resonator. *Phys. Rev. Lett.*, 108:033602, Jan 2012. 33

[SNCH+13] Amir H Safavi-Naeini, Jasper Chan, Jeff T Hill, Simon Gröblacher, Haixing Miao, Yanbei Chen, Markus Aspelmeyer, and Oskar Painter. Laser noise in cavity-optomechanical cooling and thermometry. *New Journal of Physics*, 15(3):035007, mar 2013. 33

[SNGH+13] Amir H. Safavi-Naeini, Simon Gröblacher, Jeff T. Hill, Jasper Chan, Markus Aspelmeyer, and Oskar Painter. Squeezed light from a silicon micromechanical resonator. *Nature*, 500:185–189, 2013. 4

[SPMdL+16] Cornelia Schwarz, Benjamin Pigeau, Laure Mercier de Lépinay, Aurélien G. Kuhn, Dipankar Kalita, Nedjma Bendiab, Laëtitia Marty, Vincent Bouchiat, and Olivier Arcizet. Deviation from the normal mode expansion in a coupled graphene-nanomechanical system. *Phys. Rev. Applied*, 6:064021, Dec 2016. 35

[SRA+08] A. Schliesser, R. Rivière, G. Anetsberger, O. Arcizet, and T. J. Kippenberg. Resolved-sideband cooling of a micromechanical oscillator. *Nature Physics*, 4:415–419, 2008. 4, 35

[SRB+16] Bahman Sarabi, Aruna N Ramanayaka, Alexander L Burin, Frederick C Wellstood, and Kevin D Osborn. Projected dipole moments of individual two-level defects extracted using circuit quantum electrodynamics. *Phys. Rev. Lett.*, 116(16):167002, 2016. 131

[Ste86] Stig Stenholm. The semiclassical theory of laser cooling. *Rev. Mod. Phys.*, 58:699–739, Jul 1986. 3

[SYS+19] Itay Shomroni, Amir Youssefi, Nick Sauerwein, Liu Qiu, Paul Seidler, Daniel Malz, Andreas Nunnenkamp, and Tobias J. Kippenberg. Two-tone optomechanical instability and its fundamental implications for backaction-evading measurements. *Phys. Rev. X*, 9:041022, Oct 2019. 158

[TBPS17] Y. Tsaturyan, A. Barg, E.S. Polzik, and A. Schliesser. Ultracoherent nanomechanical resonators via soft clamping and dissipation dilution. *Nature Nanotechnology*, 12:776–783, 2017. 36, 41, 48, 98, 144, 152

[TDCB+09] J. D. Teufel, T. Donner, M. A. Castellanos-Beltran, J. W. Harlow, and K. W. Lehnert. Nanomechanical motion measured with an imprecision below that at the standard quantum limit. *Nature Nanotechnology*, 4:820–823, 2009. 26, 35, 54

[TdL+11] J. D. Teufel, T. donner, Dale Li, J. W. Harlow, M. S. Allman, K. Cicak, A. J. Sirois, J. D. Whittaker, K. W. Lehnert, and R. W. Simmonds. Sideband cooling of micromechanical motion to the quantum ground state. *Nature*, 475:359–363, 2011. 4, 11, 35, 54, 114, 143, 152

[TYW74] S. Timoshenko, D. H. Young, and W. Weaver. *Vibrational Problems in Engineering*. New York: John Wiley and Sons, 1974. 36

[UWK09] Quirin P. Unterreithmeier, Eva M. Weig, and Jörg P. Kotthaus. Universal transduction scheme for nanomechanical systems based on dielectric forces. *Nature*, 458:1001–1004, April 2009. 53, 55, 62

[VKG+12] Michael R. Vissers, Jeffrey S. Kline, Jiansong Gao, David S. Wisbey, and David P. Pappas. Reduced microwave loss in trenched superconducting coplanar waveguides. *Appl. Phys. Lett.*, 100(8):082602, 2012. 131

[VS14] L. G. Villanueva and S. Schmid. Evidence of surface loss as ubiquitous limiting damping mechanism in sin micro- and nanomechanical resonators. *Phys. Rev. Lett.*, 113:227201, Nov 2014. 39, 40, 41

[WBB+11] J. Wenner, R. Barends, R. C. Bialczak, Yu Chen, J. Kelly, Erik Lucero, Matteo Mariantoni, A. Megrant, P. J. J. O'Malley, D. Sank, A. Vainsencher, H. Wang, T. C. White, Y. Yin, J. Zhao, A. N. Cleland, and John M. Martinis. Surface loss simulations of superconducting coplanar waveguide resonators. *Appl. Phys. Lett.*, 99(11):113513, 2011. 131

[WBL+17] Matthew J. Weaver, Frank Buters, Fernando Luna, Hedwig Eerkens, Kier Heeck, Sven de Man, and Dirk Bouwmeester. Coherent optomechanical state transfer between disparate mechanical resonators. *Nature Communications*, 8:824, 2017. 36

[WHW+09] H. Wang, M. Hofheinz, J. Wenner, M. Ansmann, R. C. Bialczak, M. Lenander, Erik Lucero, M. Neeley, A. D. O'Connell, D. Sank, M. Weides, A. N. Cleland, and John M. Martinis. Improving the coherence time of superconducting coplanar resonators. *Appl. Phys. Lett.*, 95(23):233508, 2009. 5, 131

[WRD+10] S. Weis, R. Rivière, S. Deléglise, E. Gavartin, O. Arcizet, A. Schliesser, and T. J. Kippenberg. Optomechanically induced transparency. *Science*, 330:1520–1523, 2010. 96

[WRNZK07] I. Wilson-Rae, N. Nooshi, W. Zwerger, and T. J. Kippenberg. Theory of ground state cooling of a mechanical oscillator using dynamical backaction. *Physical Review Letters*, 99:093901, 2007. 16

[YBE+11] S. J. C. Yates, J. J. A. Baselmans, A. Endo, R. M. J. Janssen, L. Ferrari, P. Diener, and A. M. Baryshev. Photon noise limited radiation detection with lens-antenna coupled microwave kinetic inductance detectors. *Applied Physics Letters*, 99(7):073505, 2011. 106

[YCS15] Mingyun Yuan, Martijn A. Cohen, and Gary A. Steele. Silicon nitride membrane resonators at millikelvin temperatures with quality factors exceeding 108. *Applied Physics Letters*, 107(26):263501, 2015. 35, 103

[YPR12] P.-L. Yu, T. P. Purdy, and C. A. Regal. Control of material damping in high-q membrane microresonators. *Phys. Rev. Lett.*, 108:083603, Feb 2012. 40

[YSBS15] Mingyun Yuan, Vibhor Singh, Yaroslav M. Blanter, and Gary A. Steele. Large cooperativity and microkelvin cooling with a three-dimensional optomechanical cavity. *Nature Communications*, 6(8491), 2015. 53

[ZSJ+08] B. M. Zwickl, W. E. Shanks, A. M. Jayich, C. Yang, A. C. Bleszynski Jayich, J. D. Thompson, and J. G. E. Harris. High quality mechanical and optical properties of commercial silicon nitride membranes. *Applied Physics Letters*, 92(10):103125, 2008. 5

Thibault Capelle **Unknown**

Electromechanical cooling and parametric amplification of an ultrahigh-Q mechanical oscillator

Abstract:

Keywords: optomechanics, silicon nitride, MEMS, microwave cavity, cryogenics, quantum ground state, optical cooling, quantum backaction, mechanical Fock state.

Résumé :

Mots clés : optomécanique, nitrure de silicium, MEMS, cavité micro-onde, cryogénie, état quantique fondamental, refroidissement optique, état de Fock mécanique.